

Advanced Structured Materials

J. M. P. Q. Delgado *Editor*

# Industrial and Technological Applications of Transport in Porous Materials

 Springer

# **Advanced Structured Materials**

Volume 36

*Series Editors*

Andreas Öchsner

Lucas F. M. da Silva

Holm Altenbach

For further volumes:

<http://www.springer.com/series/8611>

J. M. P. Q. Delgado  
Editor

# Industrial and Technological Applications of Transport in Porous Materials

 Springer

*Editor*

J. M. P. Q. Delgado  
LFC-Laboratorio de Física das  
Faculdade de Engenharia  
Universidade do Porto  
Porto  
Portugal

ISSN 1869-8433                      ISSN 1869-8441 (electronic)  
ISBN 978-3-642-37468-5            ISBN 978-3-642-37469-2 (eBook)  
DOI 10.1007/978-3-642-37469-2  
Springer Heidelberg New York Dordrecht London

Library of Congress Control Number: 2013946215

© Springer-Verlag Berlin Heidelberg 2013

This work is subject to copyright. All rights are reserved by the Publisher, whether the whole or part of the material is concerned, specifically the rights of translation, reprinting, reuse of illustrations, recitation, broadcasting, reproduction on microfilms or in any other physical way, and transmission or information storage and retrieval, electronic adaptation, computer software, or by similar or dissimilar methodology now known or hereafter developed. Exempted from this legal reservation are brief excerpts in connection with reviews or scholarly analysis or material supplied specifically for the purpose of being entered and executed on a computer system, for exclusive use by the purchaser of the work. Duplication of this publication or parts thereof is permitted only under the provisions of the Copyright Law of the Publisher's location, in its current version, and permission for use must always be obtained from Springer. Permissions for use may be obtained through RightsLink at the Copyright Clearance Center. Violations are liable to prosecution under the respective Copyright Law. The use of general descriptive names, registered names, trademarks, service marks, etc. in this publication does not imply, even in the absence of a specific statement, that such names are exempt from the relevant protective laws and regulations and therefore free for general use.

While the advice and information in this book are believed to be true and accurate at the date of publication, neither the authors nor the editors nor the publisher can accept any legal responsibility for any errors or omissions that may be made. The publisher makes no warranty, express or implied, with respect to the material contained herein.

Printed on acid-free paper

Springer is part of Springer Science+Business Media ([www.springer.com](http://www.springer.com))



# Preface

In the last years, several transport processes (namely, heat and mass transfer) textbooks have been published. Transport processes in porous materials is a field of great technological and industrial interest and the applied research in heat and mass transfer in porous materials has generated increasing interest over the past five decades because of the importance of porous materials and transport processes in many engineering applications. A large amount of literature has been generated on this subject and significant advances have been made in modelling fluid flow and heat and mass transfer through porous materials.

The purpose of this book, *Industrial and Technological Applications of Transport in Porous Materials*, is to provide a collection of recent contributions in the field of heat and mass transfer in porous media and their industrial and technological applications.

The main benefit of the book is that it discusses some of the most important topics related to transport phenomenon in engineering and their future applications. It includes a set of new technological applications in the field of heat and mass transfer phenomena in a porous medium domain, such as drying technology, filtration, infrared thermography, energy, recycling, etc. At the same time, these topics will be encountered in a variety of scientific and engineering disciplines, such as chemical, civil, agricultural, mechanical engineering, etc. The book is divided into several chapters that intend to be a resume of the current state of knowledge for the benefit of professional colleagues.

J. M. P. Q. Delgado

# Contents

<b>Cyclone: Their Characteristics and Drying Technological Applications</b> . . . . .	1
S. R. Farias Neto, F. P. M. Farias, J. M. P. Q. Delgado, A. G. Barbosa de Lima and A. L. Cunha	
<b>Moisture Transport Process in Vegetable Fiber Composites: Theory and Analysis for Technological Applications</b> . . . . .	37
L. H. Carvalho, E. L. Canedo, S. R. Farias Neto, A. G. Barbosa de Lima and C. J. Silva	
<b>Filtration Processes and Design of Filters</b> . . . . .	63
Antonio F. Miguel	
<b>Infrared Thermography Application in Buildings Diagnosis: A Proposal for Test Procedures</b> . . . . .	91
E. Barreira, S. S. de Freitas, V. P. de Freitas and J. M. P. Q. Delgado	
<b>Heat Transfer Behaviors of Thermal Energy Storages for High Temperature Solar Systems</b> . . . . .	119
A. Andreozzi, B. Buonomo, O. Manca, S. Nardini and S. Tamburrino	
<b>Recycling Polyurethane Foam and its Use as Filler in Renovation Mortar with Thermal Insulating Effect</b> . . . . .	141
V. Václavík, T. Dvorský, V. Dirner, J. Daxner, J. Valíček, M. Harničárová, M. Kušnerová, P. Košťál and M. Bendová	
<b>Thermal Storage Materials for Enhancing Indoor-Dwelling Temperature Conditions</b> . . . . .	171
Germán Ferreira, Ana M. López-Sabirón and Alfonso Aranda-Usón	

<b>Magnetic Silica Nanocomposites as Optical Tools in Biomedical Applications</b> . . . . .	189
Tinkara Mastnak, Matejka Turel, Aljoša Košak, Špela Korent Urek and Aleksandra Lobnik	
<b>Simulation of Precipitate Evolution in Fe-Based Alloys.</b> . . . . .	215
V. V. Popov	

# Cyclone: Their Characteristics and Drying Technological Applications

S. R. Farias Neto, F. P. M. Farias, J. M. P. Q. Delgado,  
A. G. Barbosa de Lima and A. L. Cunha

**Abstract** Cyclone is one of the most widely known device being extensively used to separate particles from a gas stream, and more recently as a modern drying technology (cyclonic dryer). In this sense, this chapter aim to briefly discuss disperse multiphase flow and heat and mass transfer theory in a cyclone as dryer, focusing principle of operation, design and selection, overall collection efficiency, particle–particle and fluid-particle interactions, particle residence time and, performance to moisture removal of moist particles. A transient three-dimensional mathematical modeling to predict fluid flow fields, particle trajectory, and gas-particle interactions (heat and mass transfer, dimensions variations and force effects) is presented and discussed. Application to sugar and alcohol industry (sugar-cane bagasse drying) has been done, and predicted results are compared with experimental data.

---

S. R. Farias Neto · A. L. Cunha  
Department of Chemical Engineering, Federal University of Campina Grande, Av. Aprígio Veloso, 882, Bodocongó, Campina Grande, PB 58429-900, Brazil  
e-mail: fariasn@deq.ufcg.edu.br

A. L. Cunha  
e-mail: actolimacunha@yahoo.com.br

F. P. M. Farias  
Department of Technology and Development, Federal University of Campina Grande, Sumé, PB, Brazil  
e-mail: fabianapimentel@ufcg.edu.br

J. M. P. Q. Delgado  
LFC—Building Physics Laboratory, Civil Engineering Department, Faculty of Engineering, University of Porto, Porto, Portugal  
e-mail: jdelgado@fe.up.pt

A. G. B. de Lima (✉)  
Department of Mechanical Engineering, Federal University of Campina Grande, Av. Aprígio Veloso, 882, Bodocongó Zip Code: 58429-900 Campina Grande, PB, Brazil  
e-mail: gilson@dem.ufcg.edu.br

**Keywords** Cyclone dryer · Sugar-cane bagasse · Disperse multiphase flow · Numerical simulation

## 1 Introduction

Disperse multiphase flows frequently occurs in different chemical, mechanical and thermal processes, for example, gas-particle or gas-droplet flows, coal combustion, pneumatic conveying, and erosion phenomena [1]. In these flows a gaseous continuous phase is seeded with droplets or particle (disperse phase) and in which it is necessary to evaluate the relative motion between them, in order, to evaluate the performance of the system or device. Further, the particle–particle interactions play an important role in determining flow pattern [2].

Several industrial processes, such as mineral processing, petroleum refining, food processing, environmental cleaning and chemical processes, requires particles separation from liquids or gas streams. Thus, different technologies, including fabric filters, scrubber, electrostatic precipitations, air classifiers, cyclone and hydrocyclone separations has been used for liquid–solid, liquid–liquid and gas–solid separations, and air pollution control [3–16].

Drying is one of the oldest and most popular process used in the agricultural products, and food, mineral, polymer, chemical, textile and pharmaceutical products industries.

There are different types of dryers (band, flash, conveyor, drum, fluid-bed, vacuum, rotary, spray and cyclone dryers). They are of diverse sizes, shapes and varieties. Because of particular characteristics of the material to be dried, each group of material is dried in a specific dryer (or class of dryers), in ways batch as continuous operation [17]. The movement of gaseous fluids through of a particle bed is inherent to drying unit operations. In the convective drying, the heated drying air and material (cold and moist) being dried are in an intimate contact continuously. Thus, heat is supplied to material, being responsible to increase the temperature and evaporate moisture of it.

The moisture evaporated at the surface of material (or into the material but that moves to surface) is carried out by fluid (drying air) flowing around of material. Obviously, in a porous particles bed inside the dryer, heat transfer occurs between particles, and between particles and dryer walls. Thus, temperature of the material is changed also because of these thermal effects.

Despite of the importance to study the different types of dryers, herein, special attention is given to more recent one, the cyclonic dryer.

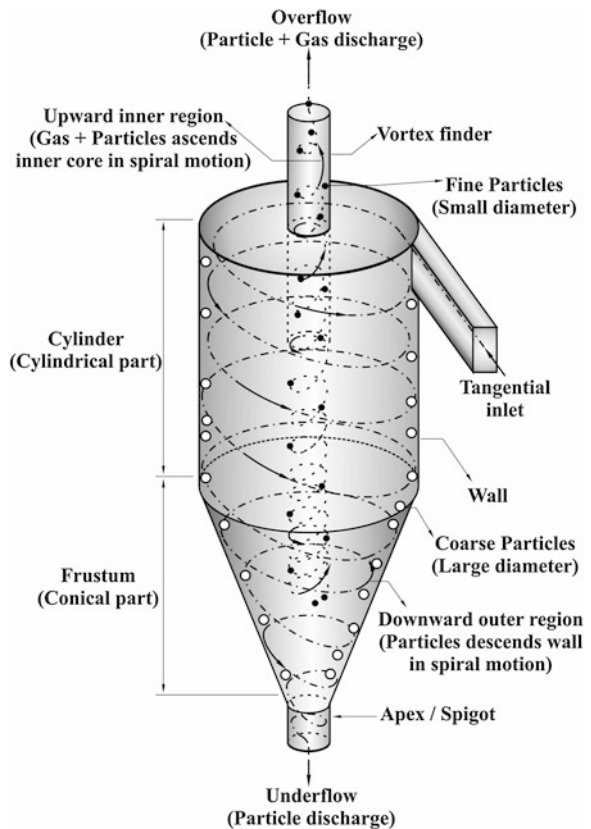
## 2 Cyclone

### 2.1 Basic Concepts

Cyclone is simple mechanical equipment with no moving parts, that operates by the action of centrifugal, gravitational and drag forces. A typical schematic diagram of a most commonly used, tangential inlet and reverse flow cyclone is illustrated in Fig. 1.

On the basis of the Fig. 1, the principle of operation is described following. The cyclone works by inducing a strongly swirling turbulent flow which is used to separate phases with different densities (a two-phase system). This two-phase mixture (fluid-particle) entering under pressure in the top of the cylindrical body of the cyclone by one tangential inlet (rectangular or circular) generates a complex three-dimensional swirling motion (spinning motion) within the cyclone, which forces particles (denser phase) toward the outer wall (because of their inertia forces) where they collide, lose momentum, and spiral in the downward direction.

**Fig. 1** Schematic diagram of a cyclone geometry and representative nomenclature



Following, the particles are collected in the outlet located at the base of the conical section of the cyclone (underflow). From this separation, gas phase moves upward in the central core and leaves the cyclone through the gas outlet tube at the top, so-called vortex finder (overflow). The vortex finder protrudes within the cyclone body for two reasons: to shield the inner vortex from the high inlet velocity, and to stabilize it [18].

Depending upon of the particle diameter, fine particles (smaller particles) are carried out by gas stream, and leave through the top.

The forces acting on a particle are either fluid dynamic or external-field forces. They include gravity, drag and centrifugal forces, the force resulting from the local velocity gradient of the fluid (the Saffman force), the force resulting from the pressure gradient (Faxen force) and force created by rotation of the particle (Magnus force). Sometimes, magnetic and electrostatic forces, and forces due to high acceleration rate in the fluid or particle (Basset force) may appear too. The Saffman, Magnus and Faxen forces are considered lift forces.

If a particle rotates transverse pressure differences appear on the surface of the particle that has resulted in additional forces (Magnus force or slip-rotation lift). The direction of this force is perpendicular to the plane of the relative velocity and the axis of rotation [19, 20].

According to Blei and Sommerfield [19], the Saffman force (or slip-shear lift) is create by shear gradients in the flow that lead to pressure gradients across the particle surface; it acts in a direction perpendicular to the velocity gradient. When the velocity of the particle is less than that of the gas phase, the Saffman force vector will point towards the axis of the cyclone, whereas it will point to the surface of the wall if the particle velocity is greater than that of the gas phase. This force can be negligible for fine particle and very small particle Reynolds number and/or low shear rates [21, 22].

The Faxen forces appear in nonuniform shear field, especially near the wall. This force is significant in particles of large diameter and high pressure gradients, for example, in shock waves. This force act in a direction perpendicular the plane defined by the relative velocity vector and the shear vector [21].

When the flow (or the particle) is accelerated at a high rate, there is a temporal delay in boundary layer development (transient effect). The Basset forces represent this transient and enhanced viscous drag effect [21]. Besides, the flow within the cyclone leads to a very large number of particle–particle and particle–wall collisions. Thus, interaction forces among the particles and interaction forces between the particles and wall surface of the cyclone occurs too.

According to Brennen et al. [2] and Kleinstreuer [21], interaction particle–particle affect individual particle trajectories and fluid flow between neighboring particles that may result in nonuniform spatial distribution of the particles. The particle–wall interaction may occur by direct impacting, interception, bouncing, rolling, and resuspension. These two-way coupling phenomena may cause particle deformation, particle aggregation or particle fission (break), and to affect particle residence time and collection efficiency of the cyclone. In turbulent flow, particle agglomeration occur, especially for small particle in the size range about 1–10  $\mu\text{m}$ , where Brownian

motion and gravitational setting can be negligible compared to turbulence-induced motion, and in higher inlet particle concentration [23, 24]. Additional comments about particles interactions can be found in Oweis et al. [25].

The competitions among the forces cited are responsible by the complex gas–solid flow pattern within the cyclone and the separation efficiency of this device. In general, it is accepted that all the forces can be treated separated, thus, the principle of superposition can be applied to calculate the magnitude of the overall force acting on the particle [19].

From this comprehensive explanation, swirl and turbulence are the two competing mechanisms that affect the separation process. According to Derksen et al. [26] the swirl induces a centrifugal force on the particulate phase which is the driving force behind the separation; turbulence disperses the particulate phase and enhances the probability that particles get caught in the exit stream (gas phase). This complex two-phase system is useful as it promote an intimate contact between the particles and the fluid (gas) and the particles and wall of the cyclone which facilitate, for example, the heat and mass transfer coupling phenomena between them.

Cyclone presents many advantages such as: few maintenance problems, low operating and capital cost, temperature and pressure limitation occurs only by the materials of constructions, it can be designed to handle a wider range of operation conditions, relatively low operating pressure drop, dry collection and disposal, low particle residence time, and requires relative small physical space. The following disadvantages can be cited: inefficiency for collecting smaller particles ( $<5\text{--}10\ \mu\text{m}$  in diameter), when operating with large gas flow rates require multiple-unit or other designs, not suitable for collecting sticky materials that would tend to cling in the interior wall, or other particle types that might tend to agglomerate and clog the exit duct, and require secondary collector to meet emissions control regulations [11, 27–30].

Mainly because of their simple structure, high separation efficiency, low cost and ease of operation, cyclone has been the oldest and most widely used equipment to separate dispersed particles from their carrying gases [8, 18, 23, 24, 26, 29, 31–41] and more recently as modern drying technology (dryer) [2, 5, 10, 11, 15–17, 24, 38, 41–44].

However, due to the extremely complex 3D swirling flows within the cyclone, to understand the separation process is crucial and it is still not completely explained. An understanding of this mechanism is essential to help in the design of the new cyclone more efficiently to operate, mainly with high inlet particle concentrations.

## ***2.2 Selection and Design of Cyclone***

Cyclone design consists of selecting an ideal configuration to be used based in particle size, separation efficiency, pressure drop, energy requirement, and cost.



There is different configuration of cyclone available in the literature that offers different performance for this device (Fig. 2).

The optimization of cyclone dimensions and configuration is, however, mainly determined by experiment, because the analyses of multiphase flow (particle and gas) are very complex. Besides, numerical calculation has been conducted too, however, by assuming severs hypothesis.

### 2.3 Collection Efficiency (Separation Performance)

Collection efficiency is one of the most important parameters used in evaluating the performance of a cyclone. Separation efficiency is affected by different parameters such as inlet particle concentration, inlet mixture velocity, cyclone geometry, wall roughness of the cyclone, particle diameter, particle density, particle–particle and particle–wall interactions, and other effects.

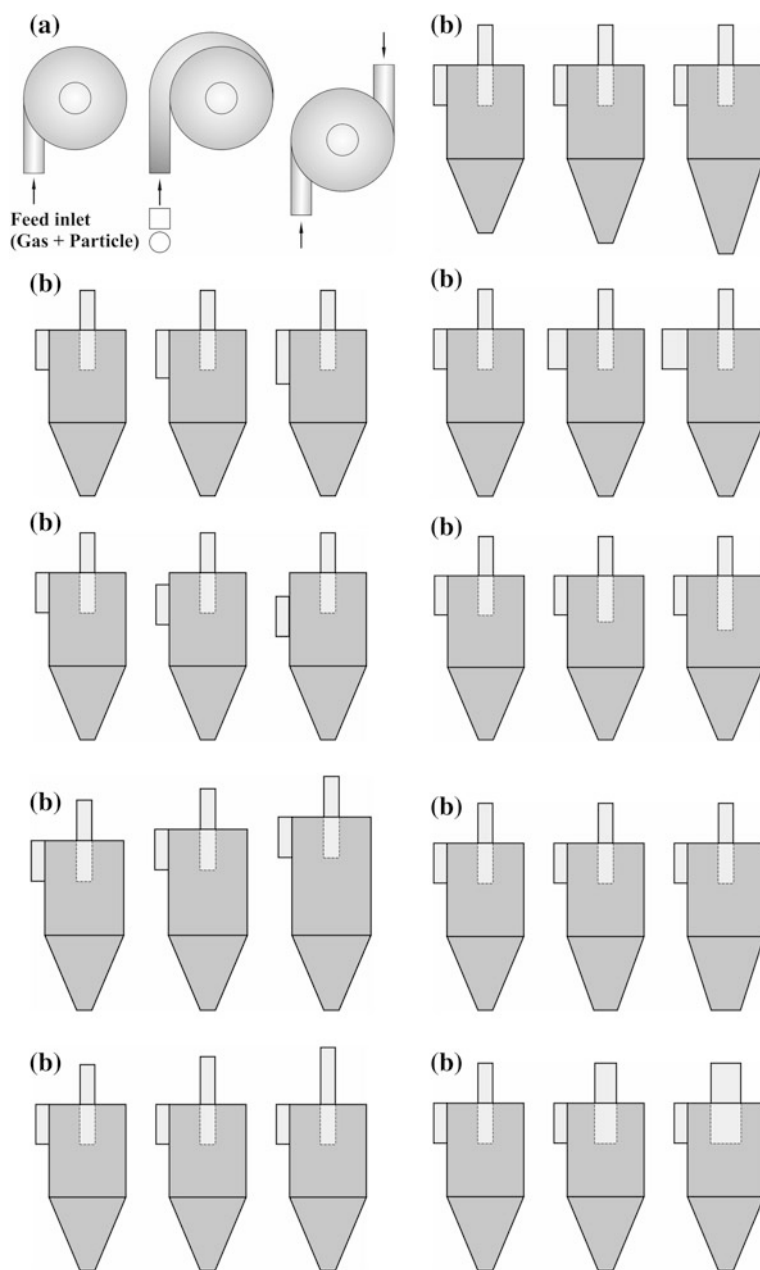
There is two ways for specify the ability of a cyclone to separate solid particle from gas stream: cut size and the particle separation efficiency. Thus, many theories have been used to predict the cyclone efficiency, consequently, various theoretical equations to calculate collection efficiency has been reported in the literature [18, 32, 35, 45, 46]. In these theories, the authors each have considered different hypothesis such as: gravitational forces negligible compared to centrifugal forces, gas density negligible compared to particle density, spherical particles, of small size and low relative velocity, relative velocity is purely radial, and radial acceleration and radial velocity of gas negligible.

The particle cut size is defined like the size of the smallest particle that is theoretically separated from the gas stream, and thus, it will be collected. On the other hand, particle collection efficiency is defined as the fraction of the inlet flow rate of solids separated in the cyclone, i.e., ratio of particles collected to particles injected. Since a cyclone usually collects particles with different sizes and shapes, it is common to calculate different efficiencies, each defined for a particular and narrow interval of particle sizes [18, 47].

Imagining indefinitely small intervals, we get a fractional or grade-efficiency of the cyclone  $\eta(\overline{dp})$  for a particle of size  $\overline{dp}$ . Thus if  $f(\overline{dp})$  is the particle size distribution at the cyclone inlet, we can calculate the overall collection efficiency as follows [18, 47].

$$\eta = \int_0^{\infty} f(\overline{dp})\eta(\overline{dp})d\overline{dp} \quad (1)$$

The overall collection efficiency can be defined still as the mass of particles removed divided by the mass entering the cyclone per unit time. It can be calculated by integrating the grade-efficiency over the particle size distribution as follows [28]:



**Fig. 2** Different cyclone configurations. **a** Tangential inlet arrangements. **b** Body arrangements

$$\eta = \int_0^1 \eta_i df \quad (2)$$

where  $f$  is the mass fraction of solids less than that size in the feed stream and  $\eta_i$  is the grade-efficiency.

Several modeling approaches to determine grade-efficiency  $\eta_i$  has been reviewed by Licht [48], Leith and Licht [10], Hashemi [27], Kanaoka et al. [47] and Cortés and Gil [18].

Tan [37] reports a model to predict the fractional efficiency of a cyclone with tangential inlet. For this author, the total efficiency of this cyclone to separate particles with a diameter  $d_p$  from a gas stream can be calculates as:

$$\eta = 1 - \exp \left[ -\pi \left( \frac{\rho_p d_p^2 V}{18\mu} \right) \frac{(r_2 + r_1) L}{r_2 HW} \right] \quad (3)$$

where  $r_2$  and  $r_1$  are the radiuses of the outer and inner tubes, respectively. The parameters  $H$  and  $W$  are the height and width of the rectangular inlet, respectively. The effective separation length  $L$  correspond to distance from the center of the inlet ( $H/2$ ) to the end of the solid inner tube (the length of the annular chamber), and  $V$  is the average gas velocity at the cyclone inlet.  $\rho_p$  and  $d_p$  are density and diameter of the particles, respectively, and  $\mu$  represents the gas viscosity.

When many particles cyclones are in series, the total separation efficiency can be expressed as follows [47]:

$$\eta = 1 - (1 - \eta_1)(1 - \eta_2) \dots (1 - \eta_n) \quad (4)$$

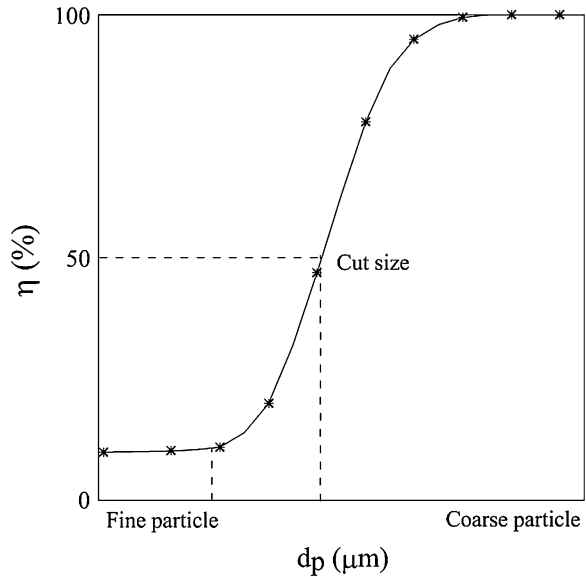
where  $\eta_1, \eta_2, \dots, \eta_n$ , are the separation cyclone efficiencies of the each cyclone, and  $n$  is the number of cyclones.

Figure 3 illustrates a typical curve (no scale) of cyclone separation efficiency as a function of particle diameter.

## 2.4 Pressure Drop

One of the most important parameters and major criteria used to evaluate the cyclone separation efficiency (cyclone performance) is the pressure drop inside the cyclone. An accurate prediction of cyclone pressure drop is very important because it relates to operating costs [32]. This parameter depends on the gas flow rate, gas temperature, solids loading, cyclone geometry, and particle properties. The total pressure drop over a cyclone consists of a sum of local losses and frictional losses. The following contributions can be cited: losses at the inlet (gas expansion loss), contraction losses at the entrance of the outlet tube (vortex finder) because of the abrupt flow area of the outlet tube, frictional loss in the double vortex within the separation space due to swirling (friction between the gas flow

**Fig. 3** Typical curve of collection efficiency



and the cyclone wall), and dissipation loss of the gas in the outlet. Among them, the expansion losses are of minor importance and the losses in the vortex finder present the largest results and represents about 80 % of the total pressure drop [18, 31, 32]. According to Hashemi [27], for a given feed flow rate, the pressure drop in spiral cyclones is lower than the pressure drop in tangential cyclones.

In general, the pressure drop over a cyclone is calculated by the difference of static pressure between the inlet pipe and outlet pipe at a given condition. For instance, the static pressure distribution at the inlet cross-section is uniform (no swirling motion), however, in the outlet pipe, this parameter is very different from its cross-sectional average due to the strong swirling flow. Thus, the dynamic pressure stored in the swirling motion may be significant [31].

In the tentative to help researcher and engineer, several empirical, theoretical and semi-theoretical formulae to calculate the pressure drop in a cyclone has been reported in the literature [17, 18, 27, 28, 31, 32, 49].

Most of these correlations focus on solid-free flow (clean gas). However, pressure drop decrease as the solid concentration increases [27, 28], but different behavior are detailed by Yang et al. [40]. According to the author, researches with solid loading are rather limited.

The calculations of pressure drop in a cyclone are required so that system power consumption can be estimated and also, in order, to select an adequate exhaust air fan.

According to Jumah and Mujumdar [28], cyclones are commercially in sizes to process 50–50,000  $\text{m}^3/\text{h}$ . When pressure drop range 0.5–1.0 kPa cyclone is considered of low-efficiency and for high-efficiency a range 2.0–2.5 kPa is expected. Gimbut et al. [32] reports that higher inlet velocities give higher collection

efficiencies for a given cyclone, but this also increase the pressure drop across the cyclone. Thus, combination of higher collection efficiency and low pressure drop is the goal, for a cyclone.

Besides, inlet velocities higher than 30 m/s cause turbulence which, in turn, leads to by passing and re-entrainment of separated particles and hence a decrease in efficiency [17]. Generally, the cyclone pressure drop is proportional to the velocity head as follows:

$$\Delta P = \alpha \frac{\rho_g V^2}{2} \quad (5)$$

where  $\rho_g$  is gas density, and  $\alpha$  and  $V$  are the pressure drop coefficient and the inlet velocity of the cyclone, respectively.

Dimensionless pressure drop coefficient  $\alpha$  is also called the Euler number, being dependent of the solid loading and properties, and cyclone geometry [18, 24, 26, 27, 31, 32, 36, 40, 49].

## 3 Cyclone Dryer: Heat and Mass Transfer and Multiphase Flow Theory

### 3.1 Background

Fundamentally, drying consists in a simultaneous heat and mass transfer phenomenon coupled with dimensions variations of the particle being dried. An appropriated dryer selection is related to drying cost, heat supply, energy saving, type and product quality, and an others important parameters [17, 42, 50, 51]. Strumillo and Kudra [51] reported different forms to classify dryers. One of them is based on hydrodynamic regime (active and no-active regime). Based on this classification, cyclone can be classified as dispersion dryer with active hydrodynamic regime (flowing stream).

For material with high sensitivity to heat both higher drying rate and lower residence time are the most essential drying parameters, in order, to reduce drying cost and to obtain the required final moisture content and high product quality of the dried material. In this sense, cyclone as dryer appears like an appropriated modern drying technology for provides drying of these disperse materials. Unfortunately, drying of moist particulate materials in cyclone has been little studied in the past and there are few reports available in the open access literature. Table 1 summarizes some different theoretical and experimental researches reported in the literature about cyclone as dryer.

From a review of literature, we verify that different parameters affect performance of the cyclone dryer and particle residence time, for example, cyclone geometry [52–55]. The cyclone dryer provides solid residence times from few seconds up to several minutes, thus facilitating drying operation and moisture

**Table 1** Different works that have used cyclone as dryer

Type of material	Drying conditions							Source		
	$T_i$ (°C)	$T_o$ (°C)	$M_i$ (% w.b.)	$M_o$ (% w.b.)	$d_p$ (mm)	$\theta_i$ (°C)	$\theta_o$ (°C)		$V_o$ (m/s)	$\frac{m_s}{m_w}$
Potatoes peeled slices	80.0	—	—	9.9	—	—	—	—	—	[56]
Silica gel	81.5	69.3	15.7	—	3.25	22.2	—	19–23	0.120	[57]
Sugar-cane bagasse	216.0	98.0	76.2	60.9	0.42–6.35	30.6	43.8	—	0.069	[53]
Residue of orange juice processing	202.1	183.5	70.9	54.0	1.00–8.00	29.8	44	—	—	[82]
S-PVC	150.0	40.0	30.0	0.2	0.15	—	38	16	—	[83]
Silica gel	150.0	113.0	20.0	6.8	0.21	—	—	15	0.050	[59]
Pinewood chips	312.0	71.0	54.0	12.8	—	—	—	—	—	[43]
Vimiflex (Polyvinyl formal ethylal resin)	Up to 145.0	40.0–60.0	30.0–50.0 (Up to 70.0)	10.0–27.0	—	—	—	—	—	[60]
Spent coffee grounds	165.4	118.9	48.8	34.4	0.70	30.3	48.1	6.1	0.020	[15]
Spent coffee grounds	160.8	84.2	94.6	76.09	—	38.1	45.5	—	0.070	[62]
Sand	70.0	—	—	—	0.30	—	—	20.1	0.240	[84]

$i$ —input,  $o$ —output,  $s$ —solid,  $w$ —water

removal. This device has been usually employed as a stand-alone-dryer and combined with other drying system, for example, pneumatic dryer. In the combined mode, the cyclone operates as cyclone separated [43, 56–61].

Early works confirmed that gas velocity, particle density, particles diameter, increase particle residence time, whereas it decreased for an increased solid–gas loading [53–55, 59]. On the other hand, Silva and Nebra [62] has considered particle shrinkage effect together heat and mass transfer and fluid flow within the cyclone dryer. According to these authors to consider shrinkage effect on the mathematical modeling provides poor results.

Besides, from analysis of the theoretical and experimental results published by the authors cited before, we verify that greatest variation in temperature and velocity takes place into the cyclone, specially, near the cyclone wall where high particles concentration is found and thus, heat transfer and friction effects are occurring more strongly.

Because of a lack of understanding of the highly complex flow patterns within the cyclone dryer and few data related in the literature, it has been designed using data correlation based on experience from existing installation and pilot plant tests.

Mathematical modeling and numerical prediction of the drying process by using cyclone dryer is a difficult task. Numerical analysis of drying process requires rigorous multiple and coupled nonlinear conservation and constitutive equation solutions. This is not a trivial mathematical problem to solve easily.

In present day, computational fluid dynamics (CFD) have now created to possibility of new related and accurate studies for these flows, including coupled heat and mass transfer, three-dimensional effects, swirl and rotation, given great improvements in modeling and in understanding of physical phenomena [53, 54, 57, 58, 63].

Now that we have discussed about drying of moist particulate material in cyclone dryer, the next step is to address discussion about modeling and simulation applied to drying process by using this drying equipment on an overall basis (macroscopic scale).

### ***3.2 Mathematical Modeling for Multiphase Flow***

For the study of multiphase systems, a distinction is usually made between systems of separated streams and dispersed flows. This distinction is a result of the required computational approach. We can distinguish the following computational strategies: Eulerian–Lagrangian approach and Eulerian–Eulerian approach. The first one is applied to very dilute flows where small discrete particles are considered in the control volume formulating the governing microscopic model equations. The second one is useful for dense flows where a relatively large number of particles are considered determining a continuous phase in the control volume formulating the governing microscopic model equations [64, 65].

According to Renade [64] in the Eulerian–Lagrangian approach the explicit motion of the interface is not modeled, which means small-scale fluid motions surrounding the particles are not considered. In this case, the continuous phase is treated as a continuum by solving the momentum equations, while the dispersed phase is solved by tracking each individual particle (solid, bubble, or droplet) using Newtonian equations of motion. In the Eulerian–Lagrangian approach, particle-level process such as reaction, heat and mass transfer, water evaporation and drying can be simulated with adequate detail. Moreover, this approach has some disadvantages, such as: Turbulent flow is necessary to use a large number of particle trajectories to obtain meaningful average which requires greater computational effort, thus limiting the volume fraction of the dispersed phase in the multiphase flow [64].

In the particular case of gas-particle flow in a cyclone dryer, which it is generally dominated by a dispersed flow, we can use the Eulerian–Lagrangian approach. In this approach, the trajectories of particles are obtained by solving an equation of motion for each particle, while the behavior of the continuous phase is modeled using the conservation equations of motion conventional. The behavior of the continuous phase is affected by motion of particles due to the viscous drag and other effects related to velocity difference between the particles and fluid. The viscous effect of the fluid tends to slow the movement of the particles.

The governing equations generally employed in the Eulerian–Lagrangian approach following are presented.

### 3.2.1 Continuous Phase

The liquid or gas phase is solved with the standard mass and momentum transport equations written as follows:

Conservation of Mass

$$\frac{\partial \rho}{\partial t} + \nabla \cdot (\rho \vec{V}) = 0 \quad (6)$$

where  $\rho$  is the fluid density,  $\vec{V}$  is the velocity vector and  $t$  is the time.

Conservation of Momentum

$$\frac{\partial(\rho \vec{V})}{\partial t} + \nabla \cdot (\rho \vec{V} \otimes \vec{V}) = -\nabla P + \nabla \cdot \tau + S_M \quad (7)$$

where  $P$  is the pressure,  $S_M$  is the momentum source and  $\tau$  is the shear stress defined as:



$$\tau = \mu \left[ \nabla \vec{V} + (\nabla \vec{V})^T - \frac{2}{3} \delta \nabla \cdot \vec{V} \right] \quad (8)$$

where  $\mu$  is the dynamic viscosity,  $\delta$  is Kronecker Delta function.

In the Eq. (7), the dyadic operator (or tensor product) of two vectors  $\vec{V}$  and  $\vec{V}'$  is given by:

$$\vec{V} \otimes \vec{V}' = \begin{bmatrix} V_x V'_x & V_x V'_y & V_x V'_z \\ V_y V'_x & V_y V'_y & V_y V'_z \\ V_z V'_x & V_z V'_y & V_z V'_z \end{bmatrix} \quad (9)$$

and the term  $\nabla \cdot (\rho \vec{V} \otimes \vec{V})$  can be obtained by:

$$\nabla \cdot (\rho \vec{V} \otimes \vec{V}) = \begin{bmatrix} \frac{\partial}{\partial x} (\rho \vec{V}_x \vec{V}_x) + \frac{\partial}{\partial y} (\rho \vec{V}_y \vec{V}_x) + \frac{\partial}{\partial z} (\rho \vec{V}_z \vec{V}_x) \\ \frac{\partial}{\partial x} (\rho \vec{V}_x \vec{V}_y) + \frac{\partial}{\partial y} (\rho \vec{V}_y \vec{V}_y) + \frac{\partial}{\partial z} (\rho \vec{V}_z \vec{V}_y) \\ \frac{\partial}{\partial x} (\rho \vec{V}_x \vec{V}_z) + \frac{\partial}{\partial y} (\rho \vec{V}_y \vec{V}_z) + \frac{\partial}{\partial z} (\rho \vec{V}_z \vec{V}_z) \end{bmatrix} \quad (10)$$

For an incompressible flow (i.e. low Mach number) the dilatation term on the right-hand side of Eq. (8) is neglected so that

$$\frac{\partial(\rho \vec{V})}{\partial t} + \nabla \cdot (\rho \vec{V} \otimes \vec{V}) = -\nabla P + \nabla \cdot \left\{ \mu \left[ \nabla \vec{V} + (\nabla \vec{V})^T \right] \right\} + S_M \quad (11)$$

In principle, Eqs. (6, 7 and 11) can be applied to describe the laminar and turbulent flows without additional information. However, according Bogdanović et al. [66], “turbulent flows at realistic Reynolds numbers span a large range of turbulent length and time scales, and would generally involve length scales much smaller than the smallest finite volume mesh, which can be practically used in a numerical analysis”. In this sense, several turbulence models have been developed to account these effects without recourse to a prohibitively fine mesh and direct numerical simulation.

## Turbulent Models

Inserting the instantaneous variables into a mean value and a fluctuating value ( $\vec{V} = \vec{U} + \vec{u}$  and  $P = P + p$ ) we obtain the time averaged continuity equation and Reynolds Averaged Navier–Stokes (RANS) equations as follows:

$$\frac{\partial \rho}{\partial t} + \nabla \cdot (\rho \vec{U}) = 0 \quad (12)$$

$$\frac{\partial(\rho \vec{U})}{\partial t} + \nabla \cdot (\rho \vec{U} \otimes \vec{U}) = -\nabla P + \nabla \cdot \left\{ \mu \left[ \nabla \vec{U} + (\nabla \vec{U})^T - \rho \overline{\vec{u}\vec{u}} \right] \right\} + S_M \quad (13)$$

where the term  $\overline{u'u'}$  that appears on the right-hand side of Eq. (13) is called the Reynolds stress tensor. In this case, we need a model for  $\overline{u'u'}$  to close the Eq. (13).

However, the averaging procedure introduces additional unknown terms (called turbulent or Reynolds stresses) containing products of the fluctuating quantities. These terms act like additional stresses in the fluid and are difficult to be determined directly. According to Davidson [67] different levels of approximation to achieve this model can be cited:

- a. *Algebraic models.* These simplest turbulence models also referred to as zero equation models use a turbulent viscosity (eddy viscosity) approach to calculate the Reynolds stress.
- b. *One-equation models.* A transport equation is solved for the turbulent kinetic energy and the unknown turbulent length scale must be given. Generally an algebraic expression is used to obtain this turbulent length scale.
- c. *Two-equation models.* These models provide independent transport equations for both the turbulence length scale, or some equivalent parameter, and the turbulent kinetic energy. Here two transport equations are derived which describe transport of two scalars. Then, the Reynolds stress tensor is solved using an assumption which relates the Reynolds stress tensor to an eddy viscosity and the velocity gradients.
- d. *Reynolds stress models.* In these models, one transport equation must be added for determining the length scale of the turbulence.

The models of turbulence associated with the RANS equations like Standard k- $\epsilon$  model, Zero Equation model, RSM model—(Reynolds Stress Model), RNG k- $\epsilon$  model (Re-normalized Group Model), NKE k- $\epsilon$  model (New k- $\epsilon$  Model due to Shih), GIR k- $\epsilon$  model (Model due to Girimaji), SZL k- $\epsilon$  model (Shi, Zhu, Lumley Model), Standard k- $\omega$  model and SST model (Shear Stress Transport Model) have been widely used in engineering and scientific research works. The choice of which turbulence model we must use is not a trivial matter. This chapter will first focus on the some turbulence models.

In the two-equation turbulence models the turbulence velocity scale is computed from the turbulent kinetic energy, which is provided from the solution of the transport equation. The turbulent length scale is estimated from two properties of the turbulence field, usually the turbulent kinetic energy and its dissipation rate. The dissipation rate of the turbulent kinetic energy is provided from the solution of the transport equation.

Two-equation model introduces two new variables into the system of equations. Thus, the continuity equation assumes the forms:

$$\frac{\partial \rho}{\partial t} + \nabla \cdot (\rho \vec{U}) = 0 \quad (14)$$

$$\frac{\partial(\rho \vec{U})}{\partial t} + \nabla \cdot (\rho \vec{U} \otimes \vec{U}) = -\nabla \mathbf{P} + \nabla \cdot \left\{ \mu_{ef} \left[ \nabla \vec{U} + (\nabla \vec{U})^T \right] \right\} + S_M \quad (15)$$

where  $\mu_{ef}$  is the effective viscosity (dynamic viscosity plus turbulent viscosity),  $\mathbf{P}$  is the modified pressure as defined by:

$$\mathbf{P} = P + \frac{2}{3} \rho k + \frac{2}{3} \mu_t \nabla \cdot \vec{U} \quad (16)$$

From the two-equation turbulence model we can cite the following models:

### *k-ε Model*

The k-ε model is based on the eddy viscosity concept, so that:

$$\mu_{ef} = \mu + \mu_t \quad (17)$$

where  $\mu_t$  is the turbulence viscosity. The k-ε model assumes that the turbulence viscosity is linked to the turbulence kinetic energy and dissipation based on the relationship:

$$\mu_t = c_\mu \rho \frac{k^2}{\varepsilon} \quad (18)$$

where  $c_\mu$  is a constant.

The values of  $k$  and  $\varepsilon$  come directly from the differential transport equations for the turbulence kinetic energy and turbulence dissipation rate as follows:

$$\frac{\partial(\rho k)}{\partial t} + \nabla \cdot (\rho \vec{U} k) = \nabla \cdot \left[ \left( \mu + \frac{\mu_t}{\sigma_k} \right) \nabla k \right] + p_k - \rho \varepsilon \quad (19)$$

$$\frac{\partial(\rho \varepsilon)}{\partial t} + \nabla \cdot (\rho \vec{U} \varepsilon) = \nabla \cdot \left[ \left( \mu + \frac{\mu_t}{\sigma_\varepsilon} \right) \nabla \varepsilon \right] + \frac{\varepsilon}{k} (C_{\varepsilon 1} p_k - C_{\varepsilon 2} \rho \varepsilon) \quad (20)$$

where  $C_{\varepsilon 1}$ ,  $C_{\varepsilon 2}$ ,  $\sigma_\varepsilon$ , and  $\sigma_k$  are constants (1.44, 1.92, 1.3 and 2.0, respectively),  $p_k$  is the turbulence production due to viscous and buoyancy forces, defined by:

$$p_k = \mu_t \nabla \vec{U} \cdot (\nabla \vec{U} + \nabla \vec{U}^T) - \frac{2}{3} \nabla \cdot \vec{U} (3\mu_t \nabla \cdot \vec{U} + \rho k) + p_{kb} \quad (21)$$

The first term that appears on the left-hand side represents the rate of change of turbulent kinetic energy and the second the convective transport. On the right-hand side, we have diffusive transport, rate of production and rate of destruction, respectively.

For incompressible flow,  $\nabla \cdot \vec{U}$  is small and the second term on the right-hand side of Eq. (21) does not contribute significantly to the production. If the full buoyancy model is being used, the buoyancy production term  $p_{kb}$  is modeled as:

$$p_{kb} = -\frac{\mu_t}{\rho\sigma_\rho}\vec{g} \cdot \nabla\rho \quad (22)$$

If the Boussinesq buoyancy model is being used we can write:

$$p_{kb} = -\frac{\mu_t}{\rho\sigma_\rho}\rho\beta\vec{g} \cdot \nabla T \quad (23)$$

where  $\beta$  is the coefficient of thermal expansion.

### *RNG k- $\varepsilon$ Model*

In this turbulent model, the transport equations for turbulence generation and dissipation are the same as those for the standard k- $\varepsilon$  model, but the model constants are different. Then, we can write:

$$\frac{\partial(\rho k)}{\partial t} + \nabla \cdot (\rho \vec{U}k) = \nabla \cdot \left[ \left( \mu + \frac{\mu_t}{\sigma_k^*} \right) \nabla k \right] + p_k - \rho\varepsilon \quad (24)$$

$$\frac{\partial(\rho\varepsilon)}{\partial t} + \nabla \cdot (\rho \vec{U}\varepsilon) = \nabla \cdot \left[ \left( \mu + \frac{\mu_t}{\sigma_\varepsilon^*} \right) \nabla \varepsilon \right] + \frac{\varepsilon}{k} (C_{\varepsilon 1}^* p_k - C_{\varepsilon 2}^* \rho\varepsilon) \quad (25)$$

where:

$$C_{\varepsilon 1}^* = 1.42 - \frac{\eta(1 - \frac{\eta}{4.38})}{(1 + \beta'\eta^3)} \quad (26)$$

being  $\sigma_k^*$ ,  $\sigma_\varepsilon^*$ ,  $\beta'$  and  $C_{\varepsilon 2}^*$  are constants (0.7179, 0.7179, 0.012 and 1.68, respectively), and

$$\eta = \sqrt{\frac{p_k}{\rho\varepsilon C_\mu'}} \quad (27)$$

### *Reynolds Stress Models*

The Boussinesq assumption is not used in the Reynolds stress models. In this case, a partial differential equation for the stress tensor is derived from the Navier-Stokes equation. These models do not use the eddy viscosity hypothesis, but solve an equation for the transport of Reynolds stresses in the fluid.

The Reynolds averaged momentum equations for the mean velocity are given by Eq. (13) rewrite as follows:

$$\frac{\partial(\rho \vec{U})}{\partial t} + \nabla \cdot (\rho \vec{U} \otimes \vec{U}) = -\nabla P + \nabla \cdot \left\{ \mu \left[ \nabla \vec{U} + (\nabla \vec{U})^T - \rho \overline{u\vec{u}} \right] \right\} + S_M \quad (28)$$

where  $\mathbf{P}$  is a modified pressure define by

$$\mathbf{P} = P + \nabla \cdot \vec{U} \left( \frac{2}{3} \mu - \xi \right) \quad (29)$$

where  $\xi$  is the bulk viscosity.

In the differential stress model,  $\overline{u\vec{u}}$  is made to satisfy a transport equation. A separate transport equation must be solved for each of the six Reynolds stress components of  $\overline{\rho u\vec{u}}$ . The differential Reynolds stress transport equation is:

$$\frac{\partial(\rho \overline{u\vec{u}})}{\partial t} + \nabla \cdot (\vec{U} \rho \overline{u_i u_j}) - \nabla \cdot \left[ \left( \mu + \frac{2}{3} \rho C \frac{k^2}{\varepsilon} \right) \nabla \overline{u_i u_j} \right] = p_R - \frac{2}{3} \delta \rho \varepsilon + G + \phi \quad (30)$$

where  $p_R$  is shear turbulence production and  $G$  is the buoyancy turbulence production,  $\phi$  is the pressure-strain correlation, and  $C$  is a constant.

The production term  $p_R$  is given by

$$p_R = -\rho \left[ \overline{u\vec{u}} (\nabla \vec{U})^T + \overline{u\vec{u}} (\nabla \vec{U}) \right] \quad (31)$$

As the turbulence dissipation appears in the individual stress equations, an equation for  $\varepsilon$  is still required. This one now has the form:

$$\frac{\partial(\rho \varepsilon)}{\partial t} + \nabla \cdot (\rho \vec{U} \varepsilon) = \nabla \cdot \left[ \left( \mu + \frac{\mu_t}{\sigma_\varepsilon} \right) \nabla \varepsilon \right] + \frac{\varepsilon}{k} (C_{\varepsilon 1} p_R - C_{\varepsilon 2} \rho \varepsilon) \quad (32)$$

where  $C_{\varepsilon 1}$ ,  $C_{\varepsilon 2}$ ,  $\sigma_\varepsilon$ , and  $\sigma_k$  are constants (1.44, 1.92, 1.3 and 2.0, respectively).

The pressure-strain correlations can be expressed in the general form:

$$\phi = \phi_1 + \phi_2 \quad (33)$$

where:

$$\phi_1 = -\rho \varepsilon \left[ C_{s1} \vec{a} + C_{s2} \left( \vec{a} \vec{a} - \frac{1}{3} \vec{a} \cdot \vec{a} \delta \right) \right] \quad (34)$$

$$\begin{aligned} \phi_2 = & -C_{r1} p_R \vec{a} + C_{r2} \rho k \vec{S} - C_{r3} \rho k \vec{S} \sqrt{\vec{a} \cdot \vec{a}} \\ & + C_{r4} \rho k \left( \vec{a} \vec{S}^T + \vec{S} \vec{a}^T - \frac{2}{3} \vec{a} \cdot \vec{S} \delta \right) + C_{r5} \rho k (\vec{a} \vec{W}^T + \vec{W} \vec{a}^T) \end{aligned} \quad (35)$$

with the anisotropy tensor  $\vec{a}$  given by:

$$\vec{a} = \frac{\overline{\vec{u} \otimes \vec{u}}}{k} - \frac{2}{3} \delta \quad (36)$$

In the Eq. (35), the strain rate  $\vec{S}$  is given as follows:

**Table 2** Different constants for the Reynolds stress models

Model	$C_{s1}$	$C_{s2}$	$C_{r1}$	$C_{r2}$	$C_{r3}$	$C_{r4}$	$C_{r5}$
LRR-IP	1.8	0.0	0.0	0.8	0.0	0.6	0.6
LRR-QI	1.8	0.0	0.0	0.8	0.0	0.873	0.655
SSG	1.7	-1.05	0.9	0.8	0.65	0.625	0.2

$$\vec{S} = \frac{1}{2} \left[ \nabla \vec{U} + (\nabla \vec{U})^T \right] \quad (37)$$

and the vorticity  $\vec{W}$  is given by:

$$\vec{W} = \frac{1}{2} \left[ \nabla \vec{U} - (\nabla \vec{U})^T \right] \quad (38)$$

There are three varieties of the standard Reynolds stress models available. These are known as LRR-IP, LRR-QI (Launder, Reece and Rodi) and SSG (Speziale, Sarkar and Gatski). Each model has different model constants and are shown in the Table 2.

### Total Energy Equation

$$\frac{\partial(\rho h_{tot})}{\partial t} - \frac{\partial p}{\partial t} + \nabla \cdot (\rho \vec{U} h_{tot}) = \nabla \cdot (\lambda \nabla T) + \nabla \cdot (\vec{U} \cdot \tau) + \vec{U} \cdot S_M + S_E \quad (39)$$

where T is the temperature,  $h_{tot}$  is the total enthalpy, related to the static enthalpy by:

$$h_{tot} = h + \frac{1}{2} \vec{U} \cdot \vec{U} \quad (40)$$

The term  $\nabla \cdot (\vec{U} \cdot \tau)$  represents the work due to viscous stresses and is called the viscous work term. The term  $\vec{U} \cdot S_M$  represents the work due to external momentum sources and is currently neglected.

### Multicomponent Equation

The transport equations for the mass fractions of components A in a multicomponent flow is given by:

$$\frac{\partial(\rho Y_A)}{\partial t} + \nabla \cdot (\rho \vec{U} Y_A) = \nabla \cdot [\rho D_A (\nabla Y_A)] + S_A \quad (41)$$

where  $Y_A$  is the mass fraction of component  $A$ , i.e.  $Y_A = \rho_A/\rho$ ,  $\rho_A$  is the density of component  $A$ ,  $\rho$  is the density,  $D_A$  is kinematic diffusivity and  $S_A$  is the source term for component  $A$  which includes the effects of chemical reactions.

### 3.2.2 Disperse Phase

To evaluate the particulate phase, we can adopt the particle transport Lagrangean model, in which the particle phase is modeled by tracking a small number of particles (solid particles, drops or bubbles) through the continuum fluid.

#### Momentum Transfer

When considering a particle traveling in a fluid medium we can say that the forces acting over them affect the particle acceleration. This fact is attributed to the difference in velocity between the particle and fluid and the displacement of fluid by the particle. The equation of motion describing this behavior is given by:

$$m_p \frac{d\vec{U}_p}{dt} = \vec{F}_D + \vec{F}_B + \vec{F}_R + \vec{F}_{VM} + \vec{F}_P + \vec{F}_{BA} \quad (42)$$

Herein  $m_p$  and  $\vec{U}_p$  represent the mass and velocity vector of particle, respectively. The right-hand side represents the total force acting on the disperse phase particle. The drag force,  $\vec{F}_D$ , due to surface shear and pressure distribution can be written as follows:

$$\vec{F}_D = \frac{1}{2} C_D \rho_F A_F |\vec{U}_F - \vec{U}_p| (\vec{U}_F - \vec{U}_p) \quad (43)$$

where  $A_F$  is the effective particle cross section (frontal particle surface area),  $\vec{U}_F$  and  $\vec{U}_p$  represent the velocity vector of the fluid (continuous phase) and particle (particulate phase), respectively. The drag coefficient,  $C_D$ , which is introduced to account for experimental results on the viscous drag of a solid sphere, depends on the flow regime (particle Reynolds number) and the properties of the continuous phase. In the literature it has been reported a large number of empirical correlations to estimate the drag coefficient [64, 65, 68–70].

The buoyancy force due to gravity (body force),  $\vec{F}_B$ , correspond the weight of the displaced fluid given by:

$$\vec{F}_B = (m_p - m_F) \vec{g} \quad (44)$$

where  $m_p$  and  $m_F$  represent mass of the particle and fluid, respectively, and  $\vec{g}$  is the gravity vector. If gravity effect is dominant, this term determines the motion of bubbles in liquids and leads solid particle sedimentation when immersed in liquids or gases.

The rotation force,  $\vec{F}_R$ , in the Eq. (42), can be determined by:

$$\vec{F}_R = m_p \left( -2\vec{\Omega} \times \vec{U}_p - \vec{\Omega} \times \vec{\Omega} \times \vec{r}_p \right) \quad (45)$$

with  $m_p$  is the particle mass,  $\Omega$  is the angular velocity and  $r_p$  is the radius of particle.

The virtual mass force or added mass force,  $\vec{F}_{VM}$ , in the Eq. (42), is observed when a particle in motion accelerates the surrounding fluid [64, 65], which can be written as follows:

$$\vec{F}_{VM} = \frac{C_{VM}}{2} m_F \left( \frac{d\vec{U}_F}{dt} - \frac{d\vec{U}_p}{dt} \right) \quad (46)$$

where  $C_{VM}$  is the virtual mass coefficient, generally equal to 1.

The pressure gradient force,  $\vec{F}_P$ , in the Eq. (42), can be calculated by:

$$\vec{F}_P = \frac{m_F}{\rho_F} \nabla p \quad (47)$$

where  $\rho_F$  represent fluid density.

According to Ansys CFX Guide [44] this force is only important if large fluid pressure gradients exist and if the particle density is smaller than or similar to the fluid density.

Finally,  $\vec{F}_{BA}$  is the Basset force or history term, which is the force associated with past movements of the particle. This force becomes important when the particle is accelerated or decelerated in the fluid. The Basset force can be derived from the motion of a single accelerating sphere in the Stokes regime [65, 71] as follows:

$$\vec{F}_{BA} = \frac{3}{2} d_p^2 \sqrt{\pi \rho_F \mu_F} \int_0^t \frac{1}{\sqrt{t - \tau_*}} \frac{\partial (|\vec{U}_F - \vec{U}_p|)}{\partial \tau_*} d\tau_* \quad (48)$$

where  $(t - \tau_*)$  represents the time elapsed since past accelerated from 0 to  $\tau_*$ .

## Heat Transfer

The rate of change of temperature for the particle is obtained from:

$$\sum (m_C C_P) \frac{dT}{dt} = Q_C + Q_M + Q_R \quad (49)$$

where  $m_C$  is the mass of the constituent in the particle,  $C_P$  is the specific heat of the particle,  $Q_C$  is the convective heat transfer given by:

$$Q_C = \pi d_p k_F \text{Nu} (T_F - T) \quad (50)$$



where  $d_p$  is the particle diameter,  $k_F$  is the thermal conductivity of the fluid,  $T_F$  and  $T$  are the temperatures of the fluid and of the particle, respectively, and Nu is the Nusselt number defined by

$$\text{Nu} = 2 + 0.6\text{Re}^{0.5} \left( \mu \frac{C_p^*}{k_F} \right)^{1/3} \quad (51)$$

where  $C_p^*$  is the specific heat of the fluid.

In the Eq. (44),  $Q_M$  represents the heat transfer associated with mass transfer defined by:

$$Q_M = \sum \frac{dm_C}{dt} L_V \quad (52)$$

where  $L_V$  is the latent heat of vaporization.

The parameter,  $Q_R$  represents the radiative heat transfer defined by:

$$Q_R = \frac{1}{4} \varepsilon_p \pi d_p^2 \left( I_f - \sigma_{SB} n_R T_p^4 \right) \quad (53)$$

where  $I_f$  is the irradiation flux on the particle surface at the location of the particle,  $n_R$  is the refractive index of the fluid, and  $\sigma_{SB}$  is the Stefan-Boltzmann constant.

### Liquid Evaporation Model

The liquid evaporation model is applied to particles with heat transfer and one component of mass transfer, and in which the continuous gas phase is at a higher temperature than the particles. The model uses two mass transfer correlations depending on whether the droplet is above or below the boiling point.

When the particle is above the boiling point, we can use

$$\frac{dm_C}{dt} = - \frac{Q_C}{L_V} \quad (54)$$

Otherwise,

$$\frac{dm_C}{dt} = \pi d_p \rho_F D_F \text{Sh} \frac{M_V}{M_M} \log \left( \frac{1 - X_{eq}}{1 - X_G} \right) \quad (55)$$

where  $\rho_F D_F$  is the dynamic diffusivity of the mass fraction in the continuum,  $M_V$  e  $M_M$  are the molecular weights of the vapor and the mixture in the continuous phase,  $X_G$  is the molar fraction in the gas phase, and  $X_{eq}$  is the equilibrium mole fraction at the droplet surface defined as:

$$X_{eq} = \frac{P_{vap}}{P_C} \quad (56)$$

where  $P_C$  is the pressure of the continuous phase and  $P_{vap}$  is the vapor pressure determinate through the Antoine equation as follows:

$$P_{vap} = P_{ref} \exp\left(A - \frac{B}{T + C}\right) \quad (57)$$

where  $P_{ref}$  is the reference pressure and  $A$ ,  $B$  and  $C$  are user-supplied coefficients.

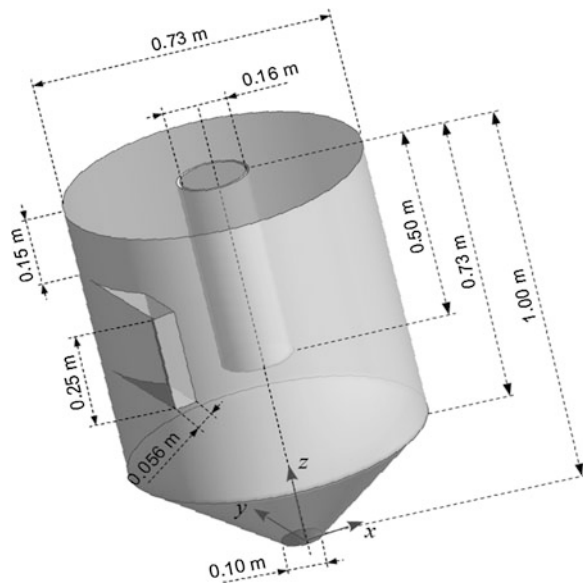
### 3.3 Application: Drying of Sugar-Cane Bagasse Using Cyclone

#### 3.3.1 Physical Problem Description

The drying process of sugar-cane bagasse is very important in sugar and alcohol industries. This biomass is used as an alternative source of energy that is used in the steps of the sugar and alcohol production processes, and it constitutes in more an income source, because the excess energy produced in the plants is sold [45, 72, 73]. These authors have studied the drying of the sugar-cane bagasse in a cyclone.

Herein, the cyclone was used to dry moist sugar-cane bagasse. The drying equipment is similar to that used by Corrêa [72] without the device of particle feeder (Venturi feeder) as illustrated in the Fig. 4. Then, particle and gas enter in the cyclone as a fluid/particle mixture.

**Fig. 4** Illustration of a cyclone dryer



### 3.3.2 Boundary Conditions and Physical Properties

A numerical solution for conservation equations was developed using ANSYS CFX commercial code which the following boundary conditions were applied to the cyclone dryer illustrated in Fig. 4.

- a. *Inlet*: Velocity profile of the gas phase in y direction was defined by a polynomial equation of degree 5 (five), by fitting to the experimental data available in Corrêa [72], Eq. (58), whereas the velocity components in the x and z directions were assumed null. For the gas phase (air), we use the following drying conditions: air temperature 489 K and air relative humidity 3.41 %.

$$u_{in} = u_{max} \left[ 1 - \left( \frac{z}{a} \right)^8 \right] \quad (58)$$

- b. *Wall*: No slip conditions at the cyclone wall/fluid interface, i.e., velocity components equal to zero, and adiabatic boundary condition, i.e. heat flux null.
- c. *Outlet*: Prescribed static pressure on the outlets cyclone dryer (underflow and overflow) equal to 101.3 kPa.

The thermo-physical properties of the gas (air) and particle (sugar-cane bagasse) used in all simulations are shown in Table 3.

### 3.3.3 Results Analysis

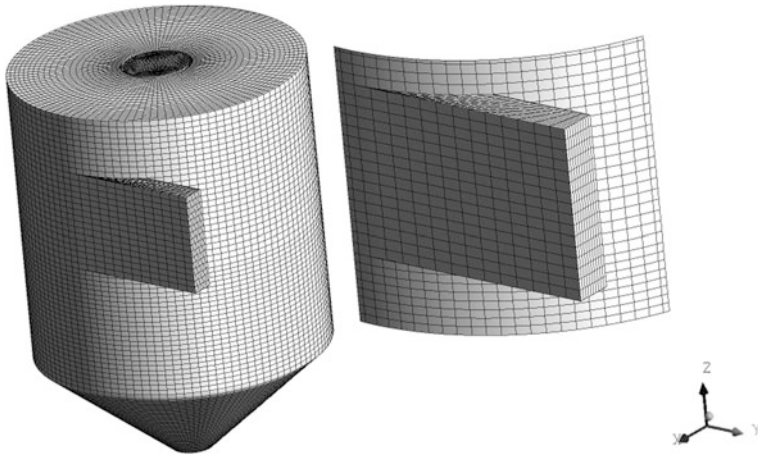
All simulations were developed using the numerical grid illustrated in Fig. 5. This mesh was generated using Ansys ICEM-CFD with 325,200 elements, which was optimal for good predictions and reasonable computational time in all simulations.

In order to reach a better understanding of the gas phase flow, the Fig. 6 shows the streamlines inside the cyclone. They originate in two points ( $x = 0.315$ ;  $y = 0.364$ ;  $z = 0.615$ ) and ( $x = 0.333$ ;  $y = 0.664$ ;  $z = 0.685$ ). These locations are close to the first half, starting at the base of the feeding duct. From the analysis of this figure we can observe the ascending behavior pattern of the gas phase in the cyclone, and the descending one near the cylindrical-conical walls, according to literature, for either cyclones or hydrocyclones [45, 74–78].

Figure 7 illustrates the pressure distribution at the surface of the cyclonic dryer. This pressure field represents the forces that the fluid exerts on the walls of the cyclone, caused by the fluid flow that enters tangentially, per unit area. Note that in general the pressure distribution remains almost uniform at the wall of the cylinder, except in the region immediately after the entry duct. In this region, it is observed an area that is severely impacted by the direct contact of solid and gas particles, thus causing a wear on the walls of the cyclone. So, this region is crucial

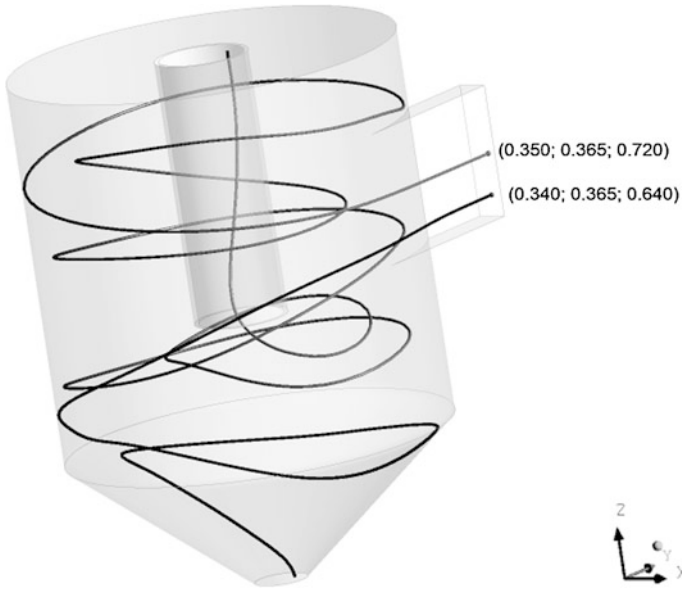
**Table 3** Thermo-physical properties of the fluid and particle

Thermo-physical parameters	Fluid (air)	Particle (sugar-cane bagasse)
Density ( $\text{kg/m}^3$ )	0.7123	685.2
Wet particle density—water plus sugar cane bagasse ( $\text{kg/m}^3$ )	–	878.4
Thermal conductivity ( $\text{W/m.K}$ )	$3.7673 \times 10^{-2}$	0.215
Latent heat of vaporization ( $\text{J/kg}$ )	–	$2.251 \times 10^6$
Specific heat ( $\text{J/kg.K}$ )	1,045.362	4,180
Diffusivity ( $\text{m}^2/\text{s}$ )	$5.7960 \times 10^{-5}$	–
Molecular weight ( $\text{kg/kmol}$ )	28.96	–
Wet bulb temperature (K)	324.81	–
Relative humidity (%)	3.41	–
Inlet temperature (K)	489	298
Initial moisture content (d.b.)	–	2.2

**Fig. 5** Numerical grid used in the simulations

in the design of such equipment, especially when the solid particle is very abrasive [79–81].

Figure 8 illustrates the mapping of pressure on the XZ and YZ plans through the axis of the cyclone. There is a similar behavior in the pressure field, where the regions of high pressure are close to the cylindrical wall. The region of lower pressure occurs into gas exit tube. Thus, provides a drop in pressure of 332 Pa. It should be noted, moreover, that there is another area of low pressure near the axis of symmetry. This is caused by the reversal flow of the gas in the proximities of the cylindrical and conical regions.



**Fig. 6** Streamlines inside the cyclone starting from two points at the cyclone inlet

**Fig. 7** Gas pressure field at the cyclone walls

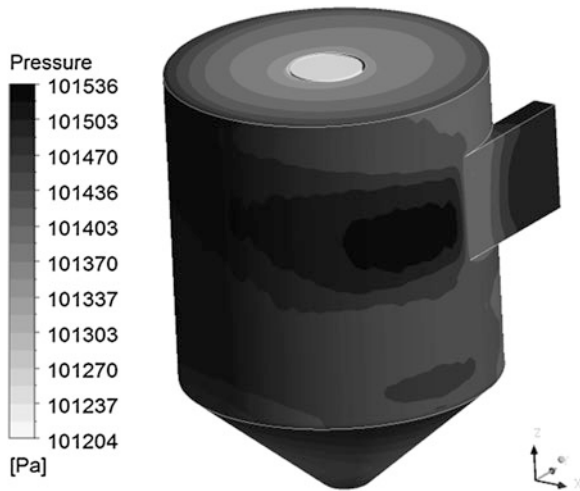
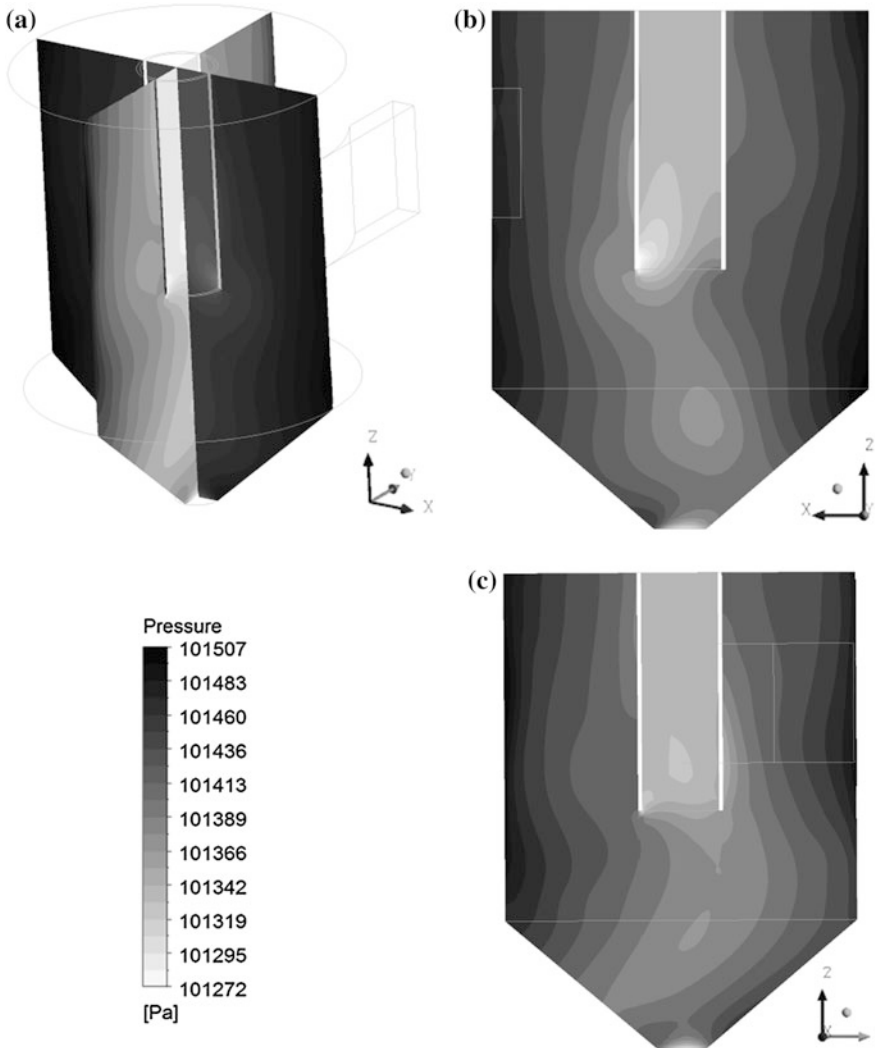


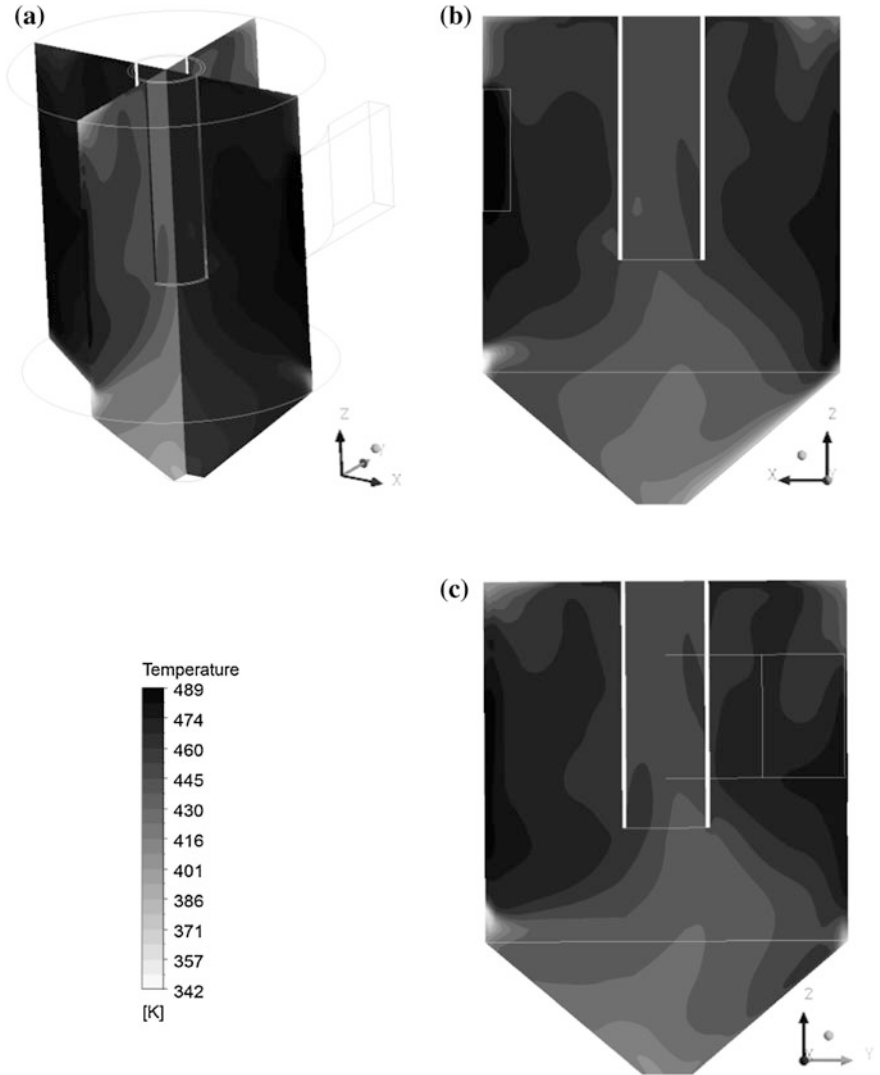
Figure 9 show the mapping of gas temperature on the XZ and YZ plans passing through the axis of the cyclone. It can be seen that the temperature fields are similar, with higher temperatures near the cylindrical walls of the cyclone. This fact can be explained by the phenomenon of heat transfer between particles and hot air (drying agent). The particles in contact with the hot air start to lose mass by



**Fig. 8** Gas pressure field: **a** XZ and YZ plans; **b** XZ plan; **c** YZ plan through the axis cyclone

water evaporation thus, affecting its moisture content and temperature. This fact is confirmed by tracking of the particles inside the cyclone, as can be seen in Fig. 10. In this figure one can observe that most of the particles are in the conical part of the cyclone, thereby reducing the temperature of the drying air in this location (Fig. 9).

Regarding the material transport and to show the effect of the particle diameter on the drying process, in the Figs. 11 to 13 are shown the behavior of temperature, moisture content, and shrinkage of two particles with initial diameters 0.42 and

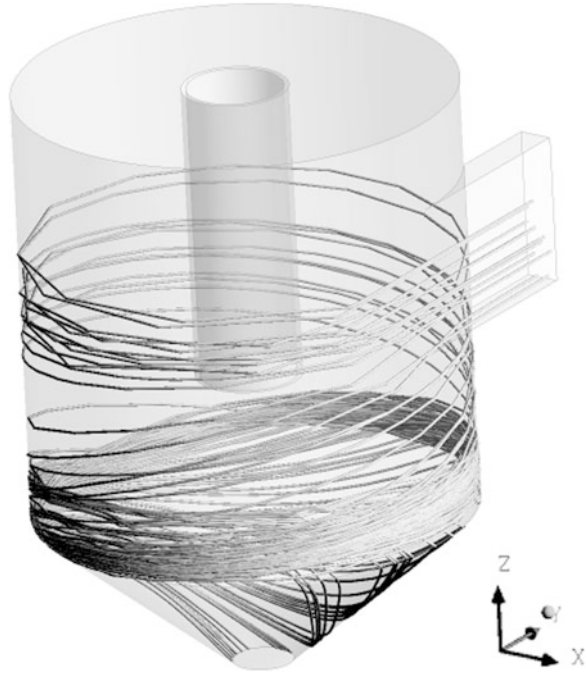


**Fig. 9** Gas temperature field: **a** XZ and YZ plans; **b** XZ plan; **c** YZ plan through the axis cyclone

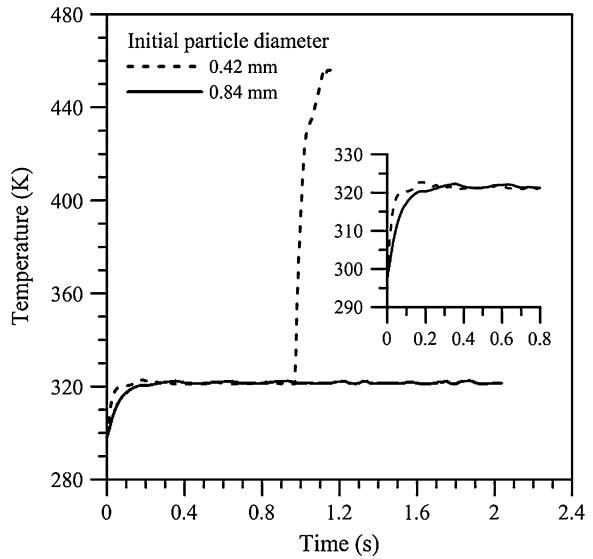
0.84 mm. It can be clearly seen that initial diameter of the particles has an important role on the sugar-cane bagasse drying.

Figure 11 show that the temperature of the particles has reached a constant value after 0.3 s, which may provide evidence to compensation between the heat transfer and mass transfer. This behavior is characteristic of a constant period of drying (constant drying rate). However, after this period, the particle with 0.42 mm diameter undergoes a sudden increase in temperature. From this moment

**Fig. 10** Particles tracking inside the cyclone

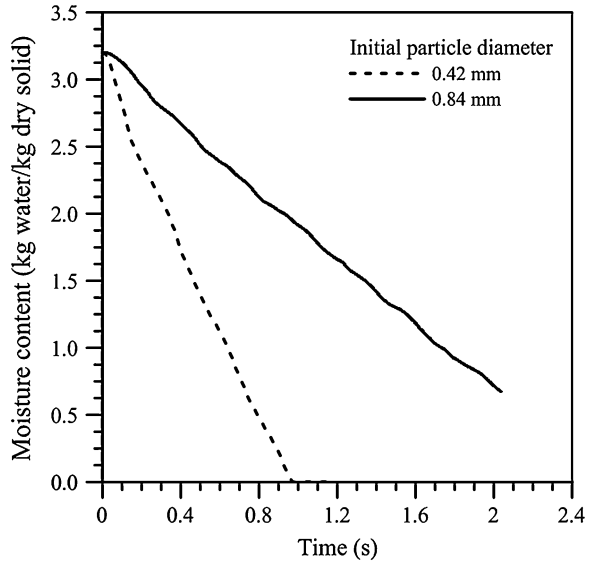


**Fig. 11** Temperature of the sugar-cane bagasse particles as a function of time

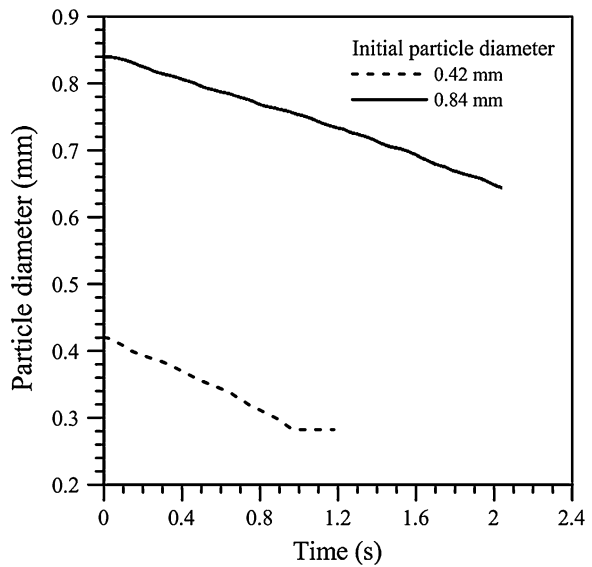




**Fig. 12** Moisture content of the sugar-cane bagasse particles as a function of time

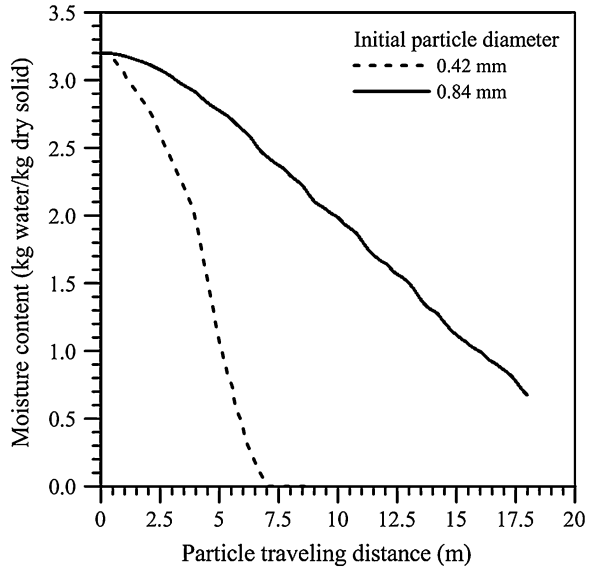


**Fig. 13** Shrinkage of the sugar-cane bagasse particles during drying process



the particle does not contain any more water (equilibrium condition), as can be seen in Fig. 12, and thus, its temperature increase quickly. This fact might indicate that the particles are internally heated by thermal conduction (dry particle). Then, is no longer, the observed shrinkage of the particles with 0.42 mm diameter (to see Fig. 13).

**Fig. 14** Particle traveling distance during the drying of sugar-cane bagasse



From the analysis of the Fig. 12 we can see that the particle with lower diameter dry first. This behavior is related to area/volume relationships of the particle. When the area/volume ratio is higher, the higher drying rate and shrinkage velocity is observed and, thus, the higher moisture removal and higher heating of the particle is verified. So, smaller particle is dried and heated more quickly.

Figure 14 shows the sugar-cane bagasse particle travelling distance during the drying process. It can be seen that the particles with 0.84 mm diameter have traveled a distance 2.17 times larger than the particles with 0.42 mm. This behavior is linked to the effect of the forces acting over the particles, mainly drag and gravitational forces [81]. The competition of these forces dominates the residence time of the particle into the cyclone.

## 4 Concluding Remarks

This chapter focuses on advanced topics related to heat and mass transfer and turbulent gas-particle flow (dispersed flow) in a cyclone dryer. This type of physical problem is motivated by its importance in many industrial processes such as mineral processing, food processing, environmental cleaning and chemical processes.

Fundamental information about the principle of operation, design, selection and classification, pressure drop and overall separation efficiency of a cyclone are given.

A mathematical modeling based on the Eulerian–Lagrangian approach is introduced to explain the complex flow of the gas phase, particle trajectory, particle residence time and heat and mass transfer between the moist particle and gas phase inside the cyclone operating as a dryer.

The three-dimensional model considers steady-state and turbulent flow for gas phase and transient state for heat and mass transfer in the particulate phase. The effect of different forces acting on the particles (that affect particle trajectory and cyclone residence time) such as drag, gravitational, centrifugal, Saffman, Magnus, Faxen and Basset forces, collisions interparticles, collisions between particle and cyclone wall, and moisture content, temperature, and shrinkage phenomena (dimensions variations) of the particle are also analyzed.

Application to predict drying process of sugar and alcohol industry residues is performed and numerical studies were conducted for different inlet particle size.

Predicted results of the moisture content and particle residence time qualitatively agree well with the experimental results of sugar-cane bagasse drying.

The numerical calculations have visualized different flow pattern and behavior of the solids concentration distribution within the device. The solids concentration is lower in the inner region of the cyclone and increases greatly in the outer region. Large particles generally have higher concentration near the wall region and small particles have higher concentration in inner vortex region.

The effects of operating conditions and geometric parameters of the cyclone in the drying were also studied.

Different results such as drying and heating kinetics and trajectory of the particles, velocity, temperature, and pressure distributions of the gas phase during drying process illustrate the effectiveness versatility and performance of the rigorous mathematical model and numerical treatment performed.

From the good results obtained we can cite that the model showed herein can be used with great confidence to predict drying process and dispersed turbulent flow in several complex practical applications.

**Acknowledgments** The authors would like to express their thanks to CNPq (Conselho Nacional de Desenvolvimento Científico e Tecnológico, Brazil), CAPES (Coordenação de Aperfeiçoamento de Pessoal de Nível Superior, Brazil), and FINEP (Financiadora de Estudos e Projetos, Brazil) for supporting this work; to the authors of the references in this paper that helped in our understanding of this complex subject, and to the Editors by the opportunity given to present our research in this book. J.M.P.Q. Delgado would like to thank Fundação para a Ciência e a Tecnologia (FCT) for financial support through the grant SFRH/BPD/84377/2012.

## References

1. Loth, E., Tryggvason, G., Tsuji, Y., Elghobashig, S.E., Crowe, C.T., Berlemont, A., Reeks, M., Simonin, O., Frank, T., Onishi, Y., van Wachem, B.: Modeling. In: Crowe, C.T. (ed.) *Multiphase Flow Handbook*. CRC Taylor & Francis, Boca Raton (2006)
2. Brennen, M.S., Narasimha, M., Holtham, P.N.: Multiphase modelling of hydrocyclones—prediction of cut-size. *Minerals Eng.* **20**, 395–406 (2007)

3. Ahmed, M.M., Ibrahim, G.A., Farghaly, M.G.: Performance of a three-product hydrocyclone. *Int. J. Miner. Process.* **91**, 34–40 (2009)
4. Bhaskar, K.U., Murthy, Y.R., Raju, M.R., Tiwari, S., Srivastava, J.K., Ramakrishnan, N.: CFD simulation and experimental validation studies on hydrocyclone. *Minerals Eng.* **20**, 60–71 (2007)
5. Dai, G.Q., Chen, W.M., Li, J.M., Chu, L.Y.: Experimental study of solid-liquid two-phase flow in a hydrocyclone. *Chem. Eng. J.* **74**, 211–216 (1999)
6. Emami, S., Tabil, L.G., Tyler, R.T., Crerar, W.J.: Starch-protein separation from chickpea flour using a hydrocyclone. *J. Food Eng.* **82**, 460–465 (2007)
7. Husveg, T., Rambeau, O., Drengstig, T., Bilstad, T.: Performance of a deoiling hydrocyclone during variable flow rates. *Minerals Eng.* **20**, 368–379 (2007)
8. Jiao, J., Zheng, Y., Sun, G., Wang, J.: Study of the separation efficiency and the flow field of a dynamic cyclone. *Separ. Purif. Technol.* **49**, 157–166 (2006)
9. Ko, J., Zahrai, S., Macchion, O.: Numerical modeling of highly swirling flows in a through-flow cylindrical hydrocyclone. *AIChE J.* **52**(10), 3334–3344 (2006)
10. Leith, D., Licht, W.: The collection efficiency of cyclone type particle collectors—a new theoretical approach. *AIChE Symp. Ser. Air pollut. Control* **68**(126), 196–206 (1972)
11. Liu, C., Wang, L., Wang, J., Liu, Q.: Investigation of energy loss mechanisms in cyclone separations. *Chem. Eng. Technol.* **28**(10), 1182–1190 (2005)
12. Martínez, L.F., Lavín, A.G., Mahamud, M.M., Bueno, J.L.: Vortex finder optimum length in hydrocyclone separation. *Chem. Eng. Process.* **47**, 192–199 (2008)
13. Neesse, T., Dueck, J.: Dynamic modelling of the hydrocyclone. *Minerals Eng.* **20**, 380–386 (2007)
14. Shi, L., Bayless, D.J.: Comparison of boundary conditions for predicting the collection efficiency of cyclones. *Powder Technol.* **173**, 29–37 (2007)
15. Silva, M.A.: Study of the drying in cyclone. In: Ph. D. thesis, mechanical engineering, State University of Campinas, S. P., Brazil (1991) (In Portuguese)
16. Wang, B., Yu, A.B.: Numerical study of particle-fluid flow in hydrocyclones with different body dimensions. *Minerals Eng.* **19**, 1022–1033 (2006)
17. Van 't Land, C.M.: *Industrial Drying Equipment: Selection and Application*. Marcel Dekker, Inc. New York (1991)
18. Cortés, C., Gil, A.: Modeling the gas and particle flow inside cyclone separators. *Progress in Energy Comb. Sci.* **33**, 409–452 (2007)
19. Blei, S., Sommerfeld, M.: CFD in drying technology—spray-dryer simulation. In: Tsotsas, E., Mujumdar, A.S. (eds.) *Modern Drying Technology: Computational Tools at Different Scales*, pp. 155–208. Wiley-VCH, Germany (2007)
20. Crowe, C.T., Michaelides, E.E.: Basic concepts and definitions. In: Crowe, C.T. (ed.) *Multiphase Flow Handbook*. CRC Taylor & Francis, Boca Raton (2006)
21. Kleinstreuer, C.: *Two-Phase Flow: Theory and Applications*. Taylor & Francis, New York (2003)
22. Xiaodong, L., Jianhua, Y., Yuchun, C., Mingjiang, N., Kefa, C.: Numerical simulation of the effects of turbulence intensity and layer on separation efficiency in a cyclone separator. *Chem. Eng. J.* **95**, 235–240 (2003)
23. Qian, F., Huang, Z., Chen, G., Zhang, M.: Numerical study of the separation characteristics in a cyclone of different inlet particle concentrations. *Comp. Chem. Eng.* **31**, 1111–1122 (2007)
24. Qian, F., Zhang, M.: Effects of the inlet section angle on the flow field of a cyclone. *Chem. Eng. Technol.* **30**(11), 1564–1570 (2007)
25. Oweis, G.F., Ceccio, S.L., Matsumoto, Y., Tropea, C., Roisman, I.V., Tsuji, Y.: Multiphase interactions. In: Crowe, C.T. (ed.) *Multiphase Flow Handbook*. CRC Taylor & Francis, Boca Raton (2006)
26. Derksen, J.J., Sundaresan, S., van den Akker, H.E.A.: Simulation of mass-loading effects in gas-solid cyclone separators. *Powder Technol.* **163**, 59–68 (2006)
27. Hashemi, S.B.: A mathematical model to compare the efficiency of cyclones. *Chem. Eng. Technol.* **29**(12), 1444–1454 (2006)

28. Jumah, R.Y., Mujumdar, A.S.: Dryer feeding systems. In: Mujumdar, A.S. (ed.) *Handbook of Industrial Drying*. Marcel Dekker, New York (1995)
29. Narasimha, M., Brennan, M., Holtham, P.N.: Large eddy simulation of hydrocyclone-prediction of air-core diameter and shape. *Int. J. Miner. Process.* **80**, 1–14 (2006)
30. Xiang, R.B., Lee, K.W.: Numerical study of flow field in cyclones of different height. *Chem. Eng. Process.* **44**, 877–883 (2005)
31. Chen, J., Shi, M.: A universal model to calculate cyclone pressure drop. *Powder Technol.* **171**, 184–191 (2007)
32. Gimbut, J., Chuah, T.G., Fakhru'l-Razi, A., Choong, T.S.Y.: The influence of temperature and inlet velocity on cyclone pressure drop: a CFD study. *Chem. Eng. Process.* **44**, 7–12 (2005)
33. Ji, Z., Xiong, Z., Wu, X., Chen, H., Wu, H.: Experimental investigations on a cyclone separator performance at an extremely low particle concentration. *Powder Technol.* **191**, 254–259 (2009)
34. Martignoni, W.P., Bernardo, S., Quintani, C.L.: Evaluation of cyclone geometry and its influence on performance parameters by computational fluid dynamics (CFD). *Braz. J. Chem. Eng.* **24**(1), 83–94 (2007)
35. Raoufi, A., Shams, M., Farzaneh, M., Ebrahimi, R.: Numerical simulation and optimization of fluid flow in cyclone vortex finder. *Chem. Eng. Process.* **47**, 128–137 (2008)
36. Raoufi, A., Shams, M., Kanani, H.: CFD analysis of flow field in square cyclones. *Powder Technol.* **191**, 349–357 (2009)
37. Tan, Z.: An analytical model for the fractional efficiency of a uniflow cyclone with a tangential inlet. *Powder Technol.* **183**, 147–151 (2008)
38. Vegini, A.A., Meier, H.F., Iess, J.J., Mori, M.: Computational fluid dynamics (CFD) analysis of cyclone separators connected in series. *Ind. Eng. Chem. Res.* **47**, 192–200 (2008)
39. Wan, G., Sun, G., Xue, X., Shi, M.: Solids concentration simulation of different size particles in a cyclone separator. *Powder Technol.* **183**, 94–104 (2008)
40. Yang, S., Yang, H., Zhang, H., Li, S., Yue, G.: A transient method to study the pressure drop characteristics of the cyclone in a CFB system. *Powder Technol.* **192**, 105–109 (2009)
41. Yoshida, H., Inada, Y., Fukui, K., Yamamoto, T.: Improvement of gas-cyclone performance by use of local fluid flow control method. *Powder Technol.* **193**, 6–14 (2009)
42. Keey, R.B.: *Drying of Loose and Particulate Materials*. Hemisphere Publishing Corporation, New York (1992)
43. Korn, O.: Cyclone dryer: a pneumatic dryer with increased solid residence time. *Drying Technol.* **19**(8), 1925–1937 (2001)
44. ANSYS CFX-Solver Theory Guide: ANSYS, Inc. southpointe 275 technology drive canonsburg, PA 15317, (2009)
45. Farias, F.P.M., Lima, A.G.B., Farias Neto, S.R.: Numerical study of thermal fluid dynamics of a cyclone as dryer. In: *Proceedings of National Congress of the Mechanical Engineering (CONEM 2006)*, vol. 1, pp. 1–10. Recife-PE, Brazil, (2006b) (In Portuguese)
46. Kaensup, W., Kulwong, S., Wongwises, S.: Comparison of drying kinetics of paddy using a pneumatic conveying dryer with and without a cyclone. *Drying Technol.* **24**, 1039–1045 (2006)
47. Kanaoka, C., Yoshida, H., Makino, H.: Particle separation systems. In: Crowe, C.T. (ed.) *Multiphase Flow Handbook*. CRC Taylor & Francis, Boca Raton (2006)
48. Licht, W.: *Air Pollution Control Engineering*. Marcel Dekker, New York (1988)
49. Zhao, B.: A theoretical approach to pressure drop across cyclone. *Chem. Eng. Technol.* **27**(10), 1105–1108 (2004)
50. Kudra, T., Mujumdar, A.S.: *Advanced Drying Technologies*. CRC Press, Boca Raton (2009)
51. Strumillo, C., Kudra, T.: *Drying: Principles Science and Design*. Gordon and Breach Science Publishers, New York (1986)
52. Benta, E.S., Silva, M.A.: Cyclonic drying of milled corncob. In: *Proceedings of Inter-American Drying Conference (IADC) A*, pp. 288–294. Itu, Brazil, (1997)

53. Corrêa, J.L.G., Graminho, D.R., Silva, M.A., Nebra, S.A.: Cyclone as a sugar cane bagasse dryer. *Chinese J. Chem. Eng.* **12**(6), 826–830 (2004)
54. Corrêa, J.L.G., Graminho, D.R., Silva, M.A., Nebra, S.A.: The cyclonic dryer—a numerical and experimental analysis of the influence of geometry on average particle residence time. *Braz. J. Chem. Eng.* **21**(1), 103–112 (2004)
55. Dibb, A., Silva, M.A.: Cyclone as dryer –the optimum geometry. In: *Proceedings of Inter-American Drying Conference (IADC)*, pp. 396–403. Itu, Brazil, **B**, (1997)
56. Akpınar, E.K., Midilli, A., Bicer, Y.: Energy and exergy of potato drying process via cyclone type dryer. *Energy Conv. Manag.* **46**, 2530–2552 (2005)
57. Bunyawanichakul, P., Kirkpatrick, M.P., Sargison, J.E., Walker, G.J.: Numerical and experimental studies of the flow field in a cyclone dryer. *J. Fluids Eng.* **128**, 1240–1248 (2006)
58. Bunyawanichakul, P., Kirkpatrick, M.P., Sargison, J.E., Walker, G.J.: A three-dimensional simulation of a cyclone dryer. In: *Proceedings of International Conference on CFD in the Process Industries CSIRO*, pp. 13–15. Melbourne, Australia, Dec (2006b)
59. Kemp, I.C., Frankum, D.P., Abrahamson, J., Saruchera, T.: Solids residence time and drying in cyclones. In: *Proceedings of 11th International Drying Conference (IDS 1998)*, pp. 581–588. Thessalonika, Greece, A (1998)
60. Osinskii, V.P., Titova, N.V., Khaustov, I.P.: Design and construction of new machines and equipment: experience of use of combined cyclone dryers. *Chem. Petrol. Eng.* **18**(6), 215–218 (1982)
61. Ulrich, W.: Cyclone dryer. In: *Proceeding of 13th International Drying Symposium (IDS 2002)*, pp. 867–873. Beijing, China, B, (2002)
62. Silva, M.A., Nebra, S.A.: Numerical simulation of drying in a cyclone. *Drying Technol.* **15**(6–8), 1731–1741 (1997)
63. Kemp, I.: Process-systems simulation tools. In: Tsotsas, E., Mujumdar, A.S. (eds.) *Modern Drying Technologies*. Wiley-VHC, Weinheim (2007)
64. Renade, V.V.: *Computational Flow Modeling for Chemical Reactor Engineering*. Academic Press, India (2002)
65. Rosa, E.S.: Isothermal multiphase flow—model of multi-fluid and mixture. In: Artmed, S.A. (ed.) *Porto Alegre, Brazil (2012)* (In Portuguese)
66. Bogdanović, B., Bogdanović-Jovanović, J., Stamenković, Ž., Majstorović, P.: The comparison of theoretical and experimental results of velocity distribution on boundary streamlines of separated flow around a hydrofoil in a straight plane cascade. *Facta Univ. Ser.: Mech. Eng.* **5**(1), 33–46 (2007)
67. Davidson, L.: *An introduction to turbulence models*, Department of thermo and fluid dynamics, Chalmers University of Technology, Göteborg, Sweden. <http://www.tfd.chalmers.se/lada> (2011). Accessed on 05 Oct 2012
68. Farias Neto, S.R., Santos, J.S.S., Crivelaro, K.C.O., Farias, F.P.M., Lima, A.G.: Heavy oils transportation in catenary pipeline riser: modeling and simulation, In: *Materials with Complex Behavior II, Advanced Structured Materials*. Springer, Berlin (2011)
69. Shoham, O., Tulsa, U.: *Mechanistic Modeling of Gas-liquid Two-phase Flow in Pipes*. Society of Petroleum Engineers, USA (2006)
70. Yang, X., Eidelman, S.: Numerical analysis of a high-velocity oxygen-fuel thermal spray system. *J. Thermal Spray Technol.* **5**(2), 175–184 (1996)
71. Thomas, P.J.: On the influence of the Basset history force on the motion of a particle through a fluid. *Phys. Fluids A* **4**(9), 2090 (1992)
72. Corrêa, J.L.G.: Discussion of cyclonic dryers design parameters. Ph.D. thesis, Mech. Eng. Fac., State University of Campinas, Campinas (SP) Brazil, (2003) (in Portuguese)
73. Farias, F.P.M., Lima, A.G.B., Farias Neto, S.R.: Influence of the geometric form of the duct of feeding of a cyclone as dryer. In: *Proceedings of 11th Brazilian Congress of Thermal Sciences and Engineering (ENCIT)*, Curitiba, Brazil (2006a) (In Portuguese)

74. Barbosa, E.S.: Geometrical and hydrodynamic aspect of a hydrocyclone in the separation process of multiphase system: application to oil industry. Ph.D. thesis, Process engineering, Federal University of Campina Grande, Brazil, 220p, (2011) (in Portuguese)
75. Cooper, C.D., Alley, F.C.: Air pollution control—a design approach. <http://engineering.dartmouth.edu/~cushman/courses/engs37/A2-Cyclone-Theory.pdf>. Accessed on 05 Mar 2004
76. Farias, F.P.M., Lima, A.G.B., Farias Neto, S.R.: Numerical investigations of the sugar cane bagasse drying in cyclone. In: Proceedings of 16th International Drying Symposium (IDS 2008), pp. 9–12. Hyderabad, India, Nov (2008)
77. Loyola, N., Tolman, S., Liang, L. Kennedy, M., Johnson, D.J.: Cyclone separators. [www.wsu.edu/~gmhyde/433\\_web\\_pages/cyclones/CycloneRptTeam3.html](http://www.wsu.edu/~gmhyde/433_web_pages/cyclones/CycloneRptTeam3.html) (1996). Accessed on 05 Mar 2004
78. Souza, J.A.R.: Drying solid via cyclones: modeling and simulation. PhD thesis, process engineering, Federal University of Campina Grande, Brazil (2012) (In Portuguese)
79. Da Silva, P., Briens, C., Bernis, A.: Development of a new rapid method to measure erosion rates in laboratory and pilot plant cyclones. *Powder Technol.* **131**(2–3), 111–119 (2003)
80. Molerus, O., Glückler, M.: Development of a cyclone separator with new design. *Powder Technol.* **86**, 37–40 (1996)
81. Nebra, S.A., Silva, M.A., Mujumdar, A.S.: Drying in cyclones—a review. *Drying Technol.* **18**(3), 791–832 (2000)
82. Gonçalves, E.C.: Cyclone drying of the orange juice processing. Master's dissertation, chemical engineering school, State University of Campinas, Brazil, pp. 87 (1996)
83. Heinze, C.: A new cyclone dryer for solid particles. *Ger. Chem. Eng* **7**(4), 274–279 (1984)
84. Włodarczyk, J.B.: Suszenie ciał stałych rozdrobnionych w układzie cyklonowym (Drying of particulate material in a cyclonic system). Ph. D. thesis, Polytechnic Institute of Chemical Engineering, pp. 300. Warsaw (1972)

# Moisture Transport Process in Vegetable Fiber Composites: Theory and Analysis for Technological Applications

L. H. Carvalho, E. L. Canedo, S. R. Farias Neto, A. G. Barbosa de Lima and C. J. Silva

**Abstract** This chapter provides theoretical and experimental information about water absorption in unsaturated polyester polymer composites reinforced with vegetable fibers. The use of raw materials from renewable sources, such as natural fibers, has shown great promise in a variety of engineering applications. Composites reinforced with natural fibers are sensitive to influences from environmental agents such as water and temperature. The organic nature of vegetable fibers is responsible for the higher moisture sensitivity of the mechanical properties of natural fiber reinforced composites when compared to synthetic fiber reinforced composites. Here, topics related to theory, experiments, mathematical modeling and numerical procedures, and technological applications for different natural fibers are presented and discussed in detail. Results of microscopy, water absorption kinetics, moisture content distribution, and area/volume relationships for unsaturated polyester composites reinforced with caroá and macambira vegetable fibers are shown and analyzed. The knowledge of moisture distribution allows the determination of areas that may show delamination problems (moisture

---

L. H. Carvalho · E. L. Canedo  
Department of Materials Engineering, Federal University of Campina Grande, Av. Aprígio Veloso, 882, Bodocongó, Campina Grande, PB 58429-900, Brazil  
e-mail: laura@dema.ufcg.edu.br

E. L. Canedo  
e-mail: ecanedo2004@yahoo.com

S. R. Farias Neto  
Department of Chemical Engineering, Federal University of Campina Grande, Av. Aprígio Veloso, 882, Bodocongó, Campina Grande, PB 58429-900, Brazil  
e-mail: fariasn@deq.ufcg.edu.br

A. G. B. de Lima (✉) · C. J. Silva  
Department of Mechanical Engineering, Federal University of Campina Grande, Av. Aprígio Veloso, 882, Bodocongó, Campina Grande, PB 58429-900, Brazil  
e-mail: gilson@dem.ufcg.edu.br

C. J. Silva  
e-mail: carlota.jsilva@gmail.com



induced degradation) due to the weakness of the fiber-matrix interface and consequently reduction in the composites mechanical properties.

**Keywords** Polymer composite · Vegetable fiber · Water sorption · Modeling · Simulation · Experimentation

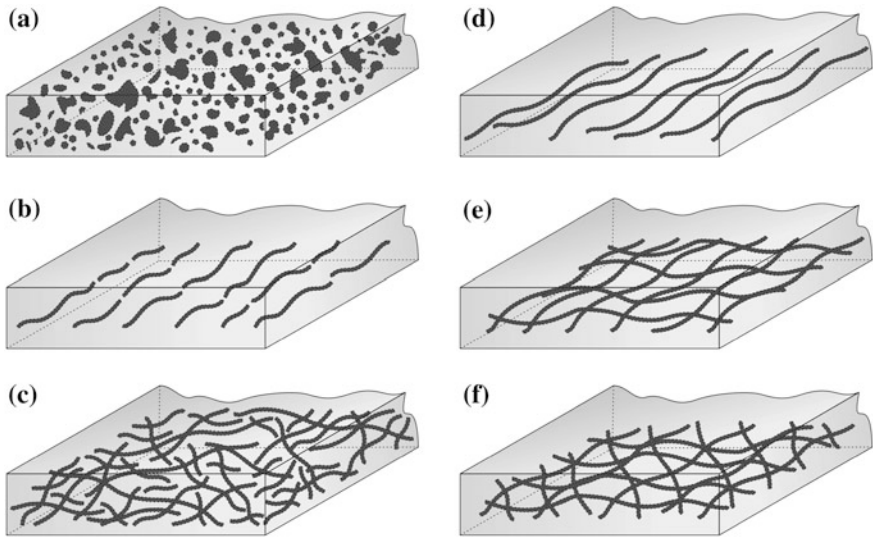
## 1 Introduction

Composites are multiphase materials consisting of one or more discontinuous phases (reinforcing filler) embedded in a continuous phase (matrix) [1]. The matrix phase can be metallic, ceramic, or polymeric, while the reinforcement can be synthetic fiber (glass, carbon, aramid, etc.) or natural fiber (sisal, ramie, jute, cotton, kenaf, pineapple, etc.) or particles (clay, mica, tungsten carbide, titanium carbide, etc.).

Polymer matrices can be classified as thermosets (epoxy, polyester, phenolic, silicone, polyimide, etc.) or thermoplastics (polyethylene, polystyrene, nylons, polycarbonate, polyether-ether ketone, polyphenylene sulfide, etc.). These matrices are most widely used due to their moderate cost, easy processibility, good chemical resistance, and low density [1]. The reinforcing material is usually harder and stronger than the matrix. Thus, composite properties are strongly dependents of the properties of their constituent (matrix and reinforcement). The goal is to achieve the best properties for a given application. The shape, size, distribution, content and filler orientation as well as the matrix/filler interfacial bonding strongly affect the initial and long term properties (hydro, thermal, electrical and mechanical) of the composites whose performance can also be affected by environmental exposure resulting in volumetric variations (or swelling)

Due to their small cross-sectional dimensions, fibers and isometric particulate materials are seldom directly used in engineering applications. For these applications they are embedded in a polymer matrix, for example, in order to form fibrous composites, or ceramic particles are embedded in a polymer matrix to form particulate composites. In general, composite materials can be classified as fiber-reinforced composites (fibrous composites) and particle-reinforced composites (particulate composites). Figure 1 illustrates a scheme for the classification and types of composite materials.

Composite materials are used in aerospace, underwater, biomedical and transportation specific applications as well as in high-tech sporting equipment.



**Fig. 1** Classification and types of composite materials. **a** Dispersed particle-reinforced, **b** discontinuous fiber-reinforced (aligned), **c** discontinuous fiber-reinforced (randomly oriented), **d** continuous fiber-reinforced (aligned), **e** continuous fiber-reinforced (aligned  $0^{\circ}$ – $90^{\circ}$  fiber orientation angle), and **f** continuous fiber-reinforced (multidirectional fiber orientation angle)

## 2 Fiber-Reinforced Composites: Biocomposites

### 2.1 Basic Concepts

Natural fibres are subdivided based on their origin, as coming from plants, animals or minerals. Plant fibres are composed of cellulose while animal fibres consist of proteins (hair, silk, and wool). Plant fibres are derived from renewable resources and are classified according to their origin as bast or soft fiber, leaf or hard fibers, seed, fruit, wood, cereal straw, and other grass fibers [2].

The major constituents of vegetable fibers are cellulose, hemicellulose, lignin, pectin, waxes and water soluble substances. Plant fibres are also known as lignocellulosic fibers or biofibers and can be considered as naturally occurring composites of cellulose fibrils embedded in a lignin matrix [3]. The cellulose fibrils are aligned along the length of the fiber, which renders maximum tensile and flexural strengths, in addition to stiffness. Vegetable fibers can be used as reinforcing fillers for polymer composites and their reinforcing efficiency is related to the fiber nature and cellulose content and to its crystallinity. The structure, microfibrillar angle, cell dimensions, defects, and fiber chemical composition are important variables that determine the overall properties of the fibres [4]. Generally, tensile strength and Young's modulus of fibers increase with increasing cellulose content, while microfibrillar angle determines the stiffness of the fibers.

The fibers will be rigid, inflexible and have high tensile strength if the microfibrils are oriented parallel to the fiber axis and more ductile if the microfibrils have a spiral orientation with respect to the fiber axis [2].

More recently, environmental concerns as well as very stringent regulations and standards have prompted the industries to research and use more eco-friendly and/or sustainable processing methods or products. In order to achieve this goal, available manufacturing processes are modified or adapted to comply with these regulations, alternative technologies are developed or else renewable biomaterials and biofibers are used to generate composite materials. Broadly defined, biocomposites are composite materials made from natural/bio fibers; the polymer matrix may be petroleum or naturally derived (biopolymer), and the former may be biodegradable or not. Biocomposites derived from plant fibers and biopolymers are likely to be more eco-friendly and such composites are termed as green composites. While synthetic matrix/plant fiber composites are not as ecofriendly, they are still more environmental friendly than an all-synthetic material.

Vegetable fibers are biodegradable, sustainable and renewable, carbon dioxide neutral and have a positive environmental impact, as they are nontoxic and non-abrasive to mixing and molding equipment, leading to significant production cost reductions. Thus, plant fibers are a choice material for biocomposite production due to their worldwide availability, economical production, safer handling and working conditions compared to synthetic reinforcements, good set of mechanical properties, low cost per volume, low density and high relative strength and stiffness, which results in composites with specific strength and stiffness comparable to that of glass reinforced ones. Their main disadvantages for polymer composite applications are related to their high moisture sorption, relatively low processing temperatures ( $\leq 200$  °C), low resistance to microorganisms and poor fiber/polymer adhesion to most polymer matrices, which ends up by compromising the composite's immediate and long term mechanical performance [2].

Since composite materials are widely used as a technological solution for the development of new products, environmental and economic concerns have pointed out to the use of vegetable fibers instead of synthetic ones (such as glass or carbon) as polymer reinforcements. The development of biocomposites is economically sound and allow for the development of environmental friendly materials with high value-added [5, 6].

According to Zhang et al. [5], more recently, several researches have pointed to the use of plant fiber with biodegradable polymers based on food, and feed such as starch plastics, soybean plastics and cellulosic plastics for producing fully biodegradable composites. As a result of intense research, reinforced-fiber polymer composites now have acceptable properties and thus being used in a large variety of industrial applications that were dominated by synthetic fibers, such as automobile and packaging industries, structural applications with modest demand on strength reliability, and lightweight construction. As construction material these composites can be applied in decking and railing products. Besides, biocomposites can be used for biomedical and orthopedic applications (bioengineering).

## 2.2 Performance of Fiber Composites

Despite their attractiveness, natural fiber reinforced polymer matrix composites are very sensitive to influences from external environmental agents such as water (in the liquid or vapor phases), relative humidity, temperature, radiation (X-rays,  $\beta$  and  $\gamma$  rays, ultraviolet), chemical agents or a combination between them [1, 6, 7]. They are also sensitive to internal factors such as fiber volume fraction and orientation. Moisture in any form is deleterious to polymer composites, especially to those reinforced by natural fibers. Vegetable fibers are hydrophilic and fiber moisture not only acts a plasticizer but makes polymer impregnation more difficult, causing weak adhesion on the polymer matrix-fiber interface, which leads to internal tensions, porosity and premature failure of the system [8–10]. Biocomposites display lower mechanical properties than synthetic fiber-reinforced composites as water sorption adversely affects the performance, physical and mechanical integrity of the composites. Thus, knowing the effect of moisture on the composite properties is fundamental for outdoor applications. The incompatibilities between natural fiber reinforced composites and water may be diminished by surface modification (chemical treatment) of the fiber or the matrix. In general it is the fiber, not the matrix, that is treated [11].

Several studies show that the mechanical properties of vegetable fiber reinforced composites significantly improve at high fiber content [12–14]. However, when fibrous polymer composites absorb moisture they suffer swelling, plasticizing, dissolving, leaching and/or hydrolyzing, resulting in discoloration, embrittlement, lower resistance to heat and weathering and lower mechanical properties. The amount of water absorbed by a sample varies as a function of its composition, dimensions, void fraction (available free volume), temperature, surface area, surface protection, and exposure time. The effects of moisture and temperature of composites on several performance parameters, such as tensile and shear strengths, elastic moduli, fatigue behavior, creep, rupture stress, response to dynamic impact, and electrical resistance, has been investigated [1]. Due to their importance, several works on the water sorption kinetics of vegetable fiber reinforced polymer composites are reported in the literature [15, 16].

In physical problems involving moisture absorption or desorption in composites, it is very important to determine the moisture content at any instant of the process. In general, the mass transfer rate from or to the body depends on different factors such as temperature, filler content, initial moisture content, and nature and orientation of the reinforcement. Further, the hydric, thermal and mechanical events (in a microscale analysis) occurring in short fiber reinforced composites are very different than those verified for a long fiber reinforced composite [17].

All the factors cited before limit the field of application of vegetable reinforced polymer composites [18–25] and new research in this area is required. For this reason, several works on the absorption kinetics of water and/or moisture in composite systems presenting analytical and/or numerical solutions are reported in the literature. However, all these works consider the diffusion through the solid to

be one-dimensional [26–33]. Yao and Ziegmann [31] related the water absorption behavior of three types of glass-fiber reinforced plastic (GRP) pipes. A model was developed from Fick's law to predict water diffusion curves of the GRP pipe specimens. It was found that only one GPR pipe specimens exhibited near-Fickian behavior and the other two behaved like a two-stage diffusion process because of the abnormal non-Fickian process. Srihari et al. [30] concluded in their studies that the composite (glass/epoxy) and neat resin casting specimens immersed in distilled water and artificial seawater exhibited Fickian behavior. Najafi et al. [32] studied water absorption of wood plastic composites. They concluded that water absorption in these composites follows the kinetics of a Fickian diffusion process. Czél and Czigány [34] in their study of water absorption of glass fiber/polyester composite pipes concluded that the Fickian diffusion model did not fit the absorption curves, but a special explicit, asymptotically correct function based on the Lucas-Washburn equation was found to approximate the water uptake process.

In some cases, in order to take into consideration three-dimensional problems, some researchers use analytical solutions applicable for long times which greatly simplify the problem [35–37]. Chateauminois et al. [35] studied the water diffusion in solids with parallelepiped shape using the short term solution of the one-dimensional Fick's law. For longer times, the water absorption kinetics was computed using the three-dimensional solution of Fick's law. Pavan et al. [36] in their studies on moisture diffusion behavior of glass/epoxy composites found that the diffusion parameters obtained from the experiment conducted up to saturation limits agreed well with the data computed. Bao and Yee [37] showed in their studies of moisture absorption based on long term absorption data that the fast Fickian diffusion is followed by a slow gradual increase in weight gain. This two-step diffusion behavior can be successfully described by the proposed two-stage diffusion model. In this two-stage model, the first and second stage of diffusion are assumed to be diffusion and relaxation-controlled, respectively.

For a more general formulation, Cavalcanti et al. [21] and Cavalcanti [38] report a three-dimensional mathematical modeling approach to describe moisture absorption in an unsaturated polyester composite reinforced by a hybrid jute/glass fabric. Predicted results on the average moisture constant inside the material during the whole process were shown and compared with experimental data, in order to validate the model and to obtain the diffusion coefficient. According to the authors a good agreement was obtained.

Due to the importance of accurately describing the water sorption phenomena in vegetable fiber reinforced polymer composites, the present work deals with the development and study of water sorption kinetics of unsaturated polyester composites reinforced with short fibers of macambira (*Bromelia Laciniosa*) and caroá (*Neoglaziovia Variegata*) fibers. Herein, experimental and theoretical (three-dimensional) studies about water absorption as a function of sample dimensions (rectangular parallelepiped shape) and temperature was conducted.

### 3 Water Diffusion in Polymer Composites

#### 3.1 Experimental Study

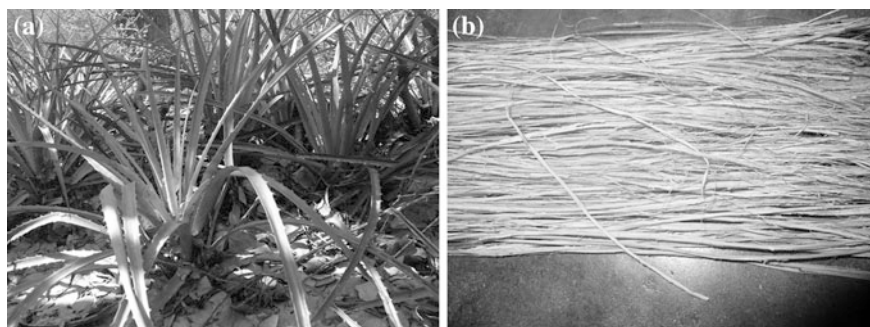
Nóbrega [24] and Nóbrega et al. [39] conducted several experiments on the water absorption of caroá fiber reinforced unsaturated polyester composites, while Cruz et al. [40] conducted similar experiments with macambira fiber reinforced unsaturated polyester composites. The unsaturated polyester was cured with 1 % MEK (methyl ethyl ketone).

The macambira fibers (Fig. 2) were obtained from the Cariri region of Paraíba State (Brazil) while the caroá fibers (Fig. 3) were obtained at a farm in Pocinhos, Paraíba State (Brazil). The fibers were washed with running water, allowed to air dry at room temperature for at least 72 h before being combed and cut up to 5 cm.

Composites with varying fiber content were compression molded. A fiber mat was produced by randomly distributing a pre-determined amount of fibers in steel molds ( $220 \times 180 \times 3$  mm and  $220 \times 180 \times 6$  mm) and compressing with two ton for 5 min at room temperature. Following the mats were removed from the mold for further use. An appropriate quantity of polyester resin was mixed with the catalyst and a small amount was poured onto the mold. The fiber mats were placed in the steel mold, impregnated with more resin and the mold was closed (8 ton).

The system was allowed to cure under pressure for 4 h at room temperature before to remove the composite plate from the mold. The composite plates obtained were post-cured in an oven at  $50\text{ }^{\circ}\text{C}$  for 48 h. Tests for mechanical properties were conducted according to ASTM standards D-3039 for tensile and D-256 for impact tests. Composites samples of  $20 \times 20$  mm were cut-off from these plates, and their edges sealed with resin prior to the water absorption test (to avoid water transport by capillarity) and dried in an air-circulating oven at  $105\text{ }^{\circ}\text{C}$  (to constant weight or dry mass).

The water absorption experiments were carried out according to the following procedure. Firstly, the pre-dried composites samples were immersed fully into a



**Fig. 2** Macambira (*Bromelia Laciniosa*). **a** Plant and **b** fibers





**Fig. 3** Caroa (*Neoglaziovia Variegata*). **a** Plant and **b** fibers

**Fig. 4 a** Caroa composite samples and **b** Macambira and caroa composites samples in water bath



water baths (Fig. 4) kept at 25, 50 and 70 °C. At regular intervals the samples were removed from the water bath, wiped with tissue paper to remove surface water and immediately weighted to  $\pm 1$  mg (uncertainty  $\pm 0.001$  g). Following, the samples were re-immersed in the water bath to continue the sorption process until the equilibrium condition is reached. Each measurement took less than 1 min, so water evaporation at the surface was insignificant.

The results of absorbed moisture were presented as mass of absorbed water by unit dry composites mass. The moisture content was computed as follows:

$$\bar{M}(t) = \frac{W_t - W_0}{W_0} \times 100\% \quad (1)$$

where  $W_0$  and  $W_t$  represent the dry weight of the composites samples ( $t = 0$ ) and the wet weight at any specific time  $t$ , respectively.

Saturation (equilibrium) condition was assumed when the daily weight gain of the composite samples was less than 0.1 %. We notice that complete immersion of composite samples in water bath constitutes the most severe physical situation; exposure to humid air result in lower equilibrium moisture content.

### 3.2 Theoretical Study

Transport phenomena in porous media represents an important research area related to heat and mass transfer, and fluid fields. Mass and heat transport through unsaturated matrices, as with heat and mass diffusion/convection through any heterogeneous media, depends on the structure of the matrix and the physical properties of each phase (fluid and solid).

One of the most difficult aspects of the analysis is structural modeling. A theoretical treatment is based upon the traditional method and start with a potential per unit time balance in a differential control volume with arbitrary shape in macroscopic scale (i.e. porous material is represented as a fictitious continuum).

By assuming local equilibrium between solid and fluid, the mass transfer phenomenon in porous media can be modeled by the macroscopic conservation equation in a short form, as follows:

$$\frac{\partial}{\partial t}(\lambda\Phi) + \nabla \cdot (\lambda\vec{v}\Phi) = \nabla \cdot (\Gamma^\Phi\nabla\Phi) + S^\Phi \quad (2)$$

In the Eq. (2), we have  $\lambda = \rho$ ;  $\Phi = M$  and  $\Gamma^\Phi = \rho D$ , where  $\rho$ ,  $M$ , and  $D$  correspond to density, moisture content, and effective mass diffusivity, respectively, and  $t$  is the time. In this same equation,  $\vec{v}$  is the velocity vector and  $S^\Phi$  is a source term.

For the best analysis, consider a dry porous media (for example, a polymer composite) of complex geometry, at low temperature, which is suddenly immersed in a flowing or stationary, heated, saturated fluid (for example, water) at a different temperature. When this dry porous media is being heated by the fluid surrounding it, heat penetrates into the solid (as the result of a temperature difference) and moisture migrates into the solid by diffusion from the surface.

Mass diffusion is a phenomenon by which matter is transported from one region in space to another due to random molecular motions [41]. Heat and mass transfer creates temperature and moisture gradients inside the solid, which, in general,



depends on the internal and external conditions of the porous media. For simplicity, several researchers report a model that assumes that water migrates at very low velocity from the external surrounding medium to the center of the solid only by liquid diffusion (diffusive effects are greater than convective effects). Gravity, capillarity, and other effects are neglected.

In situations where the solid density may be considered constant and without mass generation inside the solid, the general differential equation that describes the mass diffusion phenomenon (for example, water absorption) can be written as follows:

$$\frac{\partial M}{\partial t} = \nabla \cdot (D \nabla M) \quad (3)$$

where  $D$  is the diffusion coefficient and  $M$  is the moisture content in a dry basis. Equation (3) is called Fick's second law of diffusion.

Despite of the extended use of the Fick's second law to study diffusion process, it fails to address the complex structure of the composite due to different water absorption capacity of the polymer matrix and the natural fiber.

Based on the hypotheses reported above, the mass transfer in a solid of parallelepiped shape, of dimensions  $2R_1 \times 2R_2 \times 2R_3$  (Fig. 5), the mass conservation equation written in Cartesian coordinates for the three-dimensional case, is given as follows:

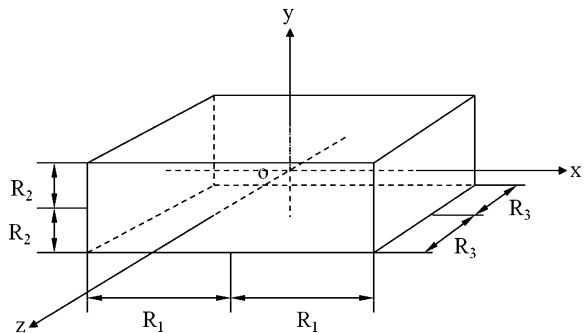
$$\frac{\partial M}{\partial t} = \frac{\partial}{\partial x} \left( D \frac{\partial M}{\partial x} \right) + \frac{\partial}{\partial y} \left( D \frac{\partial M}{\partial y} \right) + \frac{\partial}{\partial z} \left( D \frac{\partial M}{\partial z} \right) \quad (4)$$

For a well-posed mathematical model it is necessary to specify the initial and boundary conditions. Because the symmetry of the problem, we will consider only 1/8 of the volume of the solid. In this chapter, the initial, symmetry and boundary conditions are as follows:

(a) Initial condition:

$$M(x, y, z, t = 0) = M_o, \quad 0 < x < R_1, \quad 0 < y < R_2, \quad 0 < z < R_3 \quad (5)$$

**Fig. 5** Geometrical configuration of the physical problem



(b) Symmetry conditions:

$$\frac{\partial M(x=0, y, z, t)}{\partial x} = \frac{\partial M(x, y=0, z, t)}{\partial y} = \frac{\partial M(x, y, z=0, t)}{\partial z} = 0, \quad t > 0 \quad (6)$$

(c) Boundary conditions:

$$M(x=R_1, y, z, t) = M(x, y=R_2, z, t) = M(x, y, z=R_3, t) = M_e, \quad t > 0 \quad (7)$$

The average moisture content within the solid may be computed as:

$$\bar{M}(t) = \frac{1}{V} \int_V M(x, y, z, t) dV \quad (8)$$

where V is the volume of the porous solid.

In general, the diffusion coefficient has been considered constant or a function of the average moisture content or temperature, or yet as a combination between of moisture content and temperature. Then, for example, we may write:

$$D = D_o \text{Exp}(c\bar{M}) \quad (9)$$

$$D = D_1 \text{Exp}\left(\frac{d}{T}\right) \quad (10)$$

where  $D_o$ ,  $D_1$ ,  $c$  and  $d$  are constants, obtained from experimental data.

To solve the diffusion partial differential equation (Eq. 1) in conjunction with appropriate initial and boundary conditions different analytical (for example, separation of variables and Galerkin-based integral method) and numerical (for example, finite-difference, finite-element, boundary-element, and finite-volume) techniques may be used.

Based on a review of the technical literature, it was noted that some works solve analytically the diffusion problems with prescribed boundary conditions and constant thermo-physical properties. Using separation of variable technique, the analytical solution of the mass diffusion equation applied to a parallelepiped will be [42, 43]:

$$\frac{M(x, y, z, t) - M_e}{M_o - M_e} = \sum_{n=1}^{\infty} \sum_{m=1}^{\infty} \sum_{k=1}^{\infty} A_n A_m A_k \times \text{Cos}(\beta_n x) \times \text{Cos}(\beta_m y) \times \text{Cos}(\beta_k z) \times \text{Exp}[-(\beta_n^2 + \beta_m^2 + \beta_k^2)Dt] \quad (11)$$

where

$$A_n = \frac{2\text{Sen}(\beta_n R_1)}{\beta_n R_1} \quad (12)$$

$$A_m = \frac{2\text{Sen}(\beta_m R_2)}{\beta_m R_2} \quad (13)$$

$$A_k = \frac{2\text{Sen}(\beta_k R_3)}{\beta_k R_3} \quad (14)$$

Using Eq. (11) we obtain the moisture content distribution inside the porous media at different times. In this equation, the coefficients  $\beta_n$ ,  $\beta_m$  and  $\beta_k$  are the so-called eigenvalues. They are obtained as follows:

$$\text{Cos}(\beta_n R_1) = 0 \quad (15)$$

$$\text{Cos}(\beta_m R_2) = 0 \quad (16)$$

$$\text{Cos}(\beta_k R_3) = 0 \quad (17)$$

The average moisture content can be calculated by the following equation:

$$\frac{\bar{M}(t) - M_e}{M_o - M_e} = \sum_{n=1}^{\infty} \sum_{m=1}^{\infty} \sum_{k=1}^{\infty} B_n B_m B_k \cdot e^{-[\beta_n^2 + \beta_m^2 + \beta_k^2]Dt} \quad (18)$$

where

$$B_n = \frac{2}{(\beta_n R_1)^2} \quad (19)$$

$$B_m = \frac{2}{(\beta_m R_2)^2} \quad (20)$$

$$B_k = \frac{2}{(\beta_k R_3)^2} \quad (21)$$

It may be difficult to obtain the analytical solution of a partial differential equation with a high level of complexity, for example, when variable thermo-physical properties are used. In this case a numerical solution may be used as an appropriate alternative technique. We notice that the finite-volume method has been used to discretize the governing equations. Figure 6 represents the differential volume of the physical domain (Fig. 5), where the nodal points (W, E, N, S, F, T), the dimensions of the control volume ( $\Delta x$ ,  $\Delta y$ ,  $\Delta z$ ) and the distances between nodal points ( $\delta x$ ,  $\delta y$ ,  $\delta z$ ) are presented.

Assuming a fully implicit formulation, where all terms are estimated in  $t + \Delta t$ , Eq. (4) was integrated in the control volume of Fig. 4 which corresponds to the internal points of the domain, and also in time. As a result, Eq. (4) was discretized by a finite-volume method using practice B (nodal points in the center of control-volume) [44, 45] resulting in the following linear form:

$$A_P M_P^* = A_E M_E^* + A_W M_W^* + A_N M_N^* + A_S M_S^* + A_T M_T^* + A_F M_F^* + B \quad (22)$$

where

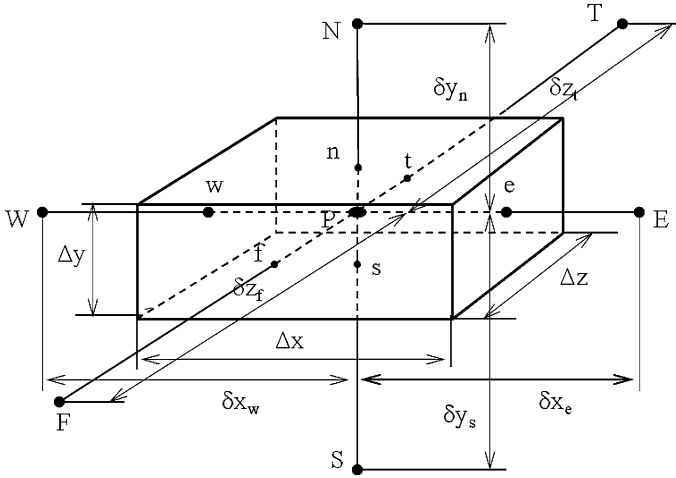


Fig. 6 Control volume used in this work

$$M^* = \frac{M - M_e}{M_o - M_e} \quad (23)$$

$$A_E = \frac{D_e \Delta y \Delta z}{\delta x_e} \quad (24)$$

$$A_W = \frac{D_w \Delta y \Delta z}{\delta x_w} \quad (25)$$

$$A_N = \frac{D_n \Delta z \Delta x}{\delta y_n} \quad (26)$$

$$A_S = \frac{D_s \Delta z \Delta x}{\delta y_s} \quad (27)$$

$$A_T = \frac{D_t \Delta x \Delta y}{\delta z_t} \quad (28)$$

$$A_F = \frac{D_f \Delta x \Delta y}{\delta z_f} \quad (29)$$

$$A_P^o = \frac{\Delta x \Delta y \Delta z}{\Delta t} \quad (30)$$

$$B = A_P^o M_p^{*o} \quad (31)$$

$$A_P = A_E + A_W + A_N + A_S + A_T + A_F + A_P^o \quad (32)$$

The diffusion coefficient (D) at the interface of the control-volume was calculated according to the literature [44]. The set of algebraic linear equations obtained from Eq. (22) (when applied for all nodal points) was solved interactively using the Gauss–Seidel method. The following convergence criterion was used:

$$|M^{*n-1} - M^{*n}| \leq 10^{-8} \quad (33)$$

where n represents the nth iteration in each time.

In practical applications, because of the large variety of materials and operating conditions, the diffusion coefficient is unknown. In general, this parameter has been found by varying it to minimize the sum of the squared deviations between the actual and predicted data. The relative deviation between the experimental and calculated values (relative residual, ERMQ) and the variance ( $S^2$ ) are defined as follows [46]:

$$ERMQ = \sum_{i=1}^m (\bar{M}_{i,Num}^* - \bar{M}_{i,Exp}^*)^2 \quad (34)$$

$$S^2 = \frac{ERMQ}{(m - 1)} \quad (35)$$

where m is the number of experimental points. The smallest values of ERMQ and  $S^2$  has been used as criteria to obtain the best value of the diffusion coefficient.

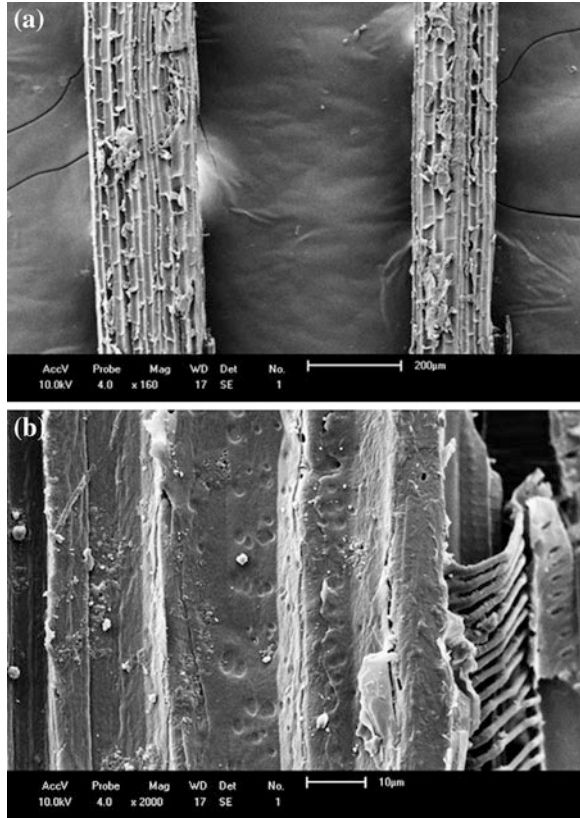
### 3.3 Results Analysis

#### 3.3.1 Morphology Characterization

In this research some fiber samples (untreated) were analyzed by scanning electron microscopy (SEM) in order to characterize the morphology of the fiber. Figures 7 and 8 present micrographs of macambira and caroá fibers in the natural state, respectively. It is verified that the arrangement is similar to other natural fibers, with spongier aspect and a thin, compacted cellular arrangement. Images obtained from SEM also showed a rougher surface, which implies that macambira fibers could be an adequate to reinforce composite materials, due to a good adhesion between fibers and matrix. After treatment or mechanical characterization the fiber suffers some degradation. Besides, since cellulose is the principal constituent with a crystalline structure, it is the main contributor towards the mechanical properties.

From the viewpoint of water absorption, cellulose fibers are difficult to dissolve because of their high crystallinity, but, they tend to retain liquids in the interfibrillar space [12].

**Fig. 7** SEM micrographs for untreated macambira fiber: **a** 160 $\times$  and **b** 2000 $\times$



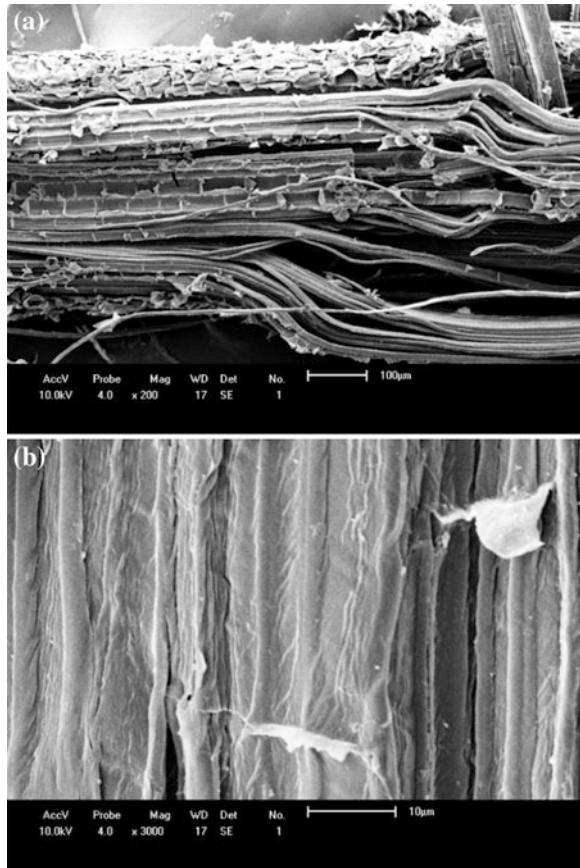
### 3.3.2 Water Absorption Kinetics

Water sorption curves for different dimensions (3 and 6 mm thickness) and temperatures as functions of water exposure (immersion) time for unsaturated polyester/macambira composites with 30 % w/w fiber contents. The general shape of the curves is similar to those of others natural fiber reinforced polymer matrix composites.

For all investigated composites the moisture content increases monotonically with water immersion time until it reaches a maximum value, the so-called equilibrium moisture content (saturation condition). This behavior strongly indicates that the macambira fibers were uniformly distributed in the matrix, in accordance to work reported in the literature [18].

The data indicates that water absorption for the composites is higher than for the matrix. Pure polyester shows a very low percentage of absorbed water. While the water sorption in equilibrium for the unsaturated polyester is about 1 %, for the composites it was about 14 %. The weight loss of pure polyester was almost insignificant, indicating minimal degradation. These results are consistent with

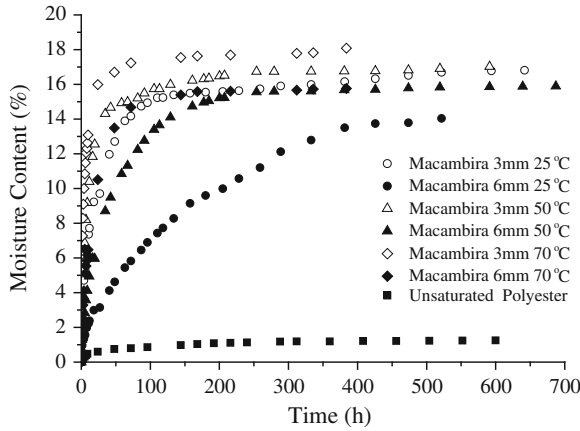
**Fig. 8** SEM micrographs for untreated caroá fiber: **a** 200 $\times$  and **b** 3000 $\times$



studies reported in the literature for similar systems [16, 18, 24, 38, 47]. Some authors attribute the increase in the water sorption by polymer composites reinforced with vegetable fiber to the hydrophilic nature and the permeability of this type of reinforcement and also to the sample surface area exposed to water. Capillarity effects and the interfacial area between fiber and matrix may contribute too.

Figure 9 also shows that water sorption for all composites increase with the area/volume ratio and temperature (Table 1). The effect of the size was more pronounced at the lower temperature.

The results indicate that, as expected, the water uptake of the composite sample immersed in a water bath at 70 °C was faster than under the other (25 °C and 50 °C) experimental conditions. This behavior is attributed to the increased water mobility within the solid at higher temperature. It is believed that higher water temperatures lead to thermal dilation of the composites and to increased composite porosity, which would, in turn, cause a faster moisture migration. Temperature activates the water diffusion process inside the sample, and sorption rate increases with the increases in temperature (thermo-activation).



**Fig. 9** Effect of sample dimensions and bath temperature in the water sorption of Macambira fiber reinforced unsaturated polyester composites

**Table 1** Moisture content and geometric data for the water sorption in vegetable fiber reinforced composites (30 % w/w fiber contents)

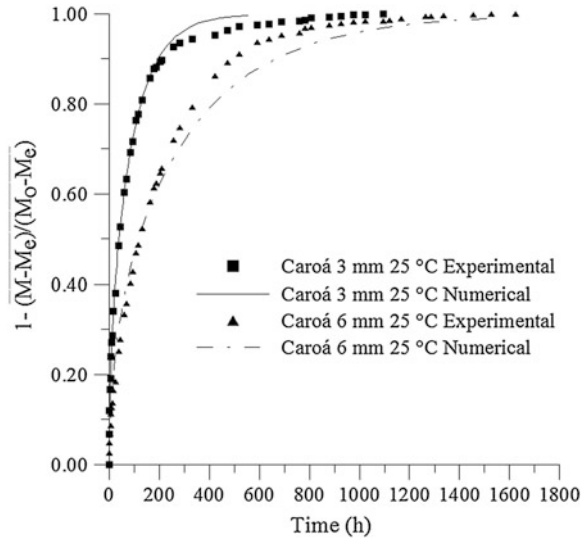
Sample	Thickness (mm)	T <sub>w</sub> (°C)	M <sub>t</sub> (%) (d. b.) (t → ∞)	Area/volume (mm <sup>2</sup> /mm <sup>3</sup> ) (t = 0)
Polyester matrix	3.00	25	1.26	866.67
Macambira composites	3.00	25	16.81	866.67
	6.00	25	14.04	533.33
	3.00	50	17.02	866.67
	6.00	50	15.89	533.33
	3.00	70	18.09	866.67
	6.00	70	16.18	533.33
Caroá composites	3.00	25	14.49	866.67
	6.00	25	14.81	533.33
	3.00	50	15.16	866.67
	6.00	50	16.08	533.33
	3.00	70	15.61	866.67
	6.00	70	16.52	533.33

These results are consistent with those reported in similar systems for unsaturated polyester/caroá composites [24, 39], unsaturated polyester/jute composites [38] and unsaturated polypropylene/sisal composites [12]. Other aspects were not analyzed, such as size and orientation of fiber (events that occurs in long fiber reinforced composites are different those observed in short fiber reinforced composites) [17], and water migration by capillarity in micro cracks inside the solid, mainly in the fiber-matrix interface where adhesion is of fundamental importance. Research in these topics is strongly recommended.

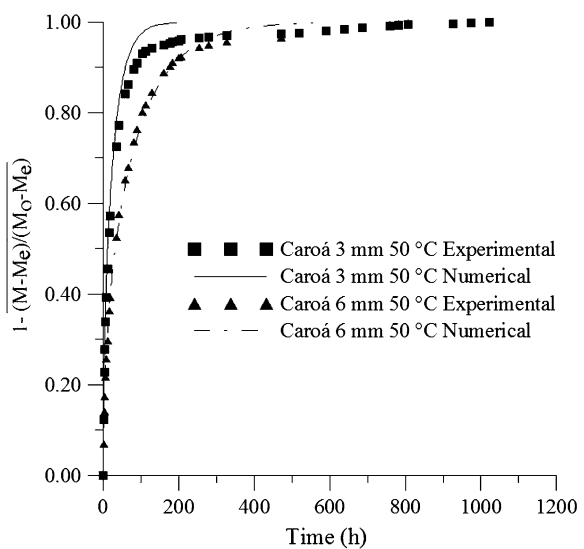
Numerical results of average moisture content of the composites under investigation were compared with the experimental data. To obtain the numerical



**Fig. 10** Comparison between predicted and experimental dimensionless mean moisture content during the water absorption in caroá fiber reinforced unsaturated polyester composites, at 25 °C

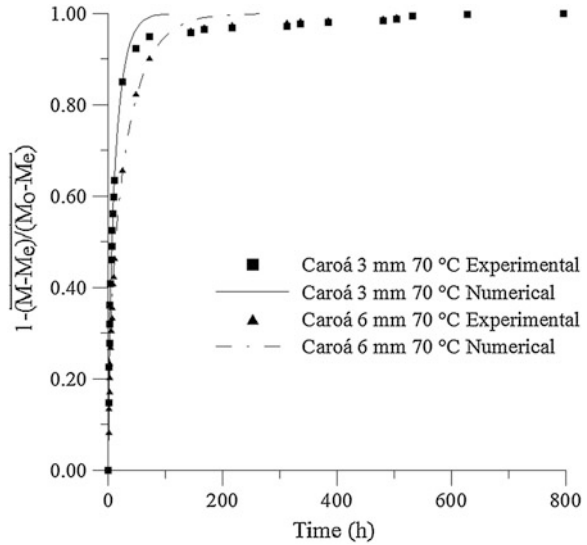


**Fig. 11** Comparison between predicted and experimental dimensionless mean moisture content during the water absorption in caroá fiber reinforced unsaturated polyester composites, at 50 °C



results, a computational code using  $20 \times 20 \times 20$  nodal points and a time step of  $\Delta t = 1$  s was developed. These parameters were obtained after a time step and mesh refining study [38, 48]. The numerical results obtained from a given mathematical model are strongly dependent on the boundary conditions, thermo-physical properties and geometry. A comparison between the experimental and numerical predicted average moisture content for the investigated composites, shown in Figs. 10, 11, 12, indicates that the model employed here is appropriate.

**Fig. 12** Comparison between predicted and experimental dimensionless mean moisture content during the water absorption in caroá fiber reinforced unsaturated polyester composites, at 70 °C



A comparison between Figs. 9, 10, 11, and 12 indicates that the wetting process in the 3-mm thick caroá reinforced composite was faster than in the 6-mm thick composite. This behavior may be attributed to the increase in solid area/volume ratio and the high water affinity for the cellulosic material. The effect is more pronounced at lower temperatures. At high temperature the kinetics of water absorption is dominated by thermal effects, and the mass diffusion inside the material is strongly dependent on the temperature.

Moisture degrades the natural fiber reinforced composites, but this effect was not measured here. However, weight loss varying with immersion time and fiber content was verified for sisal fiber reinforced polypropylene composites properly dried before [18].

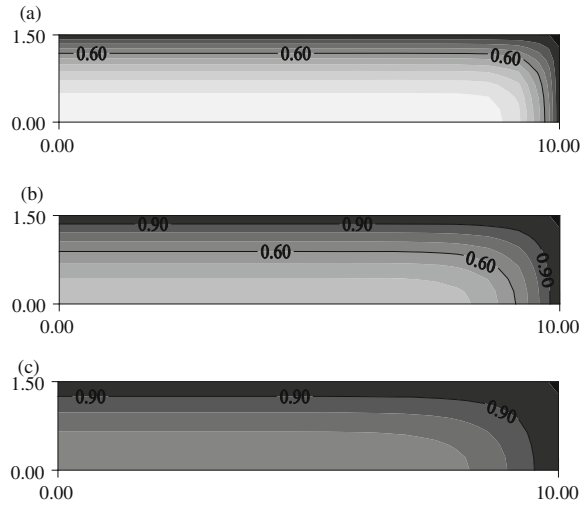
The mechanism of diffusion and structure/diffusivity relationships, have been little studied. Some authors have suggested that water diffusivity is due to morphology [49], local molecular mobility [50], free volume [51] or fiber distribution in polymer matrix [52].

According to [53] apparent water diffusivity decreases when hydrophilicity increases and it increase when temperature increases [25], showing that the fiber/polymer/water interactions strongly influence the diffusion rate within the solid. So, all factors mentioned above, including fiber concentration, thermal stability and shape, need to be studied to get a full understanding of the mechanism of moisture absorption.

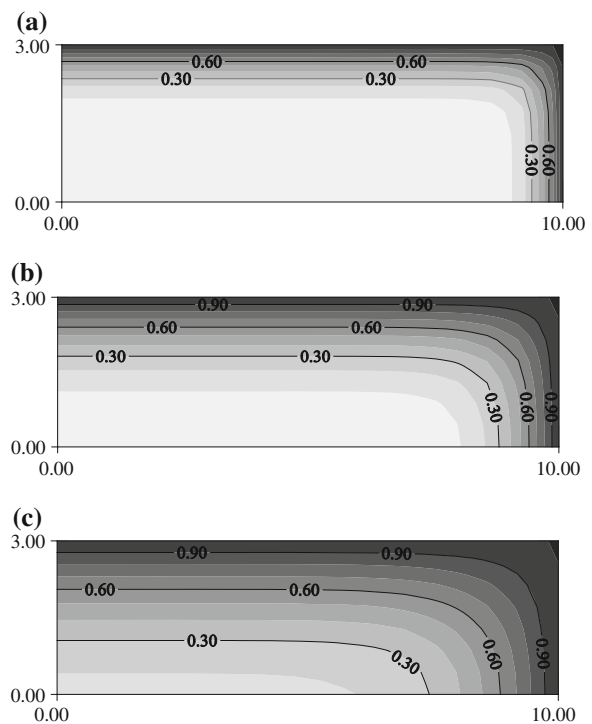
### 3.3.3 Absorbed Water Distribution

The moisture content distribution in the 70 % unsaturated polyester/30 % caroá fiber composites in the plane  $x = 5$  mm, at elapsed time of 20 h, is presented in

**Fig. 13** Moisture content profiles inside the composite 30 % caroá fiber/70 % unsaturated polyester, at 25 °C (a), 50 °C (b) and 70 °C (c) for a thickness of 3 mm, in the plane  $x = 5$  mm, elapsed time 20 h



**Fig. 14** Moisture content profiles inside the composite 30 % caroá fiber/70 % unsaturated polyester, at 25 °C (a), 50 °C (b) and 70 °C (c) for a thickness of 6 mm, in the plane  $x = 5$  mm, elapsed time 20 h



Figs. 12 and 13, showing the existence of high moisture gradients next to the vertices of the solid. Figures 13 and 14 had shown the influence of temperature on the absorption of water. It can be observed that 20 h after the test had started, the

moisture gradients at higher temperature is significantly higher for both thicknesses studied.

It is important to know the profiles and the moisture content inside the material in order to predict which areas are more sensitive to thermo-hygro-mechanical stresses, which may cause cracks and deformations, and consequently decrease the quality of the product [38, 48].

### 3.3.4 Mass Diffusion Coefficient Estimation

Tables 2 and 3 present the value of the diffusion coefficient obtained by the fit between numerical and experimental data. As expected, diffusion coefficients tend to decrease with increasing moisture content and to increase with increasing temperature for all samples. The use of mass diffusivity depending on moisture content led to numerical values that adjusted well to the experimental data, with less error than those obtained if constant diffusivity was assumed.

It is well known that diffusion processes in systems with two or more components depend on several factors such as volume fractions, nature, distribution and orientation of the fillers as well as on fiber/matrix interface characteristics [37, 47]. In general, the comparison with diffusion coefficients reported in the technical literature is very much difficult by the different models and calculation methods used, and by the different porosity, dimensions, temperature, compositions and

**Table 2** Mass diffusion and variance estimated for all wetting experiments with caroá reinforced composites and pure polyester

Sample	$D_o \times 10^{+12} \text{ m}^2/\text{s}$	c	ERMQ	$S^2 \times 10^{+3}$	Time (h)
Pure polyester	2.8	-26.0	0.267	9.54	600
Caroá 3 mm	2.2	-0.4	0.045	1.12	1095
Caroá 6 mm	2.3	-0.1	0.093	1.94	1623
Caroá 3 mm	8.0	-0.4	0.086	2.39	1022
Caroá 6 mm	8.5	-0.1	0.022	0.61	1022
Caroá 3 mm	15.0	-0.4	0.035	1.35	796
Caroá 6 mm	21.0	-0.1	0.043	1.65	796

**Table 3** Range of the mass diffusion coefficients estimated and initial and final moisture content

Sample	Fiber total content (%) / T (°C)	$D_{\text{initial}} \times 10^{+12}$ – $D_{\text{final}} \times 10^{+12} \text{ (m}^2/\text{s)}$	Initial and final Moisture content (dry basis)
Pure polyester	0/28	2.80–2.31	0–0.01252
Caroá 3 mm	30/25	2.20–2.07	0–0.14488
Caroá 6 mm		2.30–2.26	0–0.14810
Caroá 3 mm	30/50	8.00–7.53	0–0.15162
Caroá 6 mm		8.50–8.36	0–0.16067
Caroá 3 mm	30/70	15.00–14.10	0–0.15609
Caroá 6 mm		21.00–20.65	0–0.16523

**Table 4** Moisture diffusivity of composites for several temperatures and shapes

Composite sample (shape)	Time (h)	Dimension (mm)	T (°C)	$D \times 10^{+13}$ (m <sup>2</sup> /s)	Reference
Carbon-glass fiber/epoxy (rod)	5300	66.5 × 9.53	40	1.42	[25]
Carbon-glass fiber/epoxy (rod)	5300	66.5 × 9.53	60	3.84	[25]
Carbon-glass fiber/epoxy (rod)	5300	66.5 × 9.53	90	27.00	[25]
Sisal fiber/polypropylene (rectangular)	166	25 × 10 × 2.50	28	0.36	[12]
Sisal fiber/polypropylene (rectangular)	166	25 × 10 × 2.50	50	0.56	[12]
Sisal fiber/polypropylene (rectangular)	166	25 × 10 × 2.50	28	0.69	[12]
Jute-glass fiber/polyester (rectangular)	1249	20 × 20 × 2.82	28	16.50	[55]
Jute fiber/polyester (rectangular)	500	20 × 20 × 2.30	28	18.00	[56]

physical and chemical structures of the material [38, 54]. However, by comparing the mass diffusivity values of the composites obtained in this study with others, reported in Table 4, it was observed reasonable concordance. As the diffusive model was used in all works reported in the Table 4, the difference between the values may be attributed mainly to the factors: composite variety; geometry assumptions; different equilibrium moisture content; composite physical structure and expansion effects by water absorption.

## 4 Concluding Remarks

In this chapter, water absorption in natural fiber reinforced polymer matrix composites has been explored. Interest in this type of physical problem is motivated by its importance in many practical applications. The use of raw materials from renewable sources, such as vegetable fibers, has been the subject of several studies. One major disadvantage of the use of vegetable fibers in polymer composites is their hydrophilic nature and weak interfacial adhesion to the polymer matrix.

The present work deals specifically with water absorption in unsaturated polyester composites reinforced with caroá and macambira natural fibers by theoretical and experimental techniques. A consistent three-dimensional transient mathematical model was proposed, and a numerical formalism based in finite-volume method was used to solve the governing equation. Experimental tests for water absorption were performed by immersing the samples in a bath of distilled water at different temperatures, and the water uptake was measured gravimetrically along the process. For both the theoretical and experimental analysis the effect of the composite dimensions and bath temperature were studied.

From the results of apparent weight gain of the composites we conclude that: the proposed mathematical model describes adequately the process of water

diffusion inside the composites; water absorption by composites increases with fiber loading and it is higher than for the polymer matrix alone; the kinetics of water absorption is strongly influenced by temperature, the rate of absorption being higher at higher temperatures; higher rates of water diffusion were obtained at the first stages of sorption, and the sorption rate decreased at longer water immersion times; at lower temperature; sample thickness affects water absorption more than temperature; for higher temperature, the effects of the temperature in the water absorption were more relevant than those observed for changes in area/volume ratio of the sample; the regions in the neighborhood of the vertices of the solid presented the highest rates of mass transfer, being more susceptible to crack and deformation; the diffusion coefficient changes with the moisture content and temperature along the absorption process.

The information outlined in this chapter may help researchers and engineers in their study of the unknown features of related complex systems for technological applications in composites.

**Acknowledgments** The authors would like to express their thanks to CNPq (Conselho Nacional de Desenvolvimento Científico e Tecnológico, Brazil), CAPES (Coordenação de Aperfeiçoamento de Pessoal de Nível Superior, Brazil), and FAPESQ (Fundação de Apoio a Pesquisa do Estado da Paraíba, Brazil) for supporting this work; to Resana SA and VI Produtos Químicos for providing the raw-materials, and to the authors of the references in this paper that helped in our understanding of this complex subject, and to the Editors by the opportunity given to present our research in this book.

## References

1. Agarwal, B., Broutman, L.J., Chandrashekha, K.: Analysis and performance of fiber composites. John Wiley & Sons, Inc., New Jersey (2006)
2. John, M.J., Thomas, S.: Biofibres and biocomposites. *Carbohydr. Polym.* **71**(3), 343–364 (2008)
3. Jayaraman, K.: Manufacturing sisal-polypropylene composites with minimum fibre degradation. *Compos. Sci. Technol.* **63**, 367–374 (2003)
4. Satyanarayana, K.G., Ravikumar, K.K., Sukumaran, K., Mukherjee, P.S., Pillai, S.G.K., Kulkarni A.K.: Structure and properties of some vegetable fibres. Part 3. Talipot and palmyrah fibre, *J. Mat. Sci.* **21**(1), 57–63 (1986)
5. Zhang, M.Q., Rong, M.Z., Lu, X.: Fully biodegradable natural fiber composites from renewable resources: all-plant fiber composites. *Compos. Sci. Technol.* **65**, 2514–2525 (2005)
6. Callister Jr, W.D.: Materials science and engineering an introduction. John Wiley & Sons, Inc., New York (2007)
7. Thwe, M.M., Liao, K.: Effects of environmental aging on the mechanical properties of bamboo-glass fiber reinforced polymer matrix hybrid composites. *Compos. Part A: Appl. Sci. Manuf.* **33**, 43–52 (2002)
8. Li, Y., Mai, Y.-W., Ye, L.: Sisal fibre and its composites: a review of recent developments. *Compos. Sci. Technol.* **60**(11), 2037–2055 (2000)
9. Wambua, P., Ivens, J., Verpoest, I.: Natural fibres: can they replace glass in fibre reinforced plastics? *Compos. Sci. Technol.* **63**, 1259–1264 (2003)

10. Aziz, S.H., Ansell, M.P., Clarke, S.J., Panteny, S.R.: Modified polyester resins for natural fibre composites. *Compos. Sci. Technol.* **65**(3–4), 525–535 (2005)
11. Li, X., Tabil, L.G., Panigrahi, S.: Chemical treatments of natural fiber for use in natural fiber-reinforced composites: a review. *J. Polym. Environ.* **15**, 25–33 (2007)
12. Joseph, P.V., Rabello, M.S., Mattoso, L.H.C., Joseph, K., Thomas, S.: Environmental effects on the degradation behaviour of sisal fibre reinforced polypropylene composites. *Compos. Sci. Technol.* **62**, 1357–1372 (2002)
13. Wessler, K., Fogagnolo, C., Everling, M., Bernardo, H.P., Sobral, J.C., Balzer, P.S., Araujo, M.I.S.: Obtenção e caracterização de compósitos de resina poliéster e fibras de bananeira. In: Congresso de Ciência dos Materiais do Mercosul SULMAT 2004, pp. 1–6. Joinville (2004)
14. Carvalho, L.H., Lachhumanandasivam, R., Alexandre, M.E.O., Cavalcanti, W.S.: Propriedades de compósitos poliéster/fibra da folha do abacaxi. In: Congresso em Ciência dos Materiais do Mercosul. SULMAT 2004, pp. 1–6, Joinville (2004)
15. Espert, A., Vilaplana, F., Karlsson, S.: Comparison of water absorption in natural cellulosic fibres from wood and 1-year crops in polypropylene composites and its influence on their mechanical properties. *Compos. Part A.* **35**, 1267–1276 (2004)
16. Sreekala, M.S., Kumaran, M.G., Thomas, S.: Water sorption in oil palm fiber reinforced phenol formaldehyde composites. *Compos. Part A: Appl. Sci. Manuf.* **33**, 763–777 (2002)
17. Herrera-Franco, P.J., Valadez-Gonzalez, A.: A study of the mechanical properties of short natural-fiber reinforced composites. *Compos. Part B: Eng.* **36**, 597–608 (2005)
18. Chow, C.P.L., Xing, X.S., Li, R.K.Y.: Moisture absorption studies of sisal fibre reinforced polypropylene composites. *Compos. Sci. Technol.* **67**, 306–313 (2007)
19. Bledzki, A.K., Reihmane, S., Gassan, J.: Properties and modification methods for vegetable fibers for natural fiber composites. *J. Appl. Polym. Sci.* **59**, 1329–1336 (1996)
20. Clark, R.A., Ansell, M.P.: Jute and glass fibre hybrid laminates. *J. Mater. Sci.* **21**, 269–276 (1986)
21. Cavalcanti, W.S., Carvalho, L.H., Lima, A.G.B.: Water diffusion in unsaturated polyester composite reinforced by a hybrid jute/glass fabric: modeling and simulation. *Revista Matéria* **10**(1), 14–23 (2005) (In Portuguese)
22. Bledzki, A.K., Gassan, J.: Composite reinforced with cellulose based fiber. *Prog. Polym. Sci.* **24**, 221–274 (1999)
23. Andreopoulos, A.G., Tarantili, P.A.: Water sorption characteristics of epoxy resin—UHMPE fibers composites. *J. Appl. Polym. Sci.* **70**, 747–755 (1998)
24. Nóbrega, M.M.S.: Polyester matrix composite with caroá fibers (*Neoglaziovia variegata*): Mechanical characterization and water sorption. Doctorate Thesis, Process Engineering, Federal University of Campina Grande, Paraíba (2007). (In Portuguese)
25. Tsai, Y.I., Bosze, E.J., Barjasteh, E., Nutt, S.R.: Influence of hygrothermal environment on thermal and mechanical properties of carbon fiber/fiberglass hybrid composites. *Compos. Sci. Technol.* **69**(3–4), 432–437 (2009)
26. Ellis, B.E., Found, M.S.: The effects of water absorption on a polyester/chopped strand mat laminate. *Composites* **14**(3), 237–243 (1983)
27. Han, K.S., Koutsky, J.: Effect of water on the interlaminar fracture behaviour of glass fibre-reinforced polyester composites. *Composites* **14**, 67–70 (1983)
28. Camino, G., Luda, M.P., Polishchuk, A.Ya, Revellino, M., Blancon, R., Merle, G., Martinez-Veja, J.J.: Kinetic aspects of water sorption in polyester resin/glass-fibre composites. *Compos. Sci. Technol.* **57**, 1469–1482 (1997)
29. Choi, H.S., Ahn, K.J., Nan, J.-D., Chun, H.J.: Hygroscopic aspects of epoxy/carbon fiber composite laminates in aircraft environments. *Compos. Part A: Appl. Sci. Manuf.* **32**, 709–720 (2001)
30. Srihari, S., Revathi, A., Rao, R.M.V.G.K.: Hygrothermal effects on RT-cured glass-epoxy composites in immersion environments. Part A: Moisture absorption characteristics. *J. Reinf. Plast. Compos.* **21**(11), 983–991 (2002)
31. Yao, J., Ziegmann, G.: Water absorption behavior and its influence on properties of GRP pipe. *J. Compos. Mater.* **41**(8), 993–1008 (2007)

32. Najafi, K.S., Kiaefar, A., Hamidinia, E., Tajvidi, M.: Water absorption behavior of composites from sawdust and recycled plastics. *J. Reinf. Plast. Compos.* **26**(3), 341–348 (2007)
33. Katzman, H.A., Castaneda, R.M., Lee, H.S.: Moisture diffusion in composite sandwich structures. *Compos. Part A: App. Sci. Manuf.* **39**(5), 887–892 (2008)
34. Czél, G., Czigány, T.: A study of water absorption and mechanical properties of glass fiber/polyester composite pipes—Effects of specimen geometry and preparation. *J. Compos. Mater.* **42**(26), 2815–2827 (2008)
35. Chateauinois, A., Vicent, L., Chabert, B.E., Soulier, J.P.: Study of the interfacial degradation of a glass-epoxy composite during hygrothermal ageing using water diffusion measurements and dynamic mechanical thermal analysis. *Polym.* **35**(22), 4766–4774 (1994)
36. Pavan, R.M.V., Saravanan, V., Dinesh, A.R., Rao, Y.J., Srihari, S., Revathi, A.: Hygrothermal effects on painted and unpainted glass/epoxy composites—Part A: Moisture absorption characteristics. *J. Reinf. Plast. Compos.* **20**(12), 1036–1046 (2001)
37. Bao, L.R., Yee, A.F.: Moisture diffusion and hygrothermal aging in bismaleimide matrix carbon fiber composites—Part I: Uni-weave composites. *Compos. Sci. Technol.* **62**, 2099–2110 (2002)
38. Cavalcanti, W.S.: Polyester/hybrid jute-glass fabric composites: Mechanical characterization and water sorption simulation. Doctorate Thesis, Process Engineering, Federal University of Campina Grande, Paraíba (2006). (In Portuguese)
39. Nóbrega, M.M.S., Cavalcanti, W.S., Carvalho, L.H., de Lima, A.G.B.: Water absorption in unsaturated polyester composites reinforced with caroá fiber fabrics: modeling and simulation. *Mat.-wiss. u.Werkstofftech.* **41**(5), 300–305 (2010)
40. Cruz, V.C.A., Nóbrega, M.M.S., Silva, W.P., Carvalho, L.H., Lima, A.G.B.: An experimental study of water absorption in polyester composites reinforced with macambira natural fiber. *Mat.-wiss. u.Werkstofftech.* **42**(11), 979–984 (2011)
41. Farias, V.S.O., Silva, W.P., Silva, C.M.DP.S., Delgado, J.M.P.Q., Farias Neto, S.R., Lima, A.G.B.: Transient diffusion in arbitrary shape porous bodies: Numerical analysis using boundary-fitted coordinates. In: Delgado, J.M.P.Q., de Lima, A.G.B., Silva, M.V. (eds.) *Numerical analysis of heat and mass transfer in porous media*, vol. 27, pp. 85–119. Springer-Verlag, Heidelberg (2012)
42. Luikov, A.V.: Analytical heat diffusion theory. Academic Press, Inc. Ltd, London (1968)
43. Gebhart, B.: Heat conduction and mass diffusion. McGraw-Hill, Inc., New York (1993)
44. Patankar, S.V.: Numerical heat transfer and fluid flow. Hemisphere Publishing Corporation, New York (1980)
45. Maliska, C.R.: Computational heat transfer and fluid mechanics. LTC, Rio de Janeiro (2004). (In Portuguese)
46. Figliola, R.S., Beasley, D.E.: Theory and design for mechanical measurements. John Wiley & Sons, New York (1995)
47. Marcovich, N.E., Reboredo, M.M., Aranguren, M.I.: Moisture diffusion in polyester-woodflour composites. *Polym.* **40**(26), 7313–7320 (1999)
48. Nascimento, J.J.S.: Transient diffusion phenomena in parallelepiped solids. Studied case: Drying of ceramic materials. Doctorate Thesis, Mechanical Engineering, Federal University of Paraíba, João Pessoa (2002). (In Portuguese)
49. Gupta, V.B., Drzal, J.L., Rich, M.J.: The physical basis of moisture transport in a cured epoxy resin system. *J. Appl. Polym. Sci.* **30**(11), 4467–4493 (1985)
50. Lagouvardos, P.E., Pissis, P., Kyritsis, A., Daoukaki, D.: Water sorption and water-induced molecular mobility in dental composite resins. *J. Mater. Sci. Mater. Med.* **14**(9), 753–759 (2003)
51. Duda, J.L., Vrentas, J.S., Ju, S.T., Liu, H.T.: Prediction of diffusion coefficients for polymer-solvent systems. *AIChE J.* **28**, 279–285 (1982)
52. Wang, W., Sain, M., Cooper, P.A.: Study of moisture absorption in natural fiber plastic composites. *Compos. Sci. Technol.* **66**, 379–386 (2006)



53. Merdas, I., Thominette, F., Tcharkhtchi, A., Verdu, J.: Factors governing water absorption by composite matrices. *Compos. Sci. Technol.* **62**, 487–492 (2002)
54. Lima, A.G.B.: Diffusion phenomena in prolate spheroidal solids: Studied case: Drying of banana. Doctorate Thesis, Mechanical Engineering, State University of Campinas, Campinas (1999) (In Portuguese)
55. Silva, W.P., Silva C.M.D.P.S., Farias, V.S.O., Lima A.G.B.: Effect of the geometry on the description of the water absorption by composite materials using diffusion models. *Mat.-wiss. u.Werkstofftech.* **42**(8), 747–752 (2011)
56. Cavalcanti, W.S., de Lima, A.G.B., Carvalho, L.H.: Water sorption in unsaturated polyester composites reinforced with jute and jute/glass fiber fabrics: Modeling, simulation and experimentation. *Polímeros: Ciência e Tecnologia* **20**(1), 78–83 (2010) (In Portuguese)

# Filtration Processes and Design of Filters

Antonio F. Miguel

**Abstract** The process of filtration is widely used from domestic use to industry. Filters are used in vacuum cleaners and air conditioning systems but also in a wide variety of critical applications such as in the nuclear, electronic, aerospace, pharmaceutical and medical fields. How filtration process takes place? What kinds of filters are available? How to design good filters? This chapter is devoted to filtration theory, design and international standards for efficient air filters. It represents an attempt to bridge a gap in the literature by presenting an integrated view of the current state of art in this fascinating field of filtration.

**Keywords** Filtration • Aerosol • Porous media • Filters • Design

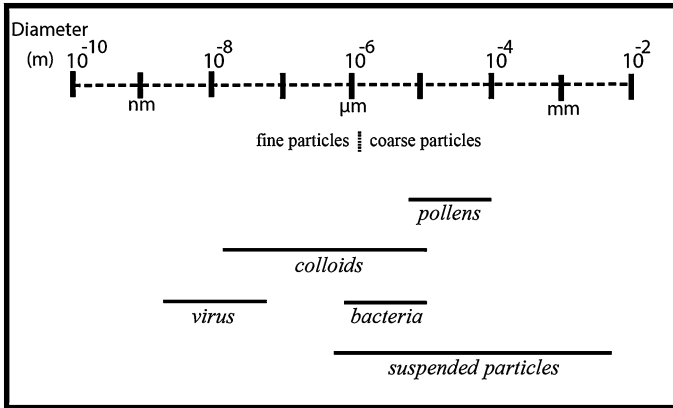
## 1 Aerosols: Characteristics and Classification

Aerosol consists of solid or liquid particles suspended in a gas. Dust, smoke, mists, fog, haze, and smog are various forms of common aerosols. The size of air molecules is about 0.3 nm and the mean free path (average distance a molecule travels between collisions) is about 70 nm, but aerosol sizes are the result of several competing processes such as the condensation, sedimentation, agglomeration, impaction, etc. In terms of the size and formation mechanism are classified into fine and coarse particles (Fig. 1). Fine particles are composed of nuclei and larger conglomerates of material that is accumulated. The nuclei mode (size < 0.1  $\mu\text{m}$ ) consists primarily of combustion particles emitted directly into the atmosphere and particles formed in the atmosphere by gas-to-particle conversion. They have relatively short lifetimes and coagulate rapidly. These

---

A. F. Miguel (✉)

Department of Physics and Geophysics Center CGE, University of Evora, Evora, Portugal  
e-mail: afm@uevora.pt



**Fig. 1** Aerosol particle size distribution

coagulated nuclei-mode particles, together with smog particles constitute the accumulation mode ( $0.1 \mu\text{m} < \text{size} < 2 \mu\text{m}$ ). Coarse particles (size  $> 2 \mu\text{m}$ ) consists of mechanically generated anthropogenic particles such as those from agriculture and surface mining, and windblown dust. Biogenic particles (e.g. viruses, intact bacterial cells, fungal cells, plant pollen grains, and insects' debris) are also available in the atmosphere mainly in coarse mode [23]. Particles larger than  $100 \mu\text{m}$  have a short lifetime in the atmosphere because they readily settle out. Additionally, a common aerosol particle size distribution is the lognormal distribution which usually fits those from a single source.

Aerosol particle concentration impairs visibility and affects air quality. They can be carried over long distances by wind and then settle on ground and water, or breathed in by people and animals. Aerosol particles are a primary component of the haze that obscures visibility in our cities. Some aerosols can contribute to acid rain issues (i.e., to make streams acidic, deplete nutrients in soil, damage of forests, farm crops, stone and other materials including monuments, etc.). Outdoor aerosol may also enter the buildings and may affect the indoor environments [45]. Aerosols are also generated inside the buildings during indoor activities such as cooking, heating, smoking, candles and incense burning, etc. Flea powder, aerosolized insecticides, cleaning products and indoor materials may also act as sources aerosols [56, 64].

Inhalable (i.e., particles smaller than  $100 \mu\text{m}$  are typically inhaled), thoracic (i.e., inhalable particles less than  $10 \mu\text{m}$  that can reach the thorax), and respirable particles (i.e., particles less than  $4 \mu\text{m}$ ), are likely to deposit in different regions of respiratory tract. Therefore, once breathed in, particles may reach the alveoli and settle, causing severe inflammation and may enter the bloodstream, circulating through all body. Epidemiological studies show that fine air pollution particles have a large impact on people health. The extent of this impact depends upon the aerosol concentration, chemical composition and exposure time. Cardiopulmonary

diseases (heart and lung diseases including asthma and bronchitis) are among the most important health effects [8, 50]. The effects are more pronounced in people who are not healthy.

The adverse effect of particulate air pollution on health has led to standards for levels of particulate matter in outdoor air [47, 48, 68]. PM10 stands for particulate matter up to 10  $\mu\text{m}$  in aerodynamic diameter which includes thoracic fraction of particles, and the 24 h standard for these particles is 150  $\mu\text{g}/\text{m}^3$  [47]. Evidence that small aerosols were particularly damaging has led to more stringent standards for levels of particulate matter. A new indicator (PM2.5) was then created for particulate matter up to 2.5  $\mu\text{m}$  in aerodynamic diameter (fine particles). The annual particles standard for PM2.5 is within the range of 12.0–13.0  $\mu\text{g}/\text{m}^3$  [47]. However, in people with asthma, even relatively low concentrations of PM2.5 air pollution worsen lung function [9]. Short-term exposure to PM2.5 also increases the risk for hospital admission for cardiovascular and respiratory diseases [11]. Authors [11] found that the largest association was for heart failure.

Not all aerosols have harmful effects on human health. Aerosolized medications have been used for centuries to treat some diseases. They play an important role in asthma and other lung complaints. There are also applications under development such as the inhalation of insulin to treat diabetes [71], treatment of lung diseases with aerosolized gene therapy (e.g., inhaled complementary DNA to treat Cystic Fibrosis) [18, 20] and vaccination via aerosol (candidates includes measles, influenza, rubella and anthrax) [32, 46]. In contrast to oral and injection therapies, the route of administration eliminates the potential for poor absorption and high metabolism in the gastrointestinal tract, eliminates losses in the liver, and the pain and discomfort that is associated to injection therapy.

## 2 Porous Media for Aerosol Filtration

Filtration is a very effective and common method for aerosol removal. Particles are collected for air refinement or aerosol sampling. Filters are made in a variety of materials such as cellulose, Teflon, nylon, polyvinyl chloride, silver, quartz, etc. They can be classified according to their structure in porous membrane filters, packed-bed filters and fibrous filters [5, 65]. There is also a new class of filters of biologically-inspired design that deserves to be also included [39, 58].

Porous membrane filters consist of cellulose ester, polyvinyl chloride, and Teflon membranes with relatively uniform microstructure channels that allows the capture of particles transported by passing air. The porosity is less than 0.85 and thickness ranges from 0.05 to 0.2 mm. Their manufacture consists of polymer films that are bombard by neutrons followed by etching process. From this procedure results an array of cylindrical holes (pores) of uniform diameter perpendicular to the surface of the filter. Within this class of filters, capillary porous membrane filters (porosity between 0.05 and 0.10) are particularly suitable for collecting particles for observation in the microscope.

Fibrous filter media composed by fibres or filaments of natural or synthetic materials have been used extensively in filtration [65]. A variety of these filters made of cellulose, polymer and quartz fibres are available, having porosities ranging from 0.55 to 0.99 and thicknesses up to 0.5 mm. These filters vary in efficiency and effectiveness.

Fibres or filaments spun into a continuous yarn results in a woven media filter. Single filaments, multifilament yarns, or twisted staple yarn characterized these media. The nature of the basic fibre or filament, and the way in which the yarns are woven together determine the properties of the filter. The regular structure and the relative strength, both mechanical and chemical, make woven materials valuable as filtration media. There are also woven filter media composed by a wide variety of wire meshes of either ferrous or non-ferrous metals. They are used to remove very large, harsh particulate under extreme conditions of temperature, corrosion and abrasion.

The so-called non-woven media filters are made up from a random array of fibres or filaments, held together to form a flexible sheet [28, 69]. They can be felts (i.e., rely on the characteristics of the fibre to provide mechanical integrity or on mechanical processing to create a fabric) and bonded fabrics (i.e., they use additional adhesive material to hold the fibres together). Non-woven filters are porous fabrics with greater flexibility and versatility.

Packed-bed filters consist of a fine granules, usually glass, quartz, metal, and activated charcoal. The porosity is higher than 0.26 [60]. Particles are collected on the surface of the beds and may be removed by washing, volatilization or using solvents. Packed-bed filters are particular suitable for corrosive aerosols at high temperature. Materials such as activated carbon, fuller's earth and ion exchange resins are also used for promoting adsorption of gaseous pollutants. Deep-bed filtration is used for gas and liquid filtration.

Biofilters are reactors for the conversion of contaminated air into harmless products of carbon dioxide, water and mineral salts. The contaminated air is passed through a bed of porous moist medium, and the contaminants are adsorbed to the medium surface where they are degraded by the microorganisms in the medium [51, 63].

Filters found in living structures are innately selective: the relevant bio-structure controls the migration of particular species through it. One of examples is the lung that filters the air that we breathe constantly with high efficiency. The adherence to lung design (i.e., T-shaped and tree-shaped design) for an enhanced performance is proposed by different authors [27, 33, 39]. Recently, the T-shaped designs for particle removal was studied by Serrenho and Miguel [58].

### 3 Manufacturing Standards for Filters

By the end of the 1940's, deep beds of graded granular coke were used for radioactive material at "Hanford Works V" (which was part of Manhattan

Project), when high activity levels were detected in particulate form [13, 30]. These filters, both used at Hanford and Savannah River sites, operated at a superficial face velocity of 0.03 m/s, and had collection efficiencies of 99.7 % for particles greater than 0.5 μm [16]. High efficiency filters for treating reactor effluent gases were also mounted at Oak Ridge National Laboratory, Tennessee [66]. The system contained fibreglass prefilters with an efficiency of 99.9 % for particles greater than 0.1 μm. These filters were known as super-interception, and super-efficiency filters due to their high retention efficiency for small particles. Later, they were termed as “High Efficiency Particulate Air” filters (HEPA) by Gilbert [19].

In the search towards standard manufacturing and test criteria for filters, HEPA filters were defined as having a retention efficiency of 99.95 % for particles greater than 0.3 μm and airflow resistance (clean filter) up to 249 Ns/m<sup>3</sup> [1, 70]. This specific particle size criterion comes probably from the results obtained from Langmuir’s studies [29]. These studies consider only interception and diffusion mechanisms of particles removal, and obtained minimum filter efficiency for particle with 0.3 μm in diameter. Subsequent studies confirmed a minimum filterable diameter, but also that it depends on filtration mechanisms involved [36, 65]. These mechanisms will be described in next the section.

Ultra Low Penetration Air (ULPA) filters is another class of filters which their efficiency is defined for particles in the 0.1 μm range, that is the minimum filterable particle size for currently HEPA filters operating at their design airflow rate.

In summary, international standards for submicrometer particles distinguish among HEPA (with five classes) and ULPA (with 3 classes) filters (Table 1).

Today, HEPA and ULPA filters satisfy the high demands for air quality in various technology industries, such as aerospace, pharmaceutical, processing, electronics, nuclear fuels and nuclear power but also in hospitals and our buildings.

**Table 1** HEPA and ULPA filters characteristics according to the Comité Européen de Normalisation (CEN classification) [36]

Filter	EN 1822-1 filters class	Efficiency (%) <sup>a</sup>
HEPA	H10	85
	H11	95
	H12	99.5
	H13	99.95
	H14	99.995
ULPA	U15	99.9995
	U16	99.99995
	U17	99.999995

<sup>a</sup> Major particle penetration size—integral efficiency (mean value of all local efficiencies measured over the filter’s face area.)

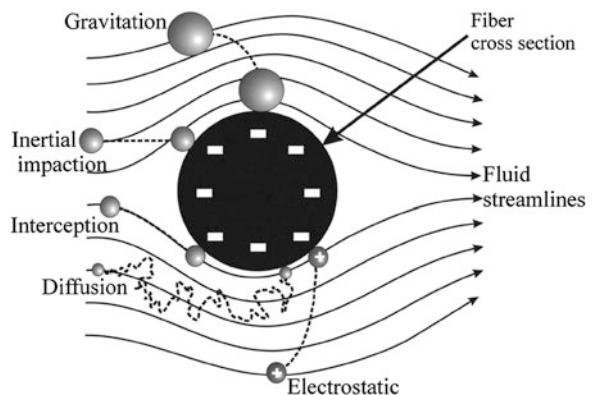
## 4 Particle Deposition Mechanisms in Filters

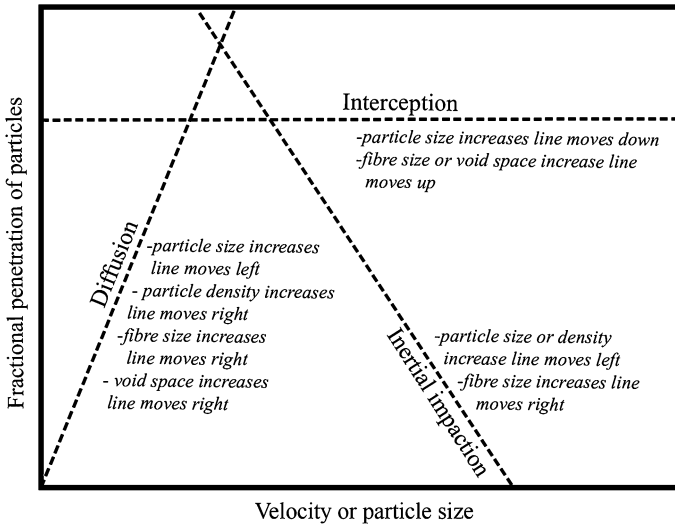
Filter media may retain particles at surface (surface filtration) and within the structure of the medium (depth filtration). Particles larger than the sizes of the filter pores deposit on the medium surface but particles smaller than the pore sizes deposit generally within the filter.

There are several mechanisms that govern the deposition of particles in filters (Fig. 2). When a particle following its fluid movement streamline comes in contact with the filter medium and becomes attached to it, the mechanism is known as interception. This takes place when a particle comes within a distance from the filter medium (i.e., fibre, bed, etc.) which is less than or equal to, the particle radius. Another possibility is when particles deviate from fluid streamlines: this greatly enhances the probability of hitting the fibre or bed and remain there. The deviation from streamlines is caused by different mechanisms:

1. Inertial impaction: the inertia of the particle that is carried by the fluid stream depends on its mass and velocity. When a particle is unable to adjust to the fluid stream turns and it continues on its previous path, it can be collected by the filter medium. The effectiveness of inertial impaction improves with the increasing particle mass and velocity and the decreasing particle size.
2. Gravitation: The settling of particles is due to the gravity, and is especially important where there are very heavy particles and very slow fluid velocities.
3. Diffusion: small particles in random directions (Brownian motion), instead of following fluid streamlines, can come in contact with the filter medium and remain there.
4. Electrostatic: experimental evidences indicated that both atmospheric particles and filter media possess electrical charges. If particles and the filter medium have charges of opposite signs, electrostatic forces arise from the Coulomb interactions between these charges, and particles come in contact with the filter medium and may remain there.

**Fig. 2** Schematic representation of particle deposition on a collector [36]





**Fig. 3** Influence of deposition mechanisms on the fractional penetration of particles-velocity curve [36]

Notice that the all five of the above-mentioned collection mechanisms are taking place simultaneously. Therefore, the collector-element efficiency,  $\eta$ , depends on the partial efficiencies of each aerosol capture mechanisms and can be obtained from

$$\eta = 1 - (1 - \eta_r)(1 - \eta_I)(1 - \eta_D)(1 - \eta_G)(1 - \eta_{el}) \tag{1}$$

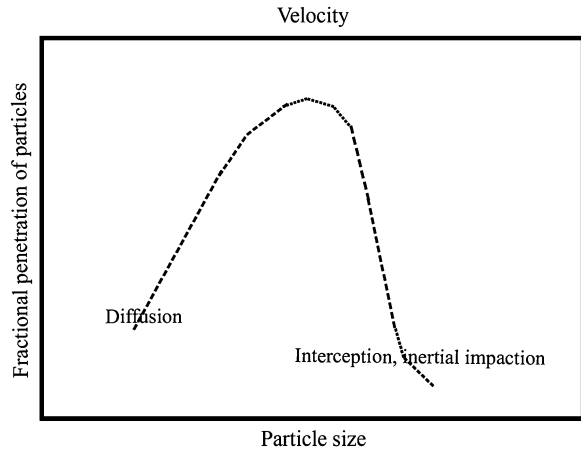
where  $\eta_r$ ,  $\eta_I$ ,  $\eta_D$ ,  $\eta_G$  and  $\eta_{el}$  are the partial efficiencies for the particle deposition due to the mechanisms of interception, inertial impaction, diffusion, gravitation and electrostatic, respectively. A comprehensive review of partial efficiencies in filters is provided by Bejan et al. [5].

The expected penetration of particles through the filter for a given filtration velocity is presented at Fig. 3. For the inertial impaction mechanism, increasing particle radius and density improves particle collection efficiency (penetration is less). For diffusion deposition mechanism, as the particle radius decreases the slope of the line decreases and the influence of this mechanism increases. Besides, the greater the open pores in the filter is, the fluid velocity in the pore space of the filter is less (i.e., pore fluid velocity is the ratio between the superficial filtration velocity and the porosity) and transit time is longer. Therefore, the contact between particle and filter medium is more likely and the filter efficiency increases. On the other hand, as pore size increases, the particle penetration increases for both the inertial impaction and direct interception.

The smallest penetration of particles (highest particle deposition) occurs for the large particles at high velocities and for the finest particles at low velocities (Fig. 4). There is an intermediate size range ( $\sim 0.1$  to  $2 \mu\text{m}$ ) where penetration has



**Fig. 4** Influence of particle size on the typical fractional penetration of particles [36]



a maximum. This range depends very much on the ratio between the particle size and the collector size [5, 65]. This maximum can be lightened by the existence of electrostatic forces (i.e., Coulomb interactions).

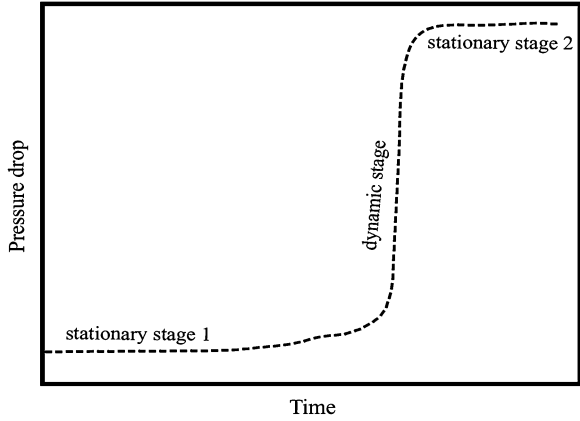
## 5 Particle Loading Performance of Filter Media

The choice of a filter is based upon fundamental attributes: the smallest particle sizes that the medium is able to retain, the dirt-holding capacity, the filter permeability to the fluid flow through it and the mechanical strength of filter medium. These attributes are closely related with the filter structure.

From the suspensions flow point of view, the filter should have high retention efficiency for particles (i.e., filter media should be characterized by low particle penetration), and a high permeability to fluid flow. In time, more and more solids are deposited in the filter leading to an increase of retention efficiency but also to a decrease in its ability to allow fluid to flow through it (i.e., reduction of filter permeability or increase of pressure drop). As a result, the pressure drop required for maintaining a constant airflow through the filter increases as the deposition process continues. The life of the filter depends greatly on this phenomenon. Therefore, the understanding of the filtration process over time, for given operating conditions, is crucial. In general, there are 3 stages that are represented in Fig. 5, [5]:

1. Particle deposition occurs in the filter structure. The filter efficiency and permeability is not very much affected in time (stationary stage 1).
2. Gradual deposition induces a gradual change of the structure of filter media. Particles start to deposit onto previous deposited particles, and pores start to clog. The filter efficiency increases and permeability decreases in time (dynamic stage).

**Fig. 5** Pressure drop through the filter in time and stages of filtration [42]



- When approaching the clogging point, the filter efficiency and permeability no longer varies with time (stationary stage 2).

Particles deposited at the stationary stage 1 don't alter dramatically the internal structure of the filter (Fig. 6). During this stage, Zhao et al. [72] suggests that deposited particles only affect the collectors' sizes of the filter (e.g., fibres, beds, etc.). Denoting that the mass of particles collected per filter area is  $M_{pA}$ , the particle-loaded collector radius,  $r_c$ , and the filter solidity (or the volume fraction of the filter material),  $\alpha$ , are given by

$$r_c = r_{co} \left( 1 + \frac{M_{pA}}{\rho_c \alpha H} \right)^{1/2} \tag{2}$$

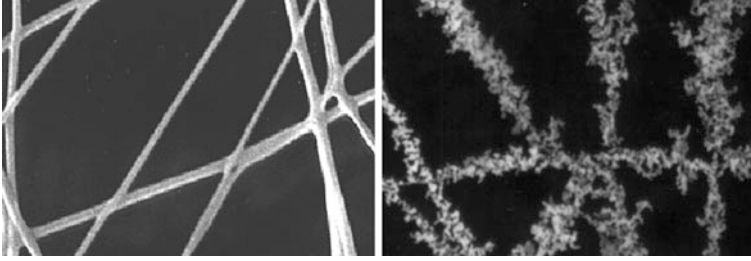
$$\alpha = \alpha_o \left( 1 + \frac{M_{pA}}{\rho_c \alpha H} \right) \tag{3}$$

where  $H$  is the filter thickness,  $\alpha_o$  is the filter solidity and  $r_{co}$  is the collector radius. The subscript  $o$  means clean filter (i.e., free of deposited particles).

Once the collectors' structure of the filter has evolved enough that no more particle collection occurs onto them, deposition onto previous deposited particles then takes place resulting in the formation of the particle cake (dynamic stage). In order to account for these circumstances, Emi et al. [14] suggest that, in fibrous filters, the collector-element efficiency evolution from clean filter is

$$\eta = \eta_o \left[ 1 + \left( \frac{M_{pA}}{0.316 b_{\eta 1} \eta_o u^{0.25}} \right)^{b_{\eta 2}} \right] \tag{4}$$

where  $\eta_o$  is the initial efficiency when the filter is clean, and  $b_{\eta 1}$  and  $b_{\eta 2}$  are, respectively, 0.0027 and 1.15 (filter mesh 200), or 0.0015 and 1.23 (filter mesh 325), and 0.0011 and 1.34 (filter mesh 500). The mesh size indicates the number of



**Fig. 6** The effect of aerosol particle loading on fibrous filter (stationary stage 1)

fibres per inch in one of the directions (warp or weft). Besides, Jung and Tien [67] suggested that for granular filters the efficiency behaves as

$$\eta = \eta_o \left[ 1 + a_{\eta 1} \left( \frac{M_{pA}}{\rho_p H} \right)^{a_{\eta 2}} \right] \quad (5)$$

For experiments performed at  $0.0017 \leq St \leq 0.038$  and  $0.00172 \leq Ir \leq 0.008$ , the coefficients  $a_{\eta 1}$  and  $a_{\eta 2}$  are given by  $a_{\eta 1} = 0.095 St^{-1.48} Ir^{0.432} 10^{3a_{\eta 2}}$   $a_{\eta 2} = 0.442 St^{-0.347} Ir^{0.24}$ , where  $St$  is the Stokes number and  $Ir$  is the interception parameter (i.e., the ratio between the particle radius and the collector radius).

### 5.1 Filter Efficiency and Fractional Penetration

The smallest particles that are totally retained constitute the “absolute rating” of a filter. However, there are particles that are able to pass through the filter medium. Concentrations of particles measured upstream and downstream of the filter allows determining the fractional penetration of particles. Alternatively, filter efficiency  $\varphi$  is defined as

$$\varphi = 1 - \Pi = 1 - \frac{c_{dst}}{c_{ust}} \quad (6)$$

Here  $\Pi$  is the fractional penetration of particles (or simply penetration), and  $c_{ust}$  and  $c_{dst}$  are the concentrations of particles upstream and downstream of the filter, respectively. Research on aerosol filtration converges towards the idea that  $\Pi$  and  $\varphi$  depend, among other factors, on filter thickness, filter microstructure, particle characteristics and the mass of particles existing within the filter [5, 21, 65]. The penetration has an exponential dependence of the filter thickness,  $H$ , and an intrinsic quantity named characteristic filtration length,  $h$ , and can be expressed as [5, 61]

$$\Pi = \exp\left(-\frac{H}{h}\right) \quad (7)$$

The filtration length depends most notably on the microstructure of the filter and on particle size [10, 21]

$$h = \frac{2r_c}{s\alpha\eta} \quad (8)$$

where  $s$  is a coefficient that can be taken as equal to  $4/[\pi(1-\alpha)]$  for fibrous filters [17, 21], and equal to 1.5–1.88 for granular beds [12, 21, 57].

## 5.2 Filter Permeability and Pressure Drop

In accordance with Darcy's law, a suspension of particles moving with a slow, steady velocity, and the pressure drop through the filter are related by [5, 37, 40, 41]

$$\Delta p = \frac{\mu}{K} H u \quad (9)$$

Here  $u$  is the superficial velocity (the velocity within the filter—the intrinsic velocity—is related with the superficial velocity through the filter porosity),  $\mu$  is the viscosity and  $K$  is the intrinsic permeability. Darcy's law is used to define the permeability of the filter, provided that the viscosity is known.

In spite of its great applicability, the concept of permeability as a global quantity that characterizes the fluid flow, which grounds the validity of Darcy law, holds only for low values of the Reynolds number (i.e., creeping flow or Stokes flow). At sufficiently high Reynolds numbers, the flow through the filter is well approximated by a nonlinear approach [5, 37, 40]

$$\Delta p = \frac{\mu}{K} H u + \rho H \beta_\beta u^2 \quad (10)$$

or

$$\Delta p = \frac{\mu}{K} (1 + \beta_\beta K^{1/2} Re_K) H u \quad (11)$$

Here  $\beta_\beta$  is usually called the inertial parameter,  $Re_K$  is the Reynolds number based on the intrinsic permeability, and this phenomenological model is known as the as Darcy-Forchheimer equation. Experimental studies have shown that the transition from linear (Darcy flow) to nonlinear (Forchheimer or non-Darcy flow) regime occurs gradually as the Reynolds number increases [5]. For a Reynolds number based on the permeability,  $Re_K$ , the linear velocity term (Darcy law) is valid when  $Re_K$  is less than the 1–10 range.

For clean filters (i.e., free from particles), several relationships can be found in the literature to estimate  $K$  [5]. A variety of standard test methods are also available to measure permeability: ISO 9237 (fabrics including industrial fabrics for technical purposes, nonwovens and made-up textile; area for test  $2 \times 10^{-3} \text{ m}^2$ ; differential pressure  $2 \times 102 \text{ Pa}$ ), ASTM D737 (textile fabrics including woven, nonwoven blankets, napped, knitted, layered and pile fabrics; area for test  $38 \times 10^{-4} \text{ m}^2$  and differential pressure  $125 \text{ Pa}$ ), EDANA 140.1–81 (nonwovens media; area for test 2 to  $5 \times 10^{-3} \text{ m}^2$  and differential pressure  $125 \text{ Pa}$ ), etc. The inertial parameter  $\beta_\beta$  can be taken as equal to  $0.043(1-\alpha)^{-2.13} \text{ K}^{-1/2}$  for a fibrous filter [34], and equal to  $0.1429(1-\alpha)^{-3/2} \text{ K}^{-1/2}$  for a granular bed [15].

Models have been also developed to predict the loading behaviour of filters. For granular air filters, the permeability is described by [26]

$$K = \frac{K_o}{1 + a_{\kappa 1} \alpha_p^{a_{\kappa 2}}} \quad (12)$$

where  $\alpha_p$  is the packing fraction of particles (i.e., the volume of deposited particles per unit volume of filter) and  $a_{\kappa 1} = 0.348 \text{ St}^{-1.2} \text{ I}_r^{0.86} 10^{3a_{\kappa 2}}$  with  $a_{\kappa 2} = 3.51 \text{ St}^{-0.092} \text{ I}_r^{0.275}$  for  $0.0017 \leq \text{St} \leq 0.038$  and  $0.00172 \leq \text{Ir} \leq 0.008$ .

The permeability of fibrous filters is described by [6]

$$K = \frac{1}{16 \left( \frac{\alpha}{r_c} + \frac{\alpha_p}{r_p} \right) \left( \frac{\alpha}{r_c} + \frac{\alpha_p}{r_p} \right)^{1/2} \left[ 1 + 56(\alpha + \alpha_p)^3 \right]} \quad (13)$$

where  $r_p$  is the radius of the aerosols particles, and the filter solidity  $\alpha$  ranges from 0.006 to 0.3. For filters with lower solidity is given by

$$K = \frac{1}{16 \left( \frac{\alpha}{r_c} + \frac{\alpha_p}{r_p} \right) \left( \frac{\alpha}{r_c} + \frac{\alpha_p}{r_p} \right)^{1/2}} \quad (14)$$

The filtration of solid aerosol particles can occur under varying humidity conditions. A number of researchers [24, 25, 35, 42, 49] have carried out extensive laboratory tests to quantify this effect on the filter permeability as a function of particle hygroscopicity and size. Results have shown an increase in permeability with the increasing humidity for loading both with non-hygroscopic particles and hygroscopic particles below the deliquescent point. Miguel [35] proposed a model to account the effect of humidity on the permeability through its influence on the packing fraction of particles.

### 5.3 Filter Performance

Particle collection efficiency is often viewed as the primary performance indicator for filters. However, the filter permeability (or the pressure drop) is particularly

important due to safety and energy-saving issues [65]. Near clogging, there is an enormous increase in the pressure drop with the risk of filter damage and more energy required to operate the system. Therefore, an ideal filter is the one that has high efficiency arresting for particles with low pressure drop.

Filter performance (or filter quality) is often defined as the ratio of the negative logarithm of penetration to the pressure drop across the filter [65]. The figure of merit resulting from this definition has the advantage that it can be calculated directly from parameters that can be measured simply. Its drawback is that it is not a dimensionless factor. Its magnitude depends on the system used, and filters must be compared for specified filtration velocity, particle diameter and particle loading. To overcome this dimensional problem, filter performance is defined as the dimensionless ratio of collector-element efficiency to the friction factor for flow [5]

$$\Omega_{\eta fa} = \frac{\eta}{f_{fa}} \tag{15}$$

Here  $f_{fa}$  is the friction factor defined as  $\Delta p/0.5 \rho u^2$ . Miguel [35] based on  $\pi$ -theorem of Buckingham suggested as an alternative relationship for evaluating filter performance, the product of the number of particles caught per unit of filter area,  $N_{pA}$ , by the filter permeability

$$\Omega_{NK} = N_{pA} K \tag{16}$$

where  $N_{pA}$  is the number of particles caught per unit of filter area ( $M_{pA}/A_f \rho_p V_p$ ) and  $V_p$  is the average volume of each particle. Substituting Eqs. (12), and (14) into Eq. (16), yields

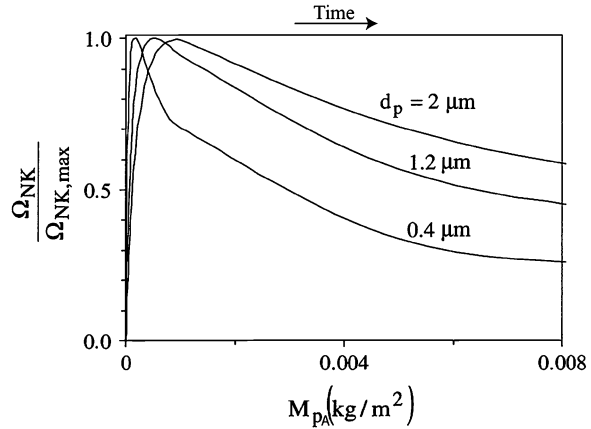
$$\Omega_{NK} = \frac{K_o M_{pA}}{\rho_p V_p (1 + a_{\kappa I} \alpha_p^{a_{\kappa^2}})} \tag{17}$$

$$\Omega_{NK} = \frac{M_{pA}}{16 \rho_p V_p \left( \frac{\alpha}{r_c} + \frac{\alpha_p}{r_p} \right) \left( \frac{\alpha}{r_c^2} + \frac{\alpha_p}{r_p^2} \right)^{1/2}} \tag{18}$$

Equations (17) and (18) are valid for granular filters and fibrous filters ( $\alpha < 0.006$ ), respectively. These equations allow a direct comparison of different filter media but also an estimation of the time evolution of the filter's performance which provides information regarding the need for filter replacement [35].

Figure 7 shows the ratio  $\Omega_{NK}/\Omega_{NK, \max}$  calculated for aerosol particles with several sizes. For each particle size there is a peak that corresponds to the maximum performance. After, the performance starts to decrease till reaching quasi-constant value, and the filter needs to be replaced. Notice that, when particle size increases the maximum value of  $\Omega_{NK}/\Omega_{NK, \max}$  drifts toward higher values of  $M_{pA}$  (or higher filtration time).

**Fig. 7** Ratio between the performance  $\Omega_{NK}$  and the maximum performance  $\Omega_{NK, \max}$  versus the mass of particles collected per fibrous filter area [35]



## 6 Modelling Particle Transport and Deposition

Some authors (e.g., [7, 53]) classified the filtration models into 3 classes: empirical or semi-empirical models (include empirical parameters obtained from observation), stochastic models (use probabilistic approaches) and network models (structure is usually conceptualized as random).

Computational fluid dynamics (CFD) is a very powerful tool for simulating particulate suspensions with deposition [22, 40]. Eulerian and Lagrangian methods may be applied to implement the task. The Eulerian method treats the particle phase as a continuum and develops its conservation equations on a control volume basis and in a similar form as that for the fluid phase. This perspective fits the view that the filtration process is a convective–dispersive phenomenon [44, 52, 61, 62]. The Lagrangian method considers particles as a discrete phase and tracks the pathway of each individual particle. In this perspective, the trajectory of particles can be predicted based on the force balance on the particle [2, 59, 67]. The choice of one of these methods depends decidedly of the objective and characteristics of the problem under examination.

There are some evidences that Lagrangian method perform a little better than the Eulerian method in predicting dispersion of pollutant around enclosures [55]. However, to date there are no comparative studies for filtration.

## 7 Fine Particle Filtration

### 7.1 Particle Deposition

Filtration of fine particles represents an example of transport in porous media which can be analyzed based on the convective–dispersive phenomenon [5, 44, 52,

61, 62]. One-dimensional transport of particles through a filter medium is governed by the dimensionless macroscopic equation

$$\frac{\partial \Phi^*}{\partial t^*} = \frac{\partial^2 C_z^*}{\partial z^{*2}} - \frac{Pe}{l_c^*} \frac{\partial C_z^*}{\partial z^*} \quad (19)$$

with

$$Pe = \frac{l_c u}{D}; t^* = \frac{Dt}{H^2}; C^* = \frac{C}{\rho_{air}}; \Phi^* = \frac{\Phi}{\rho_{air}}; l_c^* = \frac{l_c}{H}; z^* = \frac{z}{H}$$

where  $Pe$  is the Peclet number and relates convective to diffusive particulate mass transport,  $C_z$  is the concentration of particulate matter in the air stream,  $u$  is the fluid velocity,  $D$  is particle diffusion coefficient,  $t$  is the time,  $l_c$  is the characteristic length of filter collector's,  $H$  is the thickness of the filter,  $\rho_{air}$  is the air density and  $\Phi$  is the sink of particles in the filter (i.e., particles removed from the suspension), which for continuity reasons is  $\Phi = -\Phi_c - \Phi_p$ , where  $\Phi_c$  is the deposition onto the filter's collector and  $\Phi_p$  is the deposition onto previously deposited particles.

In order to solve this equation, a particle deposition rate approach is required. The rate of particle deposition onto the filter's collector and onto previously deposited particles is given by [44]

$$\frac{\partial \Phi_c^*}{\partial t^*} = \frac{Sh_c \vartheta^*}{l_c^*} C^* - \frac{k_e}{\alpha I_{pc}} \frac{Sh_c \vartheta^*}{l_c^*} \Phi_c^* \quad (20)$$

$$\frac{\partial \Phi_p^*}{\partial t^*} = \frac{k_e}{\alpha I_{pc}} \frac{Sh_p \vartheta^*}{l_c^*} \Phi_c^* \quad (21)$$

with

$$Sh = \frac{l_c \Theta}{D}; \vartheta^* = \vartheta H$$

Here  $Sh$  is the Sherwood number (represents the ratio of actual particulate mass transfer by a moving air stream to the particulate mass transfer that would occur by diffusion),  $I_{pc}$  is the aerosol particle interception parameter ( $= A_p V_c / A_c V_p$ ),  $A_p$  is the particle surface area,  $A_c$  is the filter collector surface area,  $V_p$  is the particle volume,  $V_c$  is the filter collector volume,  $\Theta$  is the particulate matter transfer coefficient,  $\vartheta$  is the specific surface area of the filter,  $\alpha$  is the solidity of a brand new (unloaded) filter, and  $k_e$  is the excluded surface area factor which has a theoretical minimum value close to 1.27.

The total deposit amount inside the filter  $\Phi^*$  is given by

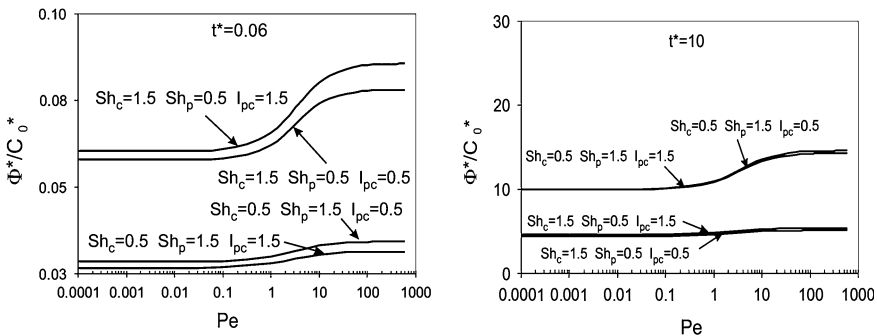


$$\Phi^* = \frac{C_0^*}{1 - \frac{b_1}{b_2} \exp[(b_1 - b_2)L^*]} \left[ \frac{1}{b_1} [\exp(b_1 H^*) - 1] - \frac{b_1}{b_2^2} [\exp(b_2 H^*) - 1] \exp[(b_1 - b_2)H^*] \right] \left\{ \frac{Sh_p \vartheta^*}{l_c^*} t^* + \frac{\alpha I_{pc}}{k_e} \left( 1 - \frac{Sh_p}{Sh_c} \right) \left[ 1 - \exp\left( -\frac{k_e}{\alpha I_{pc}} \frac{Sh_c \vartheta^*}{l_c^*} t^* \right) \right] \right\} \quad (22)$$

Figure 8 shows the effect of dimensionless numbers (Pe, Shc, Shp) and geometrical parameter  $I_{pc}$  on  $\Phi^*/C_0^*$ . The plot shows that the amount of particles deposited increases with the Peclet number, being the effect stronger for  $0.1 < Pe < 50$ . Results also indicate that during the early stages of the filtration process deposition is mainly influenced by  $Sh_c$  but at later stages  $Sh_p$  becomes more important. Therefore, during the early stages deposition is favoured when  $Sh_c$  is larger than  $Sh_p$  but later deposition is enhanced when  $Sh_p$  is larger than  $Sh_c$ . Figure 8 also reveals that  $\Phi^*/C_0^*$  is influenced by  $I_{pc}$ , being, however this influence negligible when the filter approach the clogging. Notice that, when  $Sh_c$  is larger than  $Sh_p$  the increase of interception parameter favour deposition. The opposite effect occurs when  $Sh_c$  is smaller than  $Sh_p$ .

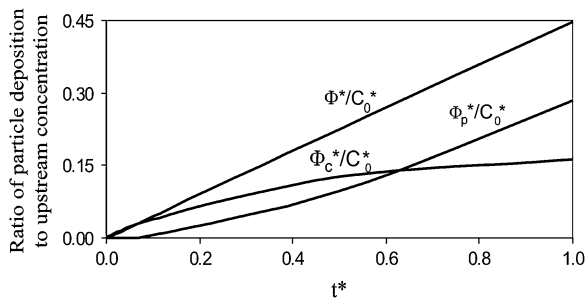
The time evolution of  $\Phi_c^*/C_0^*$ ,  $\Phi_p^*/C_0^*$  and  $\Phi^*/C_0^*$  is presented in Fig. 9. As expected, the plot shows that during the early stages of filtration the main contribution for the deposition is the fraction of particles deposited onto the filter’s collector ( $\Phi_c^*$ ). After  $t^* \sim t_{cc}^* \sim 0.62$ , fibres or beds that constitute the filter become completely covered with particles. Therefore, particles have to deposit on particles already attached to these collectors.

Consider that the life time of a filter corresponds to filter close the clogging. If  $\phi$  is the void fraction of the filter (i.e., the porosity), the life time of the filter is reached for



**Fig. 8** Effects of Peclet number, Sherwood number, interception parameter and filtration time upon  $\Phi^*/C_0^*$  ( $\alpha = 0.5$ ;  $k_e = 1.27$ ) [44]

**Fig. 9** Time evolution of  $\Phi^*/C_0^*$ ,  $\Phi_c^*/C_0^*$  and  $\Phi_p^*/C_0^*$   $C_0^*$  ( $\alpha = 0.5$ ;  $k_c = 1.27$ ) [44]



$$(\Phi^*)_{t_{life}^*} = \varphi \zeta \rho_p^* \quad (23)$$

where  $\zeta$  is the ratio between filter volume and particle volume, and  $\rho_p^*$  is the dimensionless particle density ( $\rho_p/\rho_{air}$ ). Eq. (23) may be the criterion to determine the life time of the filter.

## 7.2 Pressure Drop

The dimensionless form of Darcy's law reads (e.g., Miguel [35])

$$\Delta p^* = \frac{H^*}{K^* \text{Re}} \quad (24)$$

with

$$p^* = \frac{p}{\rho u^2}; \quad K^* = \frac{K}{l_c^2}; \quad H^* = \frac{H}{l_c}; \quad \text{Re} = \frac{\rho u l_c}{\mu}$$

For filters with porosities up to 0.8, based on the hydraulic radius theory of Carman-Kozeny

$$K^* = \frac{1}{45} \frac{\phi^3}{(1-\phi)^2} \quad (25)$$

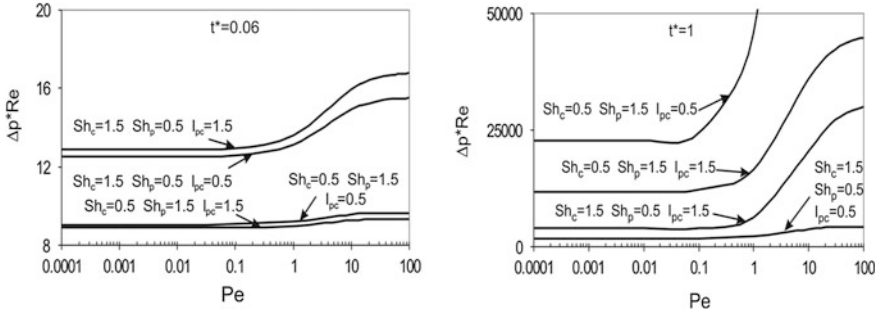
and the pressure drop reads as [44]

$$\Delta p^* = 45 \frac{H^* (1-\phi)^2}{\text{Re} \phi^3} \quad (26)$$

with

$$\phi = \phi_0 - \zeta \frac{\Phi^*}{\rho_p^*}$$

and



**Fig. 10** Effects of Peclet number, Sherwood number, interception parameter and filtration time upon  $\Delta p^*Re$  ( $\alpha = 0.5$ ;  $k_c = 1.27$ ) [44]

$$\begin{aligned} \varphi = \phi_0 - \frac{\zeta C_0^*}{\rho_p^* - \rho_p^* \frac{b_1}{b_2} \exp[(b_1 - b_2)H^*]} \left[ \frac{1}{b_1} [\exp(b_1 H^*) - 1] \right. \\ \left. - \frac{b_1}{b_2^2} [\exp(b_2 H^*) - 1] \exp[(b_1 - b_2)H^*] \right] \left\{ \frac{Sh_p \vartheta^*}{l_c^*} t^* \right. \\ \left. + \frac{\alpha I_{pc}}{k_e} \left( 1 - \frac{Sh_p}{Sh_c} \right) \left[ 1 - \exp\left( -\frac{k_e}{\alpha I_{pc}} \frac{Sh_c \vartheta^*}{l_c^*} t^* \right) \right] \right\} \end{aligned}$$

where  $\phi_0$  is porosity of a brand new (unloaded) filter and  $\zeta$  is the ratio between the filter volume and the particle volume.

The curve representing the variation of  $\Delta p^*Re$  with  $Pe$ ,  $Sh$  and  $I_{pc}$  is represented in Fig. 10. The plot reveals an increase of  $\Delta p^*Re$  with the Peclet number and this tendency is more noteworthy between 0.1 and 50. Initially  $\Delta p^*Re$  is enhanced if  $Sh_c$  is larger than  $Sh_p$  but at later stages the opposite occurs (i.e.,  $\Delta p^*Re$  is enhanced when  $Sh_p$  is larger than  $Sh_c$ ). This result stresses the importance of both  $Sh_c$  and  $Sh_p$  in the filtration process. In addition, when  $Sh_c$  is larger than  $Sh_p$  an increase of interception parameter favour pressure drop. The opposite effect occurs when  $Sh_c$  is smaller than  $Sh_p$ .

Notice also that, the tendency of variation of  $\Delta p^*Re$  with the Peclet and Sherwood numbers, as well as the interception factor is similar to  $\Phi^*/C_0^*$ . This is an expected result because the pressure drop through the filter is strongly dependent on the amount of particles deposited.

### 7.3 Filter Performance

Filter performance in terms of dimensionless quantities can be evaluated from the product of the number of particles caught per unit of filter area and the filter permeability (Eq. 16). In terms of dimensionless quantities it reads:

$$\Omega = \frac{\Phi^*}{\rho_p^* A_f^*} K^* \tag{27}$$

where  $\rho_p^*$  is the dimensionless particle density ( $\rho_p/\rho_{air}$ ) and  $A_f^*$  is the dimensionless filter area ( $A_f/l^2_c$ ). By combining Eq. (25) with (27), one obtains:

$$\Omega = \frac{1}{45\rho_p^* A_f^*} \frac{\Phi^* \left(\phi_0 - \zeta \frac{\Phi^*}{\rho_p^*}\right)^3}{\left(1 - \phi_0 + \zeta \frac{\Phi^*}{\rho_p^*}\right)^2} \tag{28}$$

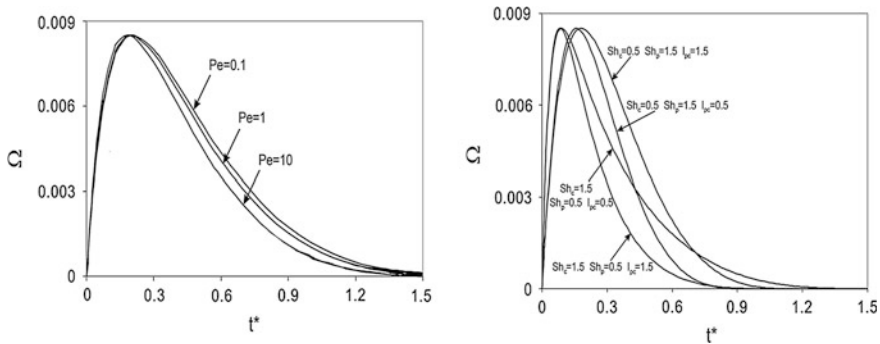
where  $\Phi^*$  is obtained from Eq. (22).

The time variation of performance is shown in Fig. 11. This plot displays four different regions: an initial steep increase until it reaches a maximum (the peak), followed by a steep decrease, a transition range and an ending range of constant performance. This last range corresponds to filter close to clogging.

### 8 Deep-Bed Filtration

Deep-bed filtration refers to filtration through beds of granular or fibrous filter material. As the suspension travels through the filter, particles deposit at different depths on the filter grains.

There are some fundamental issues concerning packing of beds that remain elusive, including the precise effect of packing arrangements on flow of suspensions. The face-centered cubic packing is the way pack identical spheres together in the densest possible way (i.e., porosity of  $1-\pi/18^{1/2}$  ( $\sim 0.260$ ) and packing density  $\pi/18^{1/2}$ ). This arrangement found in cannonballs piled at war memorials or fruit arrangements was called the Kepler conjecture [31]. The packing structure can also be presented within different arrangements (e.g., cubic, hexagonal,



**Fig. 11** Effects of Pelet number, Sherwood number and interception parameter upon the time variation of filter's performance ( $\alpha = 0.5$ ;  $k_e = 1.27$ ) [44]



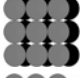
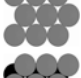
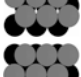
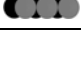
orthorhombic, etc.). In case of identical spheres, together in the densest possible way, the packing density of these structures varies between  $\pi/18^{1/2}$  (rhomboedric hexagonal or face-centered cubic) and  $\pi/6$  (simple cubic). Therefore, the packing arrangement is directly relevant to macroscopic key parameters such as the filter permeability and the fractional penetration of particles.

Serrenho and Miguel [60] performed CFD simulations to study fluid and suspension flows through 5 packing structures of fixed spheres: models SCU (simple cubic), FCC (face-centered cubic), ORT (orthogonal), HEX (hexagonal), RHE (rhomboedric hexagonal) and TET (tetragonal). These structures are constructed with spheres of same diameter and in a way that all have the same porosity (Table 2).

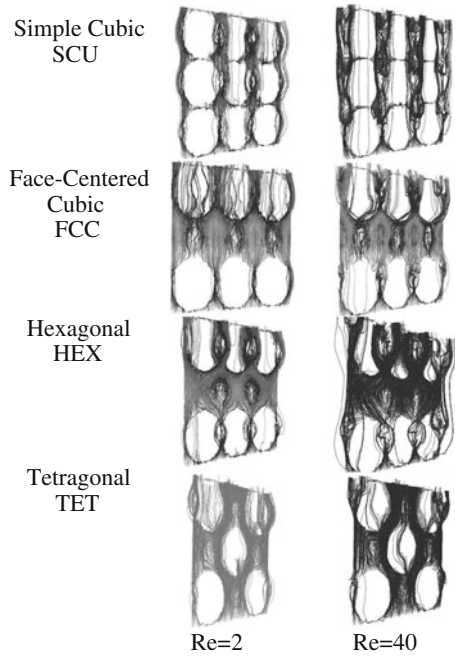
The flow pathlines that resulted from the 3D simulations ( $0.2 \leq Re \leq 40$ ) are depicted at Fig. 12. This figure shows differences between low and high Reynolds numbers: the predominant viscous forces in the momentum transport through the void geometry generates a more uniform “pathlines” velocities at  $Re = 0.2$ , whereas at  $Re = 40$  “channels” of air flow are generated due to the relevant contribution of inertial forces. Although all geometries having the same porosity the air flow coefficients are not the same (Table 3). The packing arrangements FCC and TET, RHE and ORT, and SCU and HEX present similar coefficients. SCU and HEX arrangements present the highest permeability and the lowest inertial coefficient.

Based on a Lagrangian approach, that considers particles as a discrete phase and tracks the pathway of each individual particle, the fractional penetration of

**Table 2** Ordered packing of spheres with same sphere diameter and porosity (packing density 0.42, porosity 0.52) [60]

Packing model		Arrangement
Simple cubic	SCU	
Face-centered cubic	FCC	
Orthogonal	ORT	
Hexagonal	HEX	
Rhomboedric hexagonal	RHE	
Tetragonal	TET	

**Fig. 12** Airflow pathlines within the packing arrangements (longitudinal section) [60]



**Table 3** Permeability and inertial coefficient of packing arrangements [60]

Packing model	Porosity	Permeability ( $m^2$ ) $\times 10^{-8}$	Inertial coefficient (1/m)
SCU	0.58	3.40	1650
FCC		1.82	2525
ORT		2.24	2241
HEX		3.20	1795
RHE		2.12	2277
TET		1.93	2496

particles was also evaluated [59, 60]. Particles (density 200 and 2000  $kg/m^3$ , diameters between 0.2 and 10  $\mu m$ ) are released at the inlet of the packing structure and tracked through the structure until they are trapped on the solid beds or escape through the outlet of the structure. The results are shown in Tables 4 and 5. For light particles, Reynolds number plays the major role in fractional penetration of particles (the effect of size is negligible). Besides, heavy and big size particles (i.e., particles with large inertia) have a better chance to get escape from packing structures SCU and HEX due to the existence of well-defined preferential channels of fluid flow that enable particles to cross these structures without contact with solid spheres.

**Table 4** Fractional penetration of particles per solid sphere  $\Pi$  (particles density 200 kg/m<sup>3</sup>) [60]

Packing model	$Re_D (= \rho u d_{est} / \mu)$					
	0.2			40		
	Particles size ( $\mu\text{m}$ )			Particles size ( $\mu\text{m}$ )		
	0.2	2	10	0.2	2	10
	$\Pi$			$\Pi$		
SCU	0.025	0.025	0.025	0.028	0.029	0.031
FCC	0.027	0.027	0.028	0.030	0.031	0.032
HEX	0.027	0.027	0.028	0.030	0.031	0.032
RHE	0.028	0.028	0.028	0.032	0.032	0.033
TET	0.027	0.027	0.028	0.030	0.031	0.031

**Table 5** Fractional penetration of particles per solid sphere  $\Pi$  (particles density 2000 kg/m<sup>3</sup>) [60]

Packing model	$Re_D (= \rho u d_{est} / \mu)$					
	0.2			40		
	Particles size ( $\mu\text{m}$ )			Particles size ( $\mu\text{m}$ )		
	0.2	2	10	0.2	2	10
	$\Pi$			$\Pi$		
SCU	0.025	0.025	0.026	0.029	0.030	0.032
FCC	0.027	0.027	0.027	0.031	0.032	0.023
HEX	0.027	0.028	0.028	0.031	0.031	0.035
RHE	0.027	0.028	0.028	0.032	0.034	0.026
TET	0.027	0.027	0.028	0.031	0.032	0.020

## 9 Bio-Inspired T-Shaped Filters

T-shaped structures with circular and square cross-section were studied by Serrenho and Miguel [58]. The geometric characteristics are presented in Table 6.

A Lagrangian approach to solid suspensions representation was used to obtain the fractional penetration of particles in the T-shaped structures (Table 7). It is observed that this quantity is almost not affected both by the geometry (R, RHM, S and SHM) and the Reynolds number. The penetration of particles is determined by the size of the particles.

## 10 Filter Design from Theory

Flow systems achieve high performance by acquiring a suitable design (configuration). Therefore, improving filter design is a key issue. A major step toward making system design a science is provided by the Constructal law of Adrian

**Table 6** Geometric characteristics of symmetric T-shaped structures (Fig. 13): (R) circular cross-section, (S) square cross-section; (HM) designed based on Hess-Murray law of physiology [5]. Area covered by each structure 57.2 cm<sup>2</sup> and total volume of each structure 2.4 cm<sup>3</sup> [58]

Tube geometry		d <sub>1</sub> (cm)	d <sub>2</sub> , d <sub>3</sub> (cm)	L <sub>1</sub> (cm)	L <sub>2</sub> , L <sub>3</sub> (cm)
Round	R	0.44	0.44	5.35	5.35
	RHM	0.50	0.40	6.00	4.76
Square	S	0.44	0.44	5.35	5.35
	SHM	0.45	0.36	6.00	4.76

**Table 7** The fractional penetration of particles versus the particle diameter [58]

Re	R, RHM d <sub>p</sub> (μm)				S, SHM d <sub>p</sub> (μm)			
	0.1	10	50	100	0.1	10	50	100
20	0.90	0.93	0.45	0.00	0.89	0.88	0.35	0.01
40	0.91	0.93	0.10	0.00	0.90	0.87	0.09	0.01
60	0.90	0.92	0.01	0.00	0.89	0.88	0.03	0.00
80	0.90	0.90	0.00	0.00	0.89	0.86	0.02	0.00

Bejan [4, 3, 43–37, 38]. This law states that if a system is free to morph under global constraints, the better flow design is the one that minimizes the global flow resistances, or maximizes the global flow access. Therefore, design matters and shouldn't be developed by chance.

The challenge is to design a high efficiency filter for the capture of submicrometre particles. The filter operates at low Reynolds numbers (laminar flow) and due to practical and economic reasons it must fit in a fixed volume (the global constraint). The purpose of the filter is to maximize deposition rate, or said in another way, is to have the smallest concentration possible of particles at the outlet.

Consider that the collecting elements of the filter (of cross-section YW) are smooth tubes with characteristic length d. If  $\phi$  is the porosity of the stack then the space allocated to the device permits the installation of  $\varepsilon (= \phi YW/0.25\pi d^2)$  tubes. While a large area available for the deposition of particles is desirable, the resulting penalty on fluid flow resistance is undesirable (see Sect. 5). Therefore the optimal d results from the competition between the number of tubes for large particle deposition and increasing flow resistance. The methodology presented by Reis et al. [54] is developed in two steps: finding the limits, small-d and large-d behaviour and identifying the d-value that maximizes particles' deposition within the filter. The optimal ratio d/H is given by

$$\left(\frac{d}{H}\right)_{\text{optimal}} = 3.44 \frac{\phi^{2/3}}{Be^{2/7}} \left(\frac{H}{W}\right)^{1/7} \tag{29}$$

with

$$Be = \frac{H^2 \Delta p}{\mu D_{df}}$$



Here  $Be$  is the Bejan number,  $D_{df}$  is the diffusion coefficient,  $H$  is the thickness and  $W$  is the filter width.

Another relevant situation is the optimization of granular and fibrous filters. Consider a filter that has porosity  $\phi$  and contains  $N$  collector elements (i.e. fibres, beds) with a characteristic transversal dimension  $d_K$ . This material is mounted on a cylindrical frame of volume  $V$ . Two far-off situations are considered: collector elements are very close to each other and collector elements sufficiently far apart. The optimal geometry is Reis et al. [54]

$$\left(\frac{d_K}{H}\right)_{optimal} = \left[ \frac{\lambda_K}{\lambda_\phi} \frac{\phi^3}{(1-\phi)^3} Be \right]^{1/2} \quad (30)$$

or

$$\phi_{optimal} = \frac{\Lambda^{1/3}}{1 + \Lambda^{1/3}} \quad (31)$$

with

$$\Lambda = \frac{\lambda_\phi d_K}{\lambda_K H Be}$$

where  $\lambda_\phi$  and  $\lambda_K$  are parameters that depend on the geometric arrangement (e.g., for a cubic packing are 180 and 12, respectively).

Consider now a filter with a bio-inspired design (tree-shaped or T-shaped flow structure) which the area covered by the geometry and the total volume allocated to the piping system are kept constant (the global constraint). In this design each segment (parent) gives rise to two daughter branches (Fig. 13). The minimum flow resistance is achieved if the diameters and the lengths of consecutive pipes in a bifurcation are related as [39, 41, 58]

$$d_1^{n_d} = 0.5 \left[ (1 + \lambda_d^{n_d}) d_3^{n_d} + (1 + \lambda_d^{-n_d}) d_2^{n_d} \right] \quad (32)$$

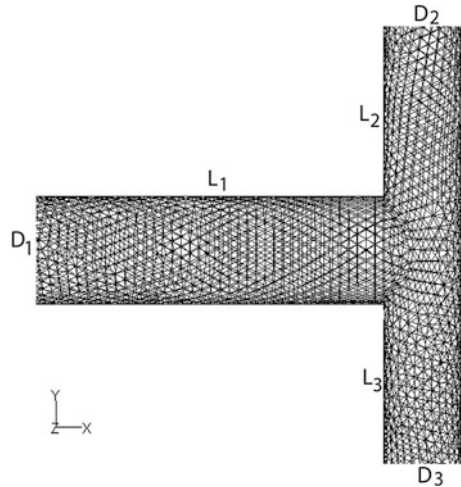
$$L_1^{n_L} = 0.5 \left[ (1 + \lambda_L^{n_L}) L_3^{n_L} + (1 + \lambda_L^{-n_L}) L_2^{n_L} \right] \quad (33)$$

with  $\lambda_d = d_2/d_3$ ,  $\lambda_L = L_2/L_3$ ,  $n_d = n_L = 3$  (laminar flow), and  $n_d = 7/3$  and  $n_L = 7$  (turbulent flow). For symmetric bifurcation pipes ( $\lambda_d = \lambda_L = 1$ ) and laminar flow, these equations become  $d_2/d_1 = L_2/L_1 = 2^{-1/3}$  which are nothing more than the Hess-Murray law of physiology. Using a similar procedure to the previous examples, we obtain (Miguel [39])

$$\left(\frac{d_1}{L_1}\right)_{optimal} = 3.73 \frac{\lambda_{tree}^{3/5}}{Be^{2/5}} \left(\frac{Y^4}{LW^2L_1}\right)^{1/5} \quad (34)$$

where  $L$  is the length of 1st parent segment,  $W$  is the filter width,  $Y$  is the height of the filter and  $\lambda_{tree}$  is a geometry factor that depends of branching level.

**Fig. 13** T-shaped structure that can be used for filtration



In Eqs. (28), (29) and (33) the optimized design of the filter is strongly dependent both on Bejan number and desired void fraction of the filter.

## References

1. ASME: Code on Nuclear Air and Gas Treatment. American Society of Mechanical Engineers ASME AG-1, New York (2003)
2. Aydın, M., Balik, G., Miguel, A.F., Reis, A.H.: Some features of flow and particle transport in porous structures. *J. Mech. Eng.* **51**, 495–500 (2005)
3. Bejan, A.: *Shape and Structure, from Engineering to Nature*. Cambridge University Press, Cambridge (2000)
4. Bejan, A., Lorente, S.: *Design with Constructal Theory*. Wiley, Hoboken (2008)
5. Bejan, A., Dincer, I., Lorente, S., Miguel, A.F., Reis, A.H.: *Porous and Complex Flow Structures in Modern Technologies*. Springer, New York (2004)
6. Bergman, W., Taylor, R.D., Miller, H.H., Biermann, A.H., Hebard, H.D., da Roza, R.A., Lum, B.Y.: Enhanced filtration program at LLNL. In: *Proceedings of 15th DOE Nuclear Air Cleaning Conference (CONF-760822)* Boston (1978)
7. Burganos, V.N., Skouras, E.D., Paraskeva, C.A., Payatakes, A.C.: Simulation of the dynamics of depth filtration of non-Brownian particles. *AIChE J.* **47**, 880–894 (2001)
8. Costa, D.L., Kodavanti, U.P.: Toxic responses of the lung to inhaled pollutants: benefits and limitations of lung-disease models. *Toxicol. Lett.* **140–141**, 195–203 (2003)
9. Dales, R., Chen, L., Frescura, A.M., Liu, L., Villeneuve, P.J.: Acute effects of outdoor air pollution on forced expiratory volume in 1 s: a panel study of schoolchildren with asthma. *Eur. Respir. J.* **34**, 316–323 (2009)
10. Davies, C.N.: *Air Filtration*. Academic Press, London (1973)
11. Dominici, F., Peng, R.D., Bell, M.L., Pham, L., McDermott, A., Zeger, S.L., Samet, J.M.: Fine particulate air pollution and hospital admission for cardiovascular and respiratory diseases. *J. Am. Med. Assoc.* **295**, 1127–1134 (2006)
12. D’Ottavio, T., Goren, L.S.: Aerosol capture in granular beds in the impaction dominated regime. *Aerosol Sci. Technol.* **2**, 91–108 (1983)

13. Durant, W.S.: Performance of Airborne Activity Confinement Systems in the Savannah River Plant Reactor Buildings. USAEC Report CONF-660904 (1966)
14. Emi, H., Wang, C.S., Tien, C.: Transient behavior of aerosol filtration in model filters. *AIChE J.* **28**, 397–405 (1982)
15. Ergun, S.: Fluid flow through packed columns. *Chem. Eng. Progr.* **48**, 89–94 (1952)
16. First, M.W., Gilbert, H.: Aerosol filtration. *Nucl. Saf.* **2**, 167–175 (1982)
17. Flagan, R.C., Seinfeld, J.H.: *Fundamentals of Air Pollution Engineering*. Prentice-Hall, Englewood Cliffs (1988)
18. Gautam, A., Waldrep, J.C., Densmore, C.L.: Aerosol gene therapy. *Mol. Biotechnol.* **23**, 51–60 (2003)
19. Gilbert, H.: High-Efficiency Particulate Air Filter Units, Inspection, Handling, Installation. AEC Report TID-7023, National Technical Information Service, Springfield (1961)
20. Griesenbach, U., Ferrari, S., Geddes, D.M., Alton, E.W.: Gene therapy progress and prospects: cystic fibrosis. *Gene Ther.* **9**, 1344–1350 (2002)
21. Hinds, W.C.: *Aerosol Technology*. Wiley, New York (1982)
22. Hosseini, S.A., Tafreshi, H.V.: Modeling particle-loaded single fiber efficiency and fiber drag using ANSYS–Fluent CFD code. *Comput. Fluids* **66**, 157–166 (2012)
23. Jaenicke, R.: Abundance of cellular material and proteins in the atmosphere. *Science* **308**, 73 (2005)
24. Joubert, A., Laborde, J.C., Bouilloux, L., Callé-Chazelet, S., Thomas, D.: Influence of humidity on clogging of flat and pleated HEPA Filters. *Aerosol Sci. Technol.* **44**, 1065–1076 (2010)
25. Joubert, A., Laborde, J.C., Bouilloux, L., Callé-Chazelet, S., Thomas, D.: Modelling the pressure drop across HEPA filters during cake filtration in the presence of humidity. *Chem. Eng. J.* **166**, 616–623 (2011)
26. Jung, Y., Tien, C.: New correlations for predicting the effect of deposition on collection efficiency and pressure drop in granular filters. *J. Aerosol Sci.* **22**, 187–200 (1991)
27. Kockmann, N., Dreher, S., Engler, M., Woias, P.: Simulation and characterization of microreactors for aerosol generation. *Microfluid. Nanofluid.* **3**, 581–589 (2007)
28. Krcma, R.: *Manual of Nonwovens*. Textile Trade Press, Manchester (1971)
29. Langmuir, I.: *Report on Smokes and Filters*, OSRD 865. Office of Scientific Research and Development, Office of Technical Services, Washington (1942)
30. Lapple, C.E.: *Deep Bed Sand and Glass Fiber Filters*. USAEC Report WASH 149 (1952)
31. Mackenzie, D.: The proof is in the packing. *Am. Sci.* **86**, 1 (1998)
32. McCarthy, M.W.: Trivalent intranasal influenza vaccine, live. *Ann. Pharmacother.* **38**, 2086–2093 (2004)
33. Mercimek, M., Yildirim, H., Miguel, A. F., Aydin, M.: Investigation of T-shape geometry for the collection of pollution particles. In: Dincer, I., Colpan, C.O., Midilli, A. (eds.) *Proceedings of the Global Conference on Global Warming 2009*, pp. 1172–1179 (2009)
34. Miguel, A.F.: Airflow through porous screens: from theory to practical considerations. *Energy Build.* **28**, 63–69 (1998)
35. Miguel, A.F.: Effect of air humidity on the evolution of permeability and performance of a fibrous filter during loading with hygroscopic and non-hygroscopic particles. *J. Aerosol Sci.* **34**, 783–799 (2003)
36. Miguel, A.F.: Porous media and filtration. In: Ingham, D.B., Bejan, A., Mamut, E., Pop, I. (eds.) *Emerging Technologies and Techniques in Porous Media*, pp. 419–431. Kluwer Academic Publishers, Dordrecht (2004)
37. Miguel, A.F.: Dendritic structures for fluid flow: laminar, turbulent and constructal design. *J. Fluids Struct.* **26**, 330–335 (2010)
38. Miguel, A.F.: Natural flow systems: acquiring their constructal morphology. *Int. J. Des. Nat. Ecodev.* **5**, 230–241 (2010)
39. Miguel, A.F.: Tree-shaped flow structures viewed from the constructal theory perspective. In: Dias, R., Martins, A.A., Lima, R., Mata, T.M. (eds.) *Single and Two-Phase Flows on*

- Chemical and Biomedical Engineering, pp. 266–291. Bentham Science Publishers, Oak Park (2012)
40. Miguel, A.F.: Non-darcy porous media flow in no-slip and slip regimes. *Therm. Sci.* **16**, 167–17 (2012)
  41. Miguel, A.F.: Lungs as a natural porous media: architecture, airflow characteristics and transport of suspended particles. In: Delgado, J.M.P.Q. (ed.) *Heat and Mass Transfer in Porous Media*, pp. 115–137. Springer, Berlin (2012)
  42. Miguel, A.F., Silva, A.M.: Experimental study of mass loading behaviour of fibrous filters. *J. Aerosol Sci.* **32**(S1), 851–852 (2001)
  43. Miguel, A.F.: Computational analysis of the role of permeability and inertia on fluid flow through porous media. In: Delgado, J.M.P.Q. (ed.) *Current Trends in Chemical Engineering*, pp. 1–19. Studium Press LLC, Houston (2010)
  44. Miguel, A.F., Reis, A.H.: Transport and deposition of fine mode particles in porous filters. *J. Porous Media* **8**, 731–744 (2006)
  45. Miguel, A.F., Reis, A.H., Melgão, M.: Urban indoor-outdoor aerosol measurements in Portugal and the global warming scenario. *Int. J. Global Warming* **1**, 356–367 (2009)
  46. Mikszta, J.A., Sullivan, V.J., Dean, C., Waterston, A.M., Alarcon, J.B., Dekker III, J.P., Brittingham, J.M., Huang, J., Hwang, C.R., Ferriter, M., Jiang, G., Mar, K., Saikh, K.U., Stiles, B.G., Roy, C.J., Ulrich, R.G., Harvey, N.G.: Protective immunization against inhalational Anthrax: a comparison of minimally invasive delivery platforms. *J. Infect. Dis.* **191**, 278–288 (2005)
  47. NAAQS.: The national ambient air quality standards for particle pollution: summary of proposed improvements to air quality standards for particle pollution and updates to the air quality index <http://www.epa.gov/pm/2012/fsstandards.pdf> (2012). Accessed 18 Oct 2012
  48. NCEA.: Air quality criteria for particulate matter. National Center for Environmental Assessment, US Environmental Protection Agency, Research Triangle Park, NC (2004)
  49. Payet, S., Boulaud, D., Madelaine, G., Renoux, A.: Penetration and pressure drop of a HEPA filter during loading with submission liquid particles. *J. Aerosol Sci.* **23**, 723–735 (1992)
  50. Pope, C.A., Burnett, R.T., Thurston, G.D., Thun, M.J., Calle, E.E., Krewski, D., Godleski, J.J.: Cardiovascular mortality and long-term exposure to particulate air pollution: epidemiological evidence of general pathophysiological pathways of disease. *Circulation* **109**, 71–77 (2004)
  51. Quigley, C., Easter, C., Burrowes, P.: Biotechnology-based odour control: design criteria and performance data. *Water Sci. Technol.* **50**, 319–326 (2004)
  52. Quintard, M., Whitaker, S.: Aerosol filtration: an analysis using the method of averaging volume. *J. Aerosol Sci.* **26**, 1227–1255 (1995)
  53. Rege, S.D., Fogler, H.S.: A network model for deep bed filtration of solid particles and emulsion drops. *AIChE J.* **11**, 1761–1772 (1988)
  54. Reis, A.H., Miguel, A.F., Bejan, A.: Constructal theory of particle agglomeration and design of air-cleaning devices. *J. Phys. D* **39**, 2311–2318 (2006)
  55. Riddle, A., Carruthers, D., Sharpe, A., McHugh, C., Stocker, J.: Comparisons between FLUENT and ADMS for atmospheric dispersion modeling. *Atmos. Environ.* **38**, 1029–1038 (2004)
  56. Rudel, R.A., Camann, D.E., John D. Spengler, J.D., Leo R. Korn, L.R., Julia, G., Brody, J.G.: Alkylphenols, pesticides, phthalates, polybrominated diphenyl ethers, and other endocrinedisrupting compounds in indoor air and dust. *Environ. Sci. Technol.* **37**, 4543–4553 (2003)
  57. Schmidt, E.W.: Filtration of aerosols in granular bed. *J. APCA* **28**, 143–157 (1978)
  58. Serrenho, A., Miguel, A. F.: Accessing the influence of Hess-Murray law on suspension flow through ramified structures. *Defect and Diffusion Forum* **334**, 322–328 (2013)
  59. Serrenho, A., Miguel, A.F.: Simulation and characterization of high porosity media for aerosol particle processing. *J. Porous Media* **12**, 1129–1138 (2009)
  60. Serrenho, A., Miguel, A.F.: Fluid flow and solid/fluid suspensions flow in 3-D packed beds of spheres: the effect of periodicity of fixed beds. *Defect Diffus. Forum* **315**, 871–876 (2011)

61. Shapiro, M., Brenner, H.: Dispersion/reaction model of aerosol collection by porous filters. *J. Aerosol Sci.* **21**, 97–125 (1990)
62. Shapiro, M., Brenner, H.: Dispersion/reaction model of aerosol collection by porous filters. *J. Aerosol Sci.* **21**, 97–125 (1990)
63. Shareefdeen, Z., Singh, A.: *Biotechnology for Odor and Air Pollution Control*. Springer, New York (2005)
64. Shoeib, M., Harner, T., Ikonou, M., Kannan, K.: Indoor and outdoor air concentrations and phase partitioning of perfluoroalkyl sulfonamides and polybrominated diphenyl ethers. *Environ. Sci. Technol.* **38**, 1313–1320 (2004)
65. Spurny, K.R.: *Advances in aerosol filtration*, CRC Press LLC, Florida (1997)
66. Stockdale, W.G., Suddath, J.C., Eister, W.K.: Control of radioactive air contamination at Oak Ridge National Laboratory. In: *Proceedings of 3rd Atomic Energy Commission Air Cleaning Conference*, pp. 55–57, Los Alamos, NM. (1950)
67. Tien, C.: *Granular Filtration of Aerosols and Hydrosols*. Butterworths, Boston (1989)
68. USEPA.: National ambient air quality standards for particulate matter. US Environmental Protection Agency. *Fed Regist* **62**, 138. [http://www.epa.gov/ttn/caaa/t1/fr\\_notices/pmnaaqs.pdf](http://www.epa.gov/ttn/caaa/t1/fr_notices/pmnaaqs.pdf) 1997. Accessed 18 Oct 2012
69. Wadsworth, L.C., Hutten, I.M.: *Handbook of Nonwoven Filter Media*. Elsevier, Oxford (2007)
70. Wepfer, R.: Characterisation of HEPA and ULPA filters by proposed new European test methods. *Filtr. Sep.* **32**, 545–550 (1995)
71. Yadav, N., Morris, G., Harding, S.E., Ang, S., Adams, G.G.: Various non-injectable delivery systems for the treatment of diabetes Mellitus. *Endocr. Metab. Immune Disord. Drug Targets* **9**, 1–13 (2009)
72. Zhao, Z.M., Tardos, G., Pfeffer, R.: Separation of airborne dust in electrostatically enhanced fibrous filters. *Chem. Eng. Commun.* **108**, 307–332 (1991)

# Infrared Thermography Application in Buildings Diagnosis: A Proposal for Test Procedures

E. Barreira, S. S. de Freitas, V. P. de Freitas and J. M. P. Q. Delgado

**Abstract** The study of hygrothermal behaviour is essential to evaluate the performance of construction components and building envelopes. Most building pathologies are related with temperature action. The use of non-destructive techniques to evaluate a building behaviour may be very useful as there is no need to destroy the building components, which would interfere with the user's life. Infrared thermography is a non-destructive testing technology that can be applied to determine the surface temperature of objects. This technology has been applied to buildings for a couple of decades, to evaluate the building performance. It has been used to detect insulation defects, air leakages, heat losses through windows, moisture and different "hidden details". This work evaluates the applicability of thermography to study the behaviour of building materials and building envelopes. A short literature review about thermography principles is presented. It is also showed the effect on the results of some factors that affect infrared thermography measurements. Several applications of infrared thermography to building diagnosis are listed, based on the work published by the scientific community. And finally, three test procedures are described in detailed to detect detachments on wall renderings, to evaluate the thermal comfort of floor coatings and to analyse the wetting and drying processes.

---

E. Barreira (✉) · S. S. de Freitas · V. P. de Freitas · J. M. P. Q. Delgado  
LFC—Building Physics Laboratory, Civil Engineering Department, Faculty of Engineering,  
University of Porto, Porto, Portugal  
e-mail: barreira@fe.up.pt

S. S. de Freitas  
e-mail: sarafreitas@fe.up.pt

V. P. de Freitas  
e-mail: vpfreita@fe.up.pt

J. M. P. Q. Delgado  
e-mail: jdelgado@fe.up.pt

**Keywords** Infrared thermography · Building materials · Building envelopes · Test procedures

## 1 Introduction

Infrared thermography (IRT) can be defined as the science of acquisition and analysis of data from non-contact thermal imaging devices. The process of thermal imaging was simplified over the years with the availability of efficient, high resolution infrared cameras that convert the infrared radiation emitted from bodies into thermal images [1], the thermograms, showing the body's superficial temperature distribution [2]. In this process, each shade expresses a specific temperature range (see Fig. 1).

Thermography has a long history, although its use has increased dramatically with the commercial and industrial applications of the past fifty years. Infrared rays were discovered in 1,800 by Sir William Herschel and approximately thirty years later the first infrared detector was developed. For a long period, infrared detectors were only used by the scientific community and for military purposes. In the end of the 60s the first commercial infrared cameras appeared and in the 90s a new generation of equipment emerged, which increased its applicability in several fields including building diagnosis.

Infrared thermography is now a useful tool for engineers, architects and consultants allowing the evaluation of existing buildings and the identification of potential problems. It is a non-contact and non-destructive technique, which is able to identify surface temperature differences [3].

Most pathologies are related with temperature action. The use of non-destructive techniques to test a building material or component may be very useful



**Fig. 1** Visible image and thermogram of the Carmo Church's façade covered with "azulejos" (ceramic tile) in Porto, Portugal

by making it possible to evaluate its behaviour without destroying it and without interfering with the users' life [4–6].

Despite thermography's potential uses in buildings, its application has not been greatly standardized. The parameters that may affect measurements aren't completely understood and interpreting the results becomes difficult and confusing.

The main objective of this work was to evaluate the applicability of thermography to study the behaviour of building materials and building envelopes. On the other hand, based on some simple experiments that were carried out at the Building Physics Laboratory (LFC) of Faculty of Engineering of Porto University (FEUP), an attempt of systematizing test procedures is made hoping that it may be valuable for future users of this technology.

## 2 Infrared Thermography

### 2.1 Principles

Infrared energy is part of the electromagnetic spectrum. It travels through space at the speed of light and can be reflected, absorbed and emitted. The wavelength ( $\lambda$ ) of infrared energy is between 0.75 and 1,000  $\mu\text{m}$ . It can be divided into three parts: near-infrared, from 0.75 to 1.5  $\mu\text{m}$ , mid-infrared, from 1.5 to 20  $\mu\text{m}$  and far-infrared, from 20 to 1,000  $\mu\text{m}$  (see Fig. 2).

The Stefan-Boltzmann law calculates the total amount of radiation emitted by the blackbody at a certain temperature  $T$ , in every direction and over all wavelength [7].

$$R_t = \sigma \cdot T^4 \tag{1}$$

where  $R_t$  is the total blackbody spectral radiance ( $\text{W}/\text{m}^2$ ),  $\sigma$  is the Stefan-Boltzmann constant ( $\sigma = 5.67 \times 10^{-8} \text{ W}/\text{m}^2\text{K}^4$ ) and  $T$  is the temperature (K).

Normally real surfaces don't behave like a blackbody. The property that reduces the emissive capacity of a real surface is emissivity ( $\varepsilon$ ) that can be defined as the ratio of the radiation emitted by the surface to the radiation emitted by a blackbody at the same temperature [7].

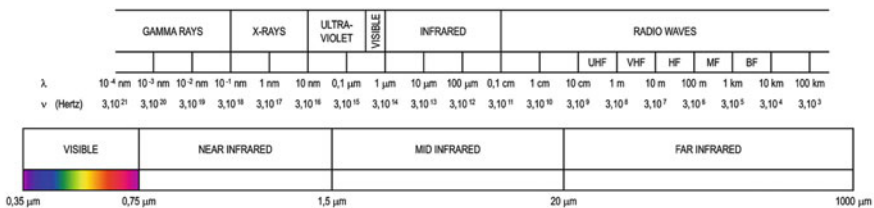


Fig. 2 Electromagnetic spectrum



$$\varepsilon = \frac{R_t}{R_t(\text{blackbody})} \quad (2)$$

When the spectral component of the radiant energy interacts with a semitransparent surface, part of the radiation may be reflected, absorbed and transmitted. The reflectivity ( $\rho$ ) is a property that determines the fraction of the incident radiation that is reflected by the surface, the absorptance ( $\alpha$ ) is a property that determines the fraction of the radiation absorbed by the surface and the transmissivity ( $\tau$ ) is the property that determines the fraction of the radiation that is transmitted through the surface. The sum of these three parameters is equal to one [8].

$$\alpha + \rho + \tau = 1 \quad (3)$$

According to the Kirchhoff Law, at thermal equilibrium, the emissivity of a surface equals its absorptance [7].

$$\alpha = \varepsilon \quad (4)$$

Considering Kirchhoff Law, Eq. (3) can be rewritten as:

$$\varepsilon + \rho + \tau = 1 \quad (5)$$

The non-blackbody emitters for which the emissivity is constant regardless of the wavelength are called grey bodies. The total amount of radiation emitted by the grey body can be calculated using the Stefan-Boltzmann law and considering the emissivity of the surface,  $\varepsilon$ .

$$R_t = \varepsilon \cdot \sigma \cdot T^4 \quad (6)$$

## 2.2 Factors Affecting Infrared Thermography Measurements

It is well known that several parameters affect thermographic measurements, namely, emissivity, reflectivity, absorptance and others [3, 9]. To evaluate the influence of some of these parameters, simple tests were carried out using the LFC's thermographic equipment, both in laboratory and "in situ".

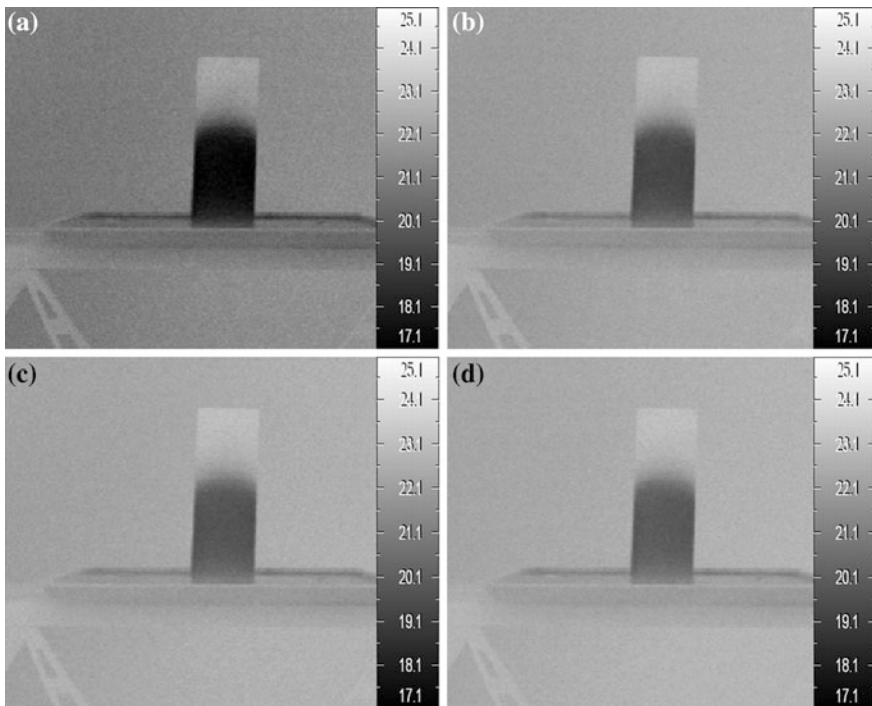
### 2.2.1 Emissivity

Emissivity is one the most important parameters in thermographic measurements, especially when a quantitative study is intended (measurement of real values of surface temperature and not only of the surface temperature differences). To assess the influence of emissivity two laboratory tests were carried out.

One of the laboratory test consisted of partially immersing a specimen of cellular concrete in water followed by a drying period. The test was performed under steady state conditions, inside a climatic chamber. Thermal images were obtained using four different values of emissivity: 0.62, 0.85, 0.91 and 0.95.

As expected [3, 9–11], the results showed that emissivity variation induced changes in the thermal images, during absorption (see Fig. 3). By looking at the thermal images it was possible to say that the images obtained with emissivity 0.62 were quite different from the remaining ones. The differences between the other thermograms (emissivity's 0.85, 0.91 and 0.95) were not very significant [12].

Another laboratory test consisted of measuring the surface temperature of a lime stone sample in hygrothermal equilibrium with the environment. Thermal images were obtained using three different values of emissivity: 0.60, 0.80 and 1.00. The surface temperatures measured at the same point on the specimen vary considerably according with the emissivity (see Fig. 4). For the lower values of emissivity, the changes in surface temperature of the lime stone specimen were greater than 1.5 °C: with emissivity of 0.60, the obtained surface temperature was 12.2 °C; with emissivity of 0.80, the surface temperature obtained was 13.9 °C and with emissivity of 1.00, the surface temperature obtained was 14.9 °C.



**Fig. 3** Thermograms of a cellular concrete specimen during absorption phase obtained with different emissivities: **a**  $\varepsilon = 0.62$ . **b**  $\varepsilon = 0.85$ . **c**  $\varepsilon = 0.91$ . **d**  $\varepsilon = 0.95$



**Fig. 4** Thermograms of lime stone specimen obtained with different emissivities: **a**  $\epsilon = 1.00$ ,  $T_{\text{measured}} = 14.9 \text{ }^\circ\text{C}$ . **b**  $\epsilon = 0.80$ ,  $T_{\text{measured}} = 13.9 \text{ }^\circ\text{C}$ . **c**  $\epsilon = 0.60$ ,  $T_{\text{measured}} = 12.2 \text{ }^\circ\text{C}$

These tests showed that if a quantitative evaluation is intended, the emissivity values must be precisely determined. However, if the study aims for a qualitative evaluation of the results, the selected emissivity value is not very important. Nevertheless, a judiciously selected emissivity value may simplify the interpretation of the thermal image.

### 2.2.2 Reflectivity

The material reflectivity may cause some problems in infrared radiation measurements. The energy captured by the camera results from the sum of two parcels, if the body is not transparent to infrared radiation:

- The body reflects a fraction of the energy emitted by the atmosphere and surrounding objects;
- The body emits radiation as a function of its surface temperature.

Several examples of reflection are presented in Fig. 5: (a) effect of reflectivity on the thermal image of a ceramic floor - the hotter area in the bottom left of the image results from the ceramic surface’s thermal reflection [13]; (b) reflection of the operator on a metallic surface; (c) reflection of a light bulb in a window.



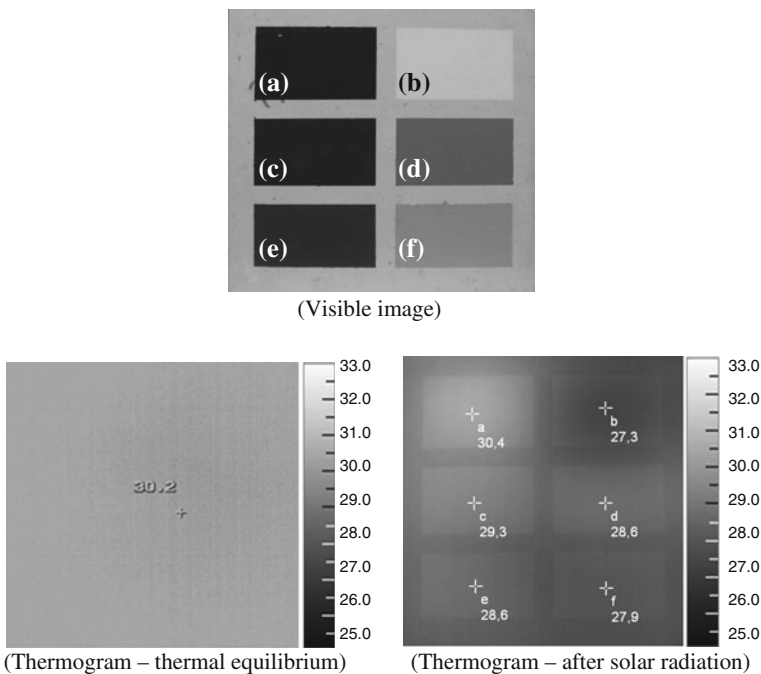
**Fig. 5** Importance of reflective surfaces on thermographic measurements: **a** effect of reflectivity on the thermal image of a ceramic floor. **b** reflection of the operator on a metallic surface. **c** reflection of a light bulb in a window

### 2.2.3 Absorptance

To assess the influence of colour/absorptance of the surface on thermographic measurements two “in situ” tests were performed. One of them consisted in obtaining thermal images of the Carmo Church, in Porto, Portugal. The Carmo Church’s east façade is covered with hand-painted ceramic tiles. The colouring varies between white and several shades of blue (see Fig. 1). The thermal image shows remarkable temperature differences caused by the colour variation [14].

The other test that was performed consisted on painting a lime stone sample using different colours and assessing the effect of absorptance (see Fig. 6: (a) black (b) white, (c) dark blue, (d) green, (e) red, (f) yellow). Thermograms were taken with the sample in thermal equilibrium with the environment and no temperature differences were detected in the thermal image. However, after the exposure of the sample to solar radiation, the surface temperatures measured on different colours were quite different. Black and dark blue presented the highest temperatures, followed by green and red, yellow and, finally, white.

When the façade is painted with different colours, especially if there is a small colour pattern, the effect of the sun can conceal completely the results obtained.



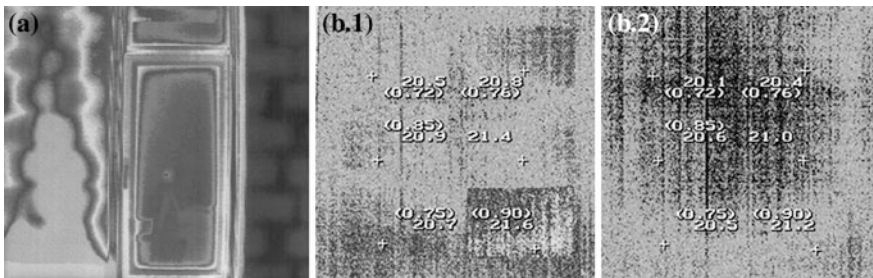
**Fig. 6** The effect of absorptance on different colours of the surface: **a** black, T(after solar radiation) = 30.4° C. **b** white, t(after solar radiation) = 27.3° C. **c** dark blue, T(after solar radiation) = 29.3° C. **d** green, T(after solar radiation) = 28.6° C. **e** red, T(after solar radiation) = 28.6° C. **f** yellow, T(after solar radiation) = 27.9° C

Even on a cloudy day, the diffuse solar radiation can affect the thermal patterns on the exterior of the building. Of course, on a plain façade solar radiation can be very useful to detect anomalies using thermography.

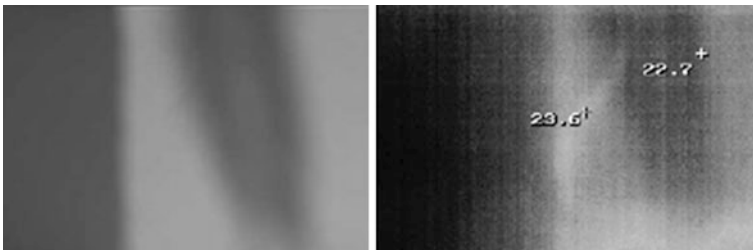
### 2.2.4 Other Factors

The existence of heat sources near the measurement area, such as radiators and artificial lights may affect the results. The severity of the interference from these sources depends on their radiation power and reflection from the surface under study (see Fig. 7).

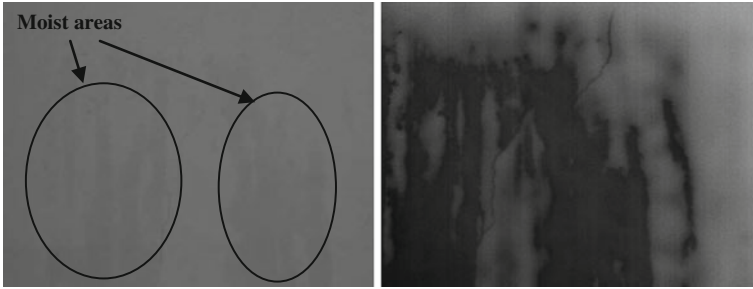
The existence of shadows on the building, resulting from the presence of other buildings, trees or other neighbouring elements can lead to wrong conclusions (see Fig. 8). Also moist surfaces, after rain fall, may affect the interpretation of the results if not taken into account (see Fig. 9). Moreover, thermography is hardly applied when objects are in thermal equilibrium and without any thermal gradient (see Fig. 10).



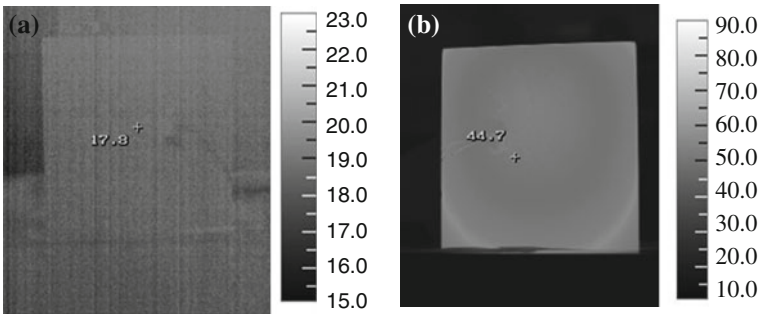
**Fig. 7** Influence of heat sources near the measurement area: **a** radiator and upward movement of warm air from the radiator (*left* side of the image). **b** effect of the operator on the measurement—**b.1** operator near the camera (with higher temperature) and **b.2** no operator near the camera (with lower temperature)



**Fig. 8** Influence of shadows (visible image and thermogram)



**Fig. 9** Influence of moist surfaces, after rain fall (visible image and thermogram)



**Fig. 10** Influence of thermal gradient: **a** sample in equilibrium with the environment and **b** sample with higher temperature than the environment

### 3 Infrared Thermography Applications to Building Assessment

Infrared thermography has been applied since 1960 in many fields for several purposes. To the building assessment, it is commonly used since the 1990s. However, during the past few years, interest in the use of thermography for building inspections has increased, mostly due to lower infrared equipment costs. This technology enables the analysis of building structure, assemblies and materials. It is possible to identify missing insulation areas, air infiltration/exfiltration, poor window seals, areas of moisture infiltration, HVAC systems, plumbing or electrical components, construction details, etc. In the following sections a brief state-of-the-art of infrared thermography applications’ to building assessment is presented.

### 3.1 Thermal Comfort of Floor Coatings

The comfort of interior floor coatings is very important for the well-being of building users, especially in bedrooms and bathrooms where people commonly walk barefoot. Although comfort depends on floor and environmental temperatures, it is also determined by the material's thermal characteristics, namely, thermal diffusivity and effusivity. Infrared thermography can be used to evaluate the comfort of interior floor coatings by comparing effects from barefoot contact with different materials [12,15,16] (see Fig. 11).

### 3.2 Detachments

Tests performed by Chew[10] pointed out the thermography potential to evaluate detachments on tile facades. The laboratory evaluation consisted on using samples composed by: concrete slab, cement sand screed with detachments of different diameters of hollowness and exterior ceramic wall tiles adhered with epoxy. After immersing the samples in water, thermograms were taken under controlled air temperature, with artificial lighting switched off and with no heat sources nearby. The test sample surface was heated up to acquire cross-sectional temperature gradient with four infrared lamps. It was possible to conclude that thermography was effective in locating the simulated detachments, especially for detachments with greater diameter.

Sakagami et al. [17] showed that using infrared thermography under microwave heating is a useful testing technique to detect superficial cracks in concrete structures. The work developed showed that applying microwave heating to the



**Fig. 11** Assessment of comfort of interior floor coatings: **a** standard temperature. **b** after being in contact with carpet. **c** after being in contact with granite

concrete structure with wet cracks, water in the cracks can be selectively heated, which leads to a specific temperature distribution around the crack enabling an easier detection. Preliminary experimental investigation was carried out for mortar-block specimens with artificial cracks using a microwave oven.

Studies made by Cerdeira et al. [18] focused on stone panel defects. Laboratory tests under controlled conditions were performed in scale models reproducing a real building envelope. The front face of the models was coated with stone panels with different thickness. In the mortar existing between the brick layer and the stone panels, a series of detachments with different size and shape were introduced to simulate the lack of adherence. A hot air generator was placed inside the models to set up the thermal gradient. The areas with defects were detected with lower temperatures than the surrounding areas as the air gap increased the thermal resistance of the wall. Higher thermal gradients between the interior and the exterior of the models lead to higher temperature differences between the defect and the surroundings. In the thinner stone panels the defects were detected more clearly. It was concluded that infrared thermography can be a valuable maintenance technique to detect detachments.

The latest study was made by Simões et al. [19] in which two set of experiments were carried out with four models of direct adhered ceramic tiles to simulate different defects and inappropriate adhesion of the adhesive layer using lock-in thermography. The tests were arranged with two halogen lamps of 2,000 W turned on for 30s and followed by a cooling phase of 60s. The results obtained showed that this technique allowed the identification of the defects, especially for those with larger dimension, but the induced detachment was not identified.

The detection of detachments in real building façades is also possible using the solar radiation as a heat source (see Fig. 12).

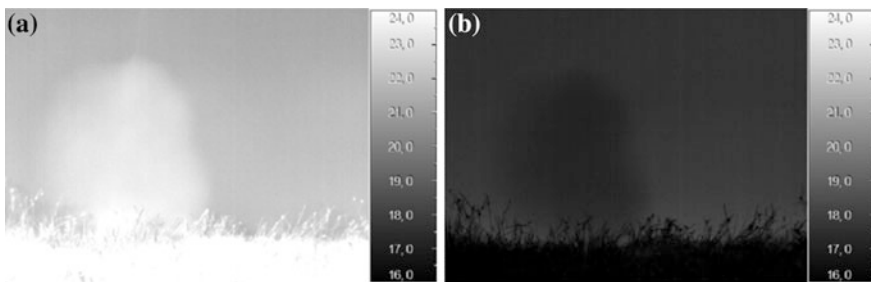


Fig. 12 Detachments observed with sunlight falling on the façade at: a 4.30 pm and b 11.30 pm



### 3.3 *Moisture Anomalies*

Dampness or changes in moisture content can also be detected by thermography, as surface temperature changes occur due to evaporative cooling [20], decrease of thermal resistance and increase of heat storage capacity of the moist material [21].

Balaras and Argiriou [22] made some recommendations for detecting water damage on roofs. They stated that inspections should be performed at night when the roof surface is still dry. Day-time surveys must be avoided once direct solar radiation can cover-up potential differences caused by the wet insulation. The moisture damage was detected by exploiting the thermal properties of water. As water has higher specific heat than other materials used on roofs, water loses or gains heat are much slower than other materials under similar conditions. A wet area retains the absorbed heat for a longer period than a dry mass and therefore takes longer to radiate heat during the night. Hence, it is detected by higher temperatures.

Avdelidis et al. [23] analysed the infrared thermography applicability in the detection of water movement and concentration in porous stones.

Grinzato and Cadelano [24] monitored the moisture content of a wall. The tests were carried out on a church fresco without applying thermal stress by artificial heat sources. The testing procedure consisted on increasing the evaporation rate of the surface by enhancing the air speed and recording, at the same time, a sequence of thermograms (before, during and after the increasing of the air speed). The results showed that it is possible to quantify the evaporation of a surface based on decreasing temperature, due to evaporation, as the intensity of the evaporation rate is related to the speed of temperature change.

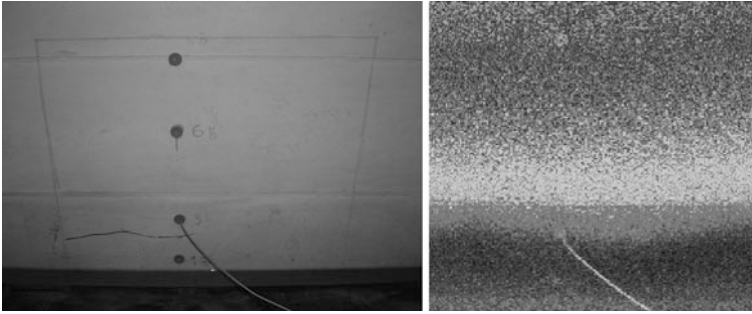
Lerma et al. [25] also evaluated the detection of moisture on a building façade by making a qualitatively map of the surface moisture based on multi-temporal thermal analysis. This analysis is based on the different thermal behaviour of wet masses compared to dry masses over time due to temperature variations.

Rajewski and Devine [26] showed that thermal anomalies can be detected during the winter as building heat is conducted through wet insulation more rapidly than through dry insulation, thus, creating a warmer surface over the wet insulation. Moisture leaks and roof water damages were identified as areas with a higher temperature since damp insulation has a different overall heat transfer coefficient.

Rising damp on walls can also be detected by infrared thermography. The water level in the wall is detected due to superficial temperature variation, which is a result of evaporation at the wetted surface (see Fig. 13).

### 3.4 *Thermal Bridges*

Infrared thermography can be used to locate the position and to assess the magnitude of thermal bridges in existing buildings, as thermal bridges increase



**Fig. 13** Moisture detection (rising damp—visible image and thermogram)

significantly heat loss through buildings components, especially with higher insulation levels (see Fig. 14).

As showed by Balaras and Argiriou [22], taking an outdoor thermogram of the structural component during winter, thermal bridges appear as light coloured areas because the heat losses from the indoor heated space cause a temperature increase. An indoor thermogram of the component during summer will show a similar image as a result of the absorbed solar heat gains from the external surface that are conducted through the building materials.

Asdrubali et al. [27] proposed an analytical methodology to quantitatively analyse some types of thermal bridges, which was validated by experimental and numerical analysis.

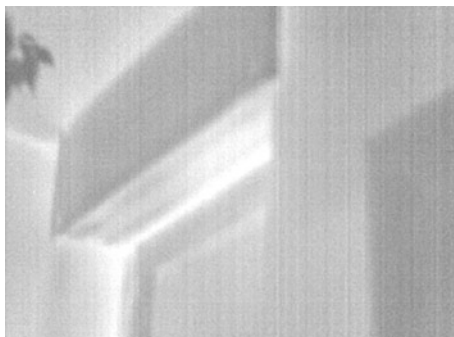
### 3.5 Air Leakage

Air leakage through windows and doors allows unwanted outdoor air to enter inside the building (infiltration) or indoor air to escape (exfiltration). Outdoor air

**Fig. 14** Thermal bridge in a building detected by IRT



**Fig. 15** Air leakage through window detected by IRT

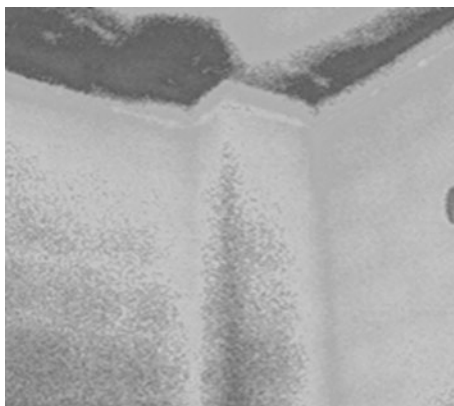


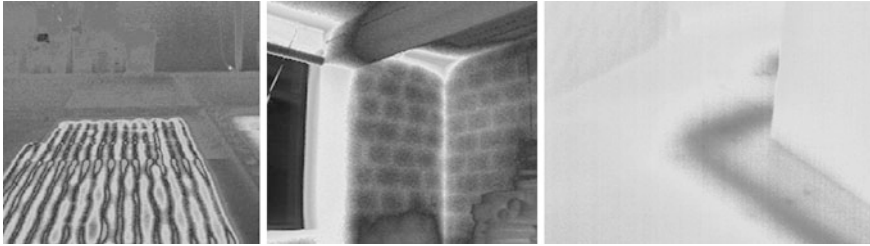
increases heat losses in winter and heat gains in summer, thus, increasing both heating and cooling loads. A common location for air infiltration is around a window or a door frame. Infrared thermography is commonly used with a blower door test running. The blower door helps exaggerate air leaking through defects in the building shell and such air leaks are detected by the infrared camera (see Fig. 15).

### ***3.6 Missing or Damaged Insulation***

Infrared thermography allows checking the effectiveness of insulation in a building [3,28]. Thermal insulation reduces heat losses by conduction through the building envelope (*i.e.* walls, roofs) during winter and heat gains during summer. Missing or damaged insulation can be located by infrared cameras (see Fig. 16). According to Balaras and Argiriou [22] when the thermogram indicates a temperature difference of about 11 °C between the internal and external surface temperature that could indicate problems with the thermal insulation.

**Fig. 16** Missing insulation detected using IRT





**Fig. 17** Detection of “hidden details” using IRT

### ***3.7 Hidden Details***

Infrared thermography can be used to detect “hidden details”, as subsurface pips, ducts, wall ties, thermal resistances from radiant floors, etc. (see Fig. 17).

## **4 Detailed of Test Procedures**

The guarantee of accurate assessment of building components using infrared thermography can only be achieved if inspection methodologies are available. This section provides detailed information about three test procedures to assess comfort of floor coatings (see Table 1), to detect detachments (see Table 2) and to evaluate wetting and drying processes of building materials (see Table 3). These tables, in a summarized and systematized manner, give particular emphasis to the objectives, procedures and obtained results. A critical analysis is presented at the end.

## **5 Conclusions**

Thermography is a non-destructive testing technology with much potential to be applied to building diagnosis. Research studies developed at the Building Physics Laboratory (LFC) revealed that emissivity is an essential parameter, since it greatly influences thermographic measurements and may restrict the application of this technology to buildings. However, if the study aims for a qualitative analysis of the results, the selected emissivity value is not very important. It was also possible to confirm the influence of the material reflectivity on the results obtained. Colour or absorptance to solar radiation must also be considered during thermographic testing, as it may mask the results and cause misinterpretation, especially if the façade is painted with different colours and there is a specific small colour pattern. Other tests carried out emphasise the effect of heat sources near the measurement area, shadows on the building and moist surfaces after rain fall. On

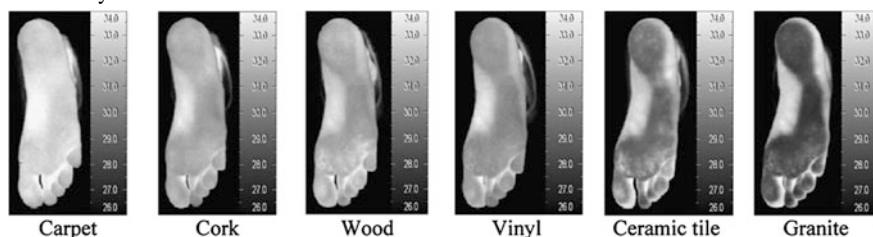
**Table 1** Resume of the comfort of floor coatings experiments

Comfort of floor coatings

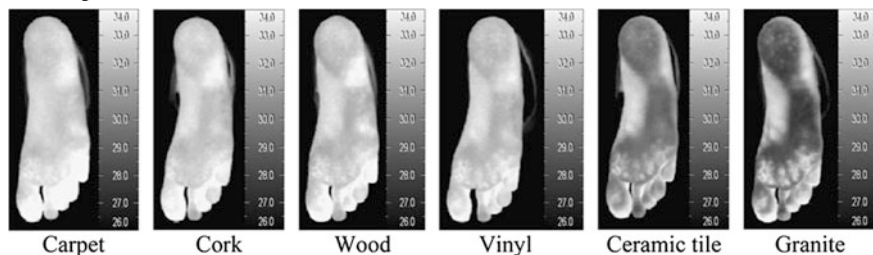
Laboratory Tests—Setup



Laboratory Tests—Results



Thermograms after 1 min of contact



Thermograms after 2 min of contact

**Objective** Assess the comfort of interior floor coatings using thermography

**References** [12,15,16]

**Procedure** The comfort is evaluated qualitatively by comparing a reference thermogram of the foot surface temperature with two thermograms made after two contact times (1 min to assess initial discomfort and 2 min to study discomfort progress over time). Six samples of floor coatings (carpet, cork, vinyl, wood, ceramic tile and granite) were used

The study was carried out inside a climatic chamber under stable conditions of temperature and relative humidity ( $T = 20\text{ }^{\circ}\text{C}$ ,  $\text{RH} = 60\%$ ) and the emissivity was set to 1.0

(continued)

**Table 1** (continued)

Comfort of floor coatings	
Results	<p>Different temperatures were obtained for the six samples that result from the different thermal characteristics of the materials related to the propagation of heat. These heat exchanges are a function of the thermal diffusivity (the higher its value, the quicker the propagation and greater the heat flow through the material) and the thermal effusivity (reflecting the ability to absorb or store heat). The heat transfer between the foot and the material will be faster with higher values of the effusivity and thermal diffusivity</p> <p>The surface temperature of the foot is always lower than the reference thermogram and it was observed that the initial contact is more comfortable with carpet followed by cork, wood, vinyl, ceramic and, finally, granite. With the increased contact time for 2 min, the thermal equilibrium is approaching and the discomfort is attenuated. An increase in the surface temperature of the foot is observed without significant differences for carpet, vinyl, wood and cork. For ceramic and granite the temperatures are lower</p>
Equipment	Thermo Tracer TH1 101 (measurement accuracy: $\pm 0.5 \text{ }^\circ\text{C}$ ; resolution: $0.1 \text{ }^\circ\text{C}$ and spectral band: $8\text{--}13 \text{ }\mu\text{m}$ )
Critical analysis	Thermography is a very interesting technique to evaluate the comfort of a bare foot in contact with floor coatings, which have the same temperature but where the heat exchange varies according to the material properties


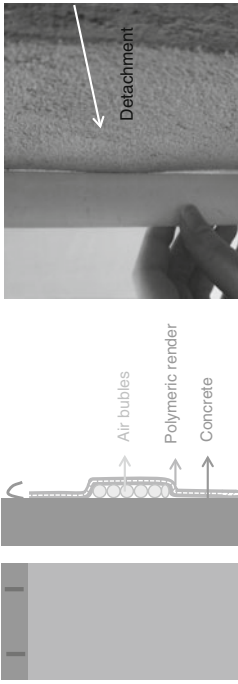
the other hand, it was also concluded that thermography cannot be used to study objects in thermal or hygroscopic equilibrium, as temperature differences between the object and the environment must be significant.

Infrared thermography is a useful technology to study the behaviour of buildings and building components. Examples of its application are presented, namely, to assess the comfort of interior floor coatings and to detect detachments of walls coatings, moisture anomalies, thermal bridges, air leakage and missing or damaged insulation.

Finally, detailed information about three test procedures is provided, summarized and systematized in the form of tables. These tables include information about the objectives of the study, test procedures, obtained results, equipment that was used and, at the end, a critical analysis of the applicability of thermography to the study carried out. The information is related with:

- Evaluation of the comfort of interior floor coatings. Thermal images were obtained from the sole of a barefoot after having been in contact with different floor materials. Since the superficial temperature variation, after contact between the foot and the material, is related with discomfort, a comparison of thermograms revealed the various material comfort levels.
- Detection of detachments of wall rendering. The detachment creates an air layer and thermal resistance to heat flows, which enables the temperature differential to be assessed. Two phases can clearly be distinguished, both in laboratory and “in situ”. In the heating phase, the thermal resistance caused by detachment impedes the absorbed heat from reaching the interior, which means that the

**Table 2** Resume of the detachments detection experiments

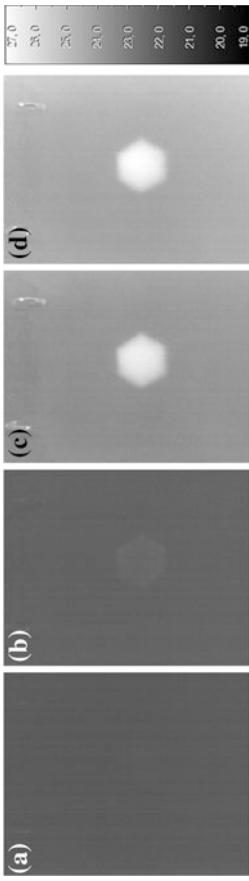
<b>Detection of Detachments</b>	
	
1 – Sample	
2 – Infrared heat source	
3 – Thermographic camera	
	
Vertical elevation	Cross-section

(continued)

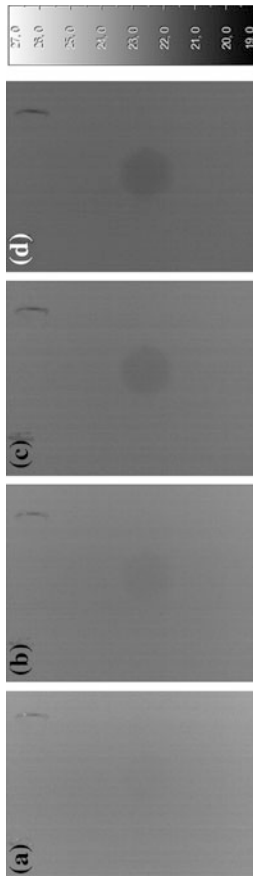
Table 2 (continued)

**Detection of Detachments**

Laboratory Tests—Results



Thermograms in the heating phase: (a) without heating, (b) start of heating, (c) 10 min. after start of heating, (d) 30 min. after start of heating



Thermograms in the cooling phase: (a) 10 min. after heating switched off, (b) 20 min. after heating switched off, (c) 40 min. after heating switched off, (d) 70 min. after heating switched off

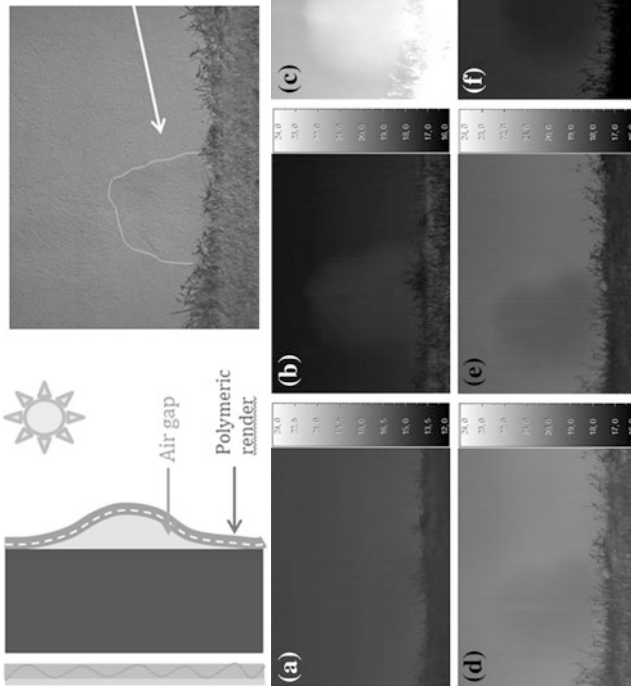
(continued)



Table 2 (continued)

Detection of Detachments

“In situ” Tests—Physical model and reality



Thermograms taken “in situ” during an October day: (a) 9.30 am (b) 12.30 pm (c) 4.30 pm (d) 5.30 pm (e) 6.30 pm (f) 11.30 pm

(continued)

Table 2 (continued)



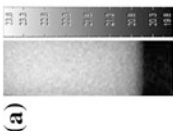
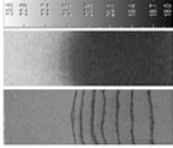

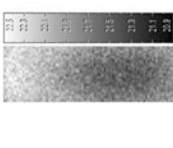

<b>Detection of Detachments</b>	
Objective	Diagnosis of façade rendering detachments
References	de Freitas et al. [29]
Procedure	<p>Assessment of detachments was performed using “dynamic thermography”. The measurements were taken in laboratory with the action of radiation from a heat source and “in situ” with the action of radiation from the sunlight</p> <p>Laboratory Tests—A series of laboratory tests was carried out on 3 equal samples of concrete in which a detachment was artificially created in the coating by inserting an air layer between the support (concrete) and the fine polymeric render. The test involved the dynamic analysis of the surface temperature variation over time, using a 500 W infrared heat source to simulate the effect of solar radiation on a façade. The three samples were placed perpendicular to the thermographic camera and heat source at a distance of 0.65 m. The test was performed under approximately constant environmental conditions (<math>T = 20\text{ }^{\circ}\text{C}</math> and <math>\text{RH} = 60\%</math>) and without natural or artificial light. Thermograms were obtained on a minute-by-minute basis in three phases: without a heat source; with the heat source switched on (for 30 min) and after the heat source was switched off (for 70 min)</p> <p>“In situ” Tests—A series of “in situ” tests was carried out on the southern façade of a residential building in Porto, Portugal, which had occasional detachments. The southern façade studied was composed of a fine polymeric render (0.004 m), cement plaster rendering (0.02 m), brick masonry (0.3 m), air layer (0.02 m), thermal insulation (0.05 m) and gypsum board (0.015 m). The test procedure consisted of taking thermograms using the solar gains throughout the day in order to permit a dynamic analysis. Additional checks of the detached zones were made using percussion. Thermograms were obtained hourly in three phases: without sunlight falling on the façade, with sunlight falling directly on the façade and after the sun had been on it</p>

(continued)

Table 2 (continued)


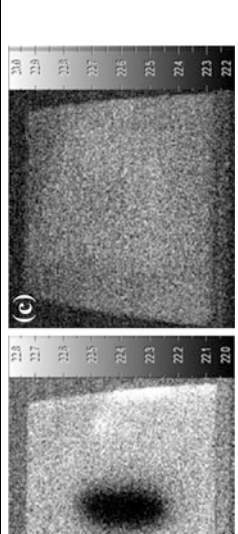
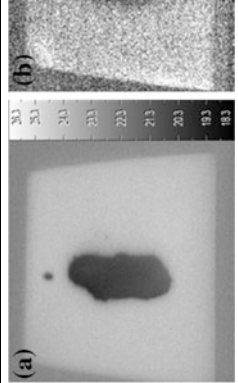
<b>Detection of Detachments</b>	
Results	<p>Defects are generally identified by differences in surface temperature between areas with and without pathologies. The detachments create an air layer and thermal resistance to heat flows, which enables the temperature differential to be assessed</p> <p>Two phases can clearly be distinguished. In the heating phase, the thermal resistance caused by detachment impedes the absorbed heat from reaching the interior, which means that the surface temperature is higher in the detachment. In contrast, in the cooling phase, the heat absorbed by the façade is prevented from reaching the surface, which means that surface temperatures are lower in the detachment, due to the reduction in thermal capacity</p> <p>The following results were obtained:</p> <ul style="list-style-type: none"> <li>• Laboratory Tests—The physical model used for the laboratory tests enabled the qualitative assessment of the detachments artificially created in three samples when subjected to action from a heat source. It was found that the defect created was clearly visible through dynamic thermography. In the cooling phase, although the temperature difference between the detachment and zone without detachment was smaller, the detachment was also observable</li> <li>• “In situ” Tests—In the morning, when the sun does not heat the façade, the detachment is not visible. At around 3 pm, when solar radiation is at its peak, the detachment is perfectly visible, showing higher temperatures than those on the zone of the façade without detachments. On the other hand, when the façade is cooling, the detachment zone cools faster, and is therefore distinguished by lower temperatures</li> </ul> <p>The tests carried out “in situ” produced results that were consistent with those of the laboratory tests. These tests prove that the application of thermography in real situations leads to positive results in the diagnosis of the pathology in analysis</p> <p>Laboratory tests—Thermo tracer TH 7,800 (measurement accuracy: <math>\pm 2\%</math> or <math>\pm 2\text{ }^{\circ}\text{C}</math>; resolution: <math>0.05\text{ }^{\circ}\text{C}</math> to <math>0.1\text{ }^{\circ}\text{C}</math> for a range of <math>-20\text{ }^{\circ}\text{C}</math> to <math>100\text{ }^{\circ}\text{C}</math>; <math>752\text{ (H)} \times 480\text{ (V)}</math> pixels and a spectral band of <math>8\text{--}14\text{ }\mu\text{m}</math>)</p> <p>“In situ” tests—Thermo tracer TH 9,100 (measurement accuracy: <math>\pm 2\%</math> or <math>\pm 2\text{ }^{\circ}\text{C}</math>; resolution: <math>0.02\text{ }^{\circ}\text{C}</math> to <math>0.06\text{ }^{\circ}\text{C}</math> for a range of <math>-20\text{ }^{\circ}\text{C}</math> to <math>100\text{ }^{\circ}\text{C}</math>; <math>320\text{ (H)} \times 240\text{ (V)}</math> pixels, and a spectral band of <math>8\text{--}14\text{ }\mu\text{m}</math>)</p>
Equipment	
Critical analysis	<p>Detachments spoil the appearance of the façade, facilitate rainwater penetration and consequently reduce the durability of the render and of the façade itself. Infrared thermography offers great potential for the diagnosis of such pathologies, generating a thermal image where the pathology can be clearly detected</p>

**Table 3** Wetting and drying processes of building materials

Wetling and drying—Moisture detection	
Laboratory tests—Setup	
 <p><b>(a)</b></p>	 <p><b>(b)</b></p>
(A) Capillary absorption and (B) wetting and drying processes	
Laboratory tests—Results	
 <p><b>(a)</b></p> <p>Specimen at 2 hours</p>	 <p>Specimen at 408 hours (end of absorption)</p>
 <p><b>(b)</b></p> <p>Specimen at 442 hours</p>	 <p>Specimen at 578 hours</p>
 <p>Specimen at 794 hours (end of drying)</p>	
(A) Capillary absorption: (a) Wetting process and (b) Drying process	

(continued)

**Table 3** (continued)  
Wetting and drying—Moisture detection

		
<p>(B) Wetting and drying processes: (a) Specimen after 48 h of wetting, (b) Specimen after 1 h of wetting and (c) Specimen at the end of the drying period</p>		
<p>Objective</p>	<p>Detection of capillary absorption and wetting and drying processes</p>	
<p>References</p>	<p>[15, 30, 31]</p>	
<p>Procedure</p>	<p>Two experiments were carried out:</p>	
<p>(A)</p>	<p>A cellular concrete specimen (<math>70 \times 70 \times 200 \text{ mm}^3</math>) was tested inside a climatic chamber under steady state conditions (<math>T = 20 \text{ }^\circ\text{C}</math> and <math>\text{RH} = 60 \%</math>). The emissivity value considered was 0.85 and the specimen was kept on water for 407 h after which the drying period started</p>	
<p>(B)</p>	<p>Two cellular concrete specimens (<math>300 \times 300 \times 20 \text{ mm}^3</math>) were tested inside a climatic chamber with 4 different conditions:</p>	
<p>(1)</p>	<p><math>T = 20 \text{ }^\circ\text{C} + \text{RH} = 60 \%</math></p>	
<p>(2)</p>	<p><math>T = 25 \text{ }^\circ\text{C} + \text{RH} = 60 \%</math></p>	
<p>(3)</p>	<p><math>T = 20 \text{ }^\circ\text{C} + \text{RH} = 40 \%</math></p>	

(continued)

**Table 3** (continued)

Wetting and drying—Moisture detection	
	The emissivity value considered was 0.85 and the specimens were subject to water dripping for one hour at a rate of 11 drops per minute
	The following results were obtained:
(A)	The test carried out demonstrated that it was possible to visualize superficial temperature variations due to rising capillarity. Moreover, it was recorded faster drying at the top and vertical edges of the specimen. At the end of the test, the superficial temperature of the specimen was uniform and the moisture distribution was not perceptible
(B)	After one hour of wetting a stained area was clearly detected. At the end of 48 h of drying, the colder area decreased. During the drying phase the specimen achieved the thermal equilibrium with different drying periods. An approximation of the drying times was made but only for superficial moisture
Equipment	Thermo tracer TH1 101 (measurement accuracy: $\pm 0.5$ °C ; resolution: 0.1 °C and spectral band: 8–13 $\mu\text{m}$ )
Critical analysis	The damages caused by moisture are a common problem that affect buildings. The detection of moisture in building components using thermography underlies in the physical principle of evaporative cooling of the surface, as surface temperature variation due to the phase change of water is significant
	It is possible to evaluate the wetting and drying process of building materials. However, it may not always be reliable and a quantitative approach can be difficult to implement. The goal is to highlight on the surface the areas related to a certain range of the evaporation rate

surface temperature is higher in the detachment. In contrast, in the cooling phase, the heat absorbed by the façade is prevented from reaching the surface, which means that surface temperatures are lower in the detachment, due to the reduction in thermal capacity.

- Assessment of the wetting and drying process of building materials. Temperature differences due to superficial water evaporation provided a mean of recognising “wet” and “dry” areas. It was also possible to evaluate the material’s approximate drying time since small superficial temperature variations indicate that moisture is rather significant. Thermography, however, detects only superficial moisture.

**Acknowledgments** The research work presented herein was supported by FEDER funds through the Operational Programme for Competitiveness Factors—COMPETE and by national funds through the FCT—Portuguese Foundation for Science and Technology, under research project PTDC/ECM/114189/2009. J.M.P.Q. Delgado would like to thank Fundação para a Ciência e a Tecnologia (FCT) for financial support through the grant SFRH/BPD/84377/2012.

## References

1. Rao, P.: Infrared thermography and its applications in civil engineering. *The Indian Concrete Journal*, **82**(5), 41–50 (2008)
2. NEC San-ei Instruments, Ltd.: TH1 101 Thermo Tracer—Operation Manual, Japan (1991)
3. Hart, J.M.: *A Practical Guide to Infra-red Thermography for Building Surveys*. Garston, Watford (1991)
4. Avdelidis, N.P., Moropoulou, A.: Applications of infrared thermography for the investigation of historic structures. *J. Cultural Heritage*, **5**(1), 119–127 (2004)
5. Grinzato, E., Vavilovb, V., Kauppinen, T.: Quantitative infrared thermography in buildings. *Energ. Build.*, **29**(1), 1–9 (1998)
6. Haralambopoulos, D.A., Paparsenos, G.F.: Assessing the thermal insulation of old buildings—The need for in situ spot measurements of thermal resistance and planar infrared thermography. *Energy Convers. Manage.*, **39**(1–2), 65–79 (1998)
7. Incropera, F.P., Witt, D.P.: *Fundamentals of Heat and Mass Transfer*- 4th ed. John Wiley & Sons ed. , New York (1996)
8. Hagentoft, C.: *Introduction to Building Physics*. Student Litteratur, Sweden (2001)
9. Chown, G.A., Burn, K. N.: Thermographic identification of buildings enclosure defects and deficiencies. *Canadian building digest* 229, Canada, NRC–IRC (1983)
10. Chew, M.Y.L.: Assessing building facades using infra-red thermography. *Struct. Survey*, **16**(2), 81–86 (1998)
11. Gaussorgues, G.: *La thermographie infrarouge—Principles, Technologies, Applications*. 4th edn. TEC & DOC, Paris, France (1999)
12. Barreira, E.: *Thermography applications in the study of buildings hygrothermal behaviour*. M.Sc. Thesis, Porto, FEUP, Portugal (in Portuguese) (2004)
13. Barreira, E., de Freitas, V.P.: Thermal images obtained from different solutions of radiant floor. Internal Report LFC/IC 134.2003, LFC, FEUP, Porto, Portugal (in Portuguese) (2003)
14. Barreira, E., de Freitas, V.P., Delgado, J.M.P.Q., Ramos, N.: Thermography applications in the study of buildings hygrothermal behaviour. Chapter published in infrared thermography. In: Prakash, R.V. (ed.) *Intech*, Croatia (2012)

15. Barreira, E., de Freitas, V.P.: Evaluation of building materials using infrared thermography. *Constr. Build. Mater.*, **21**(1), 218–224 (2007)
16. Barreira, E., de Freitas, V.P.: Thermal comfort evaluation of floor coatings using infrared thermography. *Construlink Int. J.* **3**(8), 30–38 (2004). (in Portuguese)
17. Sakagami, T., Komiyama, T., Suzuki, H.: Proposal for a new thermographic non-destructive testing technique using microwave heating, In: *Proceedings of the thermosense XXI, International society for optical engineering (SPIE), Orlando*, pp. 99–103 (1999)
18. Cerdeira, F., Vázquez, M.E., Collazo, J., Granada, E. Applicability of infrared thermography to the study of the behaviour of stone panels as building envelopes. *Energ. Build.*, **43**(8), 1845–185 (2011)
19. Simões, N., Simões, I., Tadeu, A., Serra, C.: Evaluation of adhesive bonding of ceramic tiles using active thermography. In: *Proceedings of the 11th international conference on quantitative infrared thermography, Naples, Italy* (2012)
20. Rosina, E., Ludwig, N.: Optimal thermographic procedures for moisture analysis in building materials. In: *Proceedings of society of photographic instrumentation engineers (SPIE)*, **3827**, pp. 22–33 (1999)
21. ASTM.: *ASTM C1153—10 Standard practices for location of wet insulation in roofing systems using infrared imaging*. American Society for Testing and Materials (ASTM) International (2010)
22. Balaras, C.A., Argiriou, A.A.: Infrared thermography for building diagnostics. *Energ. Build.* **34**(2), 171–183 (2002)
23. Avdelidis, N.P., Moropoulou, A., Theoulakis, P.: Detection of water deposits and movement in porous materials by infrared imaging. *Infrared Phys. Technol.* **44**(3), 183–190 (2003)
24. Grinzato, B., Cadelano, G., Bison, P.: Moisture map by IR thermography. *J. Modern Optics*, **57**(18), 1770–1778 (2010)
25. Lerma, J.L., Cabrelles, M., Portalés, C.: Multitemporal thermal analysis to detect moisture on a building façade. *Construction and Building Materials*, **25**(5), 2190–2197 (2011)
26. Rajewski, G., Devine, G.: *Building Envelope—infrared thermography, preventative roof maintenance workshop*. Building operator association (1996)
27. Asdrubali, F., Baldinelli, G., Bianchi, F.: A quantitative methodology to evaluate thermal bridges in buildings. *Appl. Energy* **97**, 365–373 (2012)
28. Ocaña, S.M.; Guerrero, I.C.; Requena, I.G. (2004). Thermographic survey of two rural buildings in Spain. *Energy and Buildings*, **36**(6), 515–523
29. de Freitas, S.S., de Freitas, V.P., Barreira, E.: Application of infrared thermography to the diagnosis of façade rendering detachment, A state of the art report on building pathology—CIB W086, CIB Edition (in Press) (2013)
30. Barreira, E., de Freitas, V.P.: Infrared thermography applications in the study of building hygrothermal behaviour. CIB W40 Meeting, Caledonian University, Glasgow (2004a)
31. Barreira, E., de Freitas, V.P.: Importance of thermography in the study of ETICS finishing coatings degradation due to algae and mildew growth. In: *Proceedings of the 10th international conference on durability of building materials and components (10DBMC), CSTB, Lyon* (2005)



# Heat Transfer Behaviors of Thermal Energy Storages for High Temperature Solar Systems

A. Andreozzi, B. Buonomo, O. Manca, S. Nardini and S. Tamburrino

**Abstract** Solar energy is an important alternative energy source that will likely be utilized in the future. One main limiting factor in the application of solar energy is its cyclic time dependence. Therefore, solar systems require energy storage to provide energy during the night and overcast periods. Although the need of thermal energy storage also exists for many other thermal applications, it is particularly notable for solar applications. It can improve the efficient use and provision of thermal energy whenever there is a mismatch between energy generation and use. In sensible thermal storage, energy is stored by changing the temperature of a storage medium. The amount of energy input to thermal energy storage by a sensible heat device is proportional to the difference between the storage final and initial temperatures, the mass of storage medium and its heat capacity. Each medium and porous matrix has its own advantages and disadvantages.

**Keywords** Thermal energy storage · Porous media · High temperature · Concentrated solar power systems · Local thermal non-equilibrium · Darcy-Brinkmann-Forchheimer model

---

A. Andreozzi (✉)

Dipartimento di Ingegneria Industriale, Università degli Studi di Napoli Federico II, Piazzale Tecchio 80 80125 Naples, Italy  
e-mail: [assunta.andreozzi@unina.it](mailto:assunta.andreozzi@unina.it)

B. Buonomo · O. Manca · S. Nardini · S. Tamburrino

Dipartimento di Ingegneria Industriale e dell'Informazione, Seconda Università degli Studi di Napoli, Via Roma 29 81031 Aversa, CE, Italy  
e-mail: [bernardo.buonomo@unina2.it](mailto:bernardo.buonomo@unina2.it)

O. Manca

e-mail: [oronzio.manca@unina2.it](mailto:oronzio.manca@unina2.it)

S. Nardini

e-mail: [sergio.nardini@unina2.it](mailto:sergio.nardini@unina2.it)

S. Tamburrino

e-mail: [salvatore.tamburrino@unina2.it](mailto:salvatore.tamburrino@unina2.it)

### Nomenclature

$a_{sf}$	Specific surface area, $m^{-1}$
$c, c_p$	Specific heat, $Jkg^{-1}K^{-1}$
$C$	Inertia coefficient
$d_p$	sphere diameter
$D$	Cylinder diameter, m
$G$	Mass velocity, $kg\ m^{-2}\ s^{-1}$
$h$	Surface heat transfer coefficient, $Wm^{-2}K^{-1}$
$h_{sf}$	Interfacial heat transfer coefficient between solid matrix and fluid, $Wm^{-2}K^{-1}$
$H$	Height of the cross section, m
$k$	Thermal conductivity, $Wm^{-1}K^{-1}$
$K$	Permeability, $m^{-2}$
$L$	Cylinder height, channel length, m
$m$	Mass flow rate, $kg\ s^{-1}$
$p$	Pressure, Pa
$Pr$	Prandtl number
$q$	Heat flux, $Wm^{-2}$
$r, z$	Cylindrical coordinates, m
$Re$	Reynolds number
$s$	Channel thickness, m
$t$	Time, s
$T$	Temperature, K
$u, v$	Velocity component, $ms^{-1}$
$x, y, z$	Cartesian coordinates, m

### Greek

$\varepsilon$	Emissivity coefficient
$\varphi$	Porosity
$\mu$	Dynamic viscosity, Pa s
$\rho$	Density, $kgm^{-3}$

### Subscripts

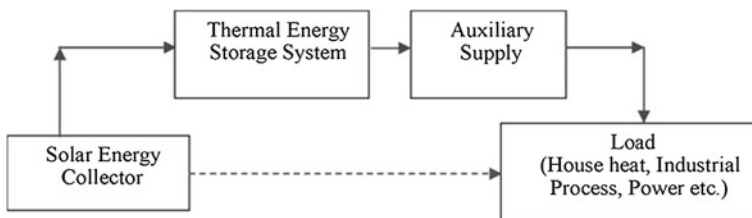
$f$	Fluid
$in$	Initial
$p$	Porous
$s$	Solid

## 1 Introduction

Energy storage not only plays an important role in the energy conservation but also improves the performance and reliability of wide range of energy systems, and becomes more important where the energy source is intermittent such as solar. Energy storage process can reduce the rate mismatch between energy supply and energy demand. Devices for the energy conservation and management are largely employed in many industrial and commercial applications to supply thermal energy, if it would be needed. Energy demands in the commercial, industrial and utility sectors vary on daily, weekly and seasonal bases. These demands can be matched thanks to thermal energy storage (TES) systems that operate synergistically. TES for thermal applications, such as space and water heating, cooling, air-conditioning, etc., has recently received much attention [1–9]. A storage system therefore constitutes an important component of the solar energy utilization system.

Solar energy is an important alternative energy source that will likely be utilized in the future. One main limiting factor in the application of solar energy is its cyclic time dependence. Therefore, solar systems require energy storage to provide energy during the night and overcast periods. A line diagram of a typical solar energy utilization system is shown in Fig. 1 [10]. Thermal energy can be stored as sensible heat, latent heat or chemical energy. An overview of major technique of storage of solar thermal energy is shown in Fig. 2 [11]. In sensible heat storage, heat is stored by increasing the storage medium temperature. In case of latent heat storage systems, the energy is stored in phase change materials. The heat is stored when the material changes phase from solid to a liquid. Thermo-chemical storage is a technique, which involves chemical reactions.

Since the first oil crisis of the 1970s, concentrated solar power (CSP) generation has become a promising alternative to conventional electricity production. Contrary to other renewable energy technologies like photovoltaic or wind power, CSP offers the advantage of thermal energy storage (TES), which allows for electricity production on demand and independently of the solar resource. The most widespread CSP technology is the parabolic trough system, where parabolic mirrors are used to concentrate sunlight onto an absorber tube located at the focus line. A heat transfer fluid (HTF) circulates in thousands of meters of lighted pipes to collect the thermal energy and then transfer it to a steam generator via a heat exchanger.



**Fig. 1** Line diagram for a solar energy utilization system [10]

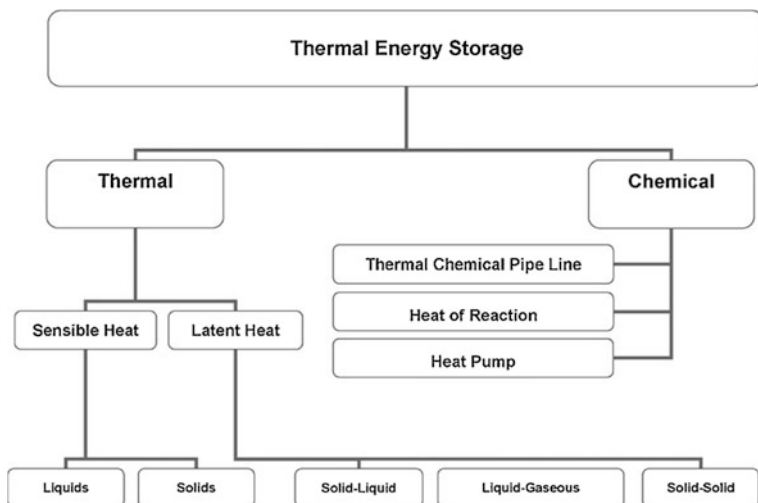


Fig. 2 Overview of thermal energy storage systems [11]

TES in concentrated solar power (CSP) technology is very important to deliver high-temperature heat in the form of sensible heat storage in a packed bed of rocks or other ceramic materials and it is especially suitable when a gas is used as the heat transfer fluid in the solar receiver [10–15]. However, some other types of porous media such as ceramic foams or honeycomb could be employed as material for High Temperature Thermal Energy Storage (HTTES) unit to realize a different sensible heat storage system with lower thermal capacity and pressure drop [4, 12, 16].

Thermal energy storage systems for concentrated solar power (CSP) plants have featured the use of molten salt [17, 18], steam [19], and concrete [20] for sensible heat, phase change materials for latent heat [19], and reversible reactions for thermochemical storage [12, 20, 21]. The use of a packed bed of rocks as sensible heat storing material and air as heat transfer fluid was studied in [22]. This method of storage concept is incorporated in solar power plants using air as working fluid [23, 24]. Its main advantages are: (a) abundant and economical storing material; (b) applicability in a wide temperature range, with limiting temperatures given by the rock's melting point; (c) direct heat transfer between working fluid and storage material; (d) no degradation or chemical instability; (e) no safety concerns, and (f) elimination of chemicals and corrosive materials.

A packed bed storage system consists of loosely packed solid material through which the heat transport fluid is circulated. Heated fluid, usually air, flows from solar collectors into a bed of graded particles from top to bottom and thermal energy is transferred from the fluid to the particles during the charging phase. Packed bed, generally, represents the most suitable energy storage unit for air based solar systems as mentioned by Coutier and Farber [25]. During the charging phase, solar heated air is forced into the top of the container, i.e., upper plenum

and then passes evenly down through the bed heating the storage and passes out through the lower plenum. Air is drawn off at the bottom and returned to the solar collectors. When energy is needed from storage, the airflow is reversed. However, some other type of porous media such as ceramic foams or honeycomb could be employed as material in the storage unit to realize a different storage system with lower thermal capacity and pressure drop.

Several investigations describe numerical simulation models for sensible heat storage in porous media [16]. The heat transfer to and from a flowing fluid to a packed bed has been the subject of many theoretical and experimental researches since Schumann's original work [26]. A one-dimensional two-phase model for packed bed system was assumed by ignoring the thermal capacity of the fluid, axial conduction both in the fluid and in the bed material. Some elaborations were performed in [27–29] to facilitate the extraction of numerical information from the solutions by providing nomograms, extensive graphs and tabulations. Numerical simulations were carried out to solve the governing equations for the packed bed by finite difference methods [30–32]. A mathematical model to evaluate the dynamic response of a packed column to an arbitrary time dependent inlet air temperature was accomplished in [33]. Different aspects of sensible heat storage systems were analyzed in [34]. It was reported that the preference of sensible heat storage system depends upon the storage period, economical viability and operating conditions. An investigation on different energy storage techniques and materials employed in sensible heat storage systems was accomplished in [35]. A comparative numerical study on packed bed thermal models suitable for sensible and latent heat thermal storage systems was presented in [36]. Four basic groups of models were investigated and the models were compared in relation to the influence of particle size, void fraction, particle material, flow rate variations, working fluid inlet temperature variations and wall thermal losses.

A method of preserving the stratification by segmenting the storage bed was numerically studied in [37]. In fact, segmenting a standard rock bed and routing the flow to segments cooler than the inlet air during charging was shown to preserve stratification throughout the bed. An experimental investigation on heat transfer and pressure drop characteristics of packed bed solar energy storage system with large sized elements of storage material was presented in [38]. Correlations were developed for Nusselt number and friction factor as function of Reynolds number, roundness and void fraction. An extensive literature review of research work on packed bed systems was presented in [10]. The effect of multiple charge and discharge cycles was studied in detail in [39]. The amplitude of temperature fluctuation, a parameter relating to the energy storage, was seen to vary significantly with distance and time. A high temperature TES was numerically parametrically analyzed by using CFD code to solve the governing equation in porous media in transient regime [40]. High temperature TES in a packed bed of rocks was studied in [13] for air-based concentrated solar power plants. A 1-D porous medium model in local thermal non equilibrium was assumed and two-phase energy conservation equations for combined convection and conduction heat transfer were solved numerically for charging/discharging cycles. A comparison

between numerical results and their experimental data was accomplished for a packed bed of crushed steatite (magnesium silicate rock) at 800 K. A thermal energy storage system, consisting of a packed bed of rocks as storing material and air as high-temperature heat transfer fluid, was analyzed for concentrated solar power (CSP) applications in [8].

The honeycomb structure is used in many applications such as heat storage, heat regenerators, drying and cooling of electronic equipment [8, 12, 14, 41–49]. A micro-cell aluminum honeycomb employed in augmenting heat transfer in compact heat exchangers was investigated by an analytical model in [41]. For convective cooling, the overall heat transfer rate was found to be elevated by about two order of magnitudes when an open channel was designed with an aluminum honeycomb core. A two-dimensional numerical simulation model to solve fluid-dynamic and thermal problem in a composite honeycomb regenerator was developed in [42]. Dynamic temperature and velocity profiles of gases and solid heat-storing materials were carried out. The energy storage was calculated and thermal performance of honeycomb heat regenerator was evaluated at different switching times and loading. A honeycomb reactor obtained by the assembling of several cavities, in order to optimize a thermo-chemical reactor for hydrogen production or high temperature heat storage, was analyzed in [43]. A simplified method to evaluate the optimized solar thermo-chemical reactor geometry also considering radiation in the cavity and conduction inside the reactive material was proposed. A honeycomb porous microchannel cooling system for electronics cooling was proposed and experimentally investigated in [44]. The design, fabrication, and test system configuration of the microchannel heat sink were reported. The experimental results allowed to conclude that the considered cooling system is able to perform heat dissipation well. A numerical investigation on a two-dimensional model for predicting heat and mass transfer in an alanate hydride reactor with metallic honeycomb structure heat exchanger was accomplished in [45]. Heat transfer process in honeycomb ceramics systems to estimate the effects of temperature difference and hole side length on heat transfer and the resistance losses was numerically investigated in [46]. The results showed that the temperature difference between the gas and honeycomb ceramics was larger, then the heat transfer effect was better, and the resistance loss was bigger. The design and characterization of monolithic heat sinks were disclosed in [47]. The proposed heat sink geometries presented a performance enhancement relative to a conventional longitudinally finned heat sink. A multiphase transport model to simulate drying of honeycomb ceramic substrates in a conventional (hot air) drier was numerically studied in [49]. Heat and moisture transport in the honeycomb walls as well as channels were modeled. Thermal storage in a honeycomb solid matrix was numerically investigated in [50]. Moreover, ceramic foams were considered as a porous matrix in a high temperature solar thermal energy storage [51].

In the following the governing equations for porous media in Local Thermal Non-Equilibrium (LTNE) are written in cylindrical coordinate to represent a TES and three different porous matrixes are examined: packed bed with spherical

particles, foam and honeycomb with square channels. Some results are shown to compare the behaviors of the different porous matrixes employed in the thermal energy storage system.

## 2 Physical Problem Description and Governing Equations

A sensible heat thermal energy storage system can be considered as a container with inside a porous matrix. Several systems have a cylindrical form and the porous matrix can be set up by a packed bed or a honeycomb with square channels or a foam. In the following it will be examined a case study of a thermal energy storage. The physical system and geometry under investigation are shown in Fig. 3. It consists of a cylinder whose diameter is equal to 0.60 m and height is 1 m. The material storage is made of alumina or cordierite and it is analyzed in three different porous medium configurations: (a) packed bed with spherical particles, (b) ceramic foam or (c) honeycomb with transversal square section channels. The heat-carrying fluid is air. Thermo-physical properties of the materials are temperature independent. In some cases radiation heat transfer effect are taken into account. Heat losses with the external environment ( $T_{amb} = 300\text{ K}$ ) are considered by setting the surface heat transfer coefficient equal to  $5\text{ W/m}^2\text{K}$ .

In the porous medium region, the generalized flow model, known as the Brinkman-Forchheimer-extended Darcy model, is used in the governing equations. The conservation equations for mass, momentum and energy are, assuming a local thermal non equilibrium condition, [52–54]:

$$\frac{\partial \phi \rho_f u_p}{\partial t} + \phi \rho_f v_p \frac{\partial u_p}{\partial r} + \phi \rho_f u_p \frac{\partial u_p}{\partial z} = -\phi \frac{\partial p}{\partial z} + \phi \mu \left( \frac{\partial^2 u_p}{\partial r^2} + \frac{1}{r} \frac{\partial u_p}{\partial r} + \frac{\partial^2 u_p}{\partial z^2} \right) - \phi^2 \frac{\mu}{K} u_p - \phi^3 \frac{C_2 \rho_f}{2} \sqrt{u_p^2 + v_p^2} u_p \tag{1}$$

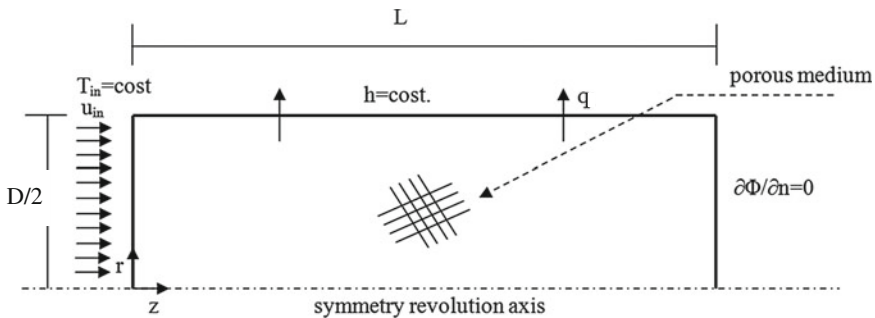


Fig. 3 Geometric configuration and physical domain

$$\begin{aligned} \frac{\partial \varphi \rho_f v_p}{\partial t} + \varphi \rho_f v_p \frac{\partial v_p}{\partial r} + \varphi \rho_f u_p \frac{\partial v_p}{\partial z} = & -\varphi \frac{\partial p}{\partial r} + \varphi \mu \left( \frac{\partial^2 v_p}{\partial r^2} + \frac{1}{r} \frac{\partial v_p}{\partial r} - \frac{v_p}{r^2} + \frac{\partial^2 v_p}{\partial z^2} \right) \\ & - \varphi^2 \frac{\mu}{K} v_p - \varphi^3 \frac{C_2 \rho_f}{2} \sqrt{u_p^2 + v_p^2} v_p \end{aligned} \quad (2)$$

$$\begin{aligned} \varphi(\rho c_p)_f \frac{\partial T_f}{\partial t} + \varphi(\rho c_p)_f \left( v_p \frac{\partial T_f}{\partial r} + u_p \frac{\partial T_f}{\partial z} \right) = & \\ \varphi k_f \left( \frac{\partial^2 T_f}{\partial r^2} + \frac{1}{r} \frac{\partial T_f}{\partial r} + \frac{\partial^2 T_f}{\partial z^2} \right) - h_{sf} a_{sf} (T_s - T_f) & \end{aligned} \quad (3)$$

$$(1 - \varphi)(\rho c)_s \frac{\partial T_s}{\partial t} = (1 - \varphi) k_s \left( \frac{\partial^2 T_s}{\partial r^2} + \frac{1}{r} \frac{\partial T_s}{\partial r} + \frac{\partial^2 T_s}{\partial z^2} \right) + h_{sf} a_{sf} (T_s - T_f) \quad (4)$$

where  $C_2 = 2 CK^{-0.5}$ .

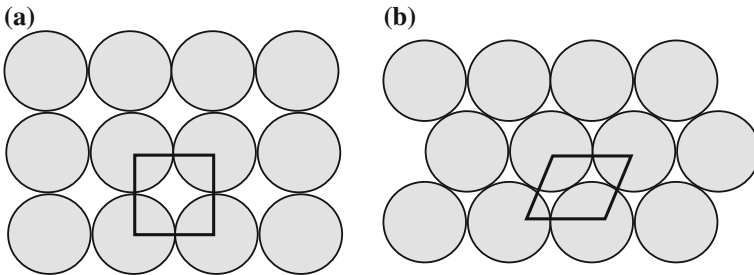
The permeability  $K$  and inertia coefficient  $C$  of porous medium depend on the porous matrix. The term  $h_{sf} a_{sf}$  is present due to the local thermal non-equilibrium assumption and it is related with the local convective heat transfer inside the porous medium between the fluid and the solid porous matrix surfaces.

The packing of sand is best illustrated by showing the packing of uniform spheres that gives the maximum and minimum porosity, Fig. 4. The cubic packing of spheres, or in line configuration, has a porosity equal to 0.48 whereas for rhombohedral packing, or staggered configuration, the porosity is 0.26. Random packing will result in a porosity of about 0.4.

The permeability coefficient  $K$  and inertia coefficient  $C$  of porous medium, in packed bed configuration are based on these two relations [54]:

$$K = \frac{d_p^2 \varphi^3}{175(1 - \varphi)^2}, \quad C = \frac{1.75}{\sqrt{150} \varphi^{1.5}}. \quad (5)$$

The convective heat transfer coefficient and the interface area per volume of packed bed [55, 56] are based on these two relations:



**Fig. 4** Packed bed with spherical particles: **a** cubic packing, **b** rhombohedral packing



$$h_{sf} = \frac{k_f(2 + 1.1 \text{Pr}^{1/3} \text{Re}_p^{0.6})}{d_p}; \quad a_{sf} = \frac{6(1 - \varphi)}{d_p} \quad (6)$$

with

$$\text{Re}_p = \frac{|v|d_p}{\nu} \quad (7)$$

For ceramic foams permeability, inertia coefficient, convective heat transfer coefficient and interface area per volume of foams are evaluated by relations given in [53, 57]. Photographs of typical foam samples are shown in Fig. 5.

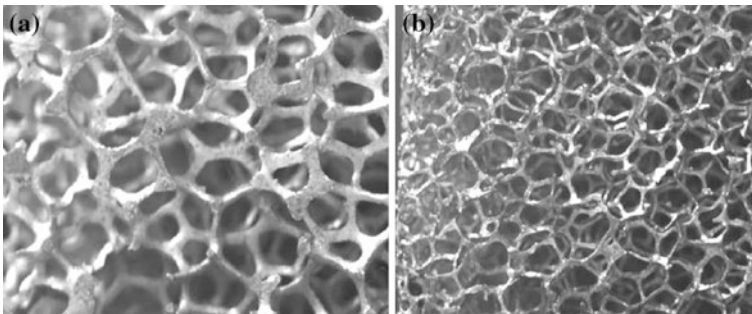
The radiative heat transfer was taken into account in the case of ceramic foams considering an effective thermal conductivity for the porous matrix which takes into account both heat conduction and thermal radiation as given in [58].

The permeability,  $K$ , and porosity,  $\varphi$ , of the considered porous medium, in honeycomb configuration, Fig. 6, are based on the following relations [55, 57].

$$K = \frac{H^4}{32(H + s)^2}; \quad \varphi = \frac{H^2}{(H + s)^2} \quad (8)$$

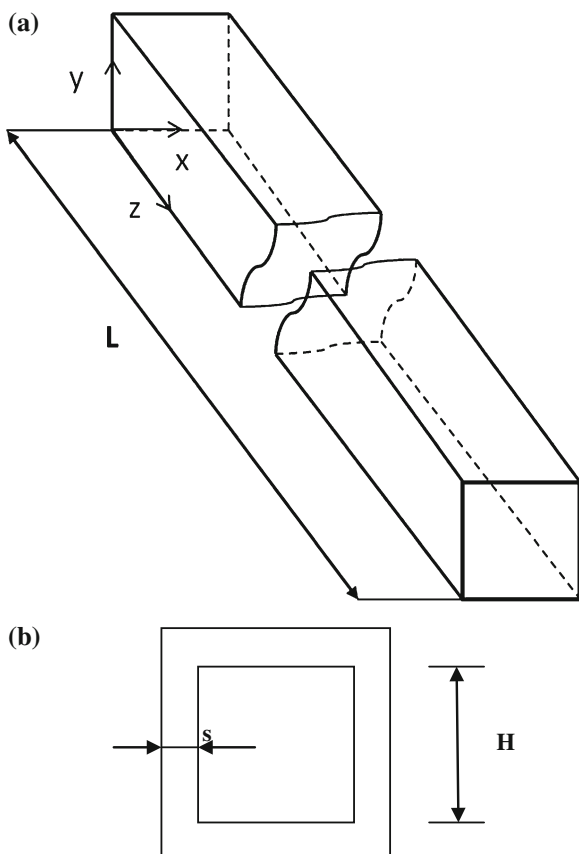
where, with reference to Fig. 6,  $H$  is the width or height of the cross section of the single channel,  $s$  is the channel thickness where the thickness and the inlet section of single channel varies with the porosity. In Table 1 are given some thermo-physical properties.

Convective heat transfer coefficient,  $h_{sf}$ , and interface area per volume,  $a_{sf}$ , have been evaluated numerically for single channel by means of a 3-dimensional convective steady state problem. The effect of radiative heat transfer is evaluated for the single channel and it is reported in terms of a surface heat transfer coefficient. This value is added to the convective heat transfer coefficient and employed in the evaluation of  $h_{sf}a_{sf}$  coefficient. The evaluated heat transfer coefficients are summarized in Table 2 both without and with radiative heat transfer.



**Fig. 5** Foam samples: **a** 5 PPI; **b** 40 PPI

**Fig. 6** Honeycombs configuration: **a** channel, **b** square transversal section



**Table 1** Thermophysical properties of cordierite

$\rho$ [kg/m <sup>3</sup> ]	$c$ [J/kg K]	$k$ [W/m K]
2,300	900	2.5

**Table 2** Heat transfer coefficients

Porosity, $\varphi$	$h$ [W/m <sup>2</sup> K] without radiation	$h$ [W/m <sup>2</sup> K] with radiation $\varepsilon = 0.9$
0.9	39.6	48.5
0.3	35.2	45.5
0.1	29.0	33.1

Different charging-discharging cycles are considered. In the charging phase the gas enters at 1,473 K whereas in discharging phase it enters countercurrent at 1,073 K. The charge, in the first cycle, starts with the heat storage system temperature set at 300 K and, in some cases ends when 90 % of maximum storable

energy, in this cycle, is reached. Then the discharging phase starts and the cycle ends when the outlet gas temperature reaches 1,173 K. The same criteria are utilized in the second cycle that starts with the heat storage system temperature set at 1,073 K.

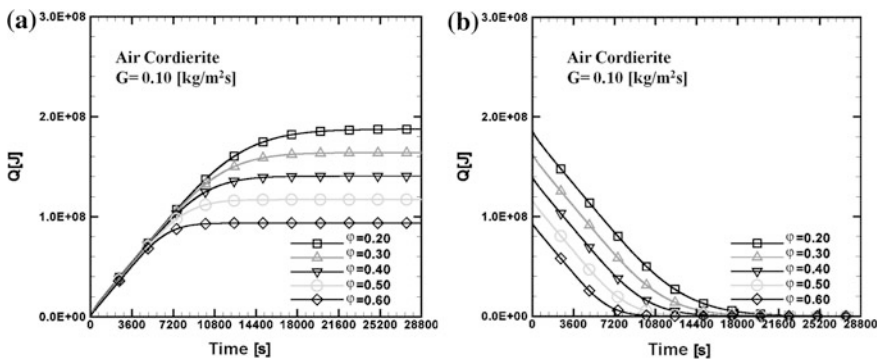
### 3 Results

First results are presented for storage obtained by a porous medium. Two different porous media are considered: spheres or foams. In all cases a ceramic material is considered. For packed bed configuration, the results are presented in terms of stored energy profiles for cordierite spheres. Five porosity values are analyzed in ranging from 0.2 to 0.6, mass flow per unit cross section,  $G$ , inlet has values equal 0.1, 0.2, and 0.3  $\text{kg/m}^2\text{s}$  for all cases.

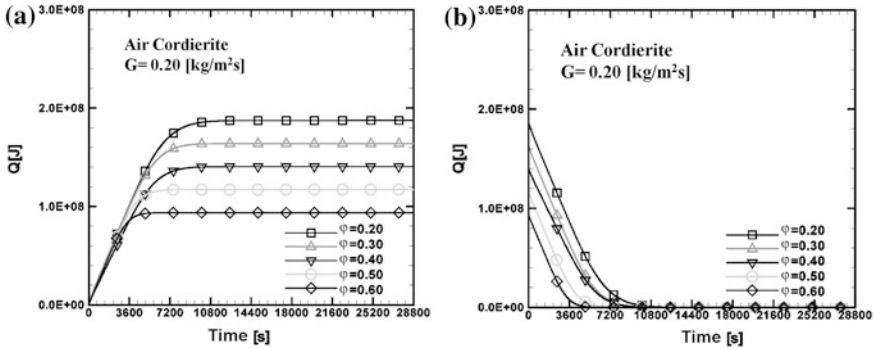
In Fig. 7, energy stored is reported as a function of time, for  $\varepsilon$  values in the range from 0.2 to 0.6 and  $G$  equal to 0.1  $\text{kg/m}^2\text{s}$ , for charge and discharge cycles. Decreasing the porosity the charging and discharging time increases due to the thermal capacity increase. Increasing the porosity value steady state conditions are reached at lower time both in charging and discharging phases.

In Figs. 8 and 9, stored thermal energy as a function of time is depicted for mass flow per unit cross section equal to 0.2 and 0.3  $\text{kg/m}^2\text{s}$ . It is noted that the steady state is attained at lower time value due to a more efficient convective heat transfer between the fluid and the solid matrix. However, increasing the mass flow rate the energy level, in the case with adiabatic external surface of the storage, any variation in the energy stored values is detected. In this case, the main result is that charging and discharging times decrease as the mass flow rate increases.

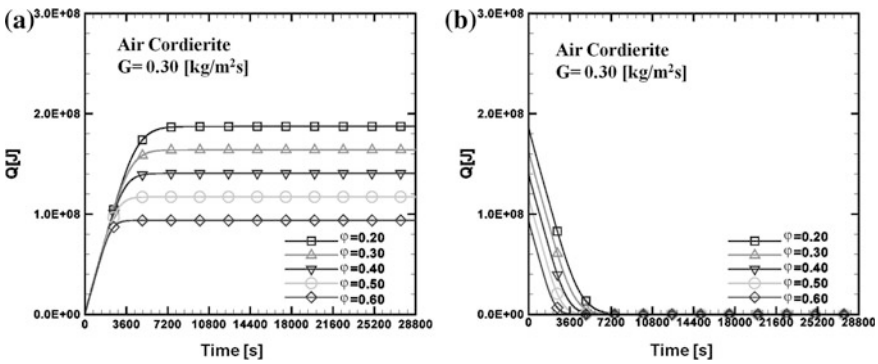
Also for ceramic foam configuration, the results are presented in terms of energy stored profiles.



**Fig. 7** Energy stored for several porosity values and  $G$  equal to 0.10  $\text{kg/m}^2\text{s}$ : **a** charge cycle, **b** discharge cycle



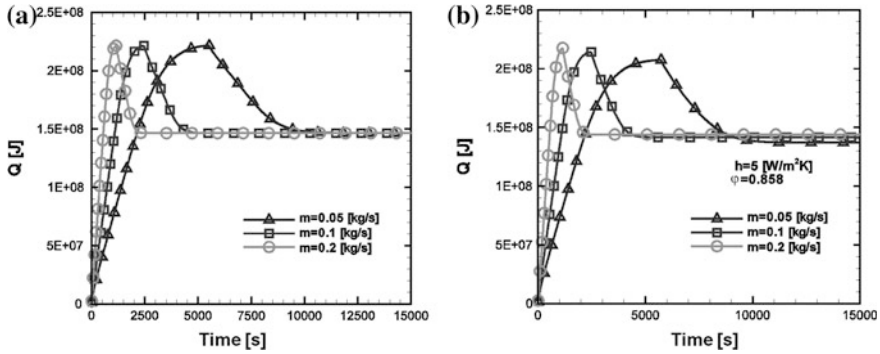
**Fig. 8** Energy stored for several porosity values and  $G$  equal to  $0.20$  kg/m<sup>2</sup>s: **a** charge cycle, **b** discharge cycle



**Fig. 9** Energy stored for several porosity values and  $G$  equal to  $0.30$  kg/m<sup>2</sup>s: **a** charge cycle, **b** discharge cycle

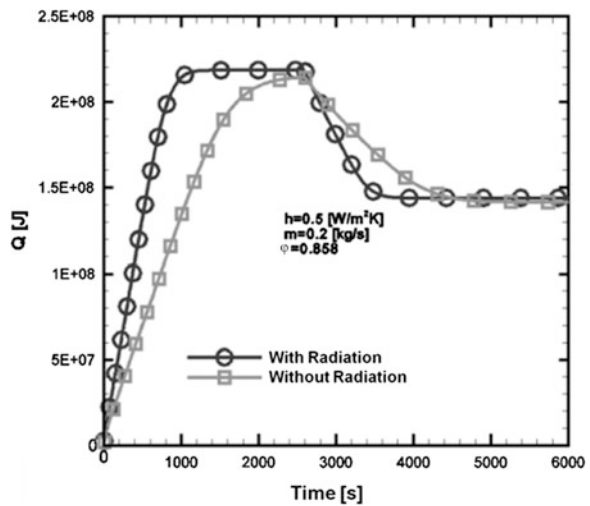
Alumina foam with porosity equal to 0.858 and 20 PPI is investigated. For charge phase the initial temperature of solid is equal to 300 K while at inlet the temperature is equal to 1,473 K. In the discharge phase the air has the inlet section opposite at the one in the charge phase and the inlet temperature is 1,073 K. In this configuration also the effect of heat transfer losses is analyzed. For all studied configurations, the heat transfer coefficient on the external surface of cylinder is assumed equal to  $5$  W/m<sup>2</sup>K. Three different mass flow rates are analyzed and they are equal to 0.050, 0.10 and 0.20 kg/s. For mass flow rate equal to 0.20 kg/s also the case with radiative heat transfer is analyzed.

Figure 10 shows stored energy profiles as a function of time for adiabatic and with heat losses cases. When mass flow per unit cross section increases charging and discharging times decrease. Steady state conditions are reached in any case. It is noticed that for the cases with heat transfer losses with an external heat transfer coefficient equal to  $5.0$  W/m<sup>2</sup>K, the energy stored value is lower than the adiabatic



**Fig. 10** Energy stored for several mass flow rate values and porosity equal to 0.858: **a** adiabatic case, **b**  $h = 5 \text{ W/m}^2 \text{ K}$

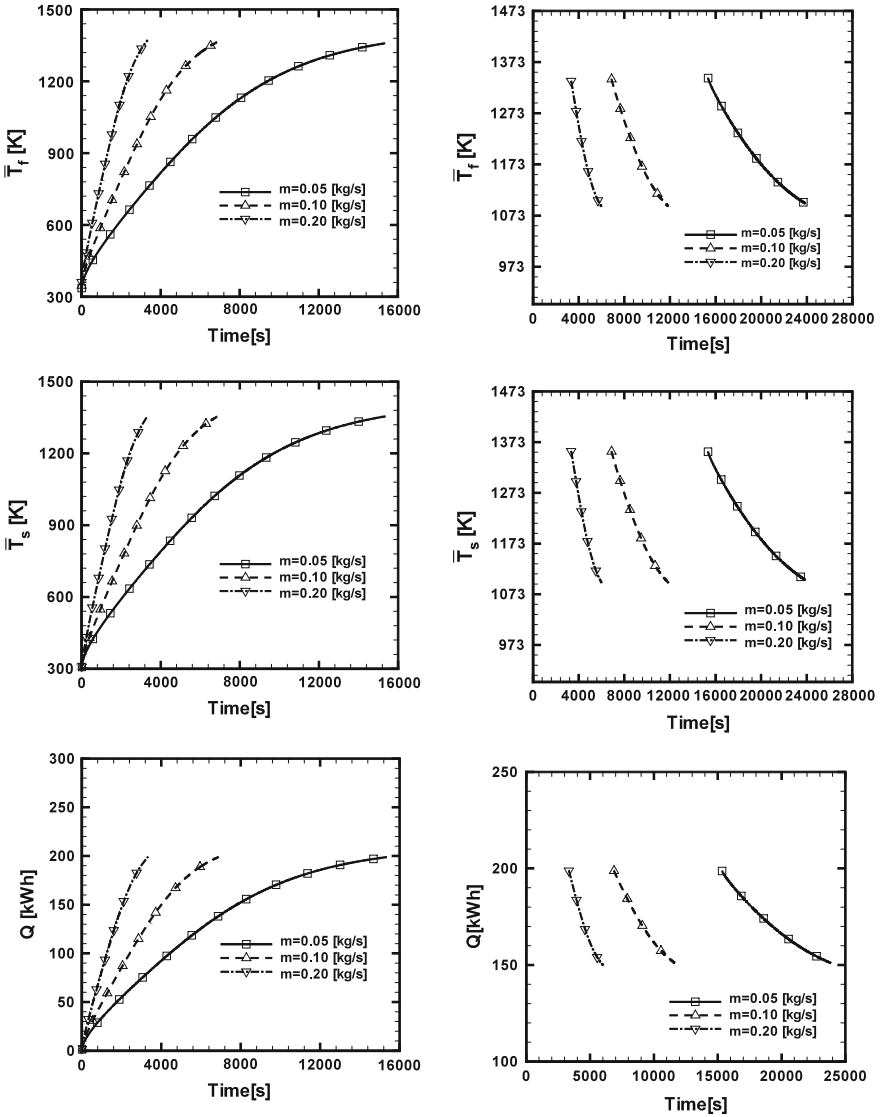
**Fig. 11** Energy stored for mass flow rate value equal to 0.2 kg/s and porosity equal to 0.858 with and without radiative heat transfer



ones. In Fig. 11 the effect of radiation heat transfer mechanism is showed. The stored energy stored are the same for both configurations studied, but for configuration with radiation heat transfer charging and discharging time decrease.

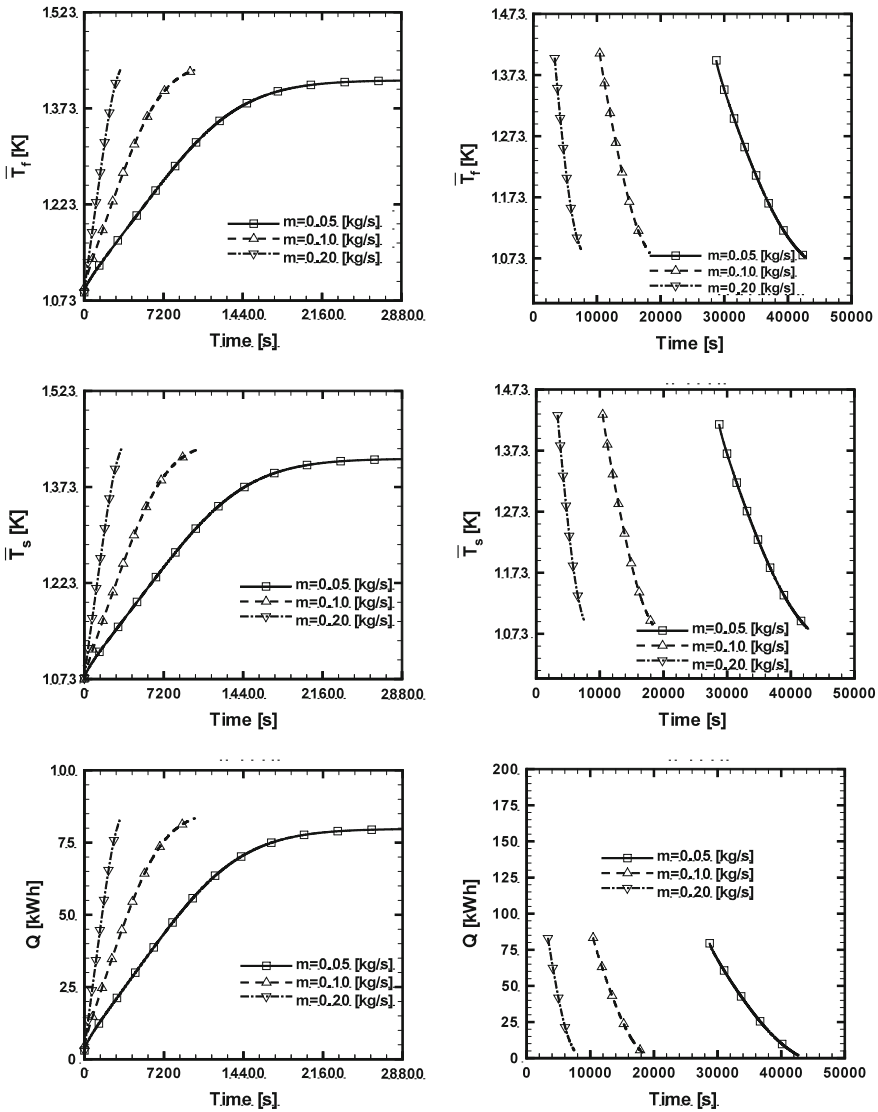
In the following results are presented for porosity equal to 0.395, spheres diameter equal to 0.010, 0.025, and 0.040 m. Mass flow inlet has values equal to 0.05, 0.10, and 0.20 kg/s for all cases.

In Fig. 12 thermal energy stored, volumetric fluid and solid average temperature are shown as function of time, for  $\phi = 0.395$  and  $d_p = 0.025 \text{ m}$ , for the first cycle. At the increase of mass flow rate, charging and discharging time decrease. Regime condition is not reached for any case. The stored thermal energy is 200 and 50 kWh are released during the discharge phase as quickly as the mass flow rate increases.



**Fig. 12** Thermal energy stored, volumetric fluid and solid average temperature for  $\varphi = 0.395$ ,  $d_p = 0.025$  m, first cycle

In Fig. 13 thermal energy stored, volumetric fluid and solid average temperature are shown as function of time, for  $\varphi = 0.395$ ,  $d_p = 0.025$  m, for the second cycle. At the increase of mass flow rate, charging and discharging time decrease. Charging and discharging time increase compared to the first cycle. Regime condition is reached only for mass flow rate equal to 0.05 kg/s during the charging

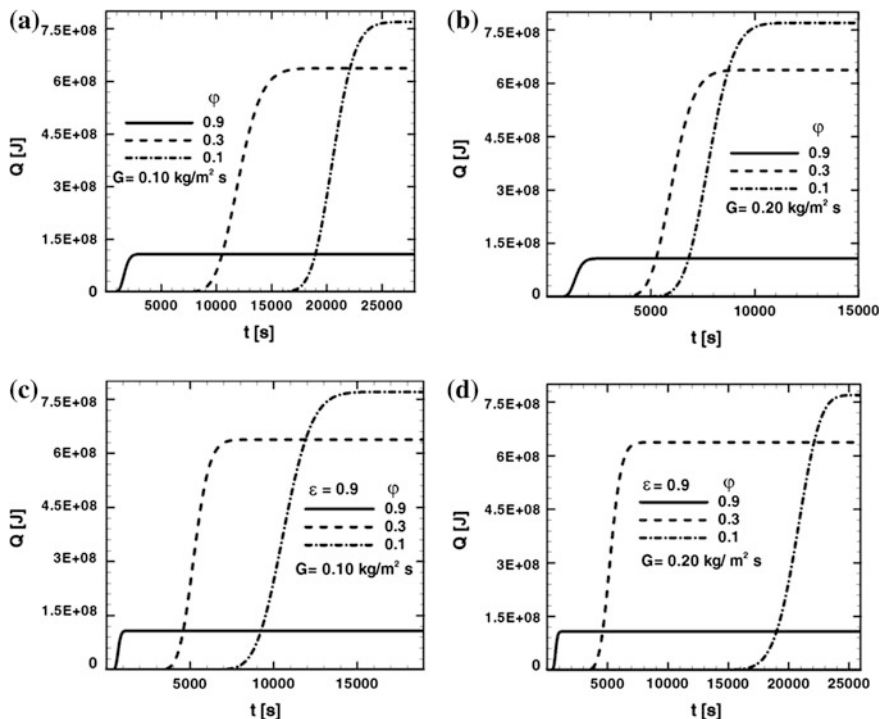


**Fig. 13** Thermal energy stored, volumetric fluid and solid average temperature for  $\epsilon = 0.395$ ,  $d_p = 0.025$  m, second cycle

phase. The energy stored value is lower than that corresponding to the stop rate, charging and discharging time decrease. The energy stored value is lower than that corresponding to the stop value. The stored thermal energy is 80 kWh for mass flow rate equal to 0.05 kg/s and is 85 kWh for  $m = 0.10$  kg/s and for  $m = 0.20$  kg/s. This energy is completely released during the discharge phase as quickly as the mass flow rate increases.

**Table 3** Second-law efficiency for packed bed configuration  $\phi = 0.395$

	I cycle			II cycle		
	Mass flow rate [kg/s]			Mass flow rate [kg/s]		
Sphere diameter [m]	0.05	0.10	0.20	0.05	0.10	0.20
0.010	0.126	0.198	0.246	0.050	0.309	0.434
0.025	0.120	0.187	0.200	0.085	0.171	0.391
0.040	0.113	0.150	0.163	0.065	0.124	0.228



**Fig. 14** Stored energy for different porosity values and mass flow;  $G = \mathbf{a}$   $0.1 \text{ kg/m}^2\text{s}$  and without radiation effect;  $\mathbf{b}$   $0.2 \text{ kg/m}^2\text{s}$  and without radiation effect;  $\mathbf{c}$   $0.1 \text{ kg/m}^2\text{s}$  and  $\epsilon = 0.9$ ;  $\mathbf{d}$   $0.2 \text{ kg/m}^2\text{s}$  and  $\epsilon = 0.9$

In Table 3, second-law efficiency of analyzed TES [59], in packed bed configuration is shown. It is noted that TES efficiency decreases increasing  $d_p$  and decreasing mass flow rate. II Cycle TES efficiency values are, generally, higher than the I Cycle ones. In this cycle only for mass flow rate equal to  $0.05 \text{ kg/s}$  TES efficiency values are less than the corresponding values of the first cycle. This is due to the system impossibility to reach stop condition in the charging phase.



**Table 4** Energy stored values

$\varphi$	Q [J]
0.9	$1.2 \times 10^8$
0.3	$6.4 \times 10^8$
0.1	$7.7 \times 10^8$

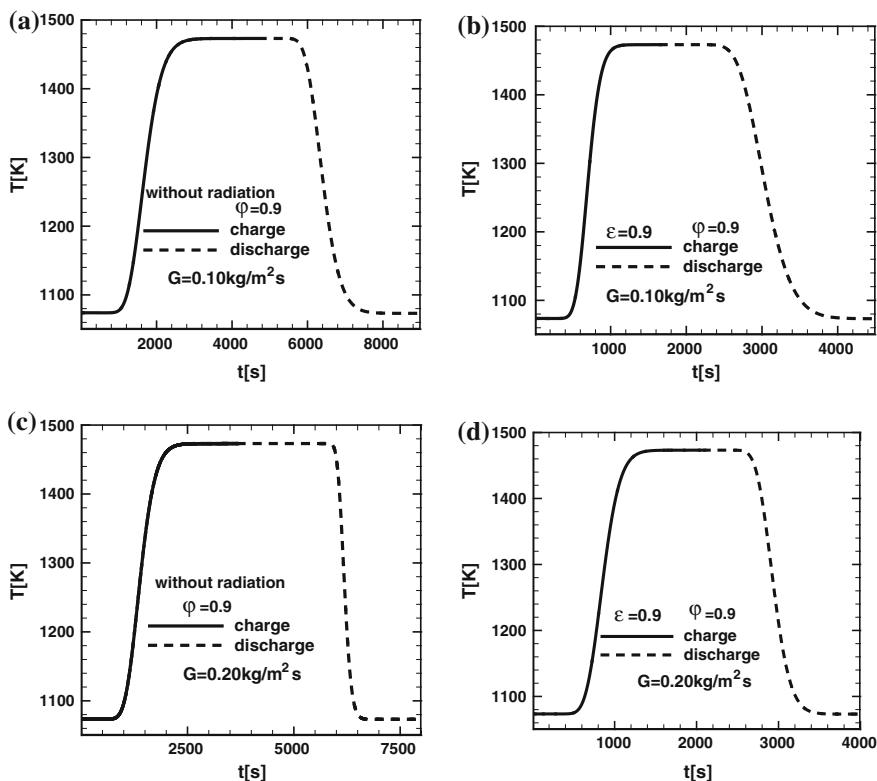
For the Honeycomb solid matrix results are presented in terms of thermal energy stored. Two different mass velocity,  $G$ , equal to 0.1 and 0.2  $\text{kg/m}^2\text{s}$  are studied for three porosities equal to 0.1, 0.3 and 0.9, the effects of radiation are taken into account for all configurations studied, the emissivity is set equal to 0.9. The analysis takes into account the outlet section to evaluate the charging time i.e., the time at which the outlet section reaches the inlet fluid temperature and the steady state is reached.

Figure 14a and b show stored thermal energy as a function of time for assigned porosity values equal to 0.9, 0.3 and 0.1, and mass flow values equal to 0.1 and 0.2  $\text{kg/m}^2\text{ s}$ , without radiation heat transfer effects. Decreasing the porosity the charging time increases due to the thermal capacity increase. Increasing the porosity value steady state conditions are reached at lower time for the charging phase. However, increasing the mass flow rate any variation in the stored energy values is detected. As expected, for assigned mass flow rate, the porosity value determines also the stored energy level whereas, for assigned porosity, the mass velocity or the mass flow rate affects the charging time of the system.

In Fig. 14c and d the radiative effects on stored thermal energy are observed. In fact, considering radiation heat transfer, any variation in stored energy values is detected but the charging time decreases.

The stored energy values at steady state condition are summarized in Table 4. It is observed that an increase of the stored energy of about 5 times is obtained passing from the porosity value equal to 0.9 to a value of 0.3 whereas passing from 0.9 to 0.1 the increase is about 6.4 times.

Figure 15 depicts the temperature behavior for charge and discharge cycle for a porosity equal to 0.9, mass flow rate per unit section area equal to 0.1 and 0.2 with and without radiation effect. The charging and discharging times decrease increasing the mass flow rate. The presence of radiative heat transfer in the porous medium determines a decrease in charging and discharging times. At decreasing of porosity charge and discharge times increase, according to the previous presented results.



**Fig. 15** Temperature profiles for porosity equal to 0.9 and **a**  $G = 0.1 \text{ kg/m}^2\text{s}$ ; **b**  $G = 0.1 \text{ kg/m}^2\text{s}$  and  $\varepsilon = 0.9$  **c**  $G = 0.2 \text{ kg/m}^2\text{s}$ ; **d**  $G = 0.2 \text{ kg/m}^2\text{s}$  and  $\varepsilon = 0.9$

## 4 Conclusions

Thermal behavior of high temperature sensible heat thermal energy storage system with different solid matrixes in cylindrical container was analyzed. The governing equations were written employing the Brinkman-Forchheimer-Darcy model in local thermal non equilibrium. The study was performed in the charge and discharge phases, analyzing the effect of packed bed with ceramic spherical particles, ceramic foams and honeycomb structure with square transversal section channels. Results in terms of temperature profiles of outlet section as a function of time allowed to determine the effects of porosity, mass flow rate and the radiation on the complete charge and discharge time. The heat losses and the presence of radiative heat transfer in porous medium determined an increase in charge and discharge times. The main effect was due to the porosity which determined also the thermal energy storage value. An optimal porosity value could be evaluated taking into account also the pressure drop and the viscous dissipation inside the system.

**Acknowledgments** This work was supported by MIUR with Art. 12 D. M. 593/2000 Grandi Laboratori “EliosLab” and grant PRIN-2009KSSKL3.

## References

1. Dell, R., Rand, D.: Energy storage—a key technology for global energy sustainability. *J. Power Sources* **100**, 2–17 (2001)
2. Dincer, I., Rosen, M.: *Thermal energy storage: System and application*. Wiley, New York (2002)
3. Beckmann, G., Gilli, P.V.: *Thermal energy storage: Basics, design applications to power generation and heat supply*. Springer, Heidelberg (2002)
4. Paksoy, H.Ö.: *Thermal energy storage for sustainable energy consumption: Fundamentals case studies and design*. Springer, Heidelberg (2007)
5. Arteconi, A., Hewitt, N.J., Polonara, F.: State of the art of thermal storage for demand-side management. *Appl. Energy* **93**, 371–389 (2012)
6. Oró, E., Gil, A., de Gracia, A., Boer, D., Cabeza, L.F.: Comparative life cycle assessment of thermal energy storage systems for solar power plants. *Renew. Energy* **44**, 166–173 (2012)
7. Lia, P., Van Lew, J., Chan, C., Karaki, W., Stephens, J., O’Brien, J.E.: Similarity and generalized analysis of efficiencies of thermal energy storage systems. *Renew. Energy* **39**, 388–402 (2012)
8. Zanganeh, G., Pedretti, A., Zavattoni, S., Barbato, M., Steinfeld, A.: Packed-bed thermal storage for concentrated solar power—pilot-scale demonstration and industrial-scale design. *Sol. Energy* **86**, 3084–3098 (2012)
9. Calvet, N., Gomez, J.C., Faik, A., Roddatis, V.V., Meffre, A., Glatzmaier, G.C., Doppiu, S., Py, X.: Compatibility of a post-industrial ceramic with nitrate molten salts for use as filler material in a thermocline storage system. *Appl. Energy* <http://dx.doi.org/10.1016/j.apenergy.2012.12.078> (2013)
10. Singh, H., Saini, R.P., Saini, J.S.: A review on packed bed solar energy storage systems. *Renew. Sust. Energy Rev.* **14**, 1059–1069 (2010)
11. Sharma, A., Tyagi, V.V., Chen, C.R., Buddhi, D.: Review on thermal energy storage with phase change materials and applications. *Renew. Sust. Energy. Rev.* **13**, 318–345 (2009)
12. Gil, A., Medrano, M., Martorell, I., Lazaro, A., Dolado, P., Zalba, B., Cabeza, L.: State of the art on high temperature thermal energy storage for power generation. Part1—concepts, materials, and modellization. *Renew. Sust. Energy Rev.* **14**, 31–55 (2010)
13. Hänchen, M., Brückner, S., Steinfeld, A.: High-temperature thermal storage using a packed bed of rocks—heat transfer analysis and experimental validation. *Appl. Thermal Eng.* **31**, 1798–1806 (2011)
14. Powell, K.M., Edgar, T.F.: Modeling and control of a solar thermal power plant with thermal energy storage. *Chem. Eng. Sci.* **71**, 138–145 (2012)
15. Liu, M., Saman, W., Bruno, F.: Review on storage materials and thermal performance enhancement techniques for high temperature phase change thermal storage systems. *Renew. Sust. Energy Rev.* **16**, 2118–2132 (2012)
16. Fernandes, D., Pitié, F., Cáceres, G., Baeyens, J.: Thermal energy storage: “How previous findings determine current research priorities”. *Energy* **39**, 246–257 (2012)
17. DeLaquil, P., Kelly, B., Lessley, R.: Solar one conversion project. *Sol. Energy Mater.* **24**, 151–161 (1991)
18. Herrmann, U., Kearney, D.W.: Survey of thermal energy storage for parabolic trough power plants. *ASME J. Sol. Energy Eng.* **124**, 145–152 (2002)
19. Steinmann, W.D., Eck, M.: Buffer storage for direct steam generation. *Sol. Energy* **80**, 1277–1282 (2006)

20. Tamme, R., Laing, D., Steinmann, W.D.: Advanced thermal energy storage technology for parabolic trough. *ASME J. Sol. Energy Eng.* **126**, 794–800 (2004)
21. Watanabe, T., Kikuchi, H., Kanzawa, A.: Enhancement of charging and discharging rates in a latent heat storage system by use of PCM with different melting temperatures. *Heat Rec. Syst. CHP* **13**, 57–66 (1993)
22. Lovegrove, K., Luzzi, A., Soldiani, I., Kreetz, H.: Developing ammonia based thermochemical energy storage for dish power plants. *Sol. Energy* **76**, 331–337 (2004)
23. Meier, A., Winkler, C., Wuillemin, D.: Experiment for modelling high temperature rock bed storage. *Sol. Energy Mater.* **24**, 255–264 (1991)
24. Bader, R., Pedretti, A., Steinfeld, A.: A 9-m-aperture solar parabolic trough concentrator based on a multilayer polymer mirror membrane mounted on a concrete structure. *ASME J. Sol. Energy Eng.* **133**, 031016 (2011)
25. Coutier, J.P., Farber, E.A.: Two applications of a numerical approach of heat transfer process within rock beds. *Sol. Energy* **29**, 451–462 (1982)
26. Schumann, T.E.W.: A liquid flowing through a porous prism. *J. Franklin Inst.* **28**, 405–416 (1929)
27. Klinkenberg, A.: Numerical evaluation of equations describing transient heat and mass transfer in packed solids. *Ind. Eng. Chem.* **40**, 1992–1994 (1948)
28. Ledoux, E.: Dynamic cooling at absorbent beds. *Ind. Eng. Chem.* **40**, 1970–1975 (1948)
29. Larsen, F.W.: Rapid calculation of temperature in a regenerative exchanger having arbitrary initial solid and fluid temperatures. *Int. J. Heat Mass Transfer* **10**, 149–168 (1967)
30. Duffie, J.A., Beckman, W.A.: *Solar energy thermal processes*. Wiley, New York (1974)
31. Klein, S.A.: Mathematical models at thermal storage. *Proceedings of solar energy storage subsystems for the heating and cooling of building*, pp. 119–128 (1975)
32. Mumma, S.A., Marvin W.C.: A method of simulating the performance of a pebble bed thermal energy storage and recovery system. ASME-AICHE heat transfer conference 1986, St. Louis, paper 76 -HT-73 (1976)
33. Saez, A.E., McCoy, B.J.: Dynamic response of a packed bed thermal storage system—a model for solar air heating. *Sol. Energy* **29**, 201–206 (1982)
34. Dincer, I., Dost, S., Li, X.: Performance analysis of sensible heat storage systems for thermal applications. *Int. J. Energy Res.* **21**, 1171–1257 (1997)
35. Fath, H.E.: Technical assessment of solar thermal energy storage technologies. *Renew. Energy* **14**, 35–40 (1998)
36. Ismail, K.A.R., Stuginsky Jr, R.: A parametric study on possible fixed bed models for PCM and sensible heat storage. *Appl. Thermal Eng.* **19**, 757–788 (1999)
37. Crandall, D., Thacher, E.: Segmented thermal storage. *Sol. Energy* **77**, 435–440 (2004)
38. Singh, R., Saini, R.P., Saini, J.S.: Nusselt number and friction factor correlations for packed bed solar energy storage system having large sized elements of different shapes. *Sol. Energy* **80**, 760–771 (2006)
39. Singh, C., Tathgir, R.G., Muralidhar, K.: Energy storage in fluid saturated porous media subjected to oscillatory flow. *Heat Mass Transfer* **45**, 427–441 (2009)
40. Andreozzi, A., Buonomo, B., Dongiacomo, V., Manca, O., Mesolella P.: Numerical analysis on different sensible thermal energy storage component in high temperature solar systems. *Proceedings of heat-SET conference on heat transfer in components and systems for sustainable energy technologies*, pp. 21–29, Opatija, Croatia, Edition GRETh, France, 20–21 Oct 2010
41. Lu, T.J.: Heat transfer efficiency of metal honeycombs. *Int. J. Heat Mass Transfer* **42**, 2031–2040 (1998)
42. Rafidi, N., Blasiak, W.: Thermal performance analysis on a two composite material honeycomb heat regenerators used for HiTAC burners. *App. Thermal Eng.* **25**, 2966–2982 (2005)
43. Tescari, S., Neveu, P., Mazet, N.: Thermochemical solar reactor: Simplified method for the geometrical optimization at a given incident flux. *Int. J. Chem. Reactor Eng.* **8**, art. no. A24 (2010)

44. Luo, X., Liu, Y., Liu, W.: A honeycomb microchannel cooling system for microelectronics cooling. *Heat Transfer Eng.* **32**, 616–623 (2011)
45. Bhourri, M., Goyette, J., Hardy, B.J., Anton, D.L.: Honeycomb metallic structure for improving heat exchange in hydrogen storage system. *Int. J. Hydrogen Energy* **36**, 6723–6738 (2011)
46. Liu, Y., Chen, X., Liu, R.: Numerical simulation of heat transfer and gas flow characteristics in honeycomb ceramics. *Adv. Mat. Res.* **156–157**, 984–987 (2011)
47. Krishnan, S., Hernon, D., Hodes, M., Mullins, J., Lyons, A.M.: Design of complex structured monolithic heat sinks for enhanced air cooling. *IEEE Trans. Comp. Packag. Manuf. Tech.* **2**(6111210), 266–277 (2012)
48. Han, X.H., Wang, Q., Park, Y.G., T'Joen, C., Sommers, A., Jacobi, A.: A review of metal foam and metal matrix composites for heat exchangers and heat sinks. *Heat Transfer Eng.* **33**, 991–1009 (2012)
49. Dhall, A., Squier, G., Geremew, M., Wood, W.A., George, J., Datta, A.K.: Modeling of multiphase transport during drying of honeycomb ceramic substrates. *Drying Tech.* **30**, 607–618 (2012)
50. Andreozzi, A., Buonomo, B., Manca, O., Tamburrino, S.: Thermal energy storages analysis for high temperature in air solar systems, submitted to *ASME J. Sol. Energy Eng.* (2013)
51. Andreozzi, A., Buonomo, B., Manca, O., Mesoella, P., Tamburrino, S.: Numerical investigation on sensible thermal energy storage with porous media for high temperature solar systems. *J. Physics: Conf. Series* **395**, paper no. 012150, doi:[10.1088/1742-6596/395/1/012150](https://doi.org/10.1088/1742-6596/395/1/012150) (2012)
52. Vafai, K.: *Handbook of Porous Media*. Marcel Dekker, New York (2000)
53. Jeng, T.M., Tzeng, S.C.: Numerical study of confined slot jet impinging on porous metallic foam heat sink. *Int. J. Heat Mass Transfer* **48**, 4685–4694 (2005)
54. Vafai, K.: Convective flow and heat transfer in variable-porosity media. *J. Fluid Mech.* **147**, 233–259 (1984)
55. Dullien, F.A.L.: *Porous Media Fluid Transport and Pore Structure*. Academic, San Diego (1979)
56. Vafai, K., Sozen, M.: Analysis of energy and momentum transport for fluid flow through a porous bed. *ASME J. Heat Transfer* **112**, 690–699 (1990)
57. Moreira, E.A., Innocentini, M.D.M., Coury, J.R.: Permeability of ceramic foams to compressible and incompressible flow. *J. Eur. Ceram. Soc.* **24**, 3209–3218 (2004)
58. Zhao, C.Y., Tassou, S.A., Lu, T.J.: Analytical considerations of thermal radiation in cellular metal foams with open cells. *Int. J. Heat Mass Transfer* **51**, 929–940 (2008)
59. Adebisi, G.A., Hodge, B.K., Steele, W.G., Jalalzadeh-Aza, A., Nsofor, E.C.: Computer simulation of a high-temperature thermal energy storage system employing multiple families of phase change storage material. *ASME J. Energy Res. Tech.* **118**, 102–111 (1996)

# Recycling Polyurethane Foam and its Use as Filler in Renovation Mortar with Thermal Insulating Effect

V. Václavík, T. Dvorský, V. Dirner, J. Daxner, J. Valíček,  
M. Harničárová, M. Kušnerová, P. Košťal and M. Bendová

**Abstract** Renovation mortars with thermal insulating effect are characterized by thermal conductivity  $\lambda$ , within the range from 0.060 to 0.200 W·m<sup>-2</sup>·K<sup>-1</sup>. To achieve such low values of thermal conductivity coefficient of composite mortar, it

---

V. Václavík (✉) · T. Dvorský · V. Dirner · M. Bendová

Department of Mining and Geology, Institute of Environmental Engineering, Institute of Clean Technologies for Mining and Utilization of Raw Materials for Engineers Use, VŠB—Technical University of Ostrava, 17 Listopadu, Ostrava—Poruba 708 33, Czech Republic  
e-mail: vojtech.vaclavik@vsb.cz

T. Dvorský

e-mail: tomas.dvorsky@vsb.cz

V. Dirner

e-mail: vojtech.dirner@vsb.cz

M. Bendová

e-mail: miroslava.bendova@vsb.cz

J. Daxner

Pórobeton Ostrava a.s., Třebovická 5543/36, Ostrava—Třebovice 722 02, Czech Republic  
e-mail: daxner@email.cz

J. Valíček · M. Kušnerová

Department of Mining and Geology, Institute of Physics, VŠB—Technical University of Ostrava, 17 listopadu, Ostrava—Poruba 708 33, Czech Republic  
e-mail: jan.valicek@vsb.cz

M. Kušnerová

e-mail: milena.kusnerova@vsb.cz

M. Harničárová

Nanotechnology Centre, VŠB—Technical University of Ostrava, 17. Listopadu 15/2172, Ostrava—Poruba 708 33, Czech Republic  
e-mail: marta.harnicarova@vsb.cz

P. Košťal

Department of Metallurgy and Materials Engineering, VŠB—Technical University of Ostrava, 17. Listopadu 15/2172, Ostrava—Poruba 708 33, Czech Republic  
e-mail: pavol.kostial@vsb.cz

is essential that the structure of this composite contains a sufficient percentage of pores filled with air and has a low volume weight. Lightweight fillers, mostly crushed or crumbled polystyrene, expanded clays, expanded obsidian or volcanic glasses, for example perlite or vermiculite, are used to achieve this effect. The article presents the results of the basic research, where polyurethane foam at the end of its life cycle, in the form of crushed polyurethane with a maximum grain size of 4 mm, is used as new filler for renovation mortars with thermal insulating effect. It describes the current methods of recycling polyurethane foam, the physical and mechanical properties of experimental mixtures of renovation mortar with thermal insulating effect and the method of its application to masonry. This is a new way of utilization of polyurethane foam at the end of its life cycle in the segment of renovation mortars with thermal insulating effect.

**Keywords** Recycling · Polyurethane foam · Filler · Renovation mortar with thermal insulating effect · Physical and mechanical properties · Application

## 1 Introduction

Constantly rising energy costs represent a large budget strain of each building. That is why the producers of building materials have always been trying to introduce new innovative products leading to reduction of these costs, while improving the comfort of living. The main factors that negatively affect the comfort of living and reduce the effectiveness of thermal insulations include humidity. The main sources of humidity in flats include respiration (breathing of living organisms, i.e. people and animals), surface evaporation of plants, evaporation of wet surfaces (during washing, mopping, etc.), steam generated by human activity (especially during cooking and showering), but also the chemical processes taking place in the flat, especially burning natural gas when cooking, precipitation, leachate and capillary water, or water in the construction introduced by the disruption of the technical building equipment (water, waste, air conditioning and recuperation unit distribution systems, etc.). The humidity of air is usually expressed as a percentage of relative humidity. However, in specific cases, especially when the basic assessment of building structures is performed, this value does not correspond with the water contained in the structure itself and it is therefore necessary to make an assessment of the balance of liquid water, using at least one of the basic orientation methods (by means of conductivity, dielectric constant). The correct method of thermal insulation, especially of building shells, requires the determination of the value of water incorporated in the building construction and making the predictive calculation of the behaviour of masonry or design in terms of the evaporability of water already used in the building and in terms of condensed and evaporative water. When the salinization of masonry is clearly detected during the construction and technical surveying, it must be assumed that there are systematic waterways in the construction. It is impossible to

apply the standard thermal insulations, which can to some extent work with condensed water in the structure; however, they are unable to reach a balance state of humidity in the masonry in terms of free water. Thermal insulation of such buildings, while removing humidity, takes advantage of materials behaving as capillary active to water. Due to their porous structure, they immediately absorb water at the first contact and they transport it in suitable time to the designated environment or they absorb it, until favourable conditions for transport of water to a designated environment in the form of water vapour are achieved. In this characteristic, the capillary active thermal insulations and their effects are close to the effect of renovation plaster systems, which, however, do not have thermal insulating properties.

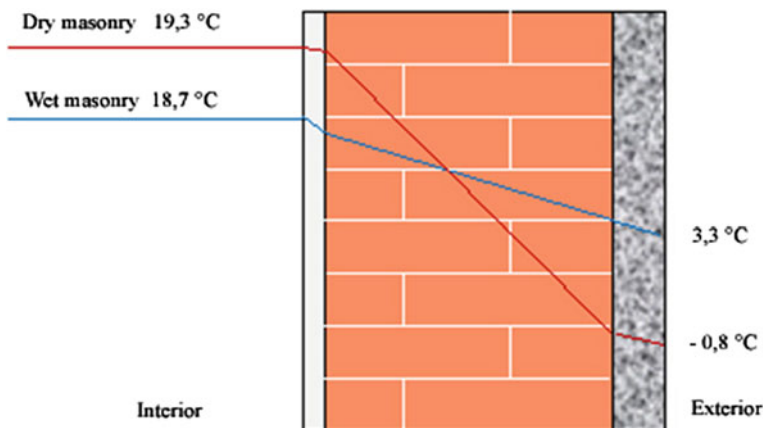
## **2 Rules of Designing External Thermal Insulation Using Capillary Active Materials**

The main criterion of quality and functionality of capillary active thermal insulation is the microclimatic model of the building interior acceptable in the long-term. Given that the impact of water in a building affects the physical, mechanical and chemical properties of building materials, it enables the spread of moulds, algae and fungi permanently reducing the thermal resistance of the masonry, in the future it will be necessary to design thermal insulation primarily from the point of view of the effect of water in specific cases. It is therefore necessary to establish a mutually balanced model in the relation between heat and water. This model represents an essential criterion, especially for the revitalization of existing buildings as well as buildings made from porous concrete, which have a tendency of high retention of water absorbed in the mass, which is difficult to evaporate. In the capillary active insulation systems, the objective is not to achieve the thermal transmittance coefficient values lower than  $0.25 \text{ W}\cdot\text{m}^{-2}\cdot\text{K}^{-1}$  at all cost, however, it is necessary and possible to achieve values in the range of  $0.30\text{--}0.35 \text{ W}\cdot\text{m}^{-2}\cdot\text{K}^{-1}$  under such moisture by weight conditions, so that the layers of masonry are able to accept another liquid phase throughout the year and throughout the entire life cycle of thermal insulation in the building from the point of view of long-term assessment of the costs of operation and maintenance of the building, compared to thermal insulation with a high vapour resistance factor. The course of temperature change in the wall for dry and wet conditions is presented in Fig. 1.

## **3 Polyurethane**

From the material viewpoint, it is rigid or semi-rigid macromolecular foam with a high proportion of closed cells. In the raw state, it is a system of two liquid components, the mixing of which under certain conditions creates moisture





**Fig. 1** The impact of moisture on heat transmission in masonry

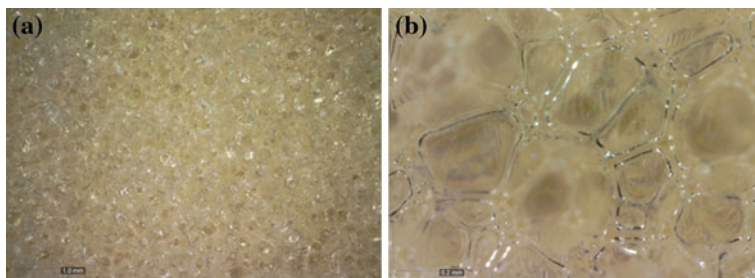
resisting, water and thermal insulating material of stable shape and dimensions, resistant against aggressive environment [1]

The basic ingredients of modern polyurethanes usually consist of the following basic components: polyhydric alcohols and isocyanates creating foam when being mixed. The methods of preparation of rigid polyurethane materials include: initiation using hard freons, soft freons, pentane or  $\text{CO}_2$ . A detailed description of the chemistry of polyurethane materials is shown [1].

Figure 2 presents a closed structure of rigid polyurethane foam with the volume weight of  $40 \text{ kg}\cdot\text{m}^{-3}$  before recycling. Table 1 shows the mechanical and thermal technical properties of rigid polyurethane foam with specific weight of  $30\text{--}100 \text{ kg}\cdot\text{m}^{-3}$ .

### 3.1 Polyurethane Foam Recycling

Nowadays, the production of polyurethanes represents about 5 % of the total volume of plastics produced. In 2007, the production of polyurethane products in



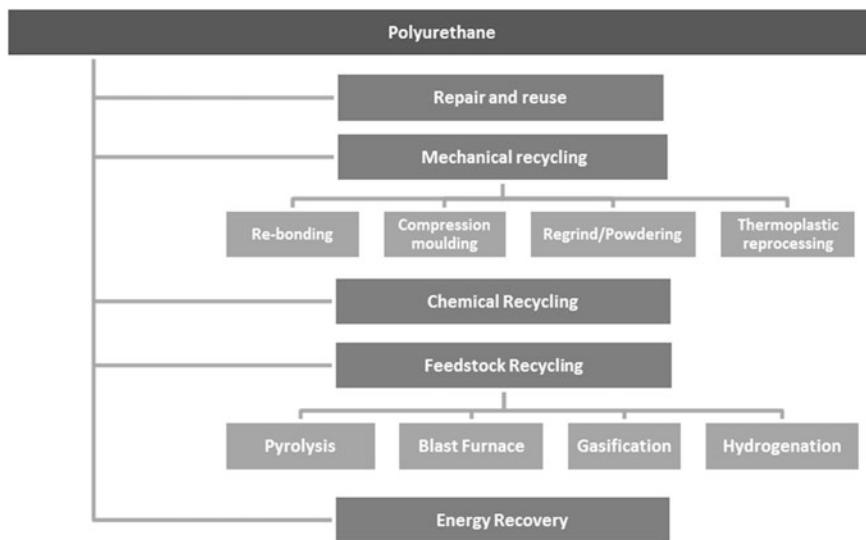
**Fig. 2** View of closed structure of PUR foam with volume weight of  $40 \text{ kg}\cdot\text{m}^{-3}$ : **a** scaled up 51.4 times, **b** scaled up 240.6 times

**Table 1** Mechanical and thermal technical properties of PUR foam

Property	Unit					
Specific weight	kg·m <sup>-3</sup>	30	40	60	80	100
<i>Mechanical properties</i>						
Strength in compr.	N·mm <sup>-2</sup>	0.20	0.25	0.40	0.60	0.90
Strength in tens.	N·mm <sup>-2</sup>	0.35	0.60	0.85	1.00	1.20
Strength to bend.	N·mm <sup>-2</sup>	0.30	0.45	0.70	0.95	1.20
Strength to shear	N·mm <sup>-2</sup>	0.15	0.20	0.30	–	–
E-module	N·mm <sup>-2</sup>	5	7	12	20	25
<i>Thermal technical properties</i>						
Thermal conductivity coefficient $\lambda$	W·m <sup>-1</sup> ·K <sup>-1</sup>			0.025		
Linear expansion coeff. (for specific weight of 30–60 kg·m <sup>-3</sup> )	1/K			5–8 • 10 <sup>-5</sup>		
Resistance to water vapour diffus. (for specific weight of 30–100 kg·m <sup>-3</sup> )	$\mu$			30–100		
<i>Absorption capacity (at 20 °C)</i>						
After 24 h	vol. %			Up to 2, max. 5		
After 28 days	vol. %			Up to 2, max. 5		
<i>Shape stability (at 30 °C)</i>						
vol. %				0, –0.2		
Temperature range	°C			–200 to +140		
Short-term	°C			+250		
Combustibility				B2		
Share size of flame retardant can influence the degree of combustibility and the properties of self-extinguishing, resistance to airborne fire and radiant heat						
Specific heat				kJ·kg <sup>-1</sup> ·K <sup>-1</sup>		
				kcal·kg <sup>-1</sup> ·°C <sup>-1</sup>		

Europe reached more than 4.5 million tons. The estimate for 2012 amounts to almost 5.25 million tons. The annual production in the Czech Republic is approximately 10,000 tons of polyurethane waste materials, in the form of rigid polyurethane foam waste. The major producers of polyurethane waste include recycling of white appliances, waste arising during foaming of PUR blocks, and formatting of PUR plates. Because polyurethane wastes contain PUR foams, which have a very low volume weight (30–50 kg·m<sup>-3</sup>) and are very bulky, it is almost impossible to effectively store this waste. As a result of that, there have been efforts in the past to develop technologies for recycling and reuse of waste polyurethane.

The most widely used methods of recycling polyurethane foam at the end of its life cycle (see Fig. 3) include mechanical recycling, chemical recycling, recycling to feedstock (thermo-chemical recycling), and energy recuperation. Chemical recycling, its description and results, are described in [2, 3], recycling to feedstock in [4, 5] and energy recuperation is presented in [6]. The most suitable method of recycling polyurethane foam at the end of its life cycle and its subsequent use as filler for mortars with heat insulating effect is mechanical recycling, which is based



**Fig. 3** Scheme of polyurethane recycling at the end of its life cycle

on the disintegration of rigid polyurethane foam, using forced-action mixer made by “Častulík”, to a grain size of 1–4 mm. There are results of experimental research dealing with the preparation of lightweight mortar in which polyurethane foam with a maximum grain size of 4 mm was used as filler, in combination with sand, fr. 0/4 mm.

Lightweight concrete is another building segment in which it is possible to use recycled crushed polyurethane. In this case, polyurethane foam is used as a substitute of lightweight aggregate. The concrete mix consists of polyurethane foam filler (grain size of 8–20 mm) in combination with sand (grain size from 0.08 to 6.3 mm). Polyurethane foam contributes to improving the workability, and to increasing the porosity of the concrete mix. Concrete strength after 28 days ranges from 10 to 15 MPa and the dynamic modulus of elasticity reaches the range of 10–15 GPa [7].

#### **4 Basic Design of Renovation Mortar Formula Based on PUR After the End of its Life Cycle**

The basic design of renovation mortar recipe with thermal insulating effect, where polyurethane foam at the end of its life cycle was used as the filler, was performed in two stages.

Polyurethane pulp with a grain size of 0/4 mm was used as filler in the first stage. Cement CEM II 32.5 N was used as the main binding component. The verification of the selection of suitable additives for renovation mortar with

thermal insulating effect was conducted during this stage. The composition of experimental recipes 1–5 was proposed at this stage.

Polyurethane pulp with a grain size of 0/1 mm was used as filler during the second stage. Cement CEM 42.5 R was used as the main binding component. In order to reduce the amount of cement, this raw material was partially replaced by metakaolin Mefisto and lime hydrate CL90-S. The basic design of renovation mortar recipes with thermal insulating effect at this stage was focused on meeting the conditions of WTA standard. The composition of experimental recipes 6–9 was proposed at this stage.

## ***4.1 Components of Renovation Mortar with Thermal Insulating Effect***

### **4.1.1 Polyurethane Foam**

Polyurethane foam waste from production of thermal insulating polyurethane boards of ZOD Brumovice, which was crushed using Častulík forced-action mixer with sieve size of 6 mm, was used as filler in the renovation mortar. The properties of waste polyurethane foam before mechanical recycling are presented in Table 2.

Using mechanical recycling, we obtained polyurethane pulp of fr. 0/4 mm. A sample of polyurethane pulp of fr. 0/1 mm was obtained from a panel sizing saw of polyurethane boards from ZOD Brumovice. Grain size curve of polyurethane pulp samples is presented graphically (Figs. 4 and 5). Figures 6 and 7 present polyurethane grains that are scaled up 206 times compared to the above shown samples. The broken structure of PUR foam after mechanical activation is clearly obvious at first glance.

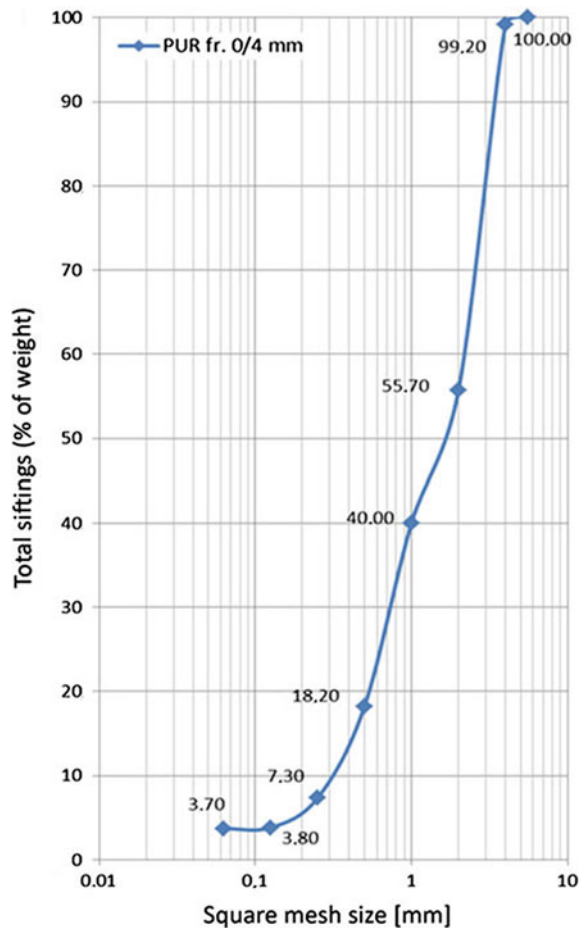
### **4.1.2 Bonding Component**

Portland cement CEM I 42.5 R and mixed cement CEM II/B–S 32,5R from cement mill Hranice na Moravě were used as the basic bonding agents for renovation mortar with thermal insulating effect. Hydrate CL90, produced by Kotouč Štramberk spol. s r.o, was used as the secondary bonding agent in renovation mortar. The third bonding component was metakaolin Mefisto K05 from České lupkové závody, a.s.

**Table 2** Properties of waste polyurethane foam before crushing

Volume weight	40 kg·m <sup>-3</sup>
Diffusion coefficient $\mu$	25
Expanding agent	CO <sub>2</sub>
Thermal conductivity coefficient	0.026 W·m <sup>-1</sup> ·K <sup>-1</sup>
Strength in compression	0.20 N·mm <sup>-2</sup>
Absorption capacity in 24 h	2.51 % of volume

**Fig. 4** Graphical expression of grain size curve of PUR pulp fr. 0/4 mm



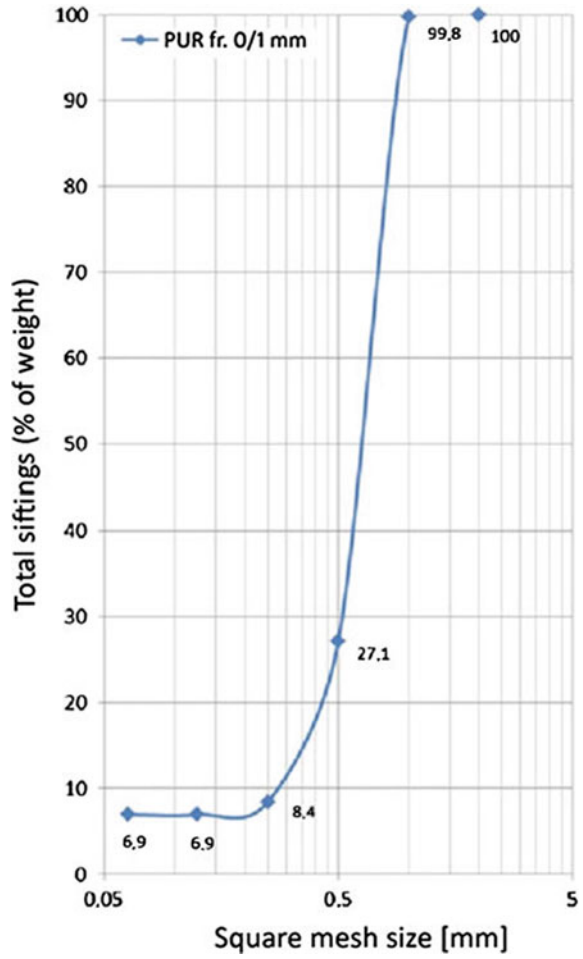
#### 4.1.3 Admixture

Very finely ground limestone with specific surface of  $3,500 \text{ cm}^2 \cdot \text{g}^{-1}$ , from Kotouč Štramberk, s.r.o, was used as the admixture for thermal insulating mortar.

#### 4.1.4 Additives

- Copolymer Vinylacetate—it is a powder additive under the brand name of Wacker 8,034 H, improving mix rheology, increasing its strength and decreasing the absorption power of insulating mortar.
- Sodium Alkylbenzene Sulphonate—it is a powder aeration additive, increasing the air content in fresh mortar.

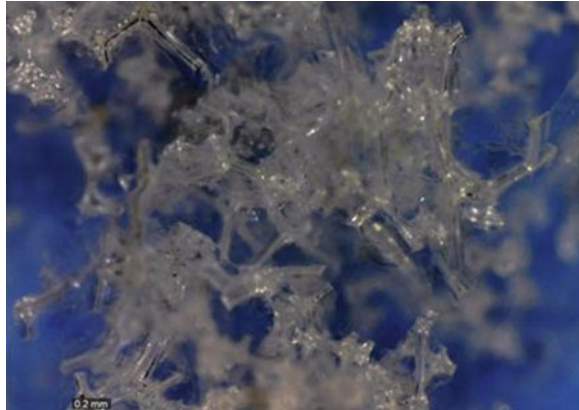
**Fig. 5** Graphical expression of grain size curve of PUR grit of fr. 0/1 mm



**Fig. 6** Detail view of PUR grain fr. 0/4 mm, scaled up 206 time



**Fig. 7** View of PUR grain fr. 0/1 mm, with disrupted cell structure, scaled up 206 times



- Calcium Lignosulphonate—this is a powder plasticizing additive, adjusting mix rheology and its setting.
- Hostapur OSB—additive improving the wetting power and increasing the content of pores in fresh and hardened mortar.

#### 4.1.5 Composition of Experimental Mixes

An overview of the composition of the designed experimental mixes of renovation mortar with thermal insulating effect of stage I and II is presented in Table 3.

**Table 3** Composition of experimental mixes of renovation mortar with thermal insulating effect

Components of renovation mortar with thermal insulating effect	Measure unit	Mix R1	Mix R2	Mix R3	Mix R4	Mix R5	Mix R6	Mix R7	Mix R8	Mix R9
PUR (crushed fr. 0/4 mm)	kg	4,60	4,60	4,60	4,60	4,60	–	–	–	–
PUR (crushed fr. 0/1 mm)	kg	–	–	–	–	–	4,60	4,60	4,60	4,60
Cement CEM II/B–S 32,5R	kg	5,25	7,61	10,50	10,50	10,50	–	–	–	–
Cement CEM I 42,5 R	kg	–	–	–	–	–	15,19	10,64	10,13	5,06
Sodium Alkylbenzene Sulphon.	kg	0,13	0,10	0,08	0,05	0,07	–	–	–	–
Calcium Lignosulphonate	kg	–	–	0,05	0,03	0,02	–	–	–	–
Copolymer Vinylacetate	kg	–	0,06	–	50	–	–	–	–	–
Hostapur OSB	kg	–	–	–	–	–	0,15	0,12	0,15	0,15
Hydrate CL90-S	kg	–	2,89	–	–	–	–	–	–	10,13
Very finely ground limestone 3500 cm <sup>2</sup> ·g <sup>-1</sup>	kg	5,25	–	–	–	–	–	–	–	–
Metakaolin Mefisto K05	kg	–	–	–	–	–	–	1,35	5,06	–
Water	kg	9,06	9,06	9,06	9,06	9,06	11,97	10,03	15,97	16,97

## 5 Preparation of Mixes of Experimental Recipes

The preparation of experimental mix recipes of renovation mortar with thermal insulating effect according to the composition presented in Table 3 took place in a mixer with forced mixing cycle (cyclone mixer) series M80/2,2 kW manufactured by Filamos s.r.o. company (see Fig. 8).

The experimental mix recipes were prepared according to the following procedure:

1. PUR pulp, together with binding component, was dosed in the mixing vessel of the mixer. The next step was the homogenization of the components in dry conditions for 3 min.
2. Dosing of additive and homogenization of all components in dry conditions for 2 min.
3. Adding the required amount of water into the mixing vessel and mixing the renovation mortar for 10 min.
4. The total time required for one mixture was 15 min.

**Fig. 8** Cyclone mixer series M80 of Filamos brand





## ***5.1 Description of Experimental Recipes***

**Mix R1:** Sufficiently dense and plastic mix is prepared after mixing with water. Once applied to the background, there is sufficient time for staff leveling, mortar seemed to be running down, and large pocket cracks would appear in real building.

**Mix R2:** This mix showed similar properties to Mix R1, however with significantly better plasticity of fresh mortar.

**Mix R3:** This mix showed the same sensory properties as Mix R2, with similar i.e. excellent plasticity. However, it was running down, but to a lesser extent than in case of Mix R1.

**Mix R4:** After mixing with water, it is sufficiently dense and plastic mix. After application to the background, there is sufficient time to staff levelling, with no signs of running down.

**Mix R5:** Very good plasticity of the mix, with no signs of running down on the test wall. Easy to level with a staff. When the surface was levelled using a staff, no tendency of the mortar to create cracks was observed.

**Mix R6:** Fresh mortar was dense, but of the so-called short type, when comparing on the test wall, the mortar began to tear after multiple surface levelling using aluminium staff.

**Mix R7:** Fresh mortar seemed to be dry once applied on the test wall. Difficult to level with a staff, with low adhesion of fresh mortar.

**Mix R8:** It was necessary to increase the amount of mixing water. After mixing, very good plasticity of the mix was observed. The mortar was very light and airy. It showed very good plasticity on the wall, without any formation of cracks.

**Mix R9:** The consistency of fresh mortar appeared to be dry, which is why the quantity of water was increased by app. 6 l compared to the original 9 l. After the end of mixing, the mix was too aerated. After application on a brick splinter, the mortar was difficult to level. There were cracks. Due to the large amount of mix water, excess water was flowing down from the mortar.

## **6 Tests of Renovation Mortar with Thermal Insulating Effect**

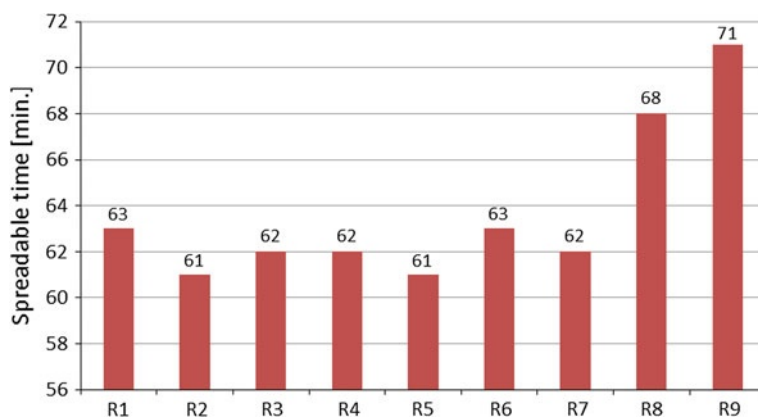
### ***6.1 Setting the Mortar Plasticity Time and the Time of Fresh Mortar Treatment***

The setting was performed according to ČSN EN 1015-9 [8]. The fresh mortar plasticity time is defined as the time necessary to achieve the specified limits of resistance against penetration of normalized rod in mortar in minutes.

The filled moulds were kept at a temperature of 22 °C in closed polyethylene bags. After removing, the moulds were placed on scales below the penetration rod.

**Table 4** Spreadable time of renovation mortar experimental mixes

Mix	R1	R2	R3	R4	R5	R6	R7	R8	R9
Spreadable time (min.)	63	61	62	62	61	63	62	68	71

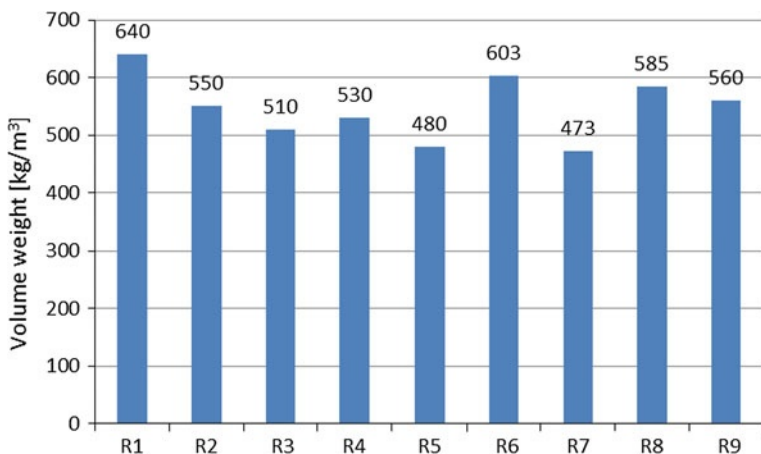
**Fig. 9** Chart of spreadable time of renovation mortar experimental mixes

The rod was slowly lowered down into the sample to a fixed line using a lever; the weight in kilograms was read and subsequently used to calculate the resistance of mortar in  $\text{N}\cdot\text{mm}^{-2}$ . The time (rounded to 1 min) required to achieve the resistance of the mix to penetration in the amount of  $0,5 \text{ N}\cdot\text{mm}^{-2}$  was measured by means of interpolation of the results obtained immediately before and after this value. The testing was carried out at suitable intervals depending on the composition of the experimental mixes. The results of the determination of the plasticity and treatment of fresh mortar are also presented in tabular form (Table 4) and graphically (Fig. 9).

The spreadable time of Mixes R1–R7 was in the interval of 61–63 min. The increased spreadable time of Mixes R8 and R9 (68 and 71 min) in comparison with other mixes was caused by higher amount of mix water (see Table 4).

## 6.2 Setting the Volume Weight of Dry Hardened Mortar

The determination was performed according to standard ČSN EN 1015-10 [9]. Three test specimens were produced from each mix. They were beams with the dimension of  $40 \times 40 \times 160 \text{ mm}$ , which were kept in a room at a temperature of  $22 \text{ }^\circ\text{C}$  for 28 days and then placed in a drying chamber at a temperature of  $(60 \pm 5) \text{ }^\circ\text{C}$  until a steady weight of the test specimen was achieved. The beams were subsequently weighed on scales and the volume weight of dry hardened



**Fig. 10** Volume weight of hardened renovation mortar with thermal insulating effect

mortar for each experimental mix was calculated. The results are presented graphically (Fig. 10) and in tabular form (Table 5).

The chart above clearly shows that the values of volume weight of hardened renovation mortar of experimental mixes ranged from 473 to 640 kg·m<sup>-3</sup>. The highest value was monitored in Mix R1 and the lowest one was found in Mix R7. The resulting values of volume weight of hardened mortar, after 28 days of ageing, were influenced by the composition of experimental mixes (see Table 3).

### 6.3 Setting the Strength Characteristics

The strength characteristics of renovation mortar were determined according to EN 1015-11 [10]. 3 test specimens were produced from each mix. They were beams with the dimensions of 40 × 40 × 160 mm. The beams in moulds were packed in polyethylene bags and stored in a room at a temperature of 22 °C for 2 days. After that they were stripped, returned back to the bags and stored this way for 5 more days. After this time, the beams were stored in a laboratory environment at 22 °C for 21 days. The beams were placed on supporting rolls in FormTest Prüfsysteme 2,201 Mega 10-200-10 testing machine, always in such a way so that the compressive force was perpendicular to the direction of the compaction of beams. The machine applied even pressure without shocks until the structure of the beams was disrupted. The measurement results are presented graphically and in tabular form (Table 5, Fig. 11).

Based on the identified strength characteristics of renovation mortar with thermal insulating effect (Fig. 11), we can say that the value of strength of experimental mixes is primarily affected by their composition, either by adding

**Table 5** Values of volume weight, tensile strength in bending and in compression of hardened mortar of experimental mixes after 28 days

Mix	Sample weight (g)	Volume weight of hardened mortar (kg·m <sup>-3</sup> )	Volume weight of hardened mortar ϕ (kg·m <sup>-3</sup> )	Compressive force in tension in bending (N)	Strength in tension in bending (MPa)	Strength in tension in bending ϕ (MPa)	Compressive force pressure 1 (N)	Compressive force pressure 2 (N)	Strength in compression 1 (MPa)	Strength in compression 2 (MPa)	Strength in compression (MPa)	Strength in compression ϕ (MPa)
R1	1	164.2	641	205	0.480	0.50	1,520	1,540	0.95	0.96	0.96	0.95
	2	162.8	636	220	0.516		1,560	1,490	0.98	0.93	0.95	
	3	164.9	644	210	0.492		1,530	1,510	0.96	0.94	0.95	
R2	1	141.0	551	250	0.586	0.61	1,940	1,920	1.21	1.20	1.21	1.21
	2	140.9	550	275	0.645		1,970	1,945	1.23	1.22	1.22	
	3	140.5	549	260	0.609		1,890	1,935	1.18	1.21	1.20	
R3	1	131.1	512	185	0.434	0.45	1,380	1,325	0.86	0.83	0.85	0.83
	2	130.6	510	195	0.457		1,305	1,360	0.82	0.85	0.83	
	3	129.7	507	190	0.445		1,260	1,290	0.79	0.81	0.80	
R4	1	135.8	530	175	0.410	0.44	1,365	1,385	0.85	0.87	0.86	0.85
	2	134.9	527	200	0.445		1,340	1,345	0.84	0.84	0.84	
	3	136.2	532	200	0.469		1,400	1,370	0.88	0.86	0.87	
R5	1	122.2	477	185	0.434	0.48	1,155	1,130	0.72	0.71	0.71	0.71
	2	121.4	474	205	0.480		1,100	1,085	0.69	0.68	0.68	
	3	125.4	490	225	0.527		1,200	1,190	0.75	0.74	0.75	
R6	1	154.3	603	150	0.352	0.36	1,080	1,130	0.68	0.71	0.69	0.69
	2	154.0	602	150	0.352		1,100	1,070	0.69	0.67	0.68	
	3	154.6	604	160	0.375		1,050	1,200	0.66	0.75	0.70	
R7	1	119.8	468	200	0.469	0.48	1,160	1,100	0.73	0.69	0.71	0.79
	2	118.5	463	230	0.539		1,380	1,450	0.86	0.91	0.88	
	3	125.1	489	190	0.445		1,350	1,150	0.84	0.72	0.78	
R8	1	149.4	584	335	0.785	0.78	2,421	2,496	1.51	1.56	1.54	1.56
	2	148.9	582	328	0.769		2,536	2,571	1.59	1.61	1.60	
	3	150.7	589	339	0.795		2,459	2,496	1.54	1.56	1.55	
R9	1	144.2	563	110	0.258	0.25	550	590	0.34	0.37	0.36	0.36
	2	144.4	564	100	0.234		600	610	0.38	0.38	0.38	
	3	141.2	552	115	0.270		570	580	0.36	0.36	0.36	

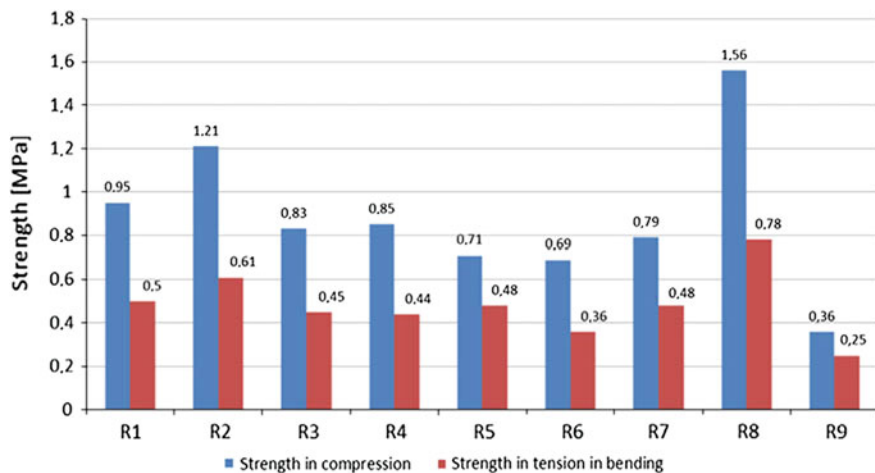


Fig. 11 Results of strength of experimental mixes after 28 days of ageing

additives or by the combination of the bonding components. It is especially important in Mix R1, Mix R2 and Mix R8. The highest value of strength in compression (1.56 MPa) and tensile strength in bending (0.78 MPa) was achieved in Mix R8, where part of the cement was replaced by metakaolin (Table 5). This is the only mix meeting the required strength of renovation mortar according to WTA [11]. It can be seen as well (Fig. 11), that the tensile strength of renovation mortar in bending in all the experimental mixes, except for Mix R5, R7 and Mix R9, corresponds to  $\frac{1}{2}$  of strength in compression. The ratio of tensile strength in bending to strength in compression varies from 0.50 to 0.54 MPa.

#### 6.4 Setting the Adhesive Strength of Hardened Mortar

The setting was performed according to ČSN EN 1015-12 [12]. DYNA Z15 pull off tester was used to determine the tensile force. The adhesive strength is defined as the maximum tensile stress produced by stress acting perpendicular to the surface of the mortar for interior and exterior plasters applied on the backing. The tensile stress is deduced using pull off targets glued to the tested circular area of mortar surface. We used a circular target with a diameter of 50 mm, which was glued on the cleaned surface of renovation mortar with epoxy resin. A ceramic splinter (burnt brick BB with dimension of  $290 \times 140 \times 65$  mm) was chosen as the backing in order to determine the adhesive strength of renovation mortar after 28 days of ageing. Five test specimens were always prepared for each experimental mix for the actual test. The test results are clearly presented in Table 6.

Based on the processed results setting the renovation mortar adhesive strength in Table 6, it is clear that the highest value of adhesive strength of renovation

**Table 6** Values of adhesive strength of experimental mixes measured on a ceramic splinter

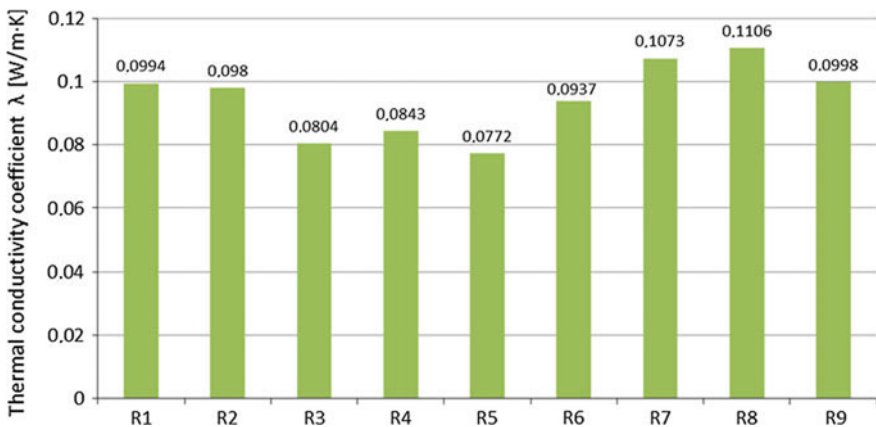
Mix	Backing adhesive strength $\sigma$ (N·mm <sup>-2</sup> )	Separation from the backing
R1	0.30	Rupture in a layer of mortar (80 % in material)
R2	0.40	Rupture in a layer of mortar (80 % in material)
R3	0.10	Rupture in a layer of mortar (100 % in material)
R4	0.15	Rupture in a layer of mortar (100 % in material)
R5	0.07	Rupture of bond between mortar and backing (100 %)
R6	0.21	Rupture in a layer of mortar (100 % in material)
R7	0.33	Rupture in a layer of mortar (80 % in material)
R8	0.43	Rupture of bond between mortar and backing (90 %)
R9	0.15	Rupture in a layer of mortar (100 % in material)

mortar to backing was achieved in experimental Mixes R2 and R8 (0.40 and 0.43 MPa), where the rupture of bond between the mortar and the backing was witnessed in the test samples of these mixes.

### 6.5 Setting the Thermal Conductivity Coefficient $\lambda$

The thermal conductivity coefficient of renovation mortar with thermal insulating effect in all experimental mixes was set by an analyser of thermal properties ISOMET Model 2114.

The measurement is based on the analysis of the thermal response of the analysed material to heat flow impulses. The heat flow is excited by electric heating of a resistance heating element embedded in a probe, which is in direct thermal contact with the test sample. The evaluation of the thermal conductivity



**Fig. 12** Results of thermal conductivity coefficient  $\lambda$  of experimental mixes

and the volumetric heat capacity is based on the temperature records collected regularly as a function of time, assuming that the heat is spread in an unlimited environment.

A surface probe intended for the measurements on solid and hard materials with a measuring range from  $0.03$  to  $2.0 \text{ W}\cdot\text{m}^{-1}\cdot\text{K}^{-1}$  was used for the measurements.

The actual measurement was performed on a 28 days old test specimen with the dimensions of  $140 \times 40 \times 160 \text{ mm}$ , which was dried at  $105 \text{ }^\circ\text{C}$  for 24 h and stored in a desiccator prior to the measurement. The measurement results are processed graphically in Fig. 12.

It is evident from Fig. 12 that the highest values of thermal conductivity coefficient  $\lambda$  were measured in Mixes, R1, R2, R6, R7, R8 and R9. The thermal conductivity coefficient varies from  $0.0937$  to  $0.1106 \text{ W}\cdot\text{m}^{-1}\cdot\text{K}^{-1}$ , while the highest value was measured in Mix R8, which was  $0.1106 \text{ W}\cdot\text{m}^{-1}\cdot\text{K}^{-1}$ . These measurements have confirmed the fact that an increase in volume weight of experimental mixes of renovation mortar with thermal insulating effect goes hand in hand with increased thermal conductivity coefficient  $\lambda$ .

## 6.6 Resistance Against Salts

The resistance of renovation mortar with thermal insulating effect against salts has been tested in experimental Mixes R6, R7, R8 and R9. Beams of size of  $40 \times 40 \times 160 \text{ mm}$  in the quantity of one set (3 pieces) from each experimental mix were used as the test specimens. On top of that, a test specimen with the dimensions of  $140 \times 40 \times 160 \text{ mm}$  was produced from each experimental mix in order to measure the thermal conductivity  $\lambda$ .

The bases of the above described test specimens after 28 days of ageing were submerged into a model salt solution according to WTA [11] on a tray on which a solution level of  $15 \pm 5 \text{ mm}$  was maintained over a period of 30 days (Fig. 13). The composition of the salt solution per 1,000 ml of demineralised water was as follows:  $35 \text{ g NaCl} + 5 \text{ g Na}_2\text{SO}_4 + 15 \text{ g NaNO}_3$ . The test specimens were

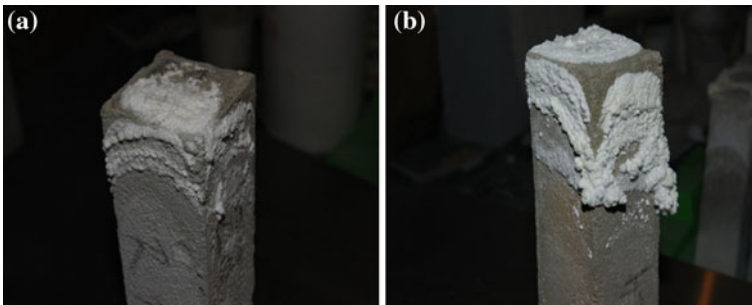
**Fig. 13** View of test specimens of experimental mix prior to the salt test, placed on a tray in the salt solution



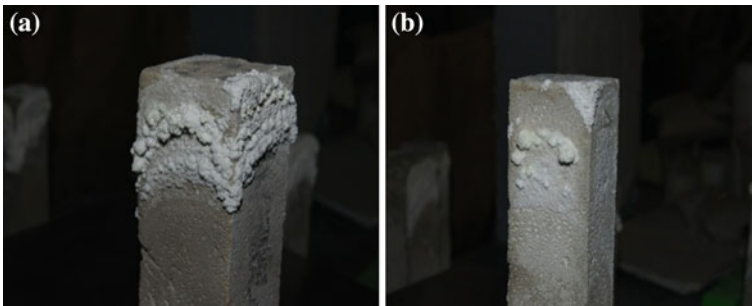
monitored during the period of 30 days, to see whether flowers of salt are not created on the surface. After 30 days, the test specimens were removed from the solution. Their surface showed clearly visible flowers of salt (Figs. 14, 15). These flowers of salt were scraped off and the test specimens were subjected to the tests of strength characteristics, i.e. determining the strength in tension in bending and the strength in compression at the end of the beams. The test results are processed in tabular form (Table 7) and graphically (Fig. 17).

These images (Figs. 14, 15) of experimental mixes clearly show that after the test specimens have been placed in a salt solution for a period of 30 days, flowers of salt were visible on the surface of the specimens of all experimental mixes. Flowers of salt were monitored on the surface of the specimens always from two third their height, and they were visible on all sides of the test specimen.

The structure of the experimental mixes R6, R7, R8 and R9 was observed on samples which either were not or were kept in salt solution according to WTA [11]. The actual observation was performed using a USB microscope Pro



**Fig. 14** View of the test specimen taken out of the salt solution according to WTA after 30 days; **a** Mix R6, **b** Mix R7



**Fig. 15** View of the test specimens taken out of the salt solution according to WTA after 30 days; **a** Mix R8, **b** Mix R9



**Table 7** Confrontation of comparative strengths and strength of renovation mortar stored in salt solution for 30 days

Mix	Strength in tension in bending (MPa)		Strength in compression (MPa)		Increase of strength in tension in bending compared to comparative strength		Increase of strength in compression compared to comparative strength	
	Comparative	Salt	Comparative	Salt	(MPa)	Multiple	(MPa)	Multiple
R6	0.36	0.71	0.69	1.32	0.35	0.97	0.63	0.91
R7	0.48	0.71	0.79	2.00	0.23	0.48	1.21	1.53
R8	0.78	1.05	1.56	2.55	0.27	0.35	0.99	0.63
R9	0.25	0.77	0.36	0.79	0.52	2.08	0.43	1.19

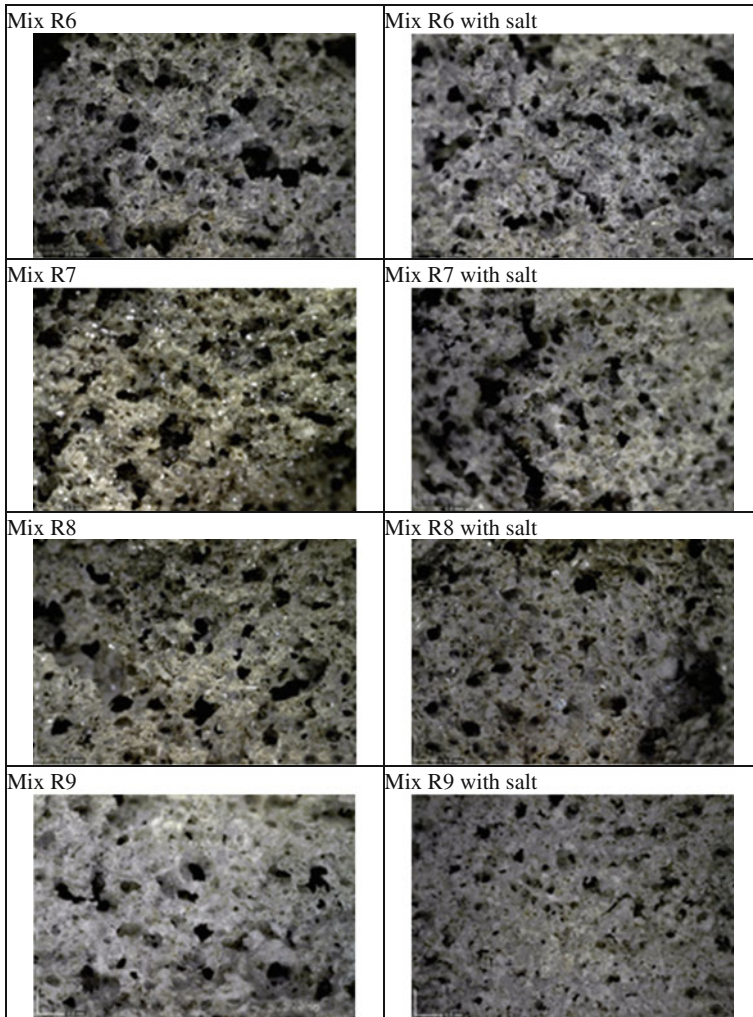
(5 megapixel) Dino-Lite (AM7013MZT). The selected magnification was 66x and 196x. The aim of the observation was to demonstrate that the structure of the samples of renovation mortar with thermal insulating effect, which were stored in salt solution for 30 days, will show crystallization of salts. It is possible to confirm the crystallization of salts in the structure of renovation mortar with thermal insulating effect on the basis of the photographs presented in Fig. 16.

Based on the above described observations result, it must be said that renovation mortar with thermal insulating effect based on polyurethane after the end of the life cycle meets the criteria for renovation mortars, which means that salts deposit and subsequently crystallize in the structure of mortar. It was also discovered (see Table 7 and Fig. 17), that with increasing salt content in the structure of renovation mortar with thermal insulating effect, the tensile strength in bending and the strength in compression increase as well. The increase in tensile strength in bending in experimental mixes R6 to R9 ranged from 0.23 to 0.52 MPa, with the strength in compression of 0.43–1.21 MPa, while the highest multiple increase of tensile strength in bending was detected in Mix 8, which was 2.08 times. The highest multiple of the strength in compression was recorded in Mix 7, 1.57 times.

The processed results make it clear (Table 8, Fig. 18) that the test specimens of experimental Mixes R6 to R9, which were stored in salt solution for 30 days, witness an increase of the thermal conductivity coefficient  $\lambda$  within the range of 10–26,6 % in comparison with the comparative specimens. The highest increase of the thermal conductivity coefficient was monitored in Mix R9.

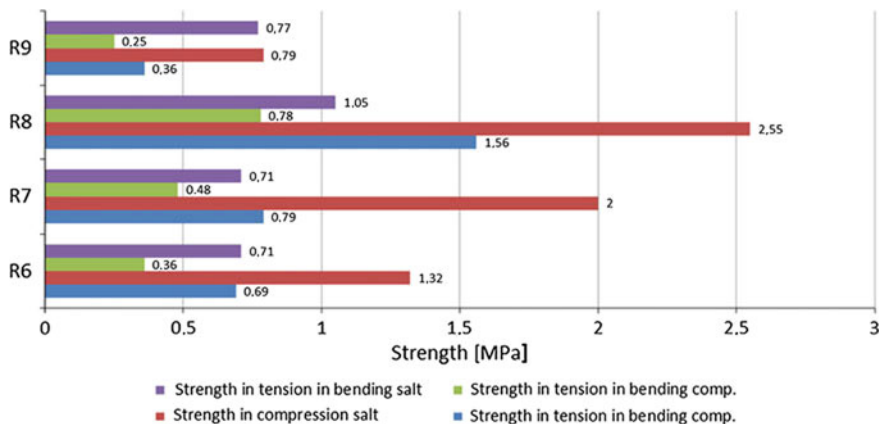
### **6.7 Setting the Capillary Absorption Coefficient of Water in Hardened Mortar**

Two test specimens with the dimensions of 40 × 40 × 160 mm were used to determine the capillary absorption coefficient of water in Mixes R6, R7, R8 and R9. The production of the test specimens, including their conditioning, was identical to the test specimens used for the tests of strength of hardened mortar in



**Fig. 16** View of the structure of renovation mortar with thermal insulating effect (without and with salt) of experimental mixes scaled up by 66 times

tension in bending and in compression. Before the testing, the test specimens were placed in a drying chamber at a temperature of  $(60 \pm 5) ^\circ\text{C}$  to stabilize their weight. Subsequently, the surface of the test specimens was coated with a sealing compound of beeswax along their long sides. The specimens were broken in half and placed in a bowl of water with their fracture edge down, and with the water level height of 10 mm. The test was terminated after 90 min, when wet spots were clearly visible on free surface of the specimens. The specimens were broken up lengthwise, and it was stated that they are fully saturated with water. Both parts

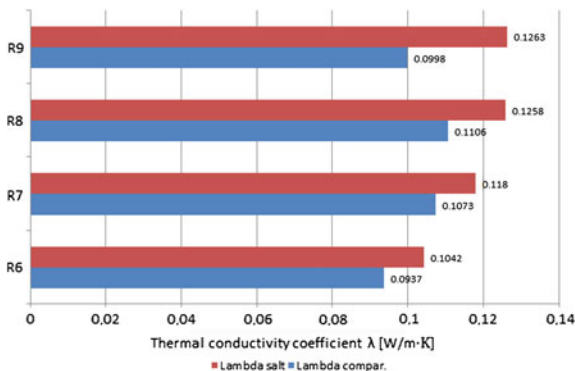


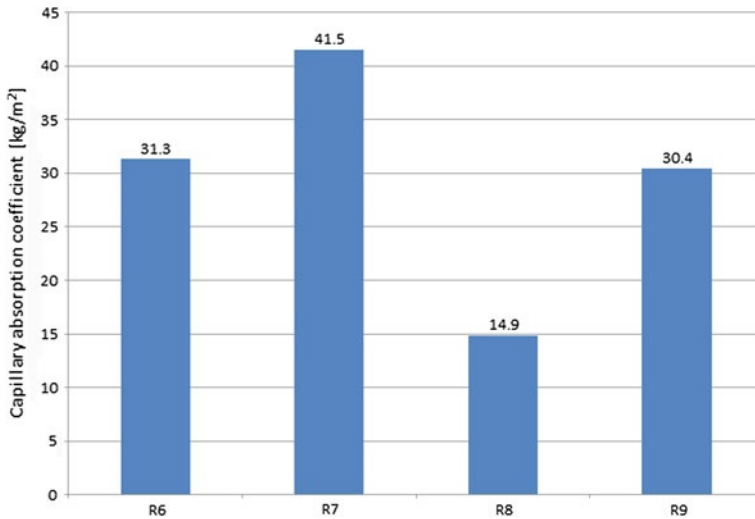
**Fig. 17** Graphical confrontation of comparative strengths and strength of renovation mortar stored in salt solution for 30 days

**Table 8** Measured values of thermal conductivity coefficient  $\lambda$  of experimental mixes after salt resistivity test

Mix	Volume weight ( $\text{kg}\cdot\text{m}^{-3}$ )	Increase of volume weight compared to comparative mixes (%)	Thermal conductivity coefficient $\lambda$ ( $\text{W}\cdot\text{m}^{-1}\cdot\text{K}^{-1}$ )	Increase of thermal conductivity coefficient $\lambda$ compared to comparative mixes (%)
R6	643	6.6	0.1042	11.2
R7	705	49.0	0.1180	10.0
R8	749	28.0	0.1258	13.7
R9	647	15.5	0.1263	26.6

**Fig. 18** Graphical comparison of thermal conductivity coefficient of comparative specimens and specimens stored in salt solution for 30 days





**Fig. 19** Graphical expression of capillary absorption coefficient of water of hardened mortar

were weighted together and the weight was recorded in the table (the value of M<sub>3</sub>). The capillary absorption coefficient was calculated as

$$C = 0.625 \cdot (M_3 - M_0) [\text{kg} \cdot \text{m}^{-2}], \tag{1}$$

where  $C$  is the capillary absorption coefficient of water for the individual test specimens ( $\text{kg} \cdot \text{m}^{-2}$ ),  $M_0$  is the weight of dried test specimen (g),  $M_3$  is the weight of soaked test specimen after 24 h (g).

The measurement results are presented graphically (Fig. 19).

The test results (Fig. 19) make it clear that the capillary absorption coefficient in Mixes R6–R9 was within the interval of 14.9–41.5  $\text{kg} \cdot \text{m}^{-2}$ , while the lowest value was measured in Mix R8, which was 14.9  $\text{kg} \cdot \text{m}^{-2}$ . The highest value was measured in Mix R7, 41.5  $\text{kg} \cdot \text{m}^{-2}$ .

### 6.8 Setting the Porosity of Hardened Renovation Mortar

The origin and development of the pore system during the hydration of the binding components is crucial for understanding the physical and chemical properties of the final product exposed to aggressive environmental impacts. It is because it affects the penetration of ions into the matrix and their interaction with the products of hydration, as well as the diffusion properties of materials. One type of porosity we can distinguish is the total porosity expressing the total number of pores in the material. In this case, it also includes the pores that are closed and do not communicate with the surroundings, which is why this value is not very

significant with regard to fluid penetration. The effective (efficient) porosity, which expresses the number of communicating pores, seems to be much more suitable. It is especially important where the aim is to determine the distribution of pore sizes. A number of different techniques have been developed in order to determine the effective porosity. However, to determine the quantity of the finest pores with the diameter of tens of nm, you need advanced modern instrumental methods including the penetration of helium, the adsorption of gas (e.g. nitrogen), the nuclear magnetic resonance, or mercury porosimetry, with the last method being the most common.

Mercury porosimetry is a common method used to determine the internal structure of a variety of porous materials such as concretes, stones, ceramics or clays. Although this method does not allow measurements of the finest pores, it does not appear to be a major problem in case of the materials studied by us, because the pores below 1 nm have minimum affect on the penetration of the media. Rapid penetration into the matrix is mainly associated with bigger pores, which is why the measurements of their share are most important for understanding the behaviour of the material. The basic principle of mercury porosimetry rests on the fact that certain pressure needs to be applied for the injection of non-wetting liquid (such as mercury into a porous material). The pressure required for the injection of mercury into the given material is a function of the dihedral angle, the surface tension of mercury and the geometry of pores. If we assume that the pores filled with mercury are approximately of cylindrical shape, the size of penetrated pores will depend on the pressure of penetrating mercury according to Washburn equation

$$\Delta P = \frac{2\gamma \cos \theta}{r}, \quad (2)$$

where  $\Delta P$  is the pressure required for injection of mercury,  $r$  is the radius of cylindrical pore,  $\gamma$  is the surface tension of mercury and  $\theta$  is the dihedral angle between mercury and the wall of cylindrical pore. According to Washburn equation, the injection of mercury into a capillary with the diameter of 18 Å would require a pressure of up to 415 MPa, because that is the value of pressure in capillary depression.

Mercury porosimetry method requires the evacuation of the sample before mercury is injected into the pores. Mercury is fed into the penetrometer reservoir, after the evacuation of all the gas from the volume of pores of the sample. After that, mercury is injected into the inter-particle space and the pores of the particles by increasing the pressure. The volume of mercury penetrating the pores is expressed directly as a function of the applied pressure. Since the mercury porosimeters are capable of exerting pressures of up to 400 MPa, this method can also determine pores in a diameter of only a few nm. The mercury porosimetry results are usually expressed as the volume of pores with respect to their size. The pore size distribution is usually expressed as a cumulative or differential curve.

Samples in the form of cuboids with the dimensions of  $15 \times 15 \times 20$  mm were prepared for the detected porosities of experimental Mixes R6–R9, and they were tested on Autopore 9,500 mercury porosimeter. This device enables the measurement of internal porosity of solid materials, the size and distribution of the volume of pores, and the total volume and surface of pores. The measurements use the characteristics of mercury, in particular its surface tension, when the increasing pressure gradually fills the volume of all pores with injected mercury, while low pressures fill the large (macro) pores and high pressures fills the smaller (meso) ones. The total volume of pores is determined by the volume of injected mercury. The diameter of pores is inversely proportional to the pressure and directly proportional to the dihedral angle between a drop of mercury and the measured surface. The device allows measurements in the pressure ranges from 0 to 345 kPa for low-pressure analysis and 0.101–228 MPa for high-pressure analysis, which provides conditions for the measurement of pore sizes in the range of 0.0055–360  $\mu\text{m}$ .

Figures 20 and 21 show the charts of cumulative and differential pore distribution curves of experimental mixtures. When evaluating the results presented in the charts, it is necessary to realize that the measuring range of the instrument is between 0.0055 and 0.360 mm and the displayed curves end at these values for this reason, not because the studied materials didn't contain pores outside this range. That is why the results obtained from the measurements of porosity can't be seen as the absolute values. Despite that, the measured data provide valuable information. The continuous curves, and in particular the differential curves, make it apparent that the distribution of pores in the individual mixes is quite different. The only common fact is that pores with the diameters smaller than 0.1  $\mu\text{m}$  don't

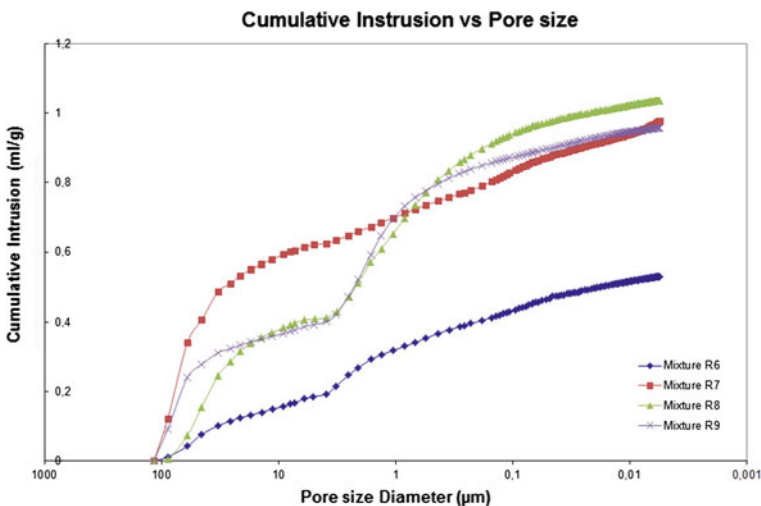


Fig. 20 Chart of cumulative curves of pore distribution

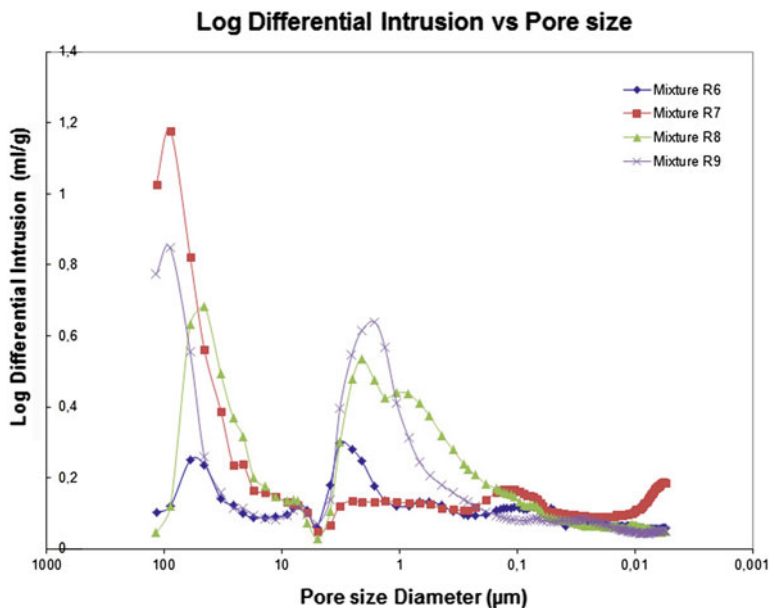


Fig. 21 Chart of differential curves of pore distribution

have significant share in the mixes, and that the pore size in all mixtures (perhaps with the exception of Mix R7) varies in a wider range.

More distinctive peaks can be seen in Mix R8, the maximum values of which reach around 45 and 2  $\mu\text{m}$ . Maximum peak values of Mix R9 are around 88 and 2  $\mu\text{m}$ . The only significant peak with the maximum value of 88  $\mu\text{m}$  is visible in Mix R7.

Mixes R8 and R9 have more significant maximum values in the share of pores with a diameter between 1 and 3  $\mu\text{m}$ , with subsequent drop to the value of 5  $\mu\text{m}$ , followed by an increase of pores into the second distinctive peak of the share of pores with a diameter between 45 and 116  $\mu\text{m}$ .

Table 9 presents the final values of porosity test of experimental mixes.

Table 9 Final values of porosity test of experimental mixes

Parameters	Mix R6	Mix R7	Mix R8	Mix R9
Total intrusion volume ( $\text{mL}\cdot\text{g}^{-1}$ )	0,5323	0,9787	1,0370	0,9586
Total pore area ( $\text{m}^2\cdot\text{g}^{-1}$ )	21,487	39,774	22,649	19,897
Median pore diameter (volume) ( $\mu\text{m}$ )	2,1380	32,5787	2,0463	2,4779
Average pore diameter (4 V/A) ( $\mu\text{m}$ )	0,0991	0,0984	0,1831	0,1927
Porosity (%)	53,6354	65,3807	68,8753	63,3898

## 7 Use of Renovation Mortar with Thermal Insulating Effect

It is a modified renovation technology using renovation mortar based on polyurethane pulp, which is used as filler in this mortar. The existing revitalization system of buildings affected by moisture is based on the removal of existing plaster, followed by intensive ventilation, or damp-proofing and, once the masonry moisture has been stable, the surface finish is repaired. The downside of the masonry stripped in such a way during the building drying time is the fact that the outer enclosure walls are exposed to frost, they face thermal stress, the impact of rain water, the impact of the atmosphere and the biological effects, i.e. algae, moss, organic and dust particles, etc. In case of internal structures, stripped masonry makes the residential use impossible or strictly limited, due to increased dust formation, and moulds growing into the walls. The common factor of both external and internal affected structures is the formation of flowers of salt, which cause surface degradation of the wall. Due to high porosity of renovation mortar with thermal insulating effect based on PUR (Mixture 8, which has a porosity of 68.9 % and the coefficient of capillary absorption of water in non-hydrophobic state of  $14.9 \text{ kg}\cdot\text{m}^{-2}$ ), it is suitable to use this mortar renovation measure for the revitalization of buildings. Renovation mortar with thermal insulating effect is applied directly on the masonry in the layer thickness of 30–50 mm, after removal of the existing plaster and after mechanical cleaning of the backing wall. The outcome of this application, after rough levelling, is a highly porous structure that protects the masonry against these negative impacts. However, thanks to high internal surface area and suitable pore size, it allows smooth ventilation of the masonry and prevents capillary rise of water into the unaffected parts of the masonry. Any salt extracts are transferred to the renovation mortar with thermal insulating effect based on PUR, which is why they will not cause any further damage to the masonry. Another positive factor includes the balanced drying of the construction, which is particularly important in mixed constructions such as clay, lime, clay brick, or stone.

Once the building have dried, it is necessary to assess the state of the renovation mortar with thermal insulating effect as well as the backing wall. If the building is not affected by the degrading effects, it is possible to keep the renovation mortar in the building as the topping coat of the internal constructions, eventually as the thermal insulation plaster of the external building shell. The test results presented in [Sect. 6.2](#) have shown that fine rigid polyurethane foam with a grain size of 0–1 mm can be used as a substitute of currently used fillers based on expanded volcanic glass, expanded vermiculite, or obsidian in renovation mortars with thermal insulating effect. The actual comparison of the developed renovation mortar with thermal insulating effect based on polyurethane (Mix R8) with the competing renovation mortars and renovation thermal insulation mortars is presented in [Table 10](#). Based on the values presented in this table, it is obvious that the values of the renovation mortar with thermal insulating effect based on



**Table 10** Comparison of renovation mortar properties

Name	Volume weight of hardened mortar ( $\text{kg}\cdot\text{m}^{-3}$ )	Grain fineness (mm)	Strength in compression ( $\text{N}\cdot\text{mm}^{-2}$ )	Thermal conductivity coefficient $\lambda$ ( $\text{W}\cdot\text{m}^{-1}\cdot\text{K}^{-1}$ )	Capillary absorption coefficient ( $\text{kg}\cdot\text{m}^{-2}$ )
<b>Mix R8</b>	<b>585</b>	<b>0-1</b>	<b>1,56</b>	<b>0,110</b>	<b>14,9</b>
Renovation brown coat WTA CEMIX	1,100-1,400	0-1,2	1,5-5	max. 0,410	min. 1,0
KVK renovation brown coat 0230 K	1,250	0-2,5	1,5-5	max. 0,420	min. 1,0
SANIER Porenausgleichsputz 208 HASIT	1,200-1,400	0-3	1,5-5	$\leq 0,390$	$> 1,0$

polyurethane (Mix R8) are comparable to those of the competing plasters. The values of the strength in compression and the capillary absorption coefficient meet the requirements of ČSN EN 998-1 [13].

## 8 Novelty and Pivotal Benefit

The novelty and pivotal benefit of renovation mortar with thermal insulating effect lies in the fact that the mortar has the moisture renovation function as well as the thermal insulation function.

Another additional practical benefit of renovation mortar with thermal insulating effect lies in the fact that this mortar does not cause degradation of the backing wall and, at the same time, there is no back salination of the wall due to the change of partial pressure and/or the influence of the moisture gradient.

Mix R8 was the optimal recipe from all the analyzed experimental mixes, according to the mandatory requirements for complementary measures of rigid renovation technologies, i.e. damp-proofing, grouting, electro-osmotic methods, etc. For this type of renovation mortar, polyurethane foam included in the cement-metakaolin matrix allows (due to its porosity, i.e. pore size and structure, and the effective modulus of elasticity) multiple increase of the capacity of accumulation of salts stored in the structure of renovation plaster with thermal insulating effect, without causing the destruction of this innovative mix. This physical effect is made possible due to increased volume of salt crystals and the associated crystallization and re-crystallization pressures in the structure of the given mix.

**Acknowledgments** This chapter was written with the support of: Grants from the budget of the Moravian-Silesian Region No. 0014/2012/RRC. Project of Institute of Clean Technologies for Mining and Utilization of Raw Materials for Energy Use, registration No. ED2.1.00/03.008.

## References

1. Filipi, B.: *Plasty*. Skripta VŠB-TU Ostrava. Sdružení požárního a bezpečnostního inženýrství, Ostrava, s. 48, (2003). ISBN 80-86634-13-2
2. Zia, K.M., Bhatti, H.N., Bhatti, I.A.: Methods for polyurethane and polyurethane composites, recycling and recovery: A review. *React. Funct. Polym.* **67**(3), 675–692 (2007)
3. Wu, C.H., Cang, C.H., Li, J.: Glycolysis of rigid polyurethane from waste refrigerators. *Polym. Degrad. Stab.* **75**(3), 413–421 (2002)
4. Kaminsky, W., Predel, M., Sadiky, A.: Feedstock recycling of polymers by pyrolysis in a fluidised bed. *Polym. Degrad. Stab.* **85**(3), 1045–1050 (2004)
5. Branca, C., Di Blasi, C., Casu, A., et al.: Reaction kinetics and morphological changes of a rigid polyurethane foam during combustion. *Thermochim. Acta* **399**(1–2), 127–137 (2003)
6. Zevenhoven, R.: Treatment and disposal of polyurethane wastes: options for recovery and recycling, 2004th edn. Helsinki University of Technology Energy Engineering and Environmental Protection, Espoo (2004). ISBN 951-22-7161-3

7. Gadea, J., Rodríguez, A., Campos, P.L., Garabito, J., Calderón, V.: Lightweight mortar made with recycled polyurethane foam. *Cement Concr. Compos.* **32**, 672–677 (2010)
8. ČSN EN 1015-9 Methods of test for mortar for masonry—Part 9: Determination of workable life and correction time of fresh mortar. Prague: Czech office for standards, metrology and testing (2000)
9. ČSN EN 1015-10 Methods of test for mortar for masonry—Part 10: Determination of dry bulk density of hardened mortar. Prague: Czech office for standards, metrology and testing (2000)
10. ČSN EN 1015-11 Methods of test for mortar for masonry—Part 11: Determination of flexural and compressive strength of hardened mortar. Prague: Czech office for standards, metrology and testing (2000)
11. WTA—Directive 2-2-91 Renovation plaster systems
12. ČSN EN 1015-12 Methods of test for mortar for masonry—Part 12: Determination of adhesive strength of hardened rendering and plastering mortars on substrates. Prague: Czech office for standards, metrology and testing (2000)
13. ČSN EN 998-1 Specification for mortar for masonry—Part 1: Rendering and plastering mortar. Prague: Czech office for standards, metrology and testing (2005)

# Thermal Storage Materials for Enhancing Indoor-Dwelling Temperature Conditions

Germán Ferreira, Ana M. López-Sabirón and Alfonso Aranda-Usón

**Abstract** The adequate impregnation of phase change materials (PCMs) into porous construction materials in a building can be significantly improved if technical and environmental aspects are evaluated. Sensible and latent heat storage using PCMs is well known technology governed by two principles Sensible Heat Storage (SHS) and Latent Heat Storage (LHS) but additional studies focused on the specific industrial applications considering its recent progress are required. One of the most recent progresses that have been achieved in this area is the large number of commercial PCMs available. This fact makes that the simple task of selecting the appropriate PCM considering technical and environmental aspects will not be evident. Large latent heat and high thermal conductivity, as well as, a melting temperature in the practical range of operation, low in cost, non-toxicant, non-corrosive and low environmental impacts are keys for choosing the suitable PCMs. In this chapter, an energy (ESP-r) and environmental (SIMAPRO) modelling study is carried out and presented for enhancing indoor-dwelling temperature conditions considering a real climate severity.

**Keywords** Phase change materials · Thermal storage · Energy modelling · ESP-r · Environmental modelling · Life cycle assessment

## Nomenclature

CS	Climate severity
$C_{ef}$	Effective heat capacity
$C_l$	Liquid specific heat

---

G. Ferreira (✉) · A. M. López-Sabirón · A. Aranda-Usón  
CIRCE, Research Centre for Energy Resources and Consumption, University of Zaragoza,  
Mariano Esquillor 15 50018 Zaragoza, Spain  
e-mail: germanf@unizar.es

G. Ferreira  
CEFT, Mechanical Engineering Department, University of Porto, Rua Dr. Roberto Frias  
4200465 Porto, Portugal

$C_s$	Solid specific heat
EM	Enthalpy method
EHCM	Effective Heat Capacity method
GHG	Greenhouse gas
HIM	Heat Integration method
HVAC	Heating, ventilating and air conditioning
L	Latent heat capacity
LCA	Life cycle assessment
LCI	Life cycle inventory
LHS	Latent heat storage
SHS	Sensible heat storage
PCM	Phase change material
$\vec{b}$	Volumetric forces
$\vec{n}$	Unitary vector perpendicular to the surface
$\vec{v}$	Velocity vector
$\vec{\sigma}$	External forces
$\vec{q}$	Heat generation
S	Surface
t	Time
$T_m$	Melting Temperature
$T_s$	Solidification Temperature
V	Volume
$\rho$	Density

## 1 Introduction

Control of phase change heat transfer and temperature of natural and artificial porous media has received considerable attention in numerous technical processes due to its importance in latent heat energy storage and other applications. One of the most interesting promises is the impregnation of phase change materials (PCMs) into porous construction materials with the objective of increasing thermal mass and optimising the control of the indoor temperature to reduce energy consumption. This promise is particularly significant since the residential and tertiary building sector demands about 40 % of worldwide energy consumption [1, 2]. Therefore, this technology represents one of the existing routes for reducing the energy consumption during the use stage of a building, and consequently, its environmental impacts [3]. However, the performance of PCMs depends not only on the heating, ventilating and air conditioning (HVAC) system properties such as the efficiency [4] but also on the climate, building design, materials and envelope characteristics [5, 6, 7, 8] which have a strong influence on the electricity consumption to maintain the indoor temperature condition.

In this sense, the thermal storage approach can manage the energy exchanged with the surrounding contributing to downsize the HVAC equipment, reduce the energy demand and increase the indoor thermal comfort. Also, energy storage components improve the energy efficiency of the systems by reducing the mismatch between supply and demand [9]. As mentioned above, this approach can be achieved by using two principles: sensible heat storage (SHS) or latent heat storage (LHS). This later is based on the heat capacity content and a variation in the temperature of the material, and therefore, thermal energy is stored by raising the temperature of a solid or liquid. In contrast, in LHS systems, such as PCMs, the heat absorption or release is generated by a phase change process [10].

Some previous studies [10, 11] have demonstrated a better performance of the LHS compared to SHS since they can passively cool and heat a living area without including heavy mass or high extra space typically required by SHS systems. The main reason is found when the latent heat and the sensible heat exchanged are compared. Consequently, the integration of PCMs in building walls, ceiling or floor is a good method to enhance the storage capacity of building envelope considering the advantages of high-energy storage density and the isothermal nature of these LHS systems [12, 13]. These materials foster the thermal inertia of the construction elements leading to lower temperature peaks.

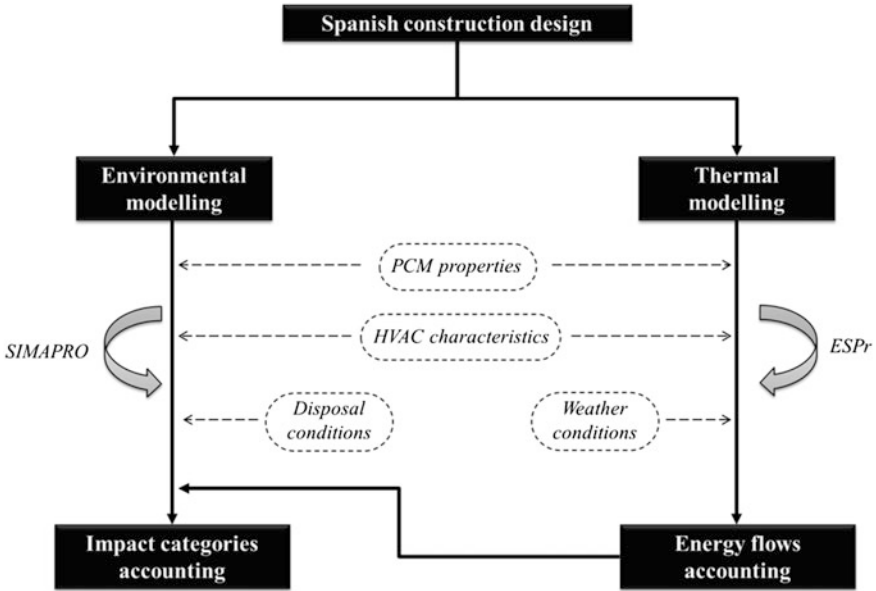
Nevertheless, selecting the appropriate PCM for the climate condition is essential to improve the heat transfer mechanism in the building since PCM performance is strongly influenced by the climate conditions as was reported by Aranda et al. [7]. It becomes even more complicated when the environmental impacts generated, due to the inclusion of PCMs in a building, must be considered for balancing them with those that can be obtained from the reduction of energy consumption and other benefits. To this end, the energy and environmental performance of these materials need to be evaluated following a whole methodology that allows obtaining results from both points of view as can be seen graphically in Fig. 1 and widely described in Sect. 2.

Therefore, this chapter is focused on modelling them using ESP-r to study the transport phenomena and SIMAPRO to evaluate midpoint environmental impact categories. This novel methodology shows how they can be integrated to improve industrial and technological applications of PCMs.

## 2 Methodology

### 2.1 PCMs Energy Modelling

The physical processes along a wall or in a room can be described from the governing equations of the fundamental principles of mass conservation, momentum and energy. Considering an arbitrary volume ( $V$ ) in a region of space, bounded by a closed surface ( $S$ ), the fundamental principles can be described by Eqs. (1), (2) and (3).



**Fig. 1** Schematic description of the methodology used in this study

$$\frac{\partial}{\partial t} \int_V \rho dV + \int_S \rho \vec{v} \cdot \vec{n} dS = 0 \quad (1)$$

$$\frac{\partial}{\partial t} \int_V \vec{v} \rho dV + \int_S \vec{v} \rho \vec{v} \cdot \vec{n} dS = \int_S \vec{n} \cdot \vec{\sigma} dS + \int_V \vec{b} \rho dV \quad (2)$$

$$\begin{aligned} \frac{\partial}{\partial t} \int_V (\mathbf{u} + \mathbf{e}_c) \rho dV + \int_S (\mathbf{u} + \mathbf{e}_c) \rho \vec{v} \cdot \vec{n} dS = & - \int_S \vec{q} \cdot \vec{n} dS \\ & + \int_S \vec{v} \cdot (\vec{n} \cdot \vec{\sigma}) dS + \int_V \vec{v} \cdot \vec{b} \rho dV + \int_V \phi \rho dV \end{aligned} \quad (3)$$

where  $\rho$  is the density,  $\vec{v}$  the velocity vector,  $\vec{n}$  the unitary vector perpendicular to the surface,  $\vec{\sigma}$  the external forces which includes pressure forces and viscous stress,  $\vec{b}$  the volumetric forces,  $\vec{q}$  the heat generation and  $\phi$  represents to an intensive property.

However, the heat transfer modelling in two-phase media or phase change process is much more complex than a single phase model.

According to several authors such as Regin [14] and Dutil [15], the main challenging tasks which hinder the thermal modelling of the phase change process can be described as,

- The moving boundary in the two phase interface
- The strongly non-linearity of the problem

- The buoyancy driven natural convection in the fluid interface
- The volume varies with the phase change in case of non-capsulated materials and the uncertainty of the interface thermal resistance between the container and the PCM when they are encapsulated
- The non-physical discontinuities between the two phases

In this regard, and especially due to the non-linear nature of the problem at moving interfaces where the displacement rate is dominated by the latent heat exchanged at the boundary, numerical analysis is generally required to obtain appropriate solutions for the thermal behaviour of two phase systems.

Finite difference methods (FDM) and finite element methods (FEM) are two popular techniques for numerical analysis. Nevertheless, several discretisation methodologies have been developed to characterised the heat transfer problem such as the variable grid method [16], the front fixing method [17] or adaptive grid generation method [18], being the fixed grid method the most extended [19].

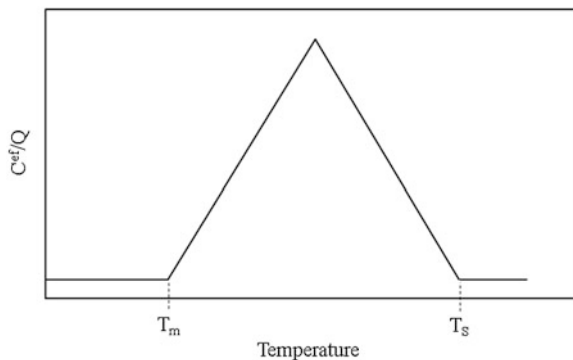
Specifically, in case of the phase change phenomenon, the heat transfer process should be modelled independently and there is a wide spectrum of additional numerical methods such as the Enthalpy Method (EM), the Effective Heat Capacity Method (EHCM) or the Heat Integration Method (HIM), where the interface position is neglected initially and the Stefan condition is assumed. The Stefan condition [20, 21] establishes the relationship between the latent heat fluxes in both sides of the phase change interface and provides the movement of the interface. This means that the amount of released latent heat due to the interface displacement and the net heat flow on the surface are equal. These methodologies are able to obtain a solution considering one or two phases.

The preferred two methods of phase change problem resolution are the EHCM and the EM. First of them is characterised by highly non-linear temperature and enthalpy dependence where the effective heat capacity is directly proportional to the stored and released energy during the phase change. The second method uses an enthalpy function as a dependent variable with the temperature. It can be graphically described as a small and width peak of capacity [22, 23].

ESP-r is an integrated energy modelling tool for the simulation of the thermal, visual and acoustic performance of buildings. This software is based on a finite volume conservation approach in which a problem (specified in terms of geometry, construction, operation, leakage distribution, etc.) is transformed into a set of conservation equations (for energy, mass, momentum, etc.) which are then integrated at successive time-steps in response to climate, occupant and control system influences [24]. The ESP-r control volume approach was adapted to describe the physical elements of the PCM model using ESP-r's zones and networks elements. Kelly [25] developed a module for ESP-r to analyse materials which are able to change their thermo-physical properties in response to some external excitation such as PCMs. In this sense, this module may be applied to a particular node within a multi-layer construction, and subsequently, to establish a time variation in the node basic thermo-physical properties [12].



**Fig. 2** Schematic representation of the effective heat capacity method



EHCM is the method applied by ESP-r to solve the phase transition in the PCM material. The method is based on a function of the latent heat of fusion and the temperature, which is defined by Eqs. 4, 5 and 6.

$$C_{ef} = \rho \cdot C_s \quad T < T_s \quad (4)$$

$$C_{ef} = \rho \cdot C_l + \frac{L}{T_m - T_s} T_s < T < T_m \quad (5)$$

$$C_{ef} = \rho \cdot C_l \quad T > T_l \quad (6)$$

Where  $L$  is the latent heat of fusion,  $T_m$  is the melting temperature, and  $T_s$  is the solidification temperature,  $C_s$  and  $C_l$  the specific heat capacity of the material in solid and liquid state respectively and  $\rho$  is the density.

As is described graphically in Fig. 2, considering a liquid–solid phase change material, this function has a narrow and finite width peak between melting and solidification temperatures where temperature fluctuations of the material are limited due to the phase change process.

However, when the temperature is lower than the melting point, the material is solid and thus, it is fully discharged. On the other hand, if the temperature is higher of the solidification temperature, the material is completely liquid and, therefore this means that it is storing energy [22].

Figure 3 shows the analysed building configuration considered for both case studies, one office including a PCM layer in the construction and another office without PCM. The buildings have the same dimensions, a plant of 16 m<sup>2</sup> and a height of 2.7 m. As can be seen in Fig. 3, there is a window in the south face which uses 35 % of the wall surface and a simple door in the north face of the office.

The construction of the offices used in the case studies was based on a typical Spanish residential structure according to the Spanish Technical Building Code [26]. Figure 4 describes graphically the layers and Table 1 shows the main physical and thermal properties of the different layers. The roof and ground are common in both buildings. The floor is made up of 5 layers consisting of earth (f),

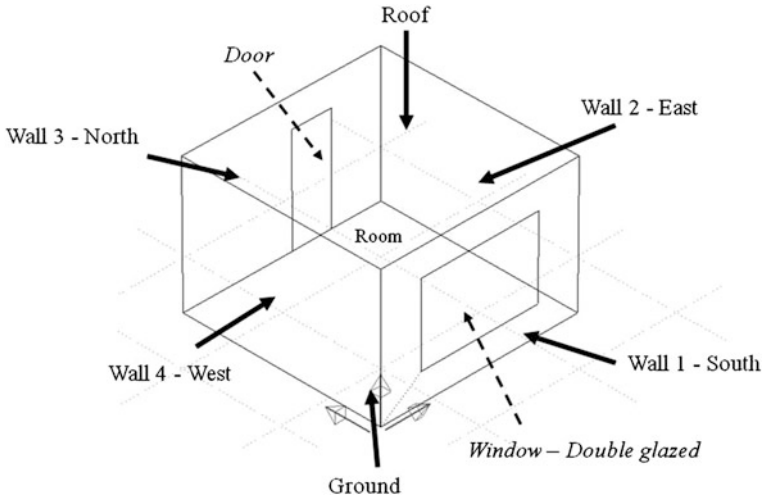


Fig. 3 Model description and orientation of the walls

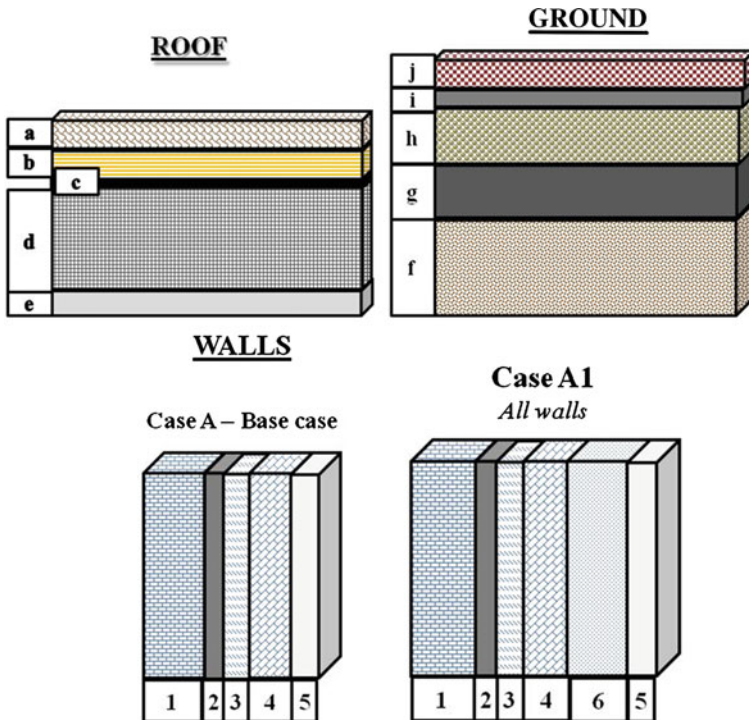


Fig. 4 Description of the main layers in roof, ground and walls of the building

**Table 1** Properties of the construction layers

	Thickness mm	Density kg/m <sup>3</sup>	Conductivity W/(m·K)	Specific heat capacity J/(kg·K)
<i>ROOF</i>				
a Ceramic outside tile	20	2,000	1	800
b EPS	20	30	0.029	1,000
c Bitumen	1	1,050	0.17	1,000
d Forged one-way concrete infilling	250	1,330	1.323	1,000
e Plasterboard (1,000 < d<1,300)	15	1,150	0.57	1,000
<i>GROUND</i>				
f Earth	350	2,000	0.52	1,840
g Mass concrete	150	2,150	1.65	1,000
h Sand and gravel	150	1,450	2.0	1,050
i Plastering mortar	15	1,900	1.3	1,000
j Inside tile	30	2,300	1.3	840
<i>WALL</i>				
1 Perforated ceramic brick	115	1,020	0.567	1,000
2 Plastering mortar	15	1,900	1.3	1,000
3 Insulation: mineral wool	20	40	0.04	1,000
4 Hollow brick (60 < E<90 mm)	70	930	0.432	1,000
5 Wall tile	20	2,300	1.3	1,000
6 PCM	3.5	300	0.25	2,000

mass concrete (g), sand and gravel (h), plastering mortar (i) and inside tile (j). The roof is structured also in five layers, a ceramic outside tile (a), an isolation material (b), bitumen (c), forged one-way concrete infilling (d) and plasterboard (e). The ground and roof description is common in both models.

On the other hand, the walls are made up of perforated ceramic brick (1), plastering mortar (2), isolation material (3), hollow brick (4) and tile (5). PCM model places the special material (6) between the hollow brick and the tile layers in the case study where PCM influence is analysed. In addition, a constant PCM load of 2.5 kg PCM/m<sup>2</sup> of the plant was distributed in the walls.

The operational details of the office have been implemented in ESP-r and they are based on a simple control loop with a constant set point within the comfort range temperature. The HVAC control set point is set in the established comfort range of temperature (21–24 °C), around 23 °C. When the room air temperature differs from this temperature, the HVAC equipment is activated being the maximum heating and cooling capacities 2,500 W. Internal gains as the gains from occupants, lighting or other electric appliances have not been applied to the model.

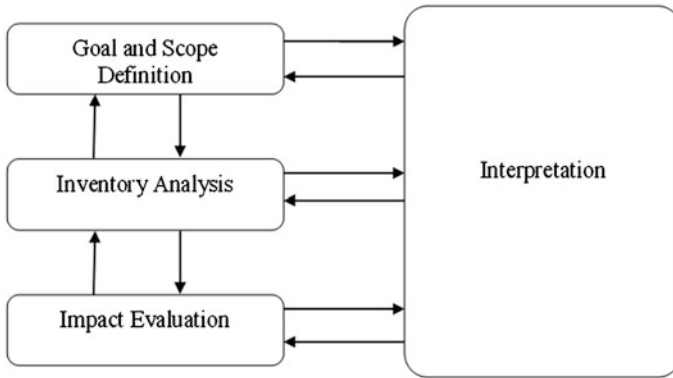


Fig. 5 Phases of an LCA

## 2.2 PCMs Environmental Modelling

The environmental analysis is based on the life cycle assessment (LCA) methodology to determine if environmental impacts and energy saving are large enough to balance those caused and consumed, respectively, during PCM manufacture and installation. LCA is a well-known methodology which has fully technically and scientifically proven for analysing the environmental impact of products and processes [27,28].

The structure of the LCA is proposed by the standard ISO 14040 [29,30]. Figure 5 shows that this methodology can be synthesised in four main phases. The first of them is focused on goal definition and scoping which defines the objective of the study, the functional unit and the limits of the system studied.

Since the studied system must be modelled as a complex sequence of unitary operations that communicate among themselves and with the environment through inputs and outputs from a life cycle perspective, clear boundaries of the system should be defined.

The second phase is the life cycle inventory (LCI) which represents the data gathering and the quantitative assessment procedures aimed at calculating the relevant inputs and outputs of a production system. This is an iterative process, which may be repeated if a need for further information emerges during its implementation.

The following phase is focused on the evaluation of the significance of the potential environmental impacts associated with data derived from the inventory phase. In this phase, the level of detail, the choice of the impacts to evaluate and the methods of evaluation depend on the objectives and scope of the study. The last phase covers the life cycle interpretation. In this phase, the interpretation of the results of the inventory phase and of the evaluation of impacts takes place, as well as obtaining all conclusions and recommendations for the improvement of the environmental performance.

Environmental impacts can be modelled from midpoint and endpoint approaches. The former are considered to be points in the cause-effect chain (environmental mechanism) of a particular impact category somewhere between stressor and endpoints [29]. This approach defines the environmental mechanism throughout the quantification of the impacts.

SIMAPRO v7.3.2 allows calculating midpoint indicators using different methods. One of the most recent and harmonised method available in this version is RECIPE. This method permits to calculate eighteen midpoint categories (e.g. ozone depletion, climate change, human toxicity, etc.).

## 2.2.1 Functional Unit and System Description

As commented above, materials and dimensions of the building envelope and PCM materials are modelled in ESP-r software to obtain the thermal behaviour through the walls and identify the benefits of integrating phase change materials in constructions elements. In this sense, two single zoned houses were developed on the building energy simulation package ESP-r. One of them incorporates the phase change material into the walls, whilst the other serves as a reference zone in order to gauge the effect of the PCM on heating and cooling loads.

For environmental analysis, the stages considered for analysing are: PCM and tile manufacturing, tile installation, use phase and PCM disposal and recycling. A non-common element between the environmental and energy analysis is the exclusion of conventional building construction materials in the former of them. Since the modification in the construction of the building with PCM is only due to inclusion of tiles doped with PCM, the environmental impact of these conventional materials is the same when comparing the case of a building without tiles. Consequently, the environmental analysis is deepened in all the stages that are necessary for manufacture, installation, removal and disposal of those tiles doped with PCM to balance them with the energy benefits obtained from the environmental analysis. Additionally, in this study, all transport stages, such as the transport of the PCM materials to the tile plant, are not included in the assessment due to the fact that the specific locations of the PCM seller, the tile plant, the building and the disposal sites are not known.

To allow the comparison of the different data, the functional unit used in this study was the standard building described before.

## 2.2.2 Climate Severities

The winter and summer climate severities (CS) quantify the climate conditions of every climatic area in the winter and summer, respectively. These variables are the result of the combination of the degree days and the solar radiation for the location studied. Their calculation comes from the Basic Document on Energy Saving (HE); section HE-1 included in the Spanish Building Technical Code [26].

**Table 2** Description of the main climate characteristic of the selected location [31]

	C1
Location	43°27'N 3°48'W
Climate	North Atlantic
Annual sunshine hours	1,638
Temperature range	4–25
Annual precipitation days	128

The winter climate severity is divided into five ranges of severity coded from A to E, where A is the lowest and E the highest severity. The summer climate severity is divided into four ranges, 1–4, from lowest to highest severity. In this regard, it is assumed that when the winter climate severity increases more energy heating is demanded. In case of summer climate severity, number 4 represents the highest energy cooling demand. Finally, if two locations have the same climate severity the energy demand associated is also the same.

There are 12 climate zones in Spain. In this study, one Spanish target area has been analysed following this criterion. C1 (Santander) has a high density of population [32] and medium winters and mild summers. Table 2 shows a more detailed description regarding the climate conditions of this location. The annual weather data associated and used in the simulation were acquired from the U.S. Department of Energy [33].

### 2.2.3 PCM Description

The PCM impregnated into porous construction materials can be based on organic (e.g. paraffin, fatty acids or polyethylene glycol) or inorganic (e.g. salt hydrates) compounds. In comparison to inorganic PCMs, the organic compounds show congruent phase changes, they are not dangerous because of their chemical stability, they can be recyclable and they have a good nucleation rate [13].

In this research, a commercial organic PCM based on paraffin and waxes is analysed. Table 3 presents the main thermal properties of this PCM where  $T_s$  is the fusion temperature,  $T_m$  is the melting temperature and  $L$  is the latent heat of fusion.

Different considerations have been followed to select this PCM: (1) the temperature of fusion of the material which should be in the range of comfort (21–24 °C) and the latent heat value which should also be high; (2) a commercial status; and (3) their usability by some industries in order to research new

**Table 3** Main properties of the PCMs considered in the research study

$T_m$ °C	$T_s$ °C	L kJ/kg
22	24	100

**Table 4** Life cycle inventory

Component/process	
Paraffin (kg)	40.00
Resin (kg)	93.8
$E_{\text{manufacturing-installation}}$ (kW h)	20

constructive elements. This is an important factor to obtain some data to be included in the environmental assessment.

### 2.2.4 Life Cycle Inventory

To develop the LCI, a constant PCM load of 2.5 kg PCM/m<sup>2</sup> has been taken into account as well as a specific quantity of resin to support the PCM layer in the tile structure. Table 4 shows the most relevant data included in the LCI for the commercial PCM selected in this research and considering the system boundaries defined.

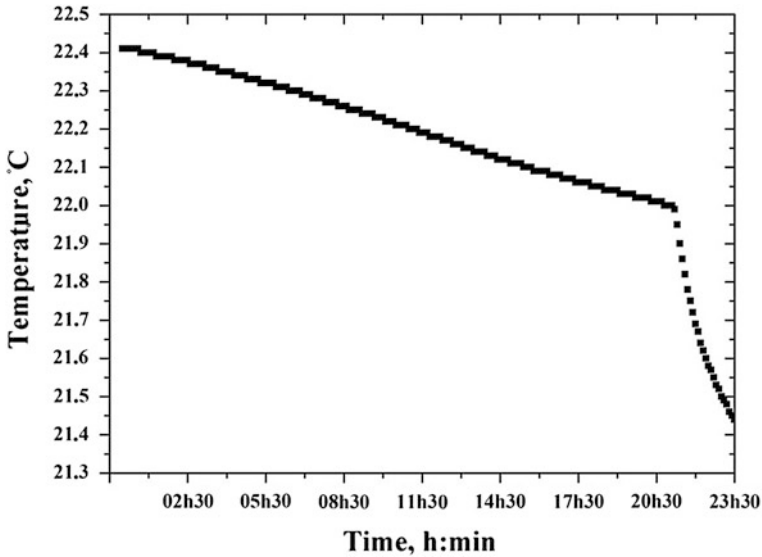
## 3 Results and Discussion

### 3.1 Effect of the PCM Addition on the HVAC Performance

In order to evaluate the effect of the introduction of the PCM material on the thermal modelling of the building and, thus, on the indoor dwelling conditions, predictions of the temperature gradient in the walls and the energy consumption in the HVAC systems for the base case study (without PCM) and case A (with PCM) were analysed under the climate severity C1.

To start with the results obtained, Fig. 6 shows the evolution of the PCM node temperature during a random day for the climate severity considered. As can be seen in Fig. 6, during the night the temperature in the phase change range is approximately stable. The main reason for this situation can be found in the fact that the PCM is discharging energy by means of the latent heat use in the phase change. However, when the PCM is completely solid, that means, it is out of the phase change temperature range, the temperature behaviour of the PCM is dominated by the sensible heat of the material and, therefore, a conventional variation of the temperature with the time is observed. In this case, a steeper slope dominates the PCM behaviour.

Additionally, Fig. 7 and Table 5 illustrate the annual energy consumption associated with the case studies involved in this research and the rate of energy saving achieved as a function of the HVAC mode in terms of heating and cooling demand in climate severity C1. In this case, the simulation demonstrates that a global reduction in energy demand is obtained by the use of PCM in the building construction.



**Fig. 6** Evolution of the PCM temperature during a random day

From the point of view of the annual energy savings, the results obtained in the simulations show that the 6.60 % of the total energy involved during the year can be avoided when the PCM are impregnated into porous construction materials.

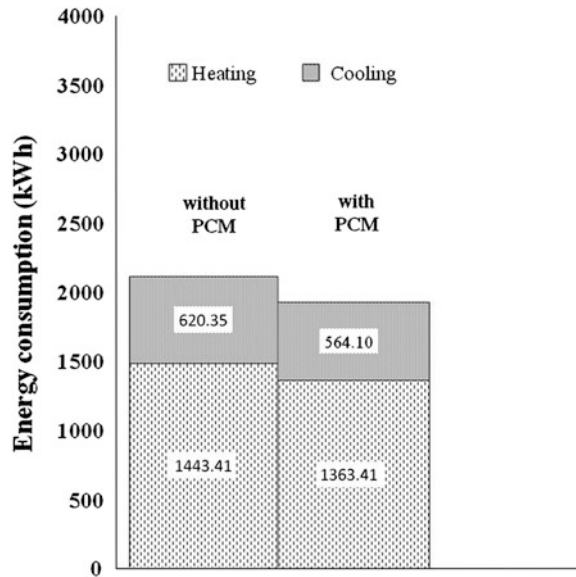
On the other hand, focusing on the HVAC system mode, data depicted in Table 5 conclude that the highest values in energy savings are obtained in the cooling mode considering that the evaluation has been performed under climate severity C1. Specifically, energy savings about 9.07 % can be achieved under this case study. However, the reductions obtained in the heating mode are quite low, since only 5.54 % of the energy involved in heating process is save by the introduction of PCM to the system.

Additionally, Table 6 shows the main energy savings obtained by annual season. In this case, higher savings are achieved in spring and autumn, 15.51 and 11.23 % respectively. The main reason for these results can be found when climate severity C1 is analysed. As was described in Table 2, this climate is characterised by medium winters and mild summers. Therefore, in winter, the outdoor temperature is lower than the phase change temperature, and rarely achieves the transition values. Similarly, in summer, temperatures are higher than the phase change temperature during all day. Therefore, in both cases the performance of the PCM by changing and discharging energy to the media is limited and higher consumptions in HVAC are found. In this cases energy savings are limited up to 2.78 % in winter and 2.12 % in summer seasons.

Nevertheless, in medium seasons as spring and autumn is possible to attain temperatures above the phase change material during the day, which decrease during the night under the phase change temperature transition. Next day, the



**Fig. 7** Annual energy consumptions by climate severity and the HVAC mode



**Table 5** Annual energy savings by PCM introduction considering HVAC mode

	Heating saving (%)	Cooling saving (%)	Total Saving (%)
C1	5.54	9.07	6.60

temperature rises again to complete other PCM transition cycle. In these cases, the PCM performance is enhancing and a higher number of charges and discharges are achieved by the PCM and thus, a relative descent in the HVAC equipment are observed.

Finally, focusing on the consumption by HVAC mode and annual season, a very low performance of the heating mode is observed in summer, as is depicted in Table 7. Nevertheless, summer season entails the highest values of cooling energy during the year. On the other hand, the highest performance on HVAC in heating mode is risen in winter.

Seasons as spring and autumn show middle energy values, although the difference between the energy consumption with PCM and without PCM is maximized, as mentioned before and observed in Table 6.

**Table 6** Energy saving by annual seasons (%)

	Winter	Spring	Summer	Autumn
C1	2.78	15.51	2.12	11.23

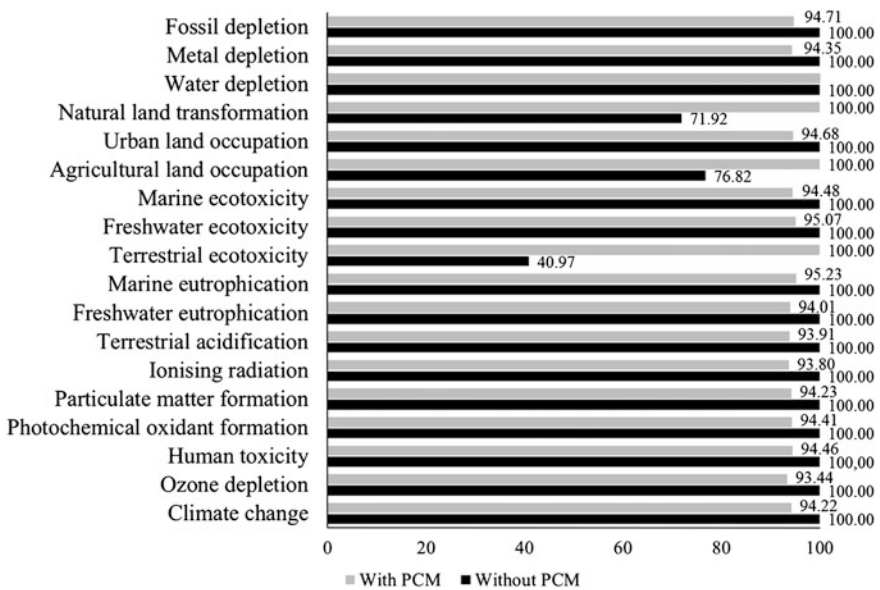
**Table 7** Energy loads by HVAC mode and annual season

	Heating (kWh)		Cooling (kWh)		Total (kWh)	
	with PCM	w/o PCM	with PCM	w/o PCM	with PCM	w/o PCM
Winter	765.97	784.19	6.50	10.39	772.47	794.58
Spring	223.75	251.45	48.27	70.50	272.02	321.95
Summer	0.14	0.92	453.18	462.23	453.32	463.15
Autumn	373.55	406.85	56.15	77.23	429.70	484.08

### 3.2 Effect of the PCM Addition on the Environmental Impact Assessment

The impact assessment was carried out with the purpose of evaluating the midpoint approach. To this end, the Recipe method with a time frame of 50 years was applied to evaluate it. This time value corresponds to the design working life in housing or office buildings, according to the Code of Structural Concrete EHE-08 approved by the Spanish Royal Decree 1247/2008 [26]. It is also assumed as a typical use stage time for a building in LCA research studies [34–36].

This study has demonstrated that the results obtained are strongly influenced by the energy involved during the use stage of the building, observing similar trends to those obtained in the analysis of the energy calculations. This means that during the useful life of the building the impacts associated with the manufacture of the



**Fig. 8** Environmental impacts of (%) the PCM analysed for the most relevant impact categories in climate severity CI

PCMs, their installation in the construction materials and their disposal stage are fully recouped through the benefits obtained by the decrease of the electrical consumption during the use stage.

As is depicted in Fig. 8, only three impact categories (agriculture land occupation, terrestrial toxicity and agriculture land transformation) show higher environmental impacts when the PCM is introduced. In this case, the PCM addition, represented by the material, process manufacturing and disposal stage, has a strong influence and the stage of use in the building lifetime is not able to compensate the environmental impacts.

However, analysing globally all the impact categories higher environmental benefices are observed by the impregnation of phase change materials (PCMs) into porous construction materials to enhance indoor-dwelling temperature conditions.

## 4 Conclusions

Results have demonstrated that tiles doped with PCM materials can be used to reduce the energy consumption needs keeping constant the occupant level comfort. It is shown that energy saving is not only dependent on the physical and thermal characteristics of the PCM, such as the fusion temperature, latent heat, etc., but also is affected by the climate severity. The environmental analysis has demonstrated that it is highly influenced by energy savings obtained by the use of PCM in a lifetime of 50 years of a building following a midpoint approach and using RECIPE method. In this sense, environmental impacts in dwellings where PCMs are involved in the construction are lower in most of the environmental categories than those where only conventional materials are used.

In addition, results reveal the importance of the PCM selection considering thermal and environmental conditions as one significant path to achieve a sustainable industrial and technological application of these materials. It establishes an innovative guideline to apply PCMs taking into account both energy and environmental modelling considering building locations.

**Acknowledgments** Alfonso Aranda-Usón and Ana M. López-Sabirón like to thank Spanish Government for financial support through the framework of the ECOM4TILE project (IPT-2011-1508-920000) co-financed by the Spanish Ministry for Science and Innovation.

## References

1. International Energy Agency (IEA): (2010) Energy balances of OECD countries. Paris
2. French Ministry of Ecology And Sustainable Development: (2004) Climate plan 2004: let's act together to challenge of climate change. Technical report
3. Aranda, A., Ferreira, G., Mainar-Toledo, M.D., Scarpellini, S., Llera Sastresa, E.: Multiple regression models to predict the annual energy consumption in the Spanish banking sector. *Energ. Buildings* **49**, 380–387 (2012)

4. Korolija, I., Marjanovic-Halburd, L., Zhang, Y., Hanby, V.I.: Influence of building parameters and HVAC systems coupling on building energy performance. *Energy Buildings* **43**, 1247–1253 (2011)
5. Ruiz, M.C., Romero, E.: Energy saving in the conventional design of a Spanish house using thermal simulation. *Energy Buildings* **43**, 3226–3235 (2011)
6. Ortiz-Rodríguez, O., Castells, F., Sonnemann, G.: Life cycle assessment of two dwellings: one in Spain, a developed country, and one in Colombia, a country under development. *Sci. Total Environ.* **408**, 2435–2443 (2010)
7. Aranda-Usón, A., Ferreira, G., López-Sabirón, A.M., Mainar-Toledo, M.D., Bribian, I.Z.: Phase change material applications in buildings: an environmental assessment for some Spanish climate severities. *Sci. Total Environ.* **444**, 16–25 (2013)
8. Zhou, S., Zhao, J.: Optimum combinations of building envelop energy-saving technologies for office buildings in different climatic regions of China. *Energy Buildings* **57**, 103–109 (2013)
9. Pasupathy, A., Velraj, R., Seeniraj, R.V.: Phase change material-based building architecture for thermal management in residential and commercial establishments. *Renew. Sustain. Energy Rev.* **12**, 39–64 (2008)
10. Sharma, A., Tyagi, V.V., Chen, C.R., Buddhi, D.: Review on thermal energy storage with phase change materials and applications. *Renew. Sustain. Energy Rev.* **13**, 318–345 (2009)
11. Zhang, Y., Zhou, G., Lin, K., Zhang, Q., Di, H.: Application of latent heat thermal energy storage in buildings: State-of-the-art and outlook. *Build. Environ.* **42**, 2197–2209 (2007)
12. Heim, D., Clarke, J.A.: Numerical modelling and thermal simulation of PCM–gypsum composites with ESP-r. *Energy Buildings* **36**, 795–805 (2004)
13. Kuznik, F., David, D., Johannes, K., Roux, J.-J.: A review on phase change materials integrated in building walls. *Renew. Sustain. Energy Rev.* **15**, 379–391 (2011)
14. Regin, A.F., Solanki, S.C., Saini, J.S.: Heat transfer characteristics of thermal energy storage system using PCM capsules: a review. *Renew. Sustain. Energy Rev.* **12**, 2438–2458 (2008)
15. Dutil, Y., Rousse, D.R., Salah, N.B., Lassue, S., Zalewski, L.: A review on phase-change materials: mathematical modeling and simulations. *Renew. Sustain. Energy Rev.* **15**, 112–130 (2011)
16. Murray, W.D., Landis, F.: Numerical and machine solutions of transient heat conduction problems involving melting or freezing. *J. Heat Transf.* **81**, 106–112 (1959)
17. Voller, V.R.: An overview in numerical methods for solving phase change problems. In: Minkowycz, W.J., Sparrow, E.M. (eds.) *Advances in numerical heat transfer*, vol I. Taylor and Francis, London (1997)
18. Provatas, N., Goldenfeld, N., Dantzig, J.: Adaptive mesh refinement computation of solidification microstructures using dynamic data structures. *J. Comput. Phys.* **148**, 265–290 (1999)
19. Feulvarch, E.: An implicit fixed-grid method for the finite-element analysis of heat transfer involving phase changes. *Numer. Heat Transfer* **51**, 585–610 (2007)
20. Fukusako, S., Seki, N.: Fundamental aspects of analytical and numerical methods on freezing and melting heat transfer problems. *Annual review of numerical fluid mechanics and heat transfer*, vol 1. Hemisphere (1987)
21. Viskanta, R.: Heat transfer during melting and solidification metals. *J. Heat Transf.* **110**, 1205–1219 (1988)
22. Heim, D.: Two solution methods of heat transfer with phase change within whole building dynamic simulation. Ninth International IBPSA Conference, Montréal, Canada. Aug 15–18 2005, pp. 397–402
23. Lamberg, P., Lehtiniemi, R., Henell, A.-M.: Numerical and experimental investigation of melting and freezing processes in phase change material storage. *Int. J. Therm. Sci.* **43**, 277–287 (2004)
24. Hand, J.W.: *The ESP-r cookbook. Strategies for deploying virtual representations of the build environment.* Energy Systems Research Unit (ESRU). University of Strathclyde, Glasgow (2010)

25. Kelly, N.J.: Towards a design environment for building integrated energy systems: the integration of electrical power flow modeling with building simulation. University of Strathclyde, (1998)
26. Ministry of Development: Government of Spain 2008. Code on Structural Concrete (EHE-08)
27. Rebitzer, G., Ekvall, T., Frischknecht, T., Hunkeler, D., Norris, G., Rydberg, T., Schmidt, W.P., Suh, S., Weidema, B.P. & Pennington, D.W.: Life cycle assessment: Part I: Framework, goal and scope definition, inventory analysis, and applications. *Environ. International*. **30**, 701–720 (2004)
28. Society of Environmental Toxicology and Chemistry (SETAC) Portugal 1993. Guidelines for Life Cycle Assessment. A Code of Practice
29. Guinee, J., Gorrée, M., Heijungs, R., Huppes, G., Kleijn, R., De Koning, A.: Life cycle assessment - an operational guide to the ISO standards. Leiden University Centre of Environmental Sciences (CML), (2001)
30. International Organization for Standardization: ISO 14040:2006—Environmental Management—Life Cycle Assessment—Principles and Framework. Geneva, Switzerland, (2006)
31. State Meteorological Agency of Spain (AEMET): Municipal weather data. (Online). Available: [www.aemet.es](http://www.aemet.es) (2011)
32. National Statistics Institute of Spain 2012: Geographic and demographic database. Spain
33. Energy Efficiency and Renewable Energy: U.S. Department Of Energy Weather Database
34. Assefa, G., Glaumann, M., Malmqvist, T., Kindembe, B., Hult, M., Myhr, U., Eriksson, O.: Environmental assessment of building properties. Where natural and social sciences meet: the case of EcoEffect. *Build. Environ.* **42**, 1458–1464 (2007)
35. Malmqvist, T., Glaumann, M., Scarpellini, S., Zabalza, I., Aranda, A., Llera, E., Díaz, S.: Life cycle assessment in buildings: the ENSLIC simplified method and guidelines. *Energy* **36**, 1900–1907 (2011)
36. Mora, R., Bitsuamlak, G., Horvat, M.: Integrated life-cycle design of building enclosures. *Build. Environ.* **46**, 1469–1479 (2011)

# Magnetic Silica Nanocomposites as Optical Tools in Biomedical Applications

Tinkara Mastnak, Matejka Turel, Aljoša Košak, Špela Korent Urek and Aleksandra Lobnik

**Abstract** As a result of their size and versatile chemistry, today's nanomaterials represent powerful tools for several biomedical applications. Various types of nanomaterials have proven to be practical, not only for determining clinically relevant parameters, but also for diagnostics, drug delivery and the treatment of diseases (e.g., cancer). Of particular promise are those nanocomposite structures with multifunctional capabilities. In this chapter we focus on magnetic silica nanocomposites, combined with an optical component, such as organic fluorescent dyes or quantum dots. The most important characteristics of these nanomaterials are presented, together with their specific uses in biomedical applications. It was observed that findings based on in-vitro measurements were not always in agreement with in-vivo applications. Additionally, the use of these nanocomposites in clinical trials remains a long-term goal.

**Keywords** Multifunctional nanoparticles · Core-shell structure · Magnetic material · Silica · Fluorescence · Biomedical applications

## 1 Introduction

Nowadays, engineering at the molecular level is seeing exponential growth in clinical science because of the availability of new investigative “nanotools”. Nanometer-sized materials used as analytical tools promise to overcome the

---

T. Mastnak · A. Košak · A. Lobnik (✉)  
University of Maribor, Faculty of Mechanical Engineering, Centre of Sensor Technology,  
Smetanova 17 SI-2000 Maribor, Slovenia  
e-mail: aleksandra.lobnik@um.si

M. Turel · A. Košak · Š. Korent Urek · A. Lobnik  
Institute for Environmental Protection and Sensors, Beloruska 7 SI-2000 Maribor, Slovenia

limitations in sensitivity and specificity in current medical diagnostic and therapeutic applications. Nanomaterials have the potential to characterize the chemical and mechanical properties within individual living cells, discover novel phenomena and processes, help in the development of new modalities for early diagnostics, and be the basis for medical treatments and prevention beyond the cellular level to that of individual organelles and even deoxyribonucleic acid (DNA), the building blocks of life [1]. Diverse applications may include nanomaterials in bioimaging, cell-tracking, sorting, bioseparation, bio- and chemosensing as well as in therapeutic applications (monitoring diseased cells and drug delivery) [1–13]. The usefulness of nanoparticles (NPs) is mainly derived from their small size, large surface area, and the kinetics for in-vivo drug delivery [4]. They enable the creation of multimodal, multifunctional “nano-agents” by functionalizing their surfaces with targeting ligands, imaging and therapeutic moieties [5]. Modification with multivalent targeting ligands makes it possible to amplify signals [14], improve avidity [15, 16], enhance binding [17] and translate molecular interactions into measurable electrical, optical, or magnetic signals. In particular, magneto-fluorescent NPs allow for dual read-outs by optical (e.g., flow cytometry, immunofluorescence) [5] and magnetic sensing (e.g., nuclear magnetic resonance or magnetoresistive detection) [18–20]. Nevertheless, for such nanoparticles to be considered for clinical trials, several criteria, such as a favorable distribution and targeting kinetics, efficient renal clearance, extended circulation, and improved tumor penetration, should be comprehensively defined.

### ***1.1 Multifunctional Nanoparticles***

Multifunctionality lies in the synchronous exploitation of different functionalities (i.e., fluorescence, magnetism and targeting moieties) of a nanostructured system. Such combinations provide the possibilities for a broad range of potential applications. The magnetic-fluorescent assays can be beneficial for in-vitro and in-vivo applications in bio-imaging, i.e., in magnetic resonance imaging (MRI) as well as in fluorescence microscopy [21–29]. Nanocomposites can be used as agents in nanomedical photodynamic and hyperthermic approaches [6, 30, 31], in diagnostics and as therapeutic tools for the simultaneous visualization and treatment of various diseases [5, 32–35]. However, the most important criteria when designing nanoprobes in the field of diagnostics and therapeutic applications is their biocompatibility and biodegradation, along with defined composition, size and surface functionalities and vigorous in-vitro and in-vivo testing for their safety and efficiency. In order to achieve these multifunctional properties, several steps in the synthesis procedure, along with many purification stages, are required. Consequently, careful planning and an accurate synthesis methodology are necessary. This is particularly important in order to avoid the quenching of fluorescent dyes attached to the particles or possible particle aggregation and precipitation. With sequential growth or coating a further combination of nanomaterials with other

functional nanostructures is able to produce a single, complex entity with multiple functions that have nanoscale dimensions and the desired functional properties. The design of various new nanocomposite materials has been the subject of much research by a variety of authors [36–49].

This chapter focuses on nanocomposite materials used in biomedical applications that combine a) magnetic characteristics (based on iron-oxide NPs), b) silica material and c) an optical component based on a variety of organic dyes, quantum dots (QDs) or up-converting phosphors (UCPs). The emerging technology of such NPs not only allows visualization, but can also provide a magnetically controllable means to investigate the physiological functions and phenomena in tissues as well as in an individual cell.

## ***1.2 Properties of Magnetic Particles***

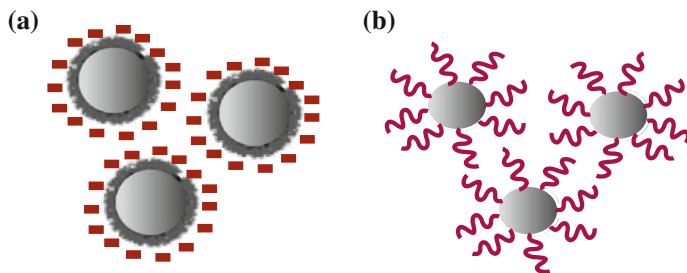
### **1.2.1 Magnetic Nanoparticles and Magnetic Fluids**

The magnetic nanomaterials in biomedical applications are usually in the form of colloidal magnetic liquids or ferrofluids, which are stable dispersions of magnetic nanoparticles in an organic or aqueous carrier medium. The magnetic nanoparticles (MNPs) in the ferrofluid should be biocompatible, inert and chemically stable. To achieve this, the size and the shape of the magnetic nanoparticles should be suitably chosen, and the surfaces of the magnetic nanoparticles should be modified to ensure their stability in the carrier liquid.

The magnetic material most often used is iron oxides, usually in the form of magnetite ( $\text{Fe}_3\text{O}_4$ ) or maghemite ( $\gamma\text{-Fe}_2\text{O}_3$ ), and the carrier liquids are usually water or various biocompatible oils. Due to their small size, the magnetic nanoparticles in carrier liquids do not sediment in a gravitational field, nor do they agglomerate due to a magnetic dipole interaction in the magnetic field gradient [50]. However, a stable suspension can only be achieved if the particles are protected against agglomeration due to the van der Waals interaction. This protection can normally be achieved by using two approaches, as shown in Fig. 1 [51, 52]. The first is called electric charge stabilization, in which a thin homogenous layer is coated on the surface of the nanoparticles. In the second a thin homogenous layer can serve as an ideal base on which chemical or biological molecules can be additionally functionalized and thus generate a repulsive force preventing the nanoparticles from colliding and thus suppressing the destabilizing effect of the van der Waals interaction [53]. In practical applications, these two approaches allow the synthesis of stable ferrofluids [51].

To obtain a stable ferrofluid in physiological media at neutral pH and with the appropriate ionic strength, the particle surfaces are usually coated with dextran, albumin or synthetic polymers such as methacrylates and organosilanes, and further functionalized with biological entities (antibodies, oligonucleotides, peptide ligands, etc.), which are covalently attached to the particle coating. The stability of





**Fig. 1** Two approaches to the protection of a magnetic core: **a** electric charge stabilization [51]; **b** organic molecule stabilization [52]

the coating determines the stability of the complex “particle surface – biological unit” [50, 54].

### 1.2.2 Magnetic Properties of Magnetic Fluids and Multifunctionality

One of the key points in biomedical applications is controlling the manipulation of ferrofluids. This is usually realized with external magnetic fields. The magnetic properties of ferrofluids made up of magnetic nanoparticles tagged to biological entities or therapeutic drugs, and stably dispersed in a physiological medium, are very important. Ferrofluids and the magnetically tagged biological molecules and therapeutic drugs, can be manipulated using an external magnetic field. This is important for transporting therapeutic drugs to the disease sites [55].

To realize the manipulation of ferrofluids and perform the desired biomedical functions, the physical properties of ferrofluids should satisfy special requirements. The typical physical properties of ferrofluids include viscosity and magnetic relaxation. Usually, the magnetic nanoparticles in ferrofluids that play important roles in biomedical applications have a superparamagnetic characteristic [55]. The magnetization of superparamagnetic nanoparticles under an external magnetic field is independent of the direction of the applied magnetic field, and it is realized through the coherent rotation of spins. Superparamagnetic nanoparticles will thus rotate under an external uniform magnetic field, and will make translational movements under an external magnetic field gradient. When the magnetic field applied to magnetic nanoparticles is removed, the magnetization of the magnetic nanoparticles relaxes back to zero due to the thermal energy of their environment. These magnetic properties are also dependent on the size of the MNPs. As the particle size decreases below a critical diameter,  $D_{\text{crit}}$ , the formation of single-domain particles becomes energetically favorable. The critical single-domain sizes for spinel iron-oxide spherical nanoparticles are estimated to be  $D_{\text{crit}} = 128$  nm for magnetite ( $\text{Fe}_3\text{O}_4$ ) and  $D_{\text{crit}} = 166$  nm for maghemite ( $\gamma\text{-Fe}_2\text{O}_3$ ) [54, 56].

As MNPs are promising candidates for clinical applications due to their unique magnetic properties and biocompatibility, a great deal of effort has recently been

made to create multifunctional magnetic nanoparticles for diagnostic and/or therapeutic applications, such as drug and gene delivery [57, 58], hyperthermia treatment [30] and as contrast agents in magnetic resonance imaging (MRI) [18–20, 59, 60]. Considerable research has been devoted to a combination of magnetic and optical (fluorescent) properties in a single nanocomposite and used for multi-targeting, multifunctional and multi-treating tools in target enrichment, separation, imaging, and detection [22, 33, 48, 57, 61, 62]. For the optical component, fluorescent dye molecules and QDs are also one of the most commonly used materials in combination with magnetic nanoparticles. In addition, Gd(III) complexes with magnetic nanoparticles are widely used to increase the sensitivity of magnetic resonance imaging (MRI). Gd(III) chelates that are grafted onto a solid magnetic support provide a highly efficient imaging agent [63, 64]. However, this chapter focuses only on the application of iron oxide (magnetite, maghemite and cobalt-ferrite) as the magnetic material in multifunctional composite nanoparticles.

### ***1.3 Properties of Silica Particles***

Silica nanoparticles (SiNPs) possess important properties that have made them very useful in bioanalysis, i.e., an extremely high optical intensity, high photostability, easy bioconjugation and controllable porosity. If appropriate synthetic conditions and particles (there can be tens of thousands of dye molecules) are used, a large number of dye molecules (either organic or inorganic) can be incorporated inside a single silica particle. Compared with polymer-based NPs, SiNPs show less aggregation and only little dye leakage [65]. With dye doping it is possible to obtain a very bright luminescence, although some fluorescence quenching occurs upon immobilization within the NPs, while photobleaching and photodegradation are usually reduced because the dye is protected from the surrounding environment. The optical signal is highly amplified compared to a single dye molecule, and when applied to bioanalysis, SiNPs provide an enhanced analytical sensitivity [66]. Due to its excellent photostability, the silica is suitable for applications where a high intensity or prolonged excitations are required. The flexible silica chemistry provides versatile routes for surface modification, because different types of functional groups can be easily introduced onto the NPs for conjugation with biomolecules [67]. Moreover, the silica surface makes these NPs chemically inert and physically stable [68]. All these properties make SiNPs excellent labeling reagents for bioanalysis in immunoassays [26–28, 69], bio-imaging [28, 70–73], multiplexed bioanalysis [69, 74] and drug delivery [58]. When a silica coating is used as shell for the MNPs this makes the MNPs biocompatible. The noncovalent surface modification of MNPs could have serious limitations for biological applications, because the exposed metal ion on the surface of the MNPs can cause metal elemental toxicities in cells [75]. The biocompatibility and flexibility of the silica material can be further enhanced by its surface functionalization with

thiol- or amino-silane precursors, which renders its surface amenable to covalent bonding with the desired biofunctional groups [24, 76, 77].

### 1.3.1 Mesoporous Silica

Silica is also a very popular material for designing mesoporous materials (MPSi) that are very suitable for drug-delivery applications [10, 29, 35, 76, 78–83]. The MPSi is obtained after the removal of the structure-directing agent leading to opening of the porosity, which allows high levels of drug loadings to be achieved. The straight channels allow for adsorbed drugs to diffuse out in a controlled manner over time frames that depend on the drug (size and chemical composition), the release medium, the pore size, the surface functionalization and the particle size and morphology. Typically, alkoxysilanes are used as silica precursors, and the use of mixtures of silanes allows for the direct or indirect incorporation of functional groups like  $-R-NH_2$ ,  $-R-COOH$ , and  $-R-SH$  onto the pore surfaces. Alternatively, functional groups can be introduced in a separate post-synthesis step, including the attachment of additional surface layers, such as poly(ethylene glycol) for minimizing the nanoparticle opsonization [84]. The release of a drug from a mesoporous structure can be controlled by the surface modification of the MPSi [80]. Furthermore, there are two functional surfaces (the particle exterior and the interior pore faces) and a modifiable morphology (controllable particle shape and size). MPSi also offers the possibility to effectively protect the pharmaceutical cargoes, such as drugs, imaging agents, enzymes, and oligonucleotides, from premature release and undesired degradation in harsh environments, such as the stomach and intestines, before reaching the designated target [85]. The characteristic properties of MPSi affect the interactions with biological components such as cells, tissues and molecules [86]. However, a detailed understanding of the behavior of MPSi in biological systems and exhaustive preclinical testing are needed to push the technology towards a clinical standard.

## 1.4 *Optical Components used in Magnetic Silica Nanocomposites*

The use of fluorescent probes has great potential not only in chemical and biochemical sensing [2, 14, 22, 58, 87–92], but also in the early detection of diseases, e.g., cancer [93].

Fluorescent probes can be used as contrast agents in optical imaging (OI) for the visualization of many different phenomena [10, 18, 35, 76, 78, 81, 94]. Compared to magnetic resonance imaging (MRI), the sensitive fluorescent agents in optical imaging systems can detect pico-to-nanomolar concentration ranges, while micro-to-millimolar is possible with MRI [10, 18, 34, 36, 76, 80, 93].

Another major advantage of OI is that it releases no ionizing radiation and could thus also be repeatedly used in the treatments of young people. This is in contrast to the large dose of radiation that is usually obtained from X-ray, computed tomography and positron-emission tomography. Since the penetration of light through the body tissue is limited, OI is possible with near-infrared (NIR) probes [24, 26, 93, 95, 96]. Today, the only two NIR fluorophores approved for clinical use by the U.S. Food and Drug Administration (FDA) are indocyanine green [95, 96] (ICG) emitting at approximately 800 nm and methylene blue (MB) emitting at approximately 700 nm.

However, other optical probes that have recently been applied in magnetic silica nanocomposites in several biochemical approaches, including diagnostics and imaging, are organic dyes (fluoresceins, rhodamines, cyanines) [24, 28, 67, 70, 73, 76, 97–99], quantum dots (e.g., CdSe/ZnS) [22, 80, 87, 91, 100–106] and up-converting phosphors (e.g., Yb, Er, Tb) [100–103]. The most common are fluorophores, such as fluoresceins (e.g., fluorescein isothiocyanate—FITC), rhodamines (e.g., rhodamine B isothiocyanate—RITC), and cyanines (e.g., Cy5.5). Rhodamines are supplements to fluoresceins, as they offer longer wavelength-emission maxima and provide opportunities for multicolor labeling or staining [81, 102]. DNA sequencing, microarray detection and fluorescence in situ hybridization (FISH) demand a number of fluorophores with distinct spectra. Rhodamines exhibit a higher photostability than fluorescein. Isothiocyanates and succinimidyl esters are available for convenient labeling [27, 101, 107–109]. Porphyrins are a class of near-infrared (NIR) fluorophores that have mostly been used in photodynamic therapy as photosensitizers to treat tumor cells, but they are also useful for in-vivo imaging studies [110, 111].

The drawbacks of organic fluorophores are their narrow excitation bands and broad emission bands with red spectral tails. For this reason, spectral overlaps can make the simultaneous monitoring of several fluorophores problematic. Many organic dyes also exhibit low photostability.

QDs are semiconductor nanocrystals that exhibit unique electro-chemiluminescent properties, strong light absorbance, bright fluorescence, size-tunable narrow emission spectra, and provide excellent fluorescence quantum yields and minimal photobleaching [89]. QDs are applicable for the labeling of biomolecules (peptides, proteins, cells, nucleic acids) and considered as an attractive alternative to traditional organic dyes [107]. QDs bind to target biomolecules through electrostatic interaction, covalent cross-linking or via the implication of specific tagging molecules. QDs can be designed to emit light at any wavelength from the infrared to visible/ultraviolet. This enables the use of a large number of colors and thus multiplexed assays can be performed [112, 113]. In contrast, a parallel analysis of different analytes is difficult to accomplish using organic dyes due to the lack of multicolor signaling at a single wavelength excitation. Moreover, the intrinsic limitations of organic dyes associated with narrow absorption and broad emission spectra can be successfully circumvented through the use of these inorganic fluorophores [107]. When specifically attached to biological materials, QDs represent powerful tagging agents for viruses [90, 100] and cancer cells [101–103].

QDs can be used as contrast agents for in-vivo tumor imaging [104, 105] or for the detection of some other clinically relevant parameters, such as glucose [87, 114], proteins [91], pathogenic bacteria [92, 115], etc.

NPs prepared using lanthanide ions like  $Tb^{3+}$ ,  $Eu^{3+}$ ,  $Sm^{3+}$ ,  $Gd^{3+}$ ,  $Yb^{3+}$ ,  $Er^{3+}$  are attractive due to their photostability, the usual presentation of a sharp emission spectrum ( $<10$  nm), a long fluorescence lifetime and a large Stokes shift ( $>150$  nm). Their surfaces can be easily modified without significantly altering their properties. These characteristics make lanthanide-based NPs suitable for use as biolabels since they enable the elimination of background and scattered fluorescence, allowing a delayed measurement on the scale of microseconds. The emissions of some lanthanides (e.g.,  $Gd^{3+}$ ) in the NIR region with NIR excitation make it possible to reach deep tissue, while avoiding photodamage to biological specimens. Lanthanide NPs do not suffer from blinking and possess excellent up-conversion fluorescence [116, 117]; therefore, these materials are also known as up-converting phosphors (UcPs). Their characteristics enable them to circumvent some of the functional limitations usually encountered by organic dyes (low optical background, high photostability and reduced instrumentation cost). The UcPNPs have been used in the development of immunoassays [118, 119], time-resolved fluorescence imaging [120, 121], drug delivery and therapy [116, 122], specific targeting [25], DNA detection [123], glucose detection [124], etc.

## 2 Structures of Magnetic Silica Nanocomposites

Various compositions incorporating materials, such as magnetic, silica and light-emitting probes, are possible for creating multifunctional nanosystems. Such structures are usually prepared via a so-called core-shell or layer-by-layer approach. Core-shells are NPs that have a core made from one material and a shell made from another. Since such an architecture offers a great opportunity to modulate the properties of both components, it continues to be the focus of many scientific efforts [125]. In a core-shell system the favorable properties of the core are maintained, while the shell functions to provide additional stabilization, passivation or chemical functionality [54]. The core-shell structure enhances the thermal and chemical stability of the NPs, improves the solubility, makes them less cytotoxic and allows the conjugation of other molecules to these particles [7, 11, 126].

Various structures were proposed by researchers within magnetic-silica-optical nanocomposites that can be used in biomedical applications, where the optical component is usually embedded or covalently linked to the silica matrix:

- (a) the core is mostly a magnetic nanoparticle, which is coated with a silica shell [7, 33, 75, 127, 128],
- (b) the core can be made of silica and the magnetic material is coated around the silica [129],

- (c) magnetic NPs can be cross-linked to the silica core surface to obtain a core-satellite composite [18],
- (d) the silica nanoparticle can incorporate magnetic nanocrystals [126],
- (e) the composite can be prepared as a mesoporous silica nanoparticle with multiple magnetite nanocrystals covering its surface [76] or being embedded inside the particle [80],
- (f) a special class of core-shell nanostructures, the so-called yolk-shell nanocapsules, which have magnetic movable cores, interstitial hollow spaces between the movable core and shell sections, and the functional shells [29].

Figure 2 shows the schemes of the most common structures used in the synthetic preparation of magnetic-silica-optical nanocomposite particles.

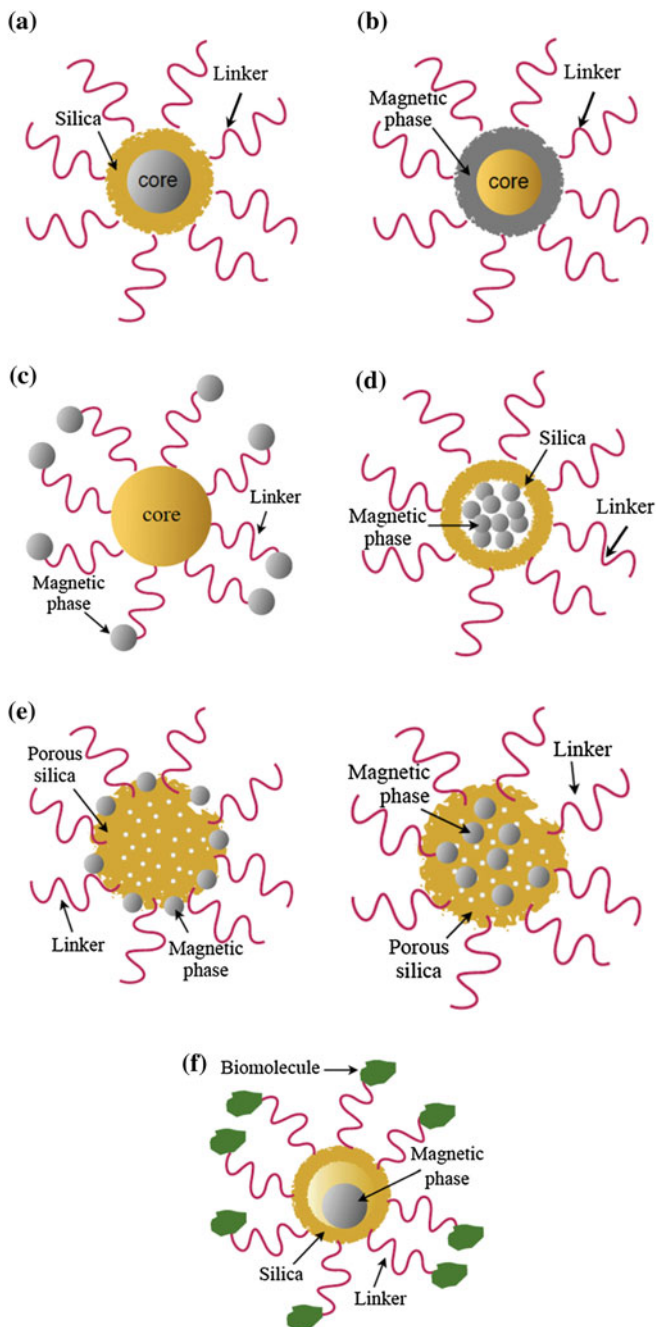
## ***2.1 Properties to be Considered When Designing Composite Nanoparticles Useful for Biomedical Applications***

The particles' physicochemical properties and the targeting ligand functionalization should be carefully considered for an optimal design that would enable the rapid clearance of the particles from the body. The first important issue is the size of the NPs. Without the clearance or biodegradation into biologically benign components, the toxicity is potentially amplified [106]. It was reported that particles with sizes between 10 and 100 nm are the best for intravenous injection and have the most prolonged blood-circulation times. These particles are small enough to evade the reticuloendothelial system (RES) of the body as well as to penetrate the small capillaries of the tissues and offer the most effective distribution in targeted tissues [130].

The second important property is the surface charge, where the positively charged NPs are known to generate a higher immune response compared to neutral or negatively charged NPs, and it was somehow proposed that a surface charge between  $-10$  and  $+10$  mV is the best for minimized nonspecific binding and rapid clearance from the blood stream [131].

Surface modification by the so-called pegylation of NPs is the third important factor that favors various physicochemical properties [130]. Pegylation is achieved with polyethylene glycol (PEG) or with other materials like polylactic acid (PLA), PLA-PEG, poly(glycolic acid), and poly( $\epsilon$ -caprolactone), poly(methylmethacrylate) [9]. Among them, PEG is the most used material; it functions as an anti-agglomeration agent for good dispersion in aqueous media. PEG prevents nonspecific binding (the uptake of the particles by other cells, i.e., opsonization) [98], enhances the incorporation of magnetic particles into cells [33] and finally enables efficient renal clearance [98].

The last important issue to consider is the targeting ligands or the surface chemistry, which is necessary to provide a biocompatible character, cell specificity, binding affinity and the purity of the ligand [129]. The choice of ligands is



◀ **Fig. 2** Common structures used in the synthetic preparation of magnetic-silica-optical nanocomposites: (a) the core is a magnetic nanoparticle, which is coated with a silica shell, (b) the core can be made of silica and the magnetic material is coated around the silica, (c) magnetic nanoparticles can be cross-linked to the silica core surface to obtain a core-satellite composite, (d) the silica nanoparticle can incorporate magnetic nanocrystals, (e) the composite can be prepared as a mesoporous silica nanoparticle with multiple magnetite nanocrystals covering its surface or being embedded inside the particle, (f) example of a special class of core-shell nanostructures, so-called yolk-shell nano-capsules, which have magnetic movable cores, interstitial hollow spaces between the movable core and shell sections, and the functional shells. The linker represents an intermediate component bonding between the particle and the molecule that gives the desired functionality to the hybrid nanocomposite

dependent on the ease of modification, conjugation, size, charge, cost, stability, etc. Different classes may include various antibodies and their fragments, aptamers, peptides, and small molecules.

### 3 Biomedical Applications of Magnetic Silica Optical Nanocomposites

Multi-functional silica nanocomposites possessing magnetic and fluorescent properties are being extensively used by researchers in the area of biomedicine in applications such as bioimaging, drug/gene delivery and therapy systems, and biosensing.

#### 3.1 *Imaging, Diagnostics, Drug Delivery*

Drug delivery, magnetic resonance and fluorescence imaging, magnetic manipulation, and cell targeting are simultaneously possible using multifunctional mesoporous silica NPs. Molecular imaging always requires accumulation of the contrast agent in the target site, often achieved by leading NPs containing contrast agent into the target. This involves accessing the target molecules hidden behind tissue barriers, necessitating the use of targeting groups. For imaging with low sensitivity, NPs bearing multiple contrast groups provide the signal amplification. The same NPs can, in principle, deliver both the contrast medium and the drug, allowing monitoring of the biodistribution and therapeutic activity simultaneously (theranostics).

A group of researchers under the leadership of Gang Liu prepared bi-functional magnetic-luminescent dansylated  $\text{Fe}_3\text{O}_4@\text{SiO}_2$  NPs by the nucleophilic substitution of dansyl chloride (a fluorescence derivatization reagent, DNS) with primary amines of aminosilane-modified  $\text{Fe}_3\text{O}_4@\text{SiO}_2$  core-shell nanostructures [23]. The resultant  $\text{Fe}_3\text{O}_4@\text{SiO}_2$ -DNS nanocomposites displayed a strong green emission



and a high T2 relaxivity in an aqueous solution. The in-vitro confocal microscopy, MR experiments and hemolysis assay results demonstrated that  $\text{Fe}_3\text{O}_4@\text{SiO}_2\text{-DNS}$  could eventually be used as a high-performance nanoprobe for cancer-cell imaging.

Some very interesting research was conducted with NPs consisting of cobalt-ferrite ( $\text{CoFe}_2\text{O}_4$ ) MNPs coated with RITC inside a silica shell and PEG on the outside to visualize a new tissue, which had not been detectable using simple stereomicroscopes [132]. The unfamiliar threadlike structure inside the lymphatic vessels of rats was demonstrated in-vivo by injecting NPs into lymph nodes and applying magnetic fields on the collecting lymph vessels so that the NPs were taken up by the thread-like structures. A fluorescent MNP solution was injected into the two nodes of each rat and the magnet was placed just above the lymphatic vessels for approximately 20 s. The NPs were taken up by the thread-like structure, but not by the walls of the lymphatic vessel. This technology will most likely provide a tool for studying the functions of the thread-like structure by using a magnetically controllable means.

Yoon et al. [33] presented in-vitro research in which cell movement upon applying an external magnetic field was demonstrated for cells containing MNPs. They used cobalt ferrite MNPs coated with a shell of amorphous silica, which contained luminescent organic dyes, such as RITC or FITC on the inside of the silica shell and biocompatible PEG on the outside. Confocal laser scanning microscopy (CLSM) images of breast-cancer cells (MCF-7) containing MNP- $\text{SiO}_2(\text{RITC})\text{-PEG}$  or MNP- $\text{SiO}_2(\text{FITC})\text{-PEG}$  showed clear emittance at various wavelengths. It was also confirmed that the core-shell MNPs could not penetrate the nucleus. They monitored the movement of the cells containing MNPs under an external magnetic field. Microscope images were captured every 0.2 s, while the external magnetic field was applied with a magnet on the outside of a Petri dish. Cobalt ferrite-silica core-shell MNPs did not show acute cytotoxicity at the level of a few tenths of a microgram (80  $\mu\text{g}/\text{mL}$ ) within a period of 48 h.

Fu et al. [24] implemented a novel approach using a magnetic micromesh and biocompatible fluorescent magnetic nanoparticles to magnetically enhance cancer targeting in live subjects. Each NP contained a superparamagnetic iron oxide core. They were coated with a biocompatible siliceous shell, followed by Cy5.5 and hence had a red fluorescence that could be detected under a fluorescence microscope. Angiosense 750, which is a near-infrared labeled fluorescent macromolecule that remains localized in the vasculature and enables the imaging of blood vessels and angiogenesis, was used for imaging the vascular leakiness. For experiments on live subjects, they selected the intensity of the tumor EGFP (enhanced green fluorescent protein) signal to monitor the effects in different experiments since NPs could extravasate out of leaky tumor vessels and remain in tumor regions for an extended time, regardless of the surface molecular specificity, in line with the enhanced permeability and retention effect of the NPs. The in-vivo magnetic targeting approach enabled the manipulation of individual NPs with single, 8 nm, superparamagnetic, iron oxide cores, which has been a great challenge in many magnetic targeting experiments.

A method has been developed to synthesize magnetic-fluorescent ZnS and silica-coated, Tb-doped,  $\gamma$ -Fe<sub>2</sub>O<sub>3</sub> nanocrystals [133]. These nanocrystals exhibit room-temperature, green photoluminescence under a 235 nm excitation wavelength and can be amine-functionalized and are non-toxic when used in-vitro. The reported bifunctional nanocrystals might have some potential in integrated imaging technology, of which MRI and fluorescence microscopy can be combined to provide better resolution in tissue and cellular imaging.

Corr et al. [110] presented research using fluorescent nanocomposites based on Fe<sub>3</sub>O<sub>4</sub> magnetic NPs, a polyhedral octaaminopropylsilsesquioxane (T<sub>8</sub>NH<sub>3</sub><sup>+</sup>Cl<sup>-</sup>) and a porphyrin derivative (5,10,15,20-Tetraphenyl-21H,23H-porphine). They used these nanocomposites to investigate their uptake and cellular localization in a phagocytic cell line and internalization by osteoblast cells. Confocal imaging confirmed the internalization of the nanocomposites, but an increase in the fluorescence was observed inside the osteoblast cells after particle uptake, presumably due to dissociation of the components in the magnetic fluorescent nanocomposites.

The controlled release of drugs from fluorescent silica NPs is attracting increasing attention because of the opportunities in cancer therapy and the treatment of other diseases. The potential of magnetic silica NPs lies in the properties of their magnetic cores combined with their drug-loading capability and the biochemical properties that can be tailored on their surfaces by using a suitable coating.

Enzyme-responsive, hybrid, magnetic iron oxide, silica NPs have been employed for multifunctional applications in selective drug delivery and intracellular tumor imaging [35]. Yang et al. developed an enzyme-responsive, doxorubicin (Dox)-peptide-coated, magnetic silica nanoparticle (SMNP) conjugate for the selectively triggered intracellular delivery of Dox into the tumor cells with specific protease enzyme expression. They examined the activity of Dox-SMNPs towards enzyme reactions by detecting the fluorescence of Dox. This was possible because free Dox exhibited a fluorescence emission at 590 nm (with an excitation at 485 nm). The fluorescence of Dox would have been quenched when the drug-modified peptide sequence was covalently tethered to the surface of the SMNPs due to electronic energy transfer. According to their results, Dox-SMNPs could easily enter into the intracellular cytoplasm and Dox could be selectively released upon the reaction of drug-conjugated SMNPs with the specific enzyme in the target cell lines. On the basis of results where the incubation times of the drug-SMNP complex were longer (e.g.,  $\geq 72$  h), the dynamic process of the drug release from the Dox-conjugated SMNP complexes in the target HT-29 cells was observed.

Another example of a multifunctional bio-application is core-shell NPs for simultaneous magnetic resonance (MR) and fluorescence imaging and for drug delivery, as demonstrated by Kim et al. [78]. They constructed discrete, monodispersed, size-controllable, core-shell, mesoporous silica NPs smaller than 100 nm by using single Fe<sub>3</sub>O<sub>4</sub> nanocrystals as cores (Fe<sub>3</sub>O<sub>4</sub>@mSiO<sub>2</sub>). They incorporated FITC and RITC into the silica walls for the fluorescence detection and increased the colloidal stability in phosphate-buffered saline (PBS) by derivatization with PEG. The cell viability and proliferative activity assays

revealed that the cell viability and proliferation were not hindered by the presence of the  $\text{Fe}_3\text{O}_4@\text{mSiO}_2(\text{R})\text{-PEG}$  up to a concentration of 10 mg/mL Fe. The results of the cellular uptake of the NPs in MCF-7 breast-cancer cells showed that a large number of the NPs were endocytosed into the cells and that the core-shell nanostructures were maintained after endocytosis. They examined the drug delivery of the NPs by testing the cytotoxic effect of doxorubicin (DOX)-loaded  $\text{Fe}_3\text{O}_4@\text{mSiO}_2(\text{R})\text{-PEG}$ . The results indicated that  $\text{Fe}_3\text{O}_4@\text{mSiO}_2$  had a potential for drug loading and delivery into cancer cells to induce cell death. They also investigated the potential for the in-vivo imaging of  $\text{Fe}_3\text{O}_4@\text{mSiO}_2(\text{R})\text{-PEG}$  by tracking the particles' passive tumor accumulation. A strong fluorescence from the tumor was observed, representing the appreciable accumulation of NPs in the tumors through the EPR (enhanced permeability and retention) effect. However, further studies need to be conducted to examine the behavior of the designed nanostructures and the potentially toxic side-effects in-vivo.

Liong et al. [10] constructed superparamagnetic iron oxide nanocrystals that they encapsulated inside mesostructured silica spheres, labeled with fluorescent dye molecules (FITC) and coated with hydrophilic (trihydroxysilylpropyl methylphosphonate) groups to prevent aggregation. These mesoporous silica NPs were detectable by MR imaging and optical methods. Fluorescence imaging and cell-viability assays showed that the NPs delivered water-insoluble drug molecules, either camptothecin (CPT) or paclitaxel (TXL), into the cells successfully. Surface conjugation with cancer-specific targeting agents (folic acid) increased the uptake into the cancer cells relative to that in non-cancerous fibroblasts.

The fabrication of uniform mesoporous dye-doped silica NPs immobilized with multiple magnetite nanocrystals on the surface (designated as  $\text{Fe}_3\text{O}_4\text{-MPSi}$ ) was reported by Lee et al. [76]. The structured system was tested for applications in simultaneous MRI, fluorescence imaging, and as a drug-delivery vehicle. The integration of numerous magnetite nanocrystals on the silica surface resulted in synergistic magnetism that enhanced the MR signal. Small dye molecules (RITC or FITC) incorporated into the silica framework imparted optical imaging modality. In addition, an anticancer drug could be loaded into the pores of the MPSi NPs for drug delivery. They also demonstrated in-vivo passive targeting of the nanocomposite particles to tumors, but they still have a long road ahead before their nanocomposites can be tested in clinical trials.

Multifunctional nanocomposite mesoporous NPs for simultaneous fluorescence and MR imaging, and pH-sensitive drug release were fabricated [94]. Researchers immobilized the NPs with a pH-responsive hydrazone bond, magnetite NPs, and the fluorescent dye (FITC). The application of a pH-sensitive hydrazone bond was used because the hydrazone bond is stable at neutral pH, but is rapidly dissociated in acidic environments, such as lysosomes, tumor sites, or infected tissues and can therefore provide the pH-sensitive release of the anti-cancer drug, DOX. The release of DOX was both time and pH dependent. Green fluorescence of the FITC was observed in the cytoplasm and red fluorescence of DOX was found in the nucleus, demonstrating that DOX was released from the MPSiNPs. The cytotoxic effect of DOX-conjugated hydrazine-MPSiNPs-FITC- $\text{Fe}_3\text{O}_4\text{-PEG}$  was also tested

on breast-cancer cells. The results showed no cytotoxicity of the bare MPSiNPs, even at high concentrations, while the cytotoxic efficacy of the DOX-conjugated MPSiNPs increased as the concentration was increased. Considering these results, the developed MPSiNPs might have the potential for drug loading and delivery into cancer cells to induce cell death.

Thomas et al. combined the advantages of mesoporous silica (MPSi with nanovalves) with those of zinc-doped, iron oxide nanocrystals (ZnNCs) to create a new generation of drug-delivery systems responsive to heat activation. Their approach to drug delivery allowed the cargo to be contained within the nanoparticle at body temperature, but resulted in the controlled release of the therapeutic agent to induce apoptosis upon local heating generated by the ZnNCs [79]. A nanovalve was chosen because it does not possess a self-opening characteristic in biological systems, is thermally stable at room temperature, and can be operated under heating. When this nanovalve is attached to the surface of a MPSi particle, an increase in temperature causes the valve to open, allowing materials contained within to diffuse out. Because the NPs contained ZnNCs, the application of an oscillating magnetic field induced local heating, which resulted in the drug-release effect. The complete magnetically activated release system was tested to determine whether magnetically induced heating would open the nanovalves, causing the release of the contained Rhodamine B molecules. Particles at room temperature were placed into an oscillating magnetic field, and the dye release was observed as a function of time. However, no studies were made to prove the biocompatibility of the NPs used in their research.

Kim et al. used magnetite nanocrystals (MNCs) and green-emitting CdSe/ZnS QDs and simultaneously embedded them in MPSi spheres (MNCs/QD-MPSi). For the investigation of MNCs-MPSi as a candidate of drug carriers for delivery, ibuprofen was selected as a model drug and adsorbed into the MPSi's with different surface properties: MNCs-MPSi with silanol groups and MNCs-MPSi-NH<sub>2</sub> with amino groups. To measure the amount of released ibuprofen, the MPSi spheres in the buffer solution were captured using a magnet. The results suggested that a favorable interaction between the amino group on the MNCs-MPSi-NH<sub>2</sub> and the carboxyl group of the ibuprofen prevents the easy release of ibuprofen [80]. These results suggest that the release rate of a drug from MNCs-MPSi could be controlled by the surface modification of the silica spheres in-vitro.

Several biological applications were tested with gold nanorods-capped magnetic core/mesoporous silica shell nano-ellipsoids (AuNRs-M-MPSiNEs) [81]. Confocal microscopy images of breast-cancer MCF-7 cells incubated with AuNRs-M-MPSiNEs-DOX were specially marked with a fluorescent stain DAPI for nuclei staining with blue fluorescence and DOX was used for the red fluorescence, indicative of the location of the AuNRs-M-MPSiNEs-DOX. The AuNRs-M-MPSiNEs were successfully used as contrast agents by in-vivo MR imaging and showed the ability to encapsulate DOX drug molecules. In the latter case, the controlled-release property was pH-dependent, which can prevent drug leakage during the blood's circulation, but increase the delivery efficacy in cancer cells, which are much more acidic than normal cells. Considering the results obtained from studies on mice,

AuNRs-M-MPSiNEs work well enough, but to show significant promise for in-vivo photothermal treatment a lot of work still needs to be done.

A core-shell nanosphere with a PVP-modified silica core followed by a functional deposition of a single-crystal iron oxide shell was developed by Hu et al. [129]. Such core-shell nanospheres offered the controlled release and non-release behavior for molecules encapsulated inside the silica core. The dense, single-crystalline shell prevented the fluorescence dye (FITC) from undesired release and the dye molecules encapsulated in the core could be released in a controllable manner through the use of a magnetic stimulus. Upon applying a high-frequency magnetic field (HFMF) to the cuvette, a large amount of dye was detected in the water solution, indicating that the dye was released only when the magnetic field was applied to the nanospheres, and that the release ceased right after the removal of the field. After being subjected to the magnetic field for a short period, crevices or cracks on a nanometer scale appeared along the boundary regions of the thin shell. These “nanocrevice” were enlarged by magnetically induced vibrations, permitting dye molecules to be released easily; and the change in the dimension of the nanocrevice was physically reversible to a certain extent, but only upon short-time exposure. If in-vivo experimental testing with an actual drug molecule gave similar results, the developed system could release drug molecules in a precise dosage in a remotely controlled manner, with the shell being ruptured when the disease site is reached.

Giri et al. reported the synthesis of a controlled-release delivery system, based on mesoporous silica nanorods (MPSiNRs) capped with superparamagnetic iron oxide NPs. Their results showed that MPSiNRs capped with superparamagnetic iron oxide NPs could be used as a stimuli-responsive, controlled-release delivery carrier. Guest molecules that are smaller than 3 nm, such as fluorescein, could be encapsulated and released from the magnet-MSN delivery system by using cell-produced antioxidants (e.g., dihydrolipoic acid) as triggers in the presence of an external magnetic field [82]. The biocompatibility and efficiency of the intracellular delivery of the magnet-MSN system offers potential in the utilization of this system to investigate inter- and intracellular chemical/neurochemical communications in-vitro.

Gene-delivery techniques efficiently introduce a gene of interest in order to express its encoded protein in a suitable host or host cell. One of the techniques that shows a lot of promise for both in-vitro and in-vivo transfection involves the use of biocompatible magnetic NPs for gene delivery. In these systems, therapeutic or reporter genes are attached to magnetic NPs, which are then focused to the target site/cells via high-field/high-gradient magnets. The technique promotes rapid transfection as well as satisfactory overall transfection levels.

Magnetic silica optical nanocomposites were used for gene delivery and cellular imaging of the angiogenic factor VEGF [34]. A scientific group developed a gene-delivery system of  $\text{Fe}_3\text{O}_4@\text{SiO}_2$  NPs doped with FITC and grafted with poly(allylamine hydrochloride) (PAH), which allowed loading of the recombinant plasmid of pIRSE2-EGFP/VEGF<sub>165</sub> (pVEGF) to form  $\text{Fe}_3\text{O}_4@\text{SiO}_2(\text{FITC})/\text{PAH}/\text{pVEGF}$  nanocomplexes for VEGF gene delivery and cellular imaging. The

constructed system was able to efficiently deliver the VEGF gene into endothelial cells and could be expressed in a sustained model after transfection.

Another angiogenic factor, bFGF, was used in research by Wu et al. [83]. They engineered core-shell-structured, magnetic mesoporous silica nanoparticles combined with heparin and FITC (MMPSiNPs-HP). The particles showed good dispersion and blood compatibility, and controlled release of the bFGF growth factor. The proliferation activity of the growth factor incorporated into the MMPSiNPs-HP was proven to be retained for at least 6 days and cell-viability assays indicated nearly no cytotoxicity up to a concentration of 200  $\mu\text{g/mL}$ . However, further studies need to be conducted to prove the particles' applicability in in-vivo.

Zhang et al. [29] described a procedure for the production of multifunctional fluorescent-magnetic polyethyleneimine functionalized  $\text{Fe}_3\text{O}_4$ -RITC-mesoporous silica yolk-shell nanocapsules ( $\text{PEI-Fe}_3\text{O}_4@\text{fmSiO}_2$  yolk shell NCs) for siRNA delivery. They confirmed the stability of complexes between  $\text{PEI-Fe}_3\text{O}_4@\text{fmSiO}_2$  yolk shell NCs and siRNA, and that siRNA was successfully protected from enzymatic attack in the physical environment. Later on they tested the efficiency of siRNA- $\text{Fe}_3\text{O}_4@\text{fmSiO}_2$  yolk-shell NCs in cancer therapy by using a housekeeping gene as a target gene, because significant down-regulation of this gene does not inhibit normal cellular functions. The results suggested that  $\text{PEI-Fe}_3\text{O}_4@\text{fmSiO}_2$  yolk-shell NCs used as siRNA delivery nanocarriers could efficiently deliver siRNA into the cytoplasm, even better than the commercial agent Lipofectamine 2000. Based on the research studies it is believed that these nanostructures show great potential as a realizable tool for efficient cancer therapy.

### 3.2 Biodetection

One of the major challenges in medicine is the rapid and accurate measurement of protein biomarkers, cells, and pathogens in biological samples. Lapresta Fernandez et al. reported on maghemite ( $\text{Fe}_2\text{O}_3$ ) nanocrystals coated with silica shells for the construction of magnetic fluorescent sensor NPs in the 50–70 nm diameter range. The magnetic cores were coated by two successive silica shells embedding two fluorophores (two different silylated dye derivatives), which enabled ratiometric pH-measurements in the pH range 5–8. Sulforhodamine B was covalently attached in the inner shell and was used as a reference dye; while a pH-sensitive fluorescein was incorporated into the outer shell. Changes in the fluorescence intensity of the pH indicator in the different pH buffered solutions indicated an easy accessibility of the embedded dye by protons through the pores of the silica shell [49].

Wilson et al. have developed a simple method for preparing microspheres that are provided with a spectral code matched to a specific recognition surface and demonstrated their use in multiplexed detection. In this method, hydrophobic trioctylphosphine oxide (TOPO)-capped  $\text{CdSe@ZnS}$  QDs are assembled between intervening layers of high-molecular-weight polyamines in an aprotic solvent. Because the amount of QDs assembled depends only on the surface area of the

microspheres and because the surface does not become more disperse during the assembly process, it allows microspheres to be furnished with resolvable spectral codes. These codes were matched to a specific recognition surface by overcoating the QDs with an outer shell of SiNPs functionalized with proteins. The SiNPs conferred stability on the microspheres in the presence of detergents and blocking proteins and provided a foundation for the covalent attachment of antigens. Because the shell was optically transparent, it had no effect on the excitation or emission properties of the QDs, and because it was chemically similar to glass, it could be activated by traditional silane chemistry. In order to functionalize the shell with a biological recognition surface, a reaction scheme that prevented irreversible aggregation of the microspheres was developed [134].

Zhang et al. [22] constructed fluorescent magnetic nanoparticles (FMNPs) with a uniform size of less than 50 nm that were prepared by the encapsulation of magnetic NPs and seven layered shell/core quantum dots ((CdSe/CdS/CdS/Cd<sub>0.75</sub>Zn<sub>0.25</sub>S/Cd<sub>0.5</sub>Zn<sub>0.5</sub>S/Cd<sub>0.25</sub>Zn<sub>0.75</sub>S/ZnS/ZnS) QDs) with shell structure compositions into a silica matrix. According to the spectral analysis, the so-prepared FMNPs have a high fluorescent quantum yield (QY). The QYs and saturation magnetizations of the FMNPs could be regulated by varying the ratio of the encapsulated QDs to MNPs. The surface of the NPs could also be modified to offer chemical groups for antibody conjugation for subsequent use in target-enrichment and fluorescent detection. The in-vitro immunofluorescence assay and flow cytometric analysis indicated that the bifunctional FMNPs-antibody bioconjugates were capable of target-enrichment, magnetic separation and can also be used as alternative fluorescent probes on flow cytometry for biodetection.

“Core-satellite” structured, dual-functional NPs comprised of a Rhodamine-dye-doped silica (DySiO<sub>2</sub>) “core” and multiple “satellites” of magnetic NPs were fabricated (DySiO<sub>2</sub>-(Fe<sub>3</sub>O<sub>4</sub>)<sub>n</sub>) [18]. The DySiO<sub>2</sub>-(Fe<sub>3</sub>O<sub>4</sub>) hybrid NPs were conjugated with HumanB1 antibodies, that are known to specifically target cells with polysialic acids (PSAs). The detection of PSAs was confirmed by simultaneous optical and MR imaging of the neuroblastoma cells expressing PSAs. The overall size of the hybrid NPs was approximately 45 nm.

In one complex study, Yoon et al. [75] developed a nanostructure where a silica shell of the silica-coated core-shell magnetic nanoparticle (MNP@SiO<sub>2</sub>) was incorporated with organic dyes (RITC or FITC). These nanostructures were then modified with functional organosilicon compounds, such as (MeO)<sub>3</sub>Si-PEG (2[methoxy(polyethyleneoxy)propyl]trimethoxysilane: CH<sub>3</sub>O(CH<sub>2</sub>CH<sub>2</sub>O)<sub>6-9</sub>-CH<sub>2</sub>CH<sub>2</sub>CH<sub>2</sub>Si(OCH<sub>3</sub>)<sub>3</sub>) and APS (3-aminopropyltriethoxysilane:(EtO)<sub>3</sub>Si-(CH<sub>2</sub>)<sub>3</sub>NH<sub>2</sub>). The surface of the dual-functionalized core-shell NPs presented two key functional groups: the PEG moiety for enhanced biocompatibility in-vivo and in-vitro, and an amine moiety for the increased applicability of the MNP. The described structure enabled the creation of MNP@SiO<sub>2</sub>(FITC)-Ab<sub>CD-10</sub> NPs with immobilized AbCD-10 antibodies and MNP@SiO<sub>2</sub>(FITC)-Ab<sub>HER-2</sub> NPs with immobilized HER-2 antibodies. The MNP@SiO<sub>2</sub>(FITC)-Ab<sub>HER-2</sub> particles specifically targeted the breast-cancer-adherent cells, and their co-treatment with MNP@SiO<sub>2</sub>(RITC) NPs, which results in their cellular uptake by endocytosis, can be used for biomedical



imaging; their specific location was confirmed by TEM measurements. The specific targeting was examined by incubation of the floating tumor SP2/0 cells (that have CD-10 receptors on their outer cell membrane) and lung-cancer cells A549 (that lack CD-10 receptors and therefore serve as a negative control). CLSM imaging confirmed the specific targeting of the SP2/0 leukemia cells. CLSM images of the MCF-7 cells after targeting and internalization of the  $\text{MNP@SiO}_2(\text{FITC})\text{-Ab}_{\text{HER-2}}$  and  $\text{MNP@SiO}_2(\text{RITC})\text{-Ab}_{\text{HER-2}}$  provided direct evidence that the  $\text{MNP@SiO}_2(\text{RITC})\text{-Ab}_{\text{HER-2}}$  were endocytosed by the MCF-7 cell. The  $\text{MNP@SiO}_2(\text{RITC})\text{-Ab}_{\text{HER-2}}$  particles were revealed as black dots on the membrane of MCF-7 cells, which suggested that the particles were not cytotoxic in-vitro (membranes would otherwise disappear rapidly upon cell death).

Multi-functional core-shell NPs possessing magnetic, up-conversion fluorescence and bio-affinity properties were synthesized and characterized. The iron oxide magnetic core was covered with ytterbium and erbium that were co-doped sodium yttrium fluoride ( $\text{NaYF}_4:\text{Yb,Er}$ ), an infrared-to-visible up-conversion phosphor. After coating with  $\text{SiO}_2$ , the streptavidin was immobilized on the particle. Streptavidin-coated magnetic/fluorescent particles were found to bind specifically to a glass slide spotted with biotinylated IgG and emit up-conversion fluorescence, confirming the successful coating of the protein and the retention of its optical activity and bio-affinity [127].

## 4 Conclusions

The wide range of possibilities for the creation of hybrid, multifunctional nanocomposites continues to be an important field of research involving a variety of groups. However, although a lot of work was already devoted into the development of multifunctional hybrid nanostructures for specific biomedical applications, several key points still need to be defined and studied.

Regarding the magnetic silica composites addressed in this review, fluorescent organic dyes are still the most used light-emitting probes in in-vivo and in-vitro studies for optical imaging, diagnostics, and therapeutic applications, mostly in drug delivery. The near-infrared and, for clinical applications the approved indocyanine green dye are not really applied in such approaches, due to the rapid protein binding, fast clearance and instability in physiologically relevant conditions [95, 96].

On the basis of physiological parameters such as hepatic filtration, tissue extravasation, tissue diffusion, and kidney excretion, it is clear that, along with the surface composition, the particle size is a key factor in the biodistribution of long-circulating NPs and in achieving therapeutic efficiency [135]. The majority of research groups synthesized magnetic silica NPs with diameters ranging from about 20 to approximately 90 nm [23, 24, 78, 127, 129], which enabled optimal intravenous injection and prolonged blood-circulation times [130]. Despite this, the blood-circulation times, which in addition to the clearance half-life and urinary



excretion are essential for the development of any therapeutic nanoparticle, have yet to be determined [136].

Another crucial issue to be taken into consideration is the stability and breakdown products of fluorescent silica magnetic NPs coatings because a “bio-compatible coating” that is initially considered stable may eventually break down into undesirable products or expose the iron oxide core, and adverse cellular responses can follow. At present the measure of biocompatibility largely focuses on the extent of the cytotoxicity observed. The criteria to define the toxicity of the NPs need to be clearly defined too, particularly as emerging studies have begun to highlight abnormal cellular responses including DNA damage, oxidative stress, mitochondrial membrane dysfunction and changes in gene expression as a result of exposure to superparamagnetic iron oxide NPs, all in the absence of cytotoxicity [137]. Given that the variety of medical applications of fluorescent magnetic silica NPs requires sufficient intracellular uptake for efficient diagnosis and treatment, understanding the potential risks associated with exposure to these NPs and the effect that the range of surface coatings used for functionality are crucial.

Despite significant success in molecular imaging and drug delivery, the release of drug moieties from silica magnetic or nanohybrids was normally achieved through a passive diffusion mechanism that could potentially undermine the targeting efficiency and specificity of the nano-bioconjugates in the living system. The development of a simple, stable, and covalently conjugated drug-nanoparticle hybrid system that would allow a more selective drug release into targeted locations upon specific biological stimuli and meanwhile would also enable the real-time monitoring of drug delivery at the single-cell level is still highly desirable and remains a challenge in the field. It is critical to design functionalized, fluorescent, magnetic silica NPs that cannot only be effectively and sufficiently internalized and are appropriately magnetizable, but also meet the demands of a particular application without a hint of cellular toxicity. These are some of many properties, including selectivity to critical cells (including tumor cells), favorable targeting and clearance profiles, and stable and selective NIR probes, that the next generations of multifunctional magnetic silica nanoparticles need to have in order to be clinically successful.

## References

1. Vo-Dinh, T.: Optical nanosensors for detecting proteins and biomarkers in individual living cells in protein nanotechnology. In: Vo-Dinh, T. (ed.) *Protein Nanotechnology: Protocols, Instrumentation, and Applications*, 1st edn. Humana Press, New Jersey (2005)
2. Demchenko, A.P.: Sensing inside living cells and tissues. In: Demchenko, A.P. (ed.) *Introduction to Fluorescence Sensing*, 1st edn. Springer, New York (2010)
3. Vo-Dinh, T., Zhang, Y.: Single-cell monitoring using fiberoptic nanosensors. *Wiley Interdiscip. Rev. Nanomed. Nanobiotechnol.* **3**, 79–85 (2011)
4. Maeda, H., Wu, J., Sawa, T., et al.: Tumor vascular permeability and the EPR effect in macromolecular therapeutics: A review. *J. Control Release* **65**, 271–284 (2000)

5. McCarthy, J.R., Weissleder, R.: Multifunctional magnetic nanoparticles for targeted imaging and therapy. *Adv. Drug Deliv. Rev.* **60**, 1241–1251 (2008)
6. Kumar, C.S.S.R., Mohamad, F.: Magnetic nanomaterials for hyperthermia-based therapy and controlled drug delivery. *Adv. Drug Deliv. Rev.* **63**, 789–808 (2011)
7. Corr, S.A., O'Byrne, A., Gun'ko, Y.K.: Multifunctional magnetic-fluorescent nanocomposites for biomedical applications. *Nanoscale Res. Lett.* **3**, 87–104 (2008)
8. Quarta, A., Di Corato, R., Manna, L., et al.: Fluorescent-magnetic hybrid nanostructures: preparation, properties, and applications in biology. *IEEE T Nanobiosci.* **6**, 298–308 (2007)
9. Masotti, A.: Multifunctional nanoparticles: Preparation and applications in biomedicine and in non-invasive bioimaging. *Recent Pat. Nanotechnol.* **4**, 53–62 (2010)
10. Liong, M., Lu, J., Kovichich, M., et al.: Multifunctional inorganic nanoparticles for imaging, targeting, and drug delivery. *ACS Nano* **2**, 889–896 (2008)
11. Sounderya, N., Zhang, Y.: Use of core/shell structured nanoparticles for biomedical applications. *Recent Pat. Biomed. Eng.* **1**, 34–42 (2008)
12. Lin, M., Zhao, Y., Wang, S., et al.: Recent advances in synthesis and surface modification of lanthanide-doped upconversion nanoparticles for biomedical application. *Biotechnol. Adv.* **30**, 1551–1561 (2012)
13. Thanh, N.T.K., Green, L.A.W.: Functionalisation of nanoparticles for biomedical applications. *Nano Today* **5**, 213–230 (2010)
14. Haun, J.B., Devaraj, N.K., Hilderbrand, S.A., et al.: Bioorthogonal chemistry amplifies nanoparticle binding and enhances the sensitivity of cell detection. *Nat. Nanotechnol.* **5**, 660–665 (2010)
15. Tassa, C., Duffner, J.L., Lewis, T.A., et al.: Binding affinity and kinetic analysis of targeted small molecule-modified nanoparticles. *Bioconjugate Chem.* **21**, 14–19 (2010)
16. Hong, S., Leroueil, P., Majoros, I., et al.: The binding avidity of a nanoparticle-based multivalent targeted drug delivery platform. *Chem. Biol.* **14**, 107–115 (2007)
17. Shaw, S.Y., Westly, E.C., Pittet, M.J., et al.: Perturbational profiling of nanomaterial biologic activity. *Proc. Natl. Acad. Sci. U.S.A.* **105**, 7387–7392 (2008)
18. Lee, J.H., Jun, Y.W., Yeon, S.I., et al.: Dual-mode nanoparticle probes for high-performance magnetic resonance and fluorescence imaging of neuroblastoma. *Angew. Chem. Int. Ed.* **45**, 8160–8162 (2006)
19. Atanasijevic, T., Shusteff, M., Fam, P., et al.: Calcium-sensitive MRI contrast agents based on superparamagnetic iron oxide nanoparticles and calmodulin. *Proc. Natl. Acad. Sci. U.S.A.* **103**, 14707–14712 (2006)
20. Lutz, J.F., Stiller, S., Hoth, A., et al.: One-pot synthesis of pegylated ultrasmall iron-oxide nanoparticles and their in vivo evaluation as magnetic resonance imaging contrast agents. *Biomacromolecules* **7**, 3132–3138 (2006)
21. Ruhland, T.M., Reichstein, P.M., Majewski, A.P., et al.: Superparamagnetic and fluorescent thermo-responsive core-shell-corona hybrid nanogels with a protective silica shell. *J. Colloid Interf. Sci.* **374**, 45–53 (2012)
22. Zhang, B., Chen, B., Wang, Y., et al.: Preparation of highly fluorescent magnetic nanoparticles for analytes-enrichment and subsequent biodetection. *J. Colloid Interf. Sci.* **353**, 426–432 (2011)
23. Liu, G., Wu, H., Zheng, H., et al.: Synthesis and applications of fluorescent-magnetic-bifunctional dansylated Fe<sub>3</sub>O<sub>4</sub>@SiO<sub>2</sub> nanoparticles. *J. Mater. Sci.* **46**, 5959–5968 (2011)
24. Fu, A., Wilson, R.J., Smith, B.R., et al.: Fluorescent magnetic nanoparticles for magnetically enhanced cancer imaging and targeting in living subjects. *ACS Nano* **6**, 6862–6869 (2012)
25. Beaurepaire, E., Buissette, V., Sauviat, M.P., et al.: Functionalized fluorescent oxide nanoparticles: artificial toxins for sodium channel targeting and imaging at the single-molecule level. *Nano Lett.* **4**, 2079–2083 (2004)
26. Deng, T., Li, J.S., Jiang, J.H., et al.: Preparation of near-ir fluorescent nanoparticles for fluorescence-anisotropy-based immunoagglutination assay in whole blood. *Adv. Funct. Mater.* **16**, 2147–2155 (2006)

27. Tan, M., Wang, G., Hai, X., et al.: Development of functionalized fluorescent europium nanoparticles for biolabeling and time-resolved fluorometric applications. *J. Mater. Chem.* **14**, 2896–2901 (2004)
28. He, X., Duan, J., Wang, K., et al.: A novel fluorescent label based on organic dye-doped silica nanoparticles for HepG liver cancer cell recognition. *J. Nanosci. Nanotechnol.* **4**, 585–589 (2004)
29. Zhang, L., Wang, T., Li, L., et al.: Multifunctional fluorescent-magnetic polyethyleneimine functionalized Fe<sub>3</sub>O<sub>4</sub>-mesoporous silica yolk-shell nanocapsules for siRNA delivery. *Chem. Commun.* **48**, 8706–8708 (2012)
30. Hergt, R., Dutz, S., Müller, R., et al.: Magnetic particle hyperthermia: nanoparticle magnetism and materials development for cancer therapy. *J. Phys-Condens. Mat.* **18**, 2919–2934 (2006)
31. Martín-Saavedra, F.M., Ruíz-Hernández, E., Boré, A., et al.: Magnetic mesoporous silica spheres for hyperthermia therapy. *Acta Biomater.* **6**, 4522–4531 (2010)
32. Song, E.Q., Hu, J., Wen, C.Y., et al.: Fluorescent-magnetic-biotargeting multifunctional nanobioprobes for detecting and isolating multiple types of tumor cells. *ACS Nano* **5**, 761–770 (2011)
33. Yoon, T.J., Kim, J.S., Kim, B.G., et al.: Multifunctional nanoparticles possessing a “magnetic motor effect” for drug or gene delivery. *Angew. Chem. Int. Ed.* **44**, 1068–1071 (2005)
34. Liu, Y., Shi, M., Xu, M., et al.: Multifunctional nanoparticles of Fe<sub>3</sub>O<sub>4</sub>@SiO<sub>2</sub>(FITC)/PAH conjugated the recombinant plasmid of pIRSE2-EGFP/VEGF<sub>165</sub> with dual functions for gene delivery and cellular imaging. *Expert Opin. Drug Deliv.* **9**, 1197–1207 (2012)
35. Yang, Y., Aw, J., Chen, K., et al.: Enzyme-responsive multifunctional magnetic nanoparticles for tumor intracellular drug delivery and imaging. *Chem. Asian J.* **6**, 1381–1389 (2011)
36. Schladt, T.D., Koll, K., Prüfer, S., et al.: Multifunctional superparamagnetic MnO@SiO<sub>2</sub> core/shell nanoparticles and their application for optical and magnetic resonance imaging. *J. Mater. Chem.* **22**, 9253–9262 (2012)
37. Runowski, M., Grzyb, T., Lis, S.: Magnetic and luminescent hybrid nanomaterials based on Fe<sub>3</sub>O<sub>4</sub> nanocrystals and GdPO<sub>4</sub>:Eu<sup>3+</sup> nanoneedles. *J. Nanopart. Res.* **14**, 1188–1196 (2012)
38. Li, L., Choo, E.S.G., Liu, Z., et al.: Double-layer silica core-shell nanospheres with superparamagnetic and fluorescent functionalities. *Chem. Phys. Lett.* **461**, 114–117 (2008)
39. Jung, Y., Guan, G., Wei, C., et al.: Multifunctional nanoprobe to enhance the utility of optical based imaging techniques. *J. Biomed. Optics* (2012). doi:[10.1117/1.JBO.17.1.016015](https://doi.org/10.1117/1.JBO.17.1.016015)
40. Ren, C., Sun, J., Zhang, Y., et al.: Preparation and characterization of novel fluorescent-magnetic nanomaterial. *J. Nanosci. Nanotechnol.* **9**, 2664–2670 (2009)
41. Hu, S.H., Liu, T.Y., Huang, H.Y., et al.: Magnetic-sensitive silica nanospheres for controlled drug release. *Langmuir* **24**, 239–244 (2008)
42. Yi, D.K., Selvan, T., Lee, S.S., et al.: Silica-coated nanocomposites of magnetic nanoparticles and quantum dots. *J. Am. Chem. Soc.* **127**, 4990–4991 (2005)
43. Sathe, T.R., Agrawal, A., Shuming, Nie: Mesoporous silica beads with semiconductor quantum dots and iron oxide nanocrystals: dual-function microcarriers for optical encoding and magnetic separation. *Anal. Chem.* **78**, 5627–5632 (2006)
44. Le Guével, X., Nooney, R., McDonagh, C., et al.: Synthesis and characterization of monodisperse, mesoporous, and magnetic sub-micron particles doped with a near-infrared fluorescent dye. *J. Solid State Chem.* **184**, 1545–1550 (2011)
45. Evans, C.W., Raston, C.L., Iyer, K.S.: Nanosized luminescent superparamagnetic hybrids. *Green Chem.* **12**, 1175–1179 (2010)
46. Makovec, D., Čampelj, S., Bele, M., et al.: Nanocomposites containing embedded superparamagnetic iron oxide nanoparticles and rhodamine 6G. *Colloids Surf. A: Physicochem. Eng. Aspects* **334**, 74–79 (2009)

47. Zhang, Y., Gong, S.W.Y., Jin, L., et al.: Magnetic nanocomposites of Fe<sub>3</sub>O<sub>4</sub>/SiO<sub>2</sub>-FITC with pH-dependent fluorescence emission. *Chin. Chem. Lett.* **20**, 969–972 (2009)
48. Maceira-Selgueiriño, V., Correa-Duarte, M.A., Spasova, M., et al.: Composite silica spheres with magnetic and luminescent functionalities. *Adv. Funct. Mater.* **16**, 509–514 (2006)
49. Lapresta Fernandez, A., Doussineau, T., Moro, A.J., et al.: Magnetic core-shell fluorescent pH ratiometric nanosensor using a Stöber coating method. *Anal. Chim. Acta* **707**, 164–170 (2011)
50. Halbreich, A., Roger, J., Pons, J.N., et al.: Biomedical applications of maghemite ferrofluid. *Biochimie* **80**, 369–390 (1998)
51. Could, P.: Nanoparticles probe biosystems. *Mater. Today* **7**, 36–43 (2004)
52. Odenbach, S.: Recent progress in magnetic fluid research. *J. Phys. Condens. Mat.* **16**, 1135–1150 (2004)
53. Connolly, J., St Pierre, T.G.: Proposed biosensors based on time-dependent properties of magnetic fluids. *J. Magn. Magn. Mater.* **225**, 156–160 (2001)
54. Varadan, V.K., Chen, L., Xie, J.: *Nanomedicine: Design and Applications of Magnetic Nanomaterials, Nanosensors and Nanosystems*. Wiley, West Sussex (2008)
55. Pankhurst, Q.A., Connolly, J., Jones, S.K., et al.: Applications of magnetic nanoparticles in biomedicine. *J. Phys. D Appl. Phys.* **36**, 167–181 (2003)
56. Leslie-Pelecky, D.L., Rieke, R.D.: Magnetic properties of nanostructured materials. *Chem. Mater.* **8**, 1770–1783 (1996)
57. Dobson, J.: Magnetic nanoparticles for drug delivery. *Drug Dev. Res.* **67**, 55–60 (2006)
58. Slowing, I.I., Trewyn, B.G., Giri, S., et al.: Mesoporous silica nanoparticles for drug delivery and biosensing. *Appl. Adv. Funct. Mater.* **17**, 1225–1236 (2007)
59. Gould, P.: Nanomagnetism shows in vivo potential. *Nano Today* **1**, 34–39 (2006)
60. Grimm, J., Perez, J.M., Josephson, L., et al.: Novel nanosensors for rapid analysis of telomerase activity. *Cancer Res.* **64**, 639–643 (2004)
61. Ge, Y., Zhang, Y., He, S., et al.: Fluorescence modified chitosan-coated magnetic nanoparticles for high-efficient cellular imaging. *Nanoscale Res. Lett.* **4**, 287–295 (2009)
62. Wilson, R., Spiller, D.G., Prior, I.A., et al.: A simple method for preparing spectrally encoded magnetic beads for multiplexed detection. *ACS Nano* **1**, 487–493 (2007)
63. Thompson, M.K., Misselwitz, B., Tso, L.S., et al.: In vivo evaluation of gadolinium hydroxypyridonate chelates: initial experience as contrast media in magnetic resonance imaging. *J. Med. Chem.* **48**, 3874–3877 (2005)
64. Duncan, A.K., Klemm, P.J., Raymond, K.N., et al.: Silica microparticles as a solid support for gadolinium phosphonate magnetic resonance imaging contrast agents. *J. Am. Chem. Soc.* **134**, 8046–8049 (2012)
65. Tan, W., Wang, K., He, X., et al.: Bionanotechnology based on silica nanoparticles. *Med. Res. Rev.* **24**, 621–638 (2004)
66. Kim, H.K., Kang, S.J., Choi, S.K., et al.: Highly efficient organic/inorganic hybrid nonlinear optic materials via sol-gel process: synthesis, optical properties, and photobleaching for channel waveguides. *Chem. Mater.* **11**, 779–788 (1999)
67. Lian, W., Litherland, S.A., Badrane, H., et al.: Ultrasensitive detection of biomolecules with fluorescent dye-doped nanoparticles. *Anal. Biochem.* **334**, 135–144 (2004)
68. Smith, J.E., Wang, L., Tan, W.: Bioconjugated silica-coated nanoparticles for bioseparation and bioanalysis. *Trends Anal. Chem.* **25**, 848–855 (2006)
69. Wang, L., Yang, C., Tan, W.: Dual-luminophore-doped silica nanoparticles for multiplexed signaling. *Nano Lett.* **5**, 37–43 (2005)
70. Bagwe, R.P., Yang, C., Hilliard, L.R., et al.: Optimization of dye-doped silica nanoparticles prepared using a reverse microemulsion method. *Langmuir* **20**, 8336–8342 (2004)
71. Yao, G., Wang, L., Wu, Y., et al.: FloDots: Luminescent nanoparticles. *Anal. Bioanal. Chem.* **385**, 518–524 (2006)
72. Bagwe, R.P., Hilliard, L.R., Tan, W.: Surface modification of silica nanoparticles to reduce aggregation and nonspecific binding. *Langmuir* **22**, 4357–4362 (2006)

73. Zhao, X., Bagwe, R.P., Tan, W.: Development of organic dye doped silica nanoparticles in reverse microemulsion. *Adv. Mater.* **16**, 173–176 (2004)
74. Wang, L., Wang, K., Santra, S., et al.: Watching silica nanoparticles glow in the biological world. *Anal. Chem.* **78**, 646–654 (2006)
75. Yoon, T.J., Nam, YuK, Kim, E., et al.: Specific targeting, cell sorting, and bioimaging with smart magnetic silica core-shell nanomaterials. *Small* **2**, 209–215 (2006)
76. Lee, J.E., Lee, N., Kim, H., et al.: Uniform mesoporous dye-doped silica nanoparticles decorated with multiple magnetite nanocrystals for simultaneous enhanced magnetic resonance imaging, fluorescence imaging, and drug delivery. *J. Am. Chem. Soc.* **132**, 552–557 (2010)
77. Koole, R., van Schooneveld, M.M., Hilhorst, J., et al.: Paramagnetic lipid-coated silica nanoparticles with a fluorescent quantum dot core: A new contrast agent platform for multimodality imaging. *Bioconjugate Chem.* **19**, 2471–2479 (2008)
78. Kim, J., Kim, H., Lee, N., et al.: Multifunctional uniform nanoparticles composed of a magnetite nanocrystal core and a mesoporous silica shell for magnetic resonance and fluorescence imaging and for drug delivery. *Angew. Chem. Int. Ed.* **47**, 8438–8441 (2008)
79. Thomas, C.R., Ferris, D.P., Lee, J.H.: Noninvasive remote-controlled release of drug molecules in vitro using magnetic actuation of mechanized nanoparticles. *J. Am. Chem. Soc.* **132**, 10623–10625 (2010)
80. Kim, J., Lee, J.E., Lee, J., et al.: Magnetic fluorescent delivery vehicle using uniform mesoporous silica spheres embedded with monodisperse magnetic and semiconductor nanocrystals. *J. Am. Chem. Soc.* **128**, 688–689 (2006)
81. Ma, M., Chen, H., Chen, Y., et al.: Au capped magnetic core/mesoporous silica shell nanoparticles for combined photothermo-/chemo-therapy and multimodal imaging. *Biomaterials* **33**, 989–998 (2012)
82. Giri, S., Trewyn, B.G., Stellmaker, M.P., et al.: Stimuli-responsive controlled-release delivery system based on mesoporous silica nanorods capped with magnetic nanoparticles. *Angew. Chem.* **117**, 5166–5172 (2005)
83. Wu, Q., Liu, C., Fan, L., et al.: Heparinized magnetic mesoporous silica nanoparticles as multifunctional growth factor delivery carriers. *Nanotechnology* **23**, 485703–485712 (2012)
84. He, Q.J., Zhang, Z., Gao, F., et al.: In vivo biodistribution and urinary excretion of mesoporous silica nanoparticles: Effects of particle size and PEGylation. *Small* **7**, 271–280 (2011)
85. Vivero-Escoto, J.L., Slowing, I.I., Trewyn, B.G., et al.: Mesoporous silica nanoparticles for intracellular controlled drug delivery. *Small* **6**, 1952–1967 (2010)
86. Mamaeva, V., Sahlgren, C., Lindén, M.: Mesoporous silica nanoparticles in medicine—recent advances. *Adv. Drug Deliv. Rev.* (2012). doi:[10.1016/j.addr.2012.07.018](https://doi.org/10.1016/j.addr.2012.07.018)
87. Wu, P., He, Y., Wang, H.F., et al.: Conjugation of glucose oxidase onto Mn-doped zns quantum dots for phosphorescent sensing of glucose in biological fluids. *Anal. Chem.* **82**, 1427–1433 (2010)
88. Slowing, I.I., Trewyn, B.G., Giri, S., et al.: Mesoporous silica nanoparticles for drug delivery and biosensing applications. *Adv. Funct. Mater.* **17**, 1225–1236 (2007)
89. Ray, S., Reddy, P.J., Choudhary, S., et al.: Emerging nanoproteomics approaches for disease biomarker detection: A current perspective. *J. Proteomics* **74**, 2660–2681 (2011)
90. Deng, Z., Zhang, Y., Yue, J., et al.: Green and orange CdTe quantum dots as effective pH-sensitive fluorescent probes for dual simultaneous and independent detection of viruses. *J. Phys. Chem. B* **111**, 12024–12031 (2007)
91. Soman, C.P., Giorgio, T.D.: Quantum dot self-assembly for protein detection with sub-picomolar sensitivity. *Langmuir* **24**, 4399–4404 (2008)
92. Mukundan, H., Xe, H., Price, D., et al.: Quantitative multiplex detection of pathogen biomarkers on multichannel waveguides. *Anal. Chem.* **82**, 136–144 (2010)
93. Herranz, M., Ruibal, A.: Optical imaging in breast cancer diagnosis: The next evolution. *J. Oncol.* (2012). doi:[10.1155/2012/863747](https://doi.org/10.1155/2012/863747)

94. Lee, J.E., Lee, D.J., Lee, N., et al.: Multifunctional mesoporous silica nanocomposite nanoparticles for pH controlled drug release and dual modal imaging. *J. Mater. Chem.* (2011). doi:[10.1039/C1JM11869B](https://doi.org/10.1039/C1JM11869B)
95. Sharma, P., Bengtsson, N.E., Walter, G.A., et al.: Gadolinium-doped silica nanoparticles encapsulating indocyanine green for near infrared and magnetic resonance imaging. *Small* **8**, 2856–2868 (2012)
96. Quan, B., Choi, K., Kim, Y.H., et al.: Near infrared dye indocyanine green doped silica nanoparticles for biological imaging. *Talanta* **99**, 387–393 (2012)
97. Guo, J., Yang, W., Deng, Y., et al.: Organic-dye-coupled magnetic nanoparticles encaged inside thermoresponsive PNIPAM microcapsules. *Small* **1**, 737–743 (2005)
98. Benezra, M., Penate-Medina, O., Zanzonico, P.B., et al.: Multimodal silica nanoparticles are effective cancer-targeted probes in a model of human melanoma. *J. Clin. Invest.* **121**, 2768–2780 (2011)
99. Rieter, W.J., Kim, J.S., Taylor, K.M.L., et al.: Hybrid silica nanoparticles for multimodal imaging. *Angew. Chem.* **119**, 3754–3756 (2007)
100. Joo, K.I., Tai, A., Wang, P.: Semiconductor nanomaterials. In: Kumar, C.S.S.R. (ed.) *Imaging and Tracking of Viruses Using Quantum Dots*, 1st edn. Wiley-VCH, Weinheim (2010)
101. Wu, X., Liu, H., Liu, J., et al.: Immunofluorescent labeling of cancer marker Her2 and other cellular targets with semiconductor quantum dots. *Nat. Biotechnol.* **21**, 41–46 (2003)
102. Smith, A.M., Dave, S., Nie, S., et al.: Multicolor quantum dots for molecular diagnostics of cancer. *Expert Rev. Mol. Diagn.* **6**, 231–244 (2006)
103. Bartneva, N., Vorobjev, I.: Quantum dots in microscopy and cytometry: Immunostaining applications. In: Méndez-Villas, A., Díaz, J. (eds.) *Microscopy: Science, Technology, Applications and Educations*, 1st edn. Formatex Research Center, Badajoz (2010)
104. Tavares, A.J., Chong, L., Petryayeva, E.: Quantum dots as contrast agents for in vivo tumor imaging: Progress and issues. *Anal. Bioanal. Chem.* **399**, 2331–2342 (2011)
105. Xing, Y., Rao, J.: Quantum dot bioconjugates for in vitro diagnostics and in vivo imaging. *Cancer Biomark.* **4**, 307–319 (2008)
106. Choi, H.S., Liu, W., Misra, P., et al.: Renal clearance of quantum dots. *Nat. Biotechnol.* **25**, 1165–1170 (2007)
107. Resch-Genger, U., Grabolle, M., Cavaliere-Jaricot, S., et al.: Quantum dots versus organic dyes as fluorescent labels. *Nat. Methods* **5**, 763–775 (2008)
108. Rieter, W.J., Kim, J.S., Taylor, K.M.L., et al.: Hybrid silica nanoparticles for multimodal imaging. *Angew. Chem. Int. Ed.* **46**, 3680–3682 (2007)
109. Lu, C.W., Hung, Y., Hsiao, J.K., et al.: Bifunctional magnetic silica nanoparticles for highly efficient human stem cell labeling. *Nano Lett.* **7**, 149–154 (2007)
110. Corr, S.A., O'Byrne, A., Gun'ko, Y.K., et al.: Magnetic-fluorescent nanocomposites for biomedical multitasking. *Chem Commun* **43**, 4474–4476 (2006)
111. Zhang, Y., Lovell, J.F.: Porphyrins as theranostic agents from prehistoric to modern times. *Theranostics* **2**, 905–915 (2012)
112. Jain, K.K.: Nanotechnology in clinical laboratory diagnostics. *Clin. Chim. Acta* **358**, 37–54 (2005)
113. Azzazy, H.M., Mansour, M.M., Kazmierczak, S.C.: From diagnostics to therapy: Prospects of quantum dots. *Clin. Biochem.* **40**, 917–927 (2007)
114. Cash, K.J., Clark, H.A.: Nanosensors and nanomaterials for monitoring glucose in diabetes. *Trends Mol. Med.* **16**, 584–593 (2010)
115. Hahn, M.A., Keng, P.C., Krauss, T.D.: Flow cytometric analysis to detect pathogens in bacterial cell mixtures using semiconductor quantum dots. *Anal. Chem.* **80**, 864–872 (2008)
116. Shen, J., Zhao, L., Han, G.: Lanthanide-doped upconverting luminescent nanoparticle platforms for optical imaging-guided drug delivery and therapy. *Adv. Drug Deliv. Rev.* (2012). doi:[10.1016/j.addr.2012.05.007](https://doi.org/10.1016/j.addr.2012.05.007)
117. Wang, F., Chatterjee, D.K., Li, Z., et al.: Synthesis of polyethylenimine/NaYF<sub>4</sub> nanoparticles with upconversion fluorescence. *Nanotechnology* (2006). doi:[10.1088/0957-4484/17/23/013](https://doi.org/10.1088/0957-4484/17/23/013)

118. Niedbala, R.S., Feindt, H., Kardos, K., et al.: Detection of analytes by immunoassay using up-converting phosphor technology. *Anal. Biochem.* **293**, 22–30 (2001)
119. Ma, Z., Dosev, D., Nichkova, M., et al.: Microarray immunoassay for phenoxybenzoic acid using polymer encapsulated Eu:Gd<sub>2</sub>O<sub>3</sub> nanoparticles as fluorescent labels. *Anal. Chem.* **77**, 6864–6873 (2005)
120. Väisänen, V., Härmä, H., Lilja, H., et al.: Time-resolved fluorescence imaging for quantitative histochemistry using lanthanide chelates in nanoparticles and conjugated to monoclonal antibodies. *Luminescence* **15**, 389–397 (2000)
121. Hu, H., Xiong, L.Q., Zhou, J.: Multimodal-luminescence core-shell nanocomposites for targeted imaging of tumor cells. *Chem. Eur. J.* **15**, 3577–3584 (2009)
122. Gai, S., Yang, P., Li, C., et al.: Synthesis of magnetic, up-conversion luminescent, and mesoporous core-shell-structured nanocomposites as drug carriers. *Adv. Funct. Mater.* **20**, 1166–1172 (2010)
123. Chen, Y., Chi, Y.M., Wen, H.M., et al.: Sensitized luminescent terbium nanoparticles: preparation and time-resolved fluorescence assay for DNA. *Anal. Chem.* **79**, 960–965 (2007)
124. Gao, F., Luo, F., Chen, X., et al.: A novel nonenzymatic fluorescent sensor for glucose based on silica nanoparticles doped with europium coordination compound. *Talanta* **80**, 202–206 (2009)
125. Chaudhuri, R.G., Paria, S.: Core/shell nanoparticles: classes, properties, synthesis mechanisms, characterization, and applications. *Chem. Rev.* **112**, 2373–2433 (2012)
126. He, R., You, X., Shao, J., et al.: Core/shell fluorescent magnetic silica-coated composite nanoparticles for bioconjugation. *Nanotechnol.* (2007). doi:[10.1088/0957-4484/18/31/315601](https://doi.org/10.1088/0957-4484/18/31/315601)
127. Lu, H., Yi, G., Zhao, S., et al.: Synthesis and characterization of multi-functional nanoparticles possessing magnetic, up-conversion fluorescence and bio-affinity properties. *J. Mater. Chem.* **14**, 1336–1341 (2004)
128. Reddy, L.H., Arias, J.L., Nicolas, J., et al.: Magnetic nanoparticles: design and characterization, toxicity and biocompatibility, pharmaceutical and biomedical applications. *Chem. Rev.* **112**, 5818–5878 (2012)
129. Hu, S.H., Chen, S.Y., Liu, D.M., et al.: Core/single-crystal-shell nanospheres for controlled drug release via a magnetically triggered rupturing mechanism. *Adv. Mater.* **20**, 2690–2695 (2008)
130. Swami, A., Shi, J., Suresh Gadde, S., et al.: Nanoparticles for targeted and temporally controlled drug delivery. In: Svenson, S., Prud'homme, R.K. (eds.) *Multifunctional Nanoparticles for Drug Delivery Applications: Imaging, Targeting, and Delivery*, 1st edn. Springer, New York (2012)
131. Davis, M.E.: The first targeted delivery of siRNA in humans via a self-assembling, cyclodextrin polymer-based nanoparticle: From concept to clinic. *Mol. Pharm.* **6**, 659–668 (2009)
132. Johng, H.M., Yoo, J.S., Yoon, T.J., et al.: Use of magnetic nanoparticles to visualize threadlike structures inside lymphatic vessels of rats. *eCAM.* **4**, 77–82 (2007)
133. Zhang, Y., Das, G.K., Xu, R., et al.: Tb-doped iron oxide: bifunctional fluorescent and magnetic nanocrystals. *J. Mater. Chem.* **19**, 3696–3703 (2009)
134. Wilson, R., Spiller, D.G., Prior, I.A., et al.: A simple method for preparing spectrally encoded magnetic beads for multiplexed detection. *ACS Nano* **1**, 487–493 (2007)
135. Alexis, F., Pridgen, E., Molnar, L.K., et al.: Factors affecting the clearance and biodistribution of polymeric nanoparticles. *Mol. Pharmaceut.* **5**, 505–515 (2008)
136. He, X., Nie, H., Wang, K., et al.: In vivo study of biodistribution and urinary excretion of surface-modified silica nanoparticles. *Anal. Chem.* **80**, 9597–9603 (2008)
137. Huang, D.M., Hsiao, J.K., Chen, Y.C., et al.: The promotion of human mesenchymal stem cell proliferation by superparamagnetic iron oxide nanoparticles. *Biomaterials* **30**, 3645–3651 (2009)

# Simulation of Precipitate Evolution in Fe-Based Alloys

V. V. Popov

**Abstract** In this chapter possibilities of simulation of precipitate evolution in Fe-based alloys are analyzed. At first separate stages of the process are considered: growth, dissolution and coarsening, and then possibilities of simulation of all the stages of evolution including nucleation in the framework of a unified approach are analyzed. The results obtained are generalized on a case of simulation of precipitate evolution in multicomponent systems. The results of numerical calculations are compared to the available experimental data. Most of examples are concerned with simulation of carbides, nitrides and carbonitride behavior at heat treatment of steels. In the concluding section of the chapter the analysis of possibilities of simulation of precipitate evolution in Fe-based alloys is summed up, and the problems retarding practical kinetic calculations in real commercial alloys are formulated.

**Keywords** Simulation • Numerical methods • Steels • Carbonitrides • Dissolution • Nucleation • Coarsening

## 1 Introduction

The second phase particles present in metal alloys can strongly affect their structure and properties, this influence being both beneficial, and adverse. Heat treatment of alloys, containing dispersed particles, should ensure such morphology, sizes and volume fraction of precipitates which provide an optimal complex of mechanical properties. In the development of precipitation hardening and ageing alloys numerous experimental studies have been carried out on the

---

V. V. Popov (✉)

Institute of Metal Physics, Ural Branch, Russian Academy of Sciences,  
S. Kovalevskaya Street, 18, Ekaterinburg, Russia 620990,  
e-mail: vpopov@imp.uran.ru



precipitates behavior at heat treatment, because without such investigations it was impossible to find a reasonable approach to the choice of alloys compositions and regimes of their heat treatment. Such studies are quite expensive and laborious, but it has been impossible to do without them till recently. The situation has considerably changed in the last years. The creation of powerful high-productive computers and decreasing deficiency of thermodynamic and diffusion data promoted an appearance of publications devoted to simulation of precipitates behavior in metal alloys. In the present paper possibilities of analytical description and simulation of precipitate evolution in metal alloys at heat treatment are analyzed by an example of Fe-based alloys. Successful simulation of evolution of structure of steels and alloys at various processes became possible recently due to high-productive computer technologies, and publications on this problem appear constantly (see, e.g., [1–8]).

In this chapter the methods of simulation of precipitates evolution in steels at isothermal annealing are considered. The main goal of this simulation is to find temporal dependence of the parameters characterizing precipitate ensemble.

The problem of precipitate evolution in an alloy corresponds to the problems of diffusion in areas with moving boundaries; it is the so-called Stephan problem [9]. At present it is not possible to solve this problem in a general form, not only by analytical, but even by numerical methods. From mathematical point of view, the boundary-value problems of diffusion for areas with moving boundaries differ principally from classical problems. The main difficulty in the solution of such problems is that the mass balance conditions at interfaces refer them to the type of non-linear problems, that is, to the problems with non-linear boundary conditions, even in case of constant diffusion coefficients. That is why, as a rule, only some particular cases are considered, using numerous simplifications and assumptions. In particular, only binary systems were mainly considered so far, for which it is much easier to obtain an analytical solution and to carry out the simulation.

Considerable progress in working out methods of solving such problems has been achieved recently due to, first of all, the development of numerical simulation methods and increasing computer power. However, a number of simplifications must be still used in simulation for two main reasons. Firstly, it is the insufficient development of the numerical methods of solving such problems, and secondly, the absence of the data on some parameters required for calculations.

We suppose that the local thermodynamic equilibrium is established at interfaces, the phase composition of the diffusion zone corresponds to the equilibrium, and the kinetics of the process is purely diffusional. Thus, it is assumed that the velocity of phase transformation at an interface is much higher than the diffusion. For the systems considered such an assumption is confirmed by a number of experimental results [10]. It is used in most of papers dealing with simulation of precipitate evolution in metal alloys, and Hillert and Agren [11] showed that calculations based on this assumption are valid even at low temperatures, when the alloying elements have the reduced mobility.

In the present chapter only the cases when the precipitate evolution is controlled by volume diffusion are considered, though it is known that this process may be

controlled by other mechanisms of mass transfer, such as, for example, dislocation diffusion or grain-boundary diffusion. However, for these cases it is, as a rule, not possible to carry out practical calculations, because of the lack of data on the values of the required parameters. Besides, in this chapter the main attention is paid to precipitates evolution in austenite at such temperatures when the mass transfer by volume diffusion is dominating.

Generally speaking, the morphology of particles must be determined as a part of the problem solution, but in this case the problem cannot be solved analytically, and that is why in most cases the particle shape is given a priori and as a rule it is chosen as spherical, and in further consideration this very assumption will be used.

As a rule, precipitates growth, dissolution and coarsening are considered as different processes, though in essence they are particular cases of one and the same process of evolution of precipitates ensemble. Separate consideration of growth, dissolution and coarsening is convenient, because the moving forces of these processes are different constituents of the free energy. In the cases of growth or dissolution it is, first of all, the chemical free energy, whereas in case of coarsening it is the surface free energy.

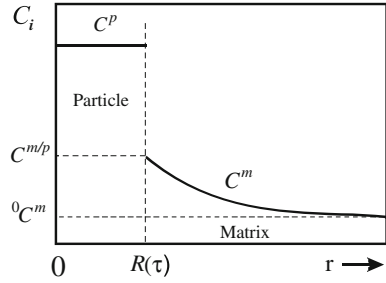
In further sections of the present chapter an attempt is undertaken to describe as generally as possible the evolution of precipitates in steels.

## **2 Simulation of Precipitates Growth and Dissolution**

In case of precipitates growth and dissolution in a metal matrix the process is mainly controlled by the system tendency to decrease its chemical free energy, which is realized through variations of the volume fraction of precipitates and concentrations of components in the matrix.

Dependently on the chemical composition of precipitates and matrix, as well as on the process temperature, an interface can shift both towards the solid solution (particle growth) and towards the particle (its dissolution) due to the reaction diffusion. Besides, the new phase layers may appear in the diffusion zone with their further growth at an expense of the initial constituents of the system. Generally speaking, considering precipitates growth and dissolution one should take into account the polydispersity of precipitates ensemble and the effect of particle sizes on equilibrium conditions at interfaces, but it is commonly assumed that at the stages of growth and dissolution the particle size distribution (PSD) affects only slightly, and its effect may be neglected. It is not always so, but at first we assume that all the particles are of the same shape and sizes, and the influence of the interface curvature on the local equilibrium conditions is not taken into account. We shall restrict our consideration to a one-dimensional case (for a spherical symmetry), as it enables to take into account the main features of the process of precipitates diffusion interaction with a matrix without an excess complication of the problem.

**Fig. 1** Concentration distribution of a solute in a spherical particle surrounding



## 2.1 Methods of Simulation of Precipitates Growth and Dissolution

The simplest description corresponds to the growth or dissolution of precipitates of constant composition in binary systems. In this case one should not take into account interaction of components in a solid solution at diffusion, and the component concentrations at interfaces are constant, and their values can be determined directly from the corresponding phase diagrams. Most of the available analytical solutions correspond to this very case. As applied to the growth and dissolution of carbides and nitrides in steels, these solutions may be used, with certain reservations, only for the case of Fe carbides growth and dissolution in carbon steels.

In the first studies of precipitate growth and dissolution, which are reviewed in [12], the growth and dissolution of one precipitate of constant composition in an infinite matrix of a binary alloy was considered, the diffusion coefficient being assumed constant. The scheme of concentration distribution of a solute in a particle surrounding is shown in Fig. 1, where  $C^p$  and  $C^m$  are the solute concentrations in the particle and matrix, respectively;  ${}^0C^m$  is the initial concentration in the matrix;  $C^{m/p}$  is the concentration in the matrix at an interface with the particle; and  $R$  is the particle radius. This case corresponds to an infinitely small volume fraction of precipitates.

Taking into account the spherical symmetry of the problem, the diffusion equation in this case has the form:

$$\frac{\partial C^m}{\partial t} = D^m \frac{1}{r^2} \frac{\partial}{\partial r} \left( r^2 \frac{\partial C^m}{\partial r} \right) \quad (1)$$

where  $D^m$  is the solute diffusivity in the matrix.

The mass balance condition at an interface, determining its velocity, is expressed as:

$$\left( \frac{C^p}{v_a^p} - \frac{C^{m/p}}{v_a^m} \right) \frac{dR}{dt} = \frac{1}{v_a^m} D^m \frac{\partial C^m}{\partial r} \Big|_{r=R} \quad (2)$$

where  $v_a^f$  is the volume per one atom of phase  $f$ .

Initial and boundary conditions for this case are:

$$R(t = 0) = R_0; \quad (3)$$

$$C^m(t = 0, R > R_0) = {}^\circ C^m; \quad (4)$$

$$C^m(t > 0, r = R) = C^{m/p}; \quad (5)$$

$$C^m(t > 0, r = \infty) = {}^\circ C^m \quad (6)$$

The boundary condition (5) serves as the local equilibrium condition, and it gives the equilibrium concentration at an interface which can be determined from the state diagram (in this case the correction on the interface curvature is not made).

The problem (1–6) was analyzed in [12], and the authors failed to find an exact analytical solution for non-zero initial radius. Three approximations were analyzed, namely, of linear gradient, stationary field and stationary interface. The linear gradient approximation assumes linear concentration profile in a matrix. According to [12], this approximation does not take into account the problem symmetry in the spherical case, which causes essential difficulties in the consideration of dissolution and makes it useless.

The stationary field approximation assumes that concentration field around the particle only slightly changes with time, and based on this assumption the left part of the diffusion equation is set equal to zero. As a result, the Laplace equation is obtained, the solution of which enables to find concentration distribution in the particle surrounding. Substitution of the as-determined concentration distribution into the mass balance equation gives the temporal dependence of precipitate sizes.

The immovable interface approximation assumes that the precipitate/matrix interface movement only slightly affects the concentration distribution in the particle surrounding, i.e., the concentration distribution is determined in the assumption that the interface is immovable. This enables to find an analytical expression for the solute concentration distribution in the matrix and analytical temporal dependence of precipitate sizes.

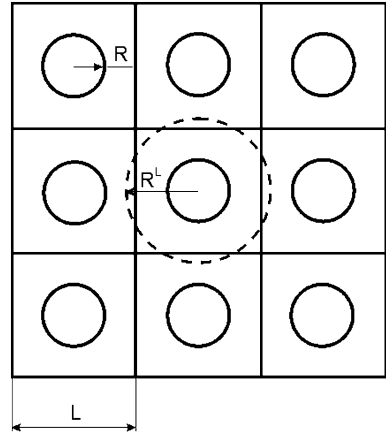
An exact analytical solution of the problem of a spherical precipitate dissolution in an infinite matrix was obtained in [13]. It should be noted, that the solution obtained is quite cumbersome and has a form of infinite series. However, comparing it with the solutions obtained based on various approximations, one can estimate correctness of the latter.

As demonstrated by an analysis carried out in [12, 14], the key parameter determining the validity of various approximations is the following one:

$$\lambda = \frac{C^{m/p} - {}^\circ C^m}{C^p - C^{m/p}}. \quad (7)$$

This analysis shows that the approximation of stationary interface is the best one at small  $|\lambda|$ . The results obtained using the stationary field approximation

**Fig. 2** The scheme of matrix partition into cells for consideration of growth and dissolution of diffusion interacting particles [14]



somewhat differ. However, with decreasing  $|\lambda|$  the results of calculations made with both approximations approach each other and the exact solution. At low  $|\lambda|$  it is quite correctly to use the stationary approximation.

In real steels a great number of second phase particles are always present, and if their density is high, these particles are in diffusion interaction, because their diffusion fields overlap, which affects the kinetics of their growth and dissolution. To solve this problem the method is usually applied which enables to consider the diffusion interaction of one particle with a matrix in a typical cell, limiting the solid solution volume, and then to extend the regularities of the diffusion interaction in this volume on the whole totality of cells enclosing all matrix. All the precipitates are assumed to have the same shape and sizes and to be uniformly distributed in the matrix, i.e. the matrix is schematically divided into identical cells with a particle in the center of each of them (Fig. 2). In this figure  $L$  is the distance between particles, and  $R^L$  is the cell radius.

The problem symmetry imposes the condition of no diffusion flow through a cell wall, i.e. the normal components of concentration gradients at the cell wall must be zero. For mathematical simplification of the problem (reducing it to a one-dimensional case) it is assumed that every particle is in the cell center, the symmetry of the cell being the same as that of the particle, and its volume being equal to that of the cubic cell shown in Fig. 2. For example, in case of spherical particles the cells also have the spherical shape, and their radius can be calculated as:

$$R^L = \left(\frac{3}{4\pi}\right)^{1/3} L = \left(\frac{3}{4\pi N_V}\right)^{1/3}, \quad (8)$$

where  $N_V$  is the number of particles in a unit volume.

Thus, the multi-particle diffusion problem is reduced to the one-particle one, and the diffusion interaction in one cell is considered. Equations describing mass transfer in the system, mass balance condition and local thermodynamic

equilibrium in this case are formulated as in the previous problem. The difference is only in the form of boundary conditions. The boundary conditions in this case instead of Eq. (6) include the following equation:

$$\left. \frac{\partial C^m}{\partial r} \right|_{r=R^L} = 0, \quad (9)$$

which expresses that the concentration gradient at a cell boundary equals to zero. These boundary conditions follow from the symmetry considerations and result from an assumption that all the particles have the same shape and size and are located at the same distances from each other.

The problems of growth and dissolution of precipitates in the limited matrix of binary systems were solved in [15–17], where quite cumbersome analytical solutions in form of infinite series were obtained. The analysis of the solutions obtained shows, that overlapping of the diffusion fields of different particles may appreciably affect the kinetics of precipitate growth and dissolution. This effect manifests itself in the fact that the velocities of precipitates growth or dissolution in the limited matrix decrease monotonically with time compared to those in an infinite matrix.

The solution of problems of precipitate growth and dissolution for multi-component systems is much more difficult than for binary, because of a number of factors. Firstly, to find concentration distributions in a particle surrounding one must solve not one differential equation, but a system of differential equations, because the flux of any component is determined not only by its concentration gradient, but by concentration gradients of all the alloy components. Secondly, unlike the case of binary systems, concentrations at interfaces are not known a priori, and to find them one must solve together with diffusion equations and mass balance equations the thermodynamic equations determining equilibrium conditions at interfaces. Thirdly, for multi-component systems diffusion coefficients commonly cannot be considered as constant. All these factors complicate the problem considerably.

That is why analytical solutions can be obtained only in the simplest cases, which are not quite adequate to the real processes in alloys at particle growth and/or dissolution.

As a rule, in the available analytical solutions for multi-component systems the model of constant diffusion coefficients is used, and they correspond to the growth or dissolution of precipitates in an infinite matrix, because in this case it is easier to find concentration distributions of components, and concentrations at interfaces do not change with time [10, 18–21]. In [10, 19–21] the obtained analytical solutions were used for calculation of the diffusion interaction kinetics for a number of carbides in steels for the case of plane symmetry and semi-infinite matrix. The comparison of these calculations with experimental data obtained on diffusion couples demonstrated their good agreement, which shows that in some cases the analytical solutions can be applied to the description of diffusion interaction in multi-component systems as well. However, they may be used only for quite a limited category of problems.

In the last decades a number of studies appeared where such problem is solved using numerical methods. There are two reasons for using the latter. Firstly, the local equilibrium at a moving interface in a multi-component system cannot be determined directly from a common phase diagram. Secondly, the realistic consideration of diffusion in multi-component systems requires solution of a system of differential equations in partial derivatives, but not of one equation as in case of binary alloys. Besides, in general one must take into account the possibility of intermediate phase formation, changes in composition of an initial particle, concentration dependences of diffusion parameters, etc.

The problem definition in case of growth or dissolution of spherical precipitates in a limited matrix of  $(N + 1)$ -component alloy, in case when intermediate phase layers may form between the particle (phase 1) and matrix (phase Q), with allowance made for diffusion processes in particles, is as follows. We assume all the particles to have the same sizes and use the above-described approach based on the matrix partition into cells and consideration of the diffusion interaction in one cell. The scheme of concentration distribution of the  $i$ -th component in a cell for this case is shown in Fig. 3, where  $C_i^f$  is the  $i$ -th component concentration in phase  $f$ ;  $C_i^{f/f+1}$  is the  $i$ -th component concentration in phase  $f$  at an interface with  $f + 1$ ;  $R^{f/f+1}$  is the coordinate of an interface between  $f$  and  $f + 1$ .

Mathematical problem definition for this case is as follows. Mass transfer in every phase is described by  $N$  differential equations of the type:

$$\frac{\partial C_i^f}{\partial t} = \frac{1}{r^2} \frac{\partial}{\partial r} \left( r^2 \sum_{l=1}^N \tilde{D}_{il}^f \frac{\partial C_l^f}{\partial r} \right), \tag{10}$$

where  $\tilde{D}_{il}^f$  are partial interdiffusion coefficients of components in phase  $f$ .

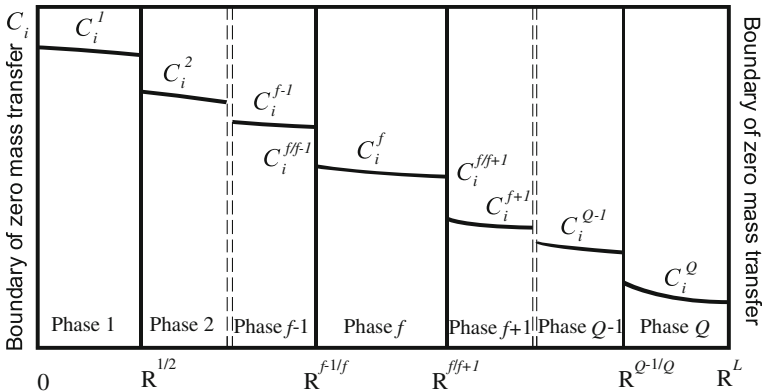


Fig. 3 The scheme of concentration distribution of the  $i$ -th component in a cell

The mass balance conditions include  $(Q-1) \times N$  equations:

$$\left( \frac{C_i^{f+1/f}}{v_a^{f+1}} - \frac{C_i^{f/f+1}}{v_a^f} \right) \frac{dR_f}{dt} = \frac{1}{v_a^f} \sum_{l=1}^N \tilde{D}_{il}^f \frac{\partial C_l^f}{\partial r} \Big|_{r=R_f} - \frac{1}{v_a^{f+1}} \sum_{l=1}^N \tilde{D}_{il}^{f+1} \frac{\partial C_l^{f+1}}{\partial r} \Big|_{r=R_f}, \quad (11)$$

Equilibrium conditions at interfaces include  $(Q-1) \times (N+1)$  equations of the type

$$\bar{G}_i^{f/f+1} = \bar{G}_i^{f+1/f}, \quad (12)$$

where  $\bar{G}_i^{f/f+1}$  is the chemical potential of component  $i$  in phase  $f$  at an interface with  $f+1$ .

Initial conditions for this case include  $Q-1$  equations of the type:

$$R^{f/(f+1)}(t=0) = R_0 \quad (13)$$

and  $N$  equations

$$C_i^1(r < R_0, t = 0) = {}^0C_i^1 \quad (14)$$

$$C_i^Q(r > R_0, t = 0) = {}^0C_i^Q, \quad (15)$$

where  ${}^0C_i^1$  and  ${}^0C_i^Q$  are initial concentrations of the  $i$ -th component in the precipitate and matrix.

Boundary conditions include  $N$  equations

$$\frac{\partial C_i^1}{\partial r} \Big|_{r=0} = 0 \quad (16)$$

$$\frac{\partial C_i^Q}{\partial r} \Big|_{r=R^L} = 0, \quad (17)$$

which determine zero concentration gradients of components in a particle center and at a cell boundary.

For multi-component systems the solution of problems of precipitate growth and dissolution requires solving differential diffusion equations for every phase together with mass balance and thermodynamic equations determining mass balance conditions and local equilibrium at interfaces. Such problems can be solved only by numerical methods.

Application of numerical methods, such as finite differences, finite elements or boundary elements methods, almost does not require any simplifications and assumptions, which are usually needed for analytical methods.

The most widely used for the solution of diffusion problems is the finite differences method (or grid method), the main advantage of which is the simplicity of its numerical realization.



Differences methods are based on substitution of a region of continuous changing of arguments of the desired functions entered into differential equations for a grid with discrete set of points-nodes. The grid functions determined in discrete nodes are taken instead of continuous change of arguments, and the derivatives entering the differential equations and boundary conditions are substituted for difference relationships. As a result of such substitution, the boundary problem in partial derivatives is reduced to a system of algebraic difference equations referred to as finite-difference scheme.

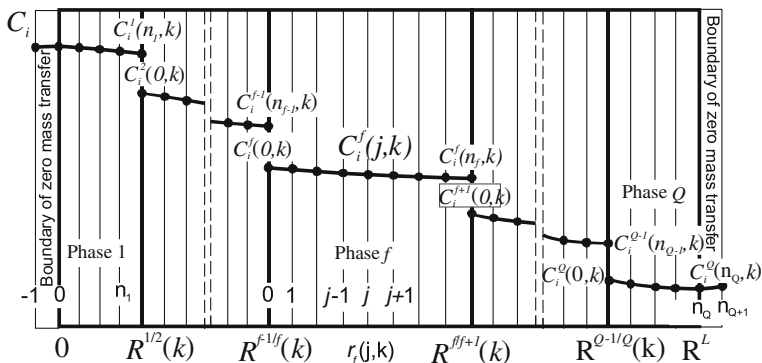
When solving nonlinear parabolic differential diffusion equations, it is advisable to use conservative (divergent) implicit finite-difference schemes [22, 23]. An essential drawback of explicit finite-difference schemes compared to the implicit ones is the dependence of stability of the former on the relationship between time and space steps. As for the implicit scheme, it is absolutely stable at any ratios of steps, which enables to reduce the calculation time, though the explicit scheme simplifies the solution of the problem. Besides, an advantage of stable schemes is that it is not required to investigate additionally the velocity of the solution convergence, as it coincides with an order of approximation of a differential equation. An error inserted when a differential equation is substituted for a finite-difference scheme depends on the accuracy of derivatives approximation in the differential equation and boundary conditions.

Solution of nonstationary problems of diffusion and heat conductivity with movable interfaces, i.e. with changing regions of physical parameters continuity, requires working out special approaches. In the problems like Stephan's problem the main difficulty is that interfaces movement results in the appearance of new nodes of a spatial grid, which belonged to another phase, in one of the adjacent phases.

By now quite enough methods of overcoming difficulties of numerical calculations, caused by movable interfaces, have been worked out [24–35]. The available methods of solving problems like Stephan's problem are reviewed and analyzed in detail in [24, 25]. The drawback of most of these methods is that their application suggests the use of uniform spatial grids with one and the same space step in different phases, and in case of multi-component multi-phase problems this may require grids with the great number of spatial nodes. There is no such drawback in the method developed in [35, 36], in which its own spatial grid with the fixed number of nodes is introduced for every phase.

The position of phase transformation boundary coincides with a cell node. At phase transformations due to the change of phase size the grid step is changed in such way, that the number of nodes in every phase remains unchanged, and interphase boundaries coincide with the same grid nodes.

Application of the finite difference method to the solution of diffusion problems in case, when the formation of intermediate phase layers is possible, requires giving their finite thickness at an initial moment. Besides, at the initial moment the spatial grid and concentrations at every node for all the phases, including those absent in the diffusion zone at the initial moment, must be given. This would not



**Fig. 4** Scheme of spatial partition and concentration distribution of the  $i$ -th component in a cell at the  $k$ -th time step

introduce a great error, if the thickness given at the initial moment is much lower than the finite phase thickness.

Let's consider the numerical solution of problem (10–17) by the finite difference method. The spatial partition was made in such way that for every phase its own spatial grid with the fixed number of nodes was introduced. Interphase boundaries coincided with the grid nodes, and the last node of phase  $f$  coincided with the zero node of phase  $f + 1$ . The allowance was made for the construction of non-uniform spatial grid. Figure 4 demonstrates the scheme of spatial partition and concentration distribution of the  $i$ -th component in a cell at the  $k$ -th time step, the following designations being used:  $r_j(j, k)$  is the  $j$ -th node coordinate of phase  $f$  at the  $k$ -th time step;  $R^{f/f+1}(k)$  is the position of phase boundary between  $f$  and  $f + 1$  at the  $k$ -th time step; and  $C_i^f(j, k)$  is the concentration of the  $i$ -th component in the  $j$ -th node of phase  $f$  at the  $k$ -th time step.

In the process of diffusion interaction every phase continuously changes its thickness, and coordinates of internal nodes of spatial grid change in such way that their distance from interphase boundaries always comprises a certain percent of the phase thickness. The internal nodes velocities are a linear combination of velocities of interfaces between the neighboring phases [35]:

$$V_f(r) = \frac{1}{R^{f/f+1} - R^{f-1/f}} \left\{ \left( R^{f/f+1} - r \right) \frac{dR^{f-1/f}}{dt} + \left( r - R^{f-1/f} \right) \frac{dR^{f/f+1}}{dt} \right\}, \tag{18}$$

where  $V_f(r)$  is the velocity of an internal point of phase  $f$  with  $r$  coordinate.

Intensity of concentration changes of components in a mobile point may be presented as follows (according to [36]):

$$\frac{dC_i^f}{dt} = \frac{\partial C_i^f}{\partial r} V_f(r) + \frac{\partial C_i^f}{\partial t} \tag{19}$$

Substitution of expressions (10) and (18) in this equation gives:

$$\begin{aligned} \frac{\partial C_i^f}{\partial t} = \frac{\partial C_i^f}{\partial r} \cdot \frac{(R^{f/f+1} - r) \frac{\partial R^{f-1/f}}{\partial t} + (r - R^{f-1/f}) \frac{\partial R^{f/f+1}}{\partial t}}{R^{f/f+1} - R^{f-1/f}} \\ + \frac{1}{r^2} \frac{\partial}{\partial r} \left( r^2 \sum_{l=1}^N \tilde{D}_{il}^f \frac{\partial C_l^f}{\partial r} \right) \end{aligned} \quad (20)$$

The following designations are introduced:  $\tilde{D}_{il}^f(j \pm 1/2, k)$  are partial coefficients of interdiffusion in phase  $f$  corresponding to component concentrations median between their values in the  $j$ -th and the nearest to it nodes of phase  $f$  in the  $k$ -th time step; and  $r_f(j \pm 1/2, k) = [r_f(j, k) + r_f(j \pm 1, k)]/2$  are coordinates of segment middles between the  $j$ -th and the nearest to it nodes of phase  $f$  in the  $k$ -th time step.

With these designations, the difference approximation of Eq. (20) may be written as follows, using the conservative absolutely stable implicit difference scheme:

$$\begin{aligned} \frac{C_i^f(j, k+1) - C_i^f(j, k)}{t(k+1) - t(k)} = \frac{C_i^f(j+1, k+1) - C_i^f(j-1, k+1)}{r_f(j+1, k+1) - r_f(j-1, k+1)} \\ \times \frac{1}{R^{f/f+1}(k+1) - R^{f-1/f}(k+1)} \\ \times \left\{ \left[ R^{f/f+1}(k+1) - r_f(j, k+1) \right] \frac{R^{f-1/f}(k+1) - R^{f-1/f}(k)}{t(k+1) - t(k)} \right. \\ \left. + \left[ r_f(j, k+1) - R^{f-1/f}(k+1) \right] \frac{R^{f/f+1}(k+1) - R^{f/f+1}(k)}{t(k+1) - t(k)} \right\} \\ + \frac{1}{r_f^2(j, k+1)} \times \frac{2}{r_f(j+1, k+1) - r_f(j-1, k+1)} \\ \times \left[ r_f^2(j+1/2, k+1) \sum_{l=1}^N \tilde{D}_{il}^f(j+1/2, k+1) \frac{C_l^f(j+1, k+1) - C_l^f(j, k+1)}{r_f(j+1, k+1) - r_f(j, k+1)} \right. \\ \left. - r_f^2(j-1/2, k+1) \sum_{l=1}^N \tilde{D}_{il}^f(j-1/2, k+1) \frac{C_l^f(j, k+1) - C_l^f(j-1, k+1)}{r_f(j, k+1) - r_f(j-1, k+1)} \right] \end{aligned} \quad (21)$$

Using boundary conditions (16) and (17), one can write the difference approximation of differential Eq. (19) for the zero node of phase 1 and the  $n_Q$ -th node of phase  $Q$  as:

$$\frac{C_i^1(0, k+1) - C_i^1(0, k)}{t(k+1) - t(k)} = \frac{6}{r_1^2(1, k+1)} \times \sum_{l=1}^N \tilde{D}_{il}^1(j/2, k+1) \cdot [C_i^1(1, k+1) - C_j^1(0, k+1)] \quad (22)$$

$$\frac{C_i^Q(n_Q, k+1) - C_i^Q(n_Q, k)}{t(k+1) - t(k)} = \frac{r_Q^2(n_Q - 1/2, k+1)}{(R^L)^2 [R^L - r_Q(n_Q - 1, k+1)]^2} \times \sum_{l=1}^N \tilde{D}_{il}^Q(n_Q - 1/2, k+1) \cdot [C_i^Q(n_Q - 1, k+1) - C_l^Q(n_Q, k+1)] \quad (23)$$

As the boundary concentrations are the concentrations in the zero and the  $n_f$ -th nodes of the spatial grid, the difference approximation of balance Eq. (11) can be written as:

$$\begin{aligned} & \left[ \frac{C_i^{f+1}(0, k+1)}{v_a^{f+1}} - \frac{C_i^f(n_f, k+1)}{v_a^f} \right] \frac{R^{f/f+1}(k+1) - R^{f/f+1}(k)}{t(k+1) - t(k)} \\ &= \frac{1}{v_a^f} \sum_{l=1}^N \tilde{D}_{il}^f(1/2, k+1) \frac{C_l^f(n_f, k+1) - C_l^f(n_f - 1, k+1)}{R^{f/f+1}(k+1) - r_f(n_f - 1, k+1)} \\ &- \frac{1}{v_a^{f+1}} \sum_{l=1}^N \tilde{D}_{il}^{f+1}(1/2, k+1) \frac{C_l^{f+1}(1, k+1) - C_l^{f+1}(0, k+1)}{r_{f+1}(1, k+1) - R^{f+1/f}(k+1)}, \end{aligned} \quad (24)$$

and the local thermodynamic equilibrium conditions at the  $ff + 1$  interface are:

$$\bar{G}_i^{f/f+1} [C_1^f(n_f, k+1), \dots, C_N^f(n_f, k+1)] = \bar{G}_i^{f+1/f} [C_1^{f+1}(0, k+1), \dots, C_N^{f+1}(0, k+1)]. \quad (25)$$

The most effective method of solving linear differential equations is the sweep method. However, in this case this method cannot be used directly, because the initial boundary problem was nonlinear, and hence the obtained system of finite-difference Eqs. (21–24) is also nonlinear. Besides, these nonlinear finite-difference equations must be solved together with transcendent thermodynamic Eq. (25), and this appreciably complicates the problem considered, because one must solve a system of transcendent equations of high dimensionality. To overcome this difficulty, an iteration procedure was used in [37], in which the whole system of equations was divided into several systems, and these systems were solved sequentially till the required accuracy was achieved. For every interface a system of thermodynamic and balance equations was solved, and then for every phase a system of difference diffusion equations was solved as well, and this procedure was repeated time and again.

We used an analogous procedure in [38], in simulation of kinetics of titanium carbide dissolution in austenite. This algorithm has a relatively slow convergence, and the solution accuracy is poorly controlled. That is why in [39, 40] we realized another approach, based on combined solution of diffusion equations, mass balance equations and thermodynamic equations.

Balance Eq. (24) contain interface coordinates, boundary concentrations and concentrations in the nodes nearest to boundaries as unknown parameters, i.e. they have the following form:

$$\begin{aligned}
 FB_i^f \left[ R^{f/f+1}(k+1), C_1^f(n_f-1, k+1), \dots, C_N^f(n_f-1, k+1), \right. \\
 \left. C_1^f(n_f, k+1), \dots, C_N^f(n_f, k+1), C_1^{f+1}(0, k+1), \dots, C_N^{f+1}(0, k+1), \right. \\
 \left. C_1^{f+1}(1, k+1), \dots, C_N^{f+1}(1, k+1) \right] = 0
 \end{aligned} \quad (26)$$

Thermodynamic equations contain only the values of boundary concentrations as unknown parameters, and they are as follows:

$$FT_i^f \left[ C_1^f(n_f, k+1), \dots, C_N^f(n_f, k+1), C_1^{f+1}(0, k+1), \dots, C_N^{f+1}(0, k+1) \right] = 0. \quad (27)$$

If concentrations the in nodes nearest to boundaries could be expressed explicitly by difference Eqs. (21–23) through the values of boundary concentrations and positions of interphase boundaries, and then substituted into balance Eq. (26), a system of not very high dimensionality would be obtained, consisting of balance and thermodynamic equations, the solution of which would give the values of boundary concentrations and positions of interphase boundaries at a new time step. Unfortunately, it is impossible to do so. However, in solving the problem by numerical methods it is quite enough that the relationship between concentrations in nodes nearest to the boundary, boundary concentrations and positions of interphase boundaries is implicitly given by (21–23), and we used this situation in working out the problem solution algorithm.

The step-by-step procedure was used in calculations, and based on the interphase boundary position and concentration distributions for the time  $t$  these parameters were calculated for  $t + \Delta t$ .

The calculation order was as follows:

1. A point of initial approximations for the values of boundary concentrations in every phase and position of interphase boundary at a new time step was chosen.
2. Points in the neighborhood of the point of initial approximations were given.
3. For the point of initial approximations and the points in its neighborhood concentration distributions in all phases were calculated. In every case the spatial grid was reconstructed taking into account the boundary shift at the transition to a new time step, and concentration distributions in the phases

present were found through the solution of the system of difference Eq. (21–23) by the sweep method. Iteration procedures together with the sweep method were used in solution of difference equations. The finite-difference equations were linearized, i.e. diffusion coefficients were substituted in them for concentrations taken in the previous iteration, and for the first iteration in the previous time step.

4. The value of functions  $FB_i^f$  and  $FT_i^f$  were calculated in the point of initial approximations and in the points in its neighborhood, for which the values of boundary concentrations and positions of interphase boundary were used, as well as the values of concentrations in the nodes nearest to the boundary, determined at the third step.
5. The values of the derivatives of functions  $FB_i^f$  and  $FT_i^f$  for boundary concentrations and interface coordinates in a point corresponding to the initial approximations were found by the numerical differentiation.
6. Corrections to the initial approximations and specified values of the unknowns were found by the Newton-Raffson method based on the determined values of  $FB_i^f$  and  $FT_i^f$  functions and their derivatives.

The data obtained in the cycle (2–6) were used as an initial approximation for the new iteration, i.e. the calculation was repeated from point 2. If the consequent iteration differed from the previous one by a value smaller than the given convergence accuracy, then the iteration exit was performed.

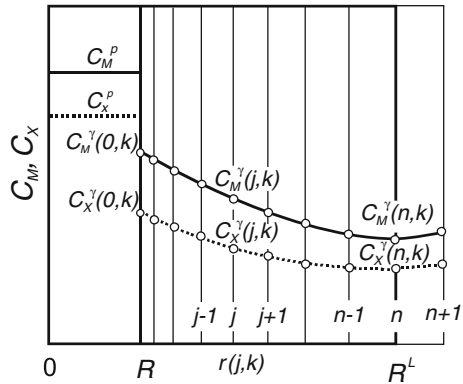
As mentioned above, in solving difference equations one must use iteration procedures together with the sweep method, i.e. solve systems of equations many times, because of concentration dependences of diffusion coefficients, which considerably increase the computation time. To accelerate the calculation procedure, in our further studies we used a parallel algorithm of matrix sweep, which was realized on a multi-processor computation complex [41].

## ***2.2 Simulation of Carbides and Nitrides Growth and Dissolution in Austenite***

Solutions of diffusion problems like Stephan's problem for multi-phase multi-component systems are concerned with difficulties caused not only by their complex numerical realization, but with the absence in many cases of the required data on various parameters. Very often it is for this reason that different simplifications are to be used, and one has to restrict consideration to a relatively small number of components.

By now, because of the deficiency of data on the diffusion parameters, it is actually impossible to carry out practical calculations of growth or dissolution of particles in the systems with more than three components.

**Fig. 5** The scheme of spatial partition and concentration distributions of components in a cell for a case of carbide or nitride dissolution in steel



Let's consider application of the method described in the previous section for simulation of growth and dissolution of carbides and nitrides of constant composition,  $Fe_zM_{(1-z)}X_n$ , in the austenite of triple Fe-M-X systems (where M is a carbide- or nitride-forming element, and X is carbon or nitrogen). The scheme of concentration distribution and spatial grid construction in a cell for this case is shown in Fig. 5. The Fe-M-X systems can be considered as model relative to real steels. Analysis of the results of calculations of dissolution kinetics of carbides and nitrides in such systems may be helpful in the proper choice of heat treatment of steels.

Taking into account, that the diffusion mobility of interstitial elements is much higher than that of substitutional, a simplified method suggested in [22, 42] can be used for the description of interdiffusion in austenite. In this case the mass transfer in the system can be described by a system of equations:

$$\frac{\partial C_M^\gamma}{\partial t} = \frac{1}{r^2} \frac{\partial}{\partial r} \left( r^2 \widehat{D}_M^\gamma \frac{\partial C_M^\gamma}{\partial r} \right), \tag{28}$$

$$\frac{\partial C_X^\gamma}{\partial t} = \frac{1}{r^2} \frac{\partial}{\partial r} \left( r^2 \widetilde{D}_{XX}^\gamma \frac{\partial C_X^\gamma}{\partial r} + r^2 \widetilde{D}_{XM}^\gamma \frac{\partial C_M^\gamma}{\partial r} \right), \tag{29}$$

where indexes M and X denote, respectively, the carbide- or nitride-forming element and carbon or nitrogen;  $\widehat{D}_M^\gamma$  is the effective coefficient of interdiffusion of substitutional element in the austenite of the triple system Fe-M-X.

Conditions at a cell boundary are:

$$\left. \frac{\partial C_M^\gamma}{\partial r} \right|_{r=R^L} = 0 \tag{30}$$

and

$$\left. \frac{\partial C_X^\gamma}{\partial r} \right|_{r=R^L} = 0 \tag{31}$$

Mass balance conditions at an interphase boundary are expressed by the equations:

$$\left( \frac{C_M^p}{v_a^p} - \frac{C_M^{\gamma/p}}{v_a^{\gamma/p}} \right) \frac{dR}{dt} = \frac{1}{v_a^{\gamma}} \widehat{D}_M^{\gamma} \frac{\partial C_M^{\gamma}}{\partial r} \Big|_{r=R} \quad (32)$$

and

$$\left( \frac{C_X^p}{v_a^p} - \frac{C_X^{\gamma/p}}{v_a^{\gamma/p}} \right) \frac{dR}{dt} = \frac{1}{v_a^{\gamma}} \left( \widetilde{D}_{XX}^{\gamma} \frac{\partial C_X^{\gamma}}{\partial r} \Big|_{r=R} + \widetilde{D}_{XM}^{\gamma} \frac{\partial C_M^{\gamma}}{\partial r} \Big|_{r=R} \right). \quad (33)$$

Taking into account the constant composition of interstitial phase  $M_zFe_{(1-z)}X_n$ , the local thermodynamic equilibrium conditions at the interphase boundary take the form:

$$z\overline{G}_M^{\gamma/p} + (1-z)\overline{G}_{Fe}^{\gamma/p} + n\overline{G}_X^{\gamma/p} = G_{M_zFe_{1-z}X_n}, \quad (34)$$

where  $G_{M_zFe_{1-z}X_n}$  is the Gibbs energy of one  $M_zFe_{1-z}X_n$  formula unit.

For sparingly soluble carbides and nitrides of  $MX_n$  type the equilibrium conditions can be expressed by solubility products of these compounds in austenite.

Equations (19), describing concentration changes of components in mobile nodes, taking into account expressions (18) and (28–29), in this case take the form:

$$\frac{\partial C_M^{\gamma}}{\partial t} = \frac{\partial C_M^{\gamma}}{\partial r} \left[ \frac{R^L - r}{R^L - R} \frac{dR}{dt} \right] + \frac{1}{r^2} \frac{\partial}{\partial r} \left[ r^2 \widehat{D}_M^{\gamma} \frac{\partial C_M^{\gamma}}{\partial r} \right] \quad (35)$$

and

$$\frac{\partial C_X^{\gamma}}{\partial t} = \frac{\partial C_X^{\gamma}}{\partial r} \left[ \frac{R^L - r}{R^L - R} \frac{dR}{dt} \right] + \frac{1}{r^2} \frac{\partial}{\partial r} \left[ r^2 \left( \widetilde{D}_{XX}^{\gamma} \frac{\partial C_X^{\gamma}}{\partial r} + \widetilde{D}_{XM}^{\gamma} \frac{\partial C_M^{\gamma}}{\partial r} \right) \right]. \quad (36)$$

In the difference approximation Eq. (35–36) take the form:

$$\begin{aligned} \frac{C_M^{\gamma}(j, k+1) - C_M^{\gamma}(j, k)}{t(k+1) - t(k)} &= \frac{C_M^{\gamma}(j+1, k+1) - C_M^{\gamma}(j-1, k+1)}{r(j+1, k+1) - r(j-1, k+1)} \times \frac{R^L - r(j, k+1)}{R^L - R(k+1)} \\ &\times \frac{R(k+1) - R(k)}{t(k+1) - t(k)} + \frac{1}{r_f^2(j, k+1)} \times \frac{2}{r_f(j+1, k+1) - r_f(j-1, k+1)} \\ &\times \left\{ \frac{r^2(j+1/2, k+1)}{r(j+1, k+1) - r(j, k+1)} \widehat{D}_M^{\gamma}(j+1/2, k+1) \left[ C_M^{\gamma}(j+1, k+1) - C_j^f(j, k+1) \right] \right. \\ &\left. - \frac{r^2(j-1/2, k+1)}{r(j, k+1) - r(j-1, k+1)} \widehat{D}_M^{\gamma}(j-1/2, k+1) \left[ C_M^{\gamma}(j, k+1) - C_j^f(j-1, k+1) \right] \right\} \end{aligned} \quad (37)$$



$$\begin{aligned}
& \frac{C_X^{\gamma}(j, k+1) - C_X^f(j, k)}{t(k+1) - t(k)} = \frac{C_X^{\gamma}(j+1, k+1) - C_X^{\gamma}(j-1, k+1)}{r(j+1, k+1) - r(j-1, k+1)} \times \frac{R^L - r(j, k+1)}{R^L - R(k+1)} \\
& \times \frac{R(k+1) - R(k)}{t(k+1) - t(k)} + \frac{1}{r_j^2(j, k+1)} \times \frac{2}{r_j(j+1, k+1) - r_j(j-1, k+1)} \\
& \times \left\{ \frac{r^2(j+1/2, k+1)}{r(j+1, k+1) - r(j, k+1)} [\tilde{D}_{XX}^{\gamma}(j+1/2, k+1)(C_X^{\gamma}(j+1, k+1) - C_X^{\gamma}(j, k+1)) \right. \\
& + \tilde{D}_{XM}^{\gamma}(j+1/2, k+1)(C_M^{\gamma}(j+1, k+1) - C_M^{\gamma}(j, k+1))] \\
& \left. - \frac{r^2(j-1/2, k+1)}{r(j, k+1) - r(j-1, k+1)} [\tilde{D}_{XX}^{\gamma}(j-1/2, k+1)(C_X^{\gamma}(j, k+1) - C_X^f(j-1, k+1)) \right. \\
& \left. + \tilde{D}_{XM}^{\gamma}(j-1/2, k+1)(C_M^{\gamma}(j, k+1) - C_M^{\gamma}(j-1, k+1))] \right\}
\end{aligned} \tag{38}$$

Based on the boundary conditions (30–31), the difference approximation for a node located at a cell boundary takes the form:

$$\begin{aligned}
& \frac{C_M^{\gamma}(n, k+1) - C_M^{\gamma}(n, k)}{t(k+1) - t(k)} = \frac{r^2(n-1/2, k+1)}{(R^L)^2 [R^L - r(n-1, k+1)]^2} \\
& \times \hat{D}_M^{\gamma}(n-1/2, k+1) \times [C_M^{\gamma}(n-1, k+1) - C_M^{\gamma}(n, k+1)]
\end{aligned} \tag{39}$$

$$\begin{aligned}
& \frac{C_X^{\gamma}(n, k+1) - C_X^{\gamma}(n, k)}{t(k+1) - t(k)} = \frac{r^2(n-1/2, k+1)}{(R^L)^2 [R^L - r(n-1, k+1)]^2} \\
& \times \left\{ \tilde{D}_{XX}^{\gamma}(n-1/2, k+1) \times [C_X^{\gamma}(n-1, k+1) - C_X^{\gamma}(n, k+1)] \right. \\
& \left. + \tilde{D}_{XM}^{\gamma}(n-1/2, k+1) \times [C_M^{\gamma}(n-1, k+1) - C_M^{\gamma}(n, k+1)] \right\}
\end{aligned} \tag{40}$$

The difference approximation of balance Eq. (32–33) can be written as:

$$\begin{aligned}
& \left( \frac{C_M^p}{v_a^p} - \frac{C_M^{\gamma}(0, k+1)}{v_a^{\gamma}} \right) \frac{R(k+1) - R(k)}{t(k+1) - t(k)} \\
& = \frac{1}{v_a^{\gamma}} \hat{D}_M^{\gamma}(1/2, k+1) \frac{C_M^{\gamma}(1, k+1) - C_M^{\gamma}(0, k+1)}{r(1, k+1) - r(0, k+1)}
\end{aligned} \tag{41}$$

$$\begin{aligned}
& \left( \frac{C_X^p}{v_a^p} - \frac{C_X^{\gamma}(0, k+1)}{v_a^{\gamma}} \right) \frac{R(k+1) - R(k)}{t(k+1) - t(k)} \\
& = \frac{1}{v_a^{\gamma}} \left\{ \tilde{D}_{XX}^{\gamma}(1/2, k+1) \frac{C_X^{\gamma}(1, k+1) - C_X^{\gamma}(0, k+1)}{r(1, k+1) - r(0, k+1)} \right. \\
& \left. + \tilde{D}_{XM}^{\gamma}(1/2, k+1) \frac{C_M^{\gamma}(1, k+1) - C_M^{\gamma}(0, k+1)}{r(1, k+1) - r(0, k+1)} \right\}
\end{aligned} \tag{42}$$

Using the grid variables, Eq. (34), expressing conditions of local thermodynamic equilibrium at an interphase boundary, takes the form:

$$\begin{aligned}
& z\bar{G}_M^{\gamma}[C_M^{\gamma}(0, k+1), C_X^{\gamma}(0, k+1)] \\
& + (1-z)\bar{G}_{Fe}^{\gamma}[C_M^{\gamma}(0, k+1), C_X^{\gamma}(0, k+1)] \\
& n\bar{G}_X^{\gamma}[C_M^{\gamma}(0, k+1), C_X^{\gamma}(0, k+1)] = G_{M_zFe_{1-z}X_n}
\end{aligned} \tag{43}$$

The system of Eqs. (37–43) relates the interphase boundary position to the concentration distribution at the previous and consequent time  $s$ , i.e. it describes the system evolution with time.

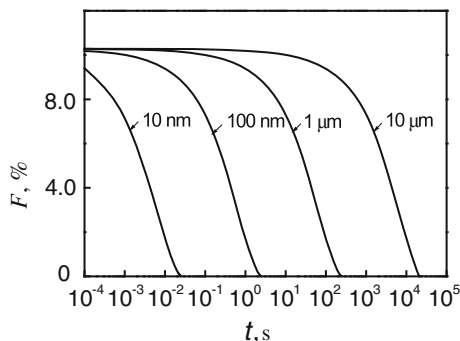
The calculations were done using the algorithm described in the previous section. In [10, 39, 40, 43] we carried out calculations of dissolution kinetics of carbides and nitrides in austenite, analyzed factors affecting their dissolution kinetics, and constructed kinetic nomograms for determination of the degree of dissolution of some carbides and nitrides in austenite. In these calculations it was assumed that at the initial moment the maximal possible amount of an excess phase is present in the steel of corresponding composition.

Dissolution of precipitates in multi-component systems differs from that in binary systems because in the former the dissolution kinetics is determined by the diffusion of atoms of several elements. Relationships between the diffusion mobility of components, the character of their interaction and compositions of the dissolving phase and matrix determine the values of boundary concentrations and concentration distributions of components in the matrix. In case of the limited matrix, diffusion fields of different precipitates may overlap, and due to different diffusion mobility of components the overlapping for different elements occurs at different steps of the process.

At carbides and nitrides dissolution simultaneous diffusion of metal elements and interstitials occurs. Diffusion coefficients of carbide- and nitride-forming elements are approximately by a factor of 4 lower than those of carbon and nitrogen. That is why the particle dissolution velocity is determined first of all by the diffusion mobility of atoms of slowly diffusing carbide- or nitride-forming element. The velocity of diffusion of interstitial atoms and the character of their interaction with the atoms of carbide- or nitride-forming element determine the value of the metal atom boundary concentration, which in its turn determines its concentration gradient in the matrix at an interface with the particle, the flux from the particle into the matrix and the velocity of dissolution. Besides, one should keep in mind that in most cases the carbon concentration increase in solid solution results in higher diffusion mobility of metal atoms [10].

As demonstrated by the analysis carried out in [40], the diffusion fields overlapping may cause considerable slowing of dissolution process. Overlapping of the diffusion fields of interstitial elements is achieved at the very first stages of the process, whereas their overlapping for the carbonitride-forming element is much less probable and is possible only at the late stages of dissolution process. The effect of overlapping of the interstitial element diffusion fields is the stronger the greater is its concentration change in the matrix. The effect of overlapping for the carbonitride-forming element is the more considerable the closer is the steel composition to the maximal solubility of interstitial phase.

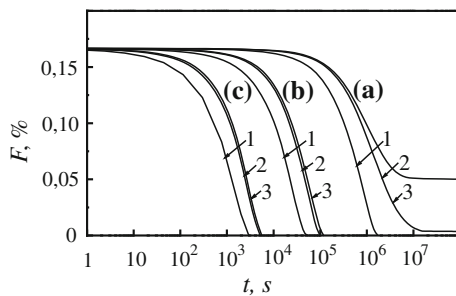
**Fig. 6** Effect of spherical particle sizes of  $\eta$ -carbide  $\text{Fe}_3\text{W}_3\text{C}$  on their dissolution kinetics in a steel with 0.5 % C and 13 % W at 13,000 C



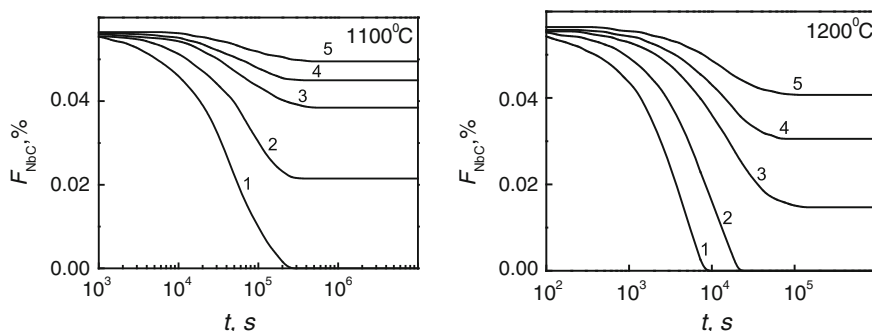
Kinetics of precipitates dissolution to a great extent depends on their initial size. It is known [44], that when precipitates dissolve in infinite matrix, the degree of their dissolution is determined by the value of  $t/R_0^2$ , i.e. the time required for the achievement of a certain degree of dissolution is proportional to their square radius. In case of the limited matrix the proportionality of time needed for the achievement of certain degree of precipitates dissolution to their square radius is not obvious, because the change of precipitates initial radius along with their constant volume fraction results in the change of distances between particles, i.e. of cell size. That is why calculations of dissolution kinetics of spherical particles of different radii in steels of one and the same chemical composition were carried out. The results of calculations for spherical particles of  $\eta$ -carbide  $\text{Fe}_3\text{W}_3\text{C}$  are shown in Fig. 6, which demonstrates temporal dependences of the volume fraction of precipitates ( $F$ ). It is seen, that when precipitates dissolve in the limited matrix, the time required for an achievement of the given dissolution degree is proportional to their initial radius, as in case of infinite matrix. This proportionality is valid in a wide range of particle sizes and is observed even at a relatively high volume fraction of precipitates.

Based on the results of calculations, kinetic nomograms were constructed, which make possible to determine the degree of carbides and nitrides dissolution in steels of various compositions after different times of holding at various temperatures. These nomograms represent temporal dependences of volume fractions of corresponding phases. As mentioned above, it was assumed that in the initial state the maximal possible amount of the appropriate carbide or nitride phase is formed. The nomograms were constructed only for one initial radius of precipitates (1  $\mu\text{m}$ ), because the time required for an achievement of an appropriate degree of precipitates dissolution is proportional to their square radius, and hence these nomograms can be used for any initial particle size. Examples of such nomograms for  $\text{VC}_{0.88}$ , NbC, TiC, VN and NbN are given in Figs. 7, 8, 9, 10, 11.

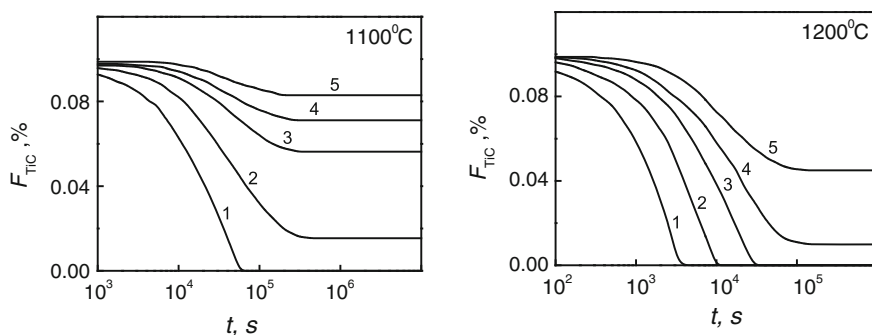
Calculations of dissolution kinetics of carbides and nitrides of group IV–V elements were carried out for typical compositions of constructional steels (0.1 wt. % V, 0.05 wt. % Nb, 0.05 wt. % Ti, 0.05–0.5 wt. % C, and 0.01–0.03 wt. % N).



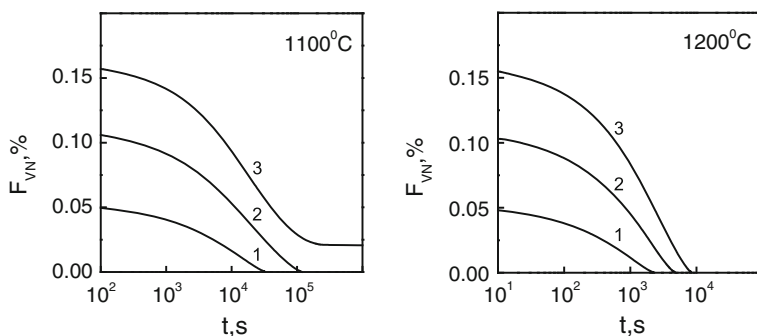
**Fig. 7** Nomogram for determination of  $VC_{0.88}$  dissolution degree at austenization of steels with 0.1 wt. % V and 0.1 (1), 0.3 (2) and 0.5 wt % C (3) at 900 (a), 1,000 (b) and 1,100 °C (c)



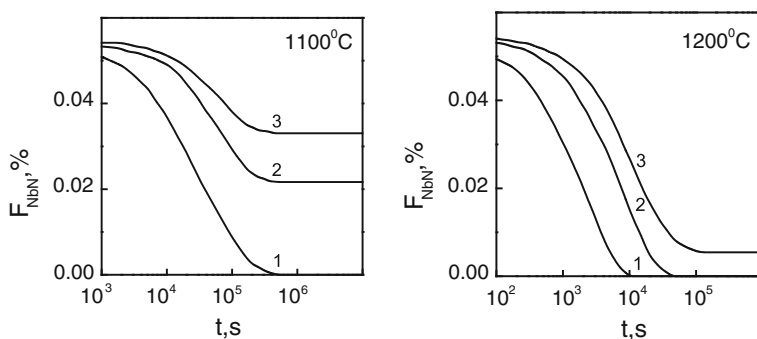
**Fig. 8** Nomograms for determination of NbC dissolution degree at austenization at various temperatures of steels with 0.05 wt % Nb and various carbon content: 1–0.05; 2–0.1; 3–0.2; 4–0.3; 5–0.5 wt % C



**Fig. 9** Nomograms for determination of TiC dissolution degree at austenization at various temperatures of steels with 0.05 wt % Ti and various carbon content: 1–0.05; 2–0.1; 3–0.2; 4–0.3; 5–0.5 wt % C



**Fig. 10** Nomograms for determination of VN dissolution degree at austenitization at various temperatures of steels with 0.1 wt. % V and various nitrogen content: 1–0.01; 2–0.02; 3–0.03 wt. % N



**Fig. 11** Nomograms for determination of NbN dissolution degree at austenitization at various temperatures of steels with 0.05 wt. % Nb and various nitrogen content: 1–0.01; 2–0.02; 3–0.03 wt. % N

Using the nomograms shown in Figs. 7, 8, 9, 10, 11, one can determine the degree of dissolution of carbides and nitrides at austenitization during the given time, the time required for an achievement of a given degree of their dissolution and the time of their complete dissolution, but one must know the average particle size in the initial state. As an example, let's determine the degree of niobium carbides dissolution in steel with 0.05 wt. % Nb and 0.1 wt. % C at 1,100 °C after isothermal annealing for 3,600 s, if the initial average size of the carbides was 200 nm. Let's use the nomogram in Fig. 8 (curve 2 for 1,100 °C). It was constructed for the initial size of 1  $\mu\text{m}$ , whereas in the steel under consideration their size is 5 times smaller. It means that the time required for an achievement of a certain degree of dissolution is 25 times shorter than that according to the nomogram. Hence, we must determine from the nomogram the degree of carbides dissolution during  $3,600 \times 25 = 90,000$  s. For this time their volume fraction decreases from 0.056 to 0.033 %, i.e. 41 % of the carbide phase dissolves.

The nomograms shown in Figs. 7, 8, 9, 10, 11 enable to make some general conclusions on the kinetics of carbide and nitride dissolution in steels at austenization. The precipitate dissolution is the slower the higher is thermal stability of an interstitial phase. It is seen that vanadium carbides and nitrides dissolve considerably faster than that of niobium and titanium. It is because the element concentrations in a matrix at its interface with a precipitate is the lower the higher is the thermal stability of the dissolving phase. With increasing content of carbon and nitrogen in a steel carbides and nitrides dissolution slows down, which results from decreasing concentration of a carbonitride-forming element at an interface with a dissolving particle. At relatively low temperatures complete dissolution may not be achieved. In this case the dissolving phase thermodynamic stability and carbon and nitrogen content in the steel will determine the maximal achievable degree of dissolution and the time required for the establishment of equilibrium.

The rising of heating temperature considerably affects the kinetics of precipitate dissolution. In this case not only equilibrium conditions at interfaces are changed, but the diffusion coefficients of components in matrix are increased.

Using such nomograms, one can choose the heat treatment regime ensuring the given degree of dissolution of an exceed phase.

It should be noted that the effect of kinetic factors manifests itself mainly at relatively low austenization temperatures (lower than  $\sim 1,000$  °C). At higher temperatures precipitates with not too coarse sizes, as a rule, dissolve very quickly, and the degree of the second phase dissolution is determined by thermodynamic factors. However, if in the initial state very coarse particles have formed in a steel, or if a heat treatment connected with fast and short-time heating is used, then the degree of precipitates dissolution will depend on kinetic factors at higher temperatures as well.

### ***2.3 Simulation of Diffusion Interaction of Carbonitrides of Varying Composition with Matrix***

As mentioned above, the lack of parameters required for calculations is one the reasons for making various simplifications and assumptions in simulation of precipitates evolution. Particularly, almost in all the available models of precipitate evolution the constant precipitate composition is assumed.

However, in some cases precipitates composition changes in the process of their evolution. In particular, in steels doped with strong carbonitride-forming elements of groups IV-V, carbonitrides can be formed, the composition of which can change at heat treatment due to the diffusion processes in them [10].

Calculations of the diffusion interaction of carbonitride precipitates of variable composition in steels were made in [45, 46]. The main problem was the absence of information on diffusion parameters in carbonitrides. That is why in our

calculations instead of coefficients of tracer diffusion of C and N in carbonitrides we used coefficients of diffusion of carbon and nitrogen in carbides and nitrides, respectively.

Calculations of the diffusion interaction of Ti carbonitrides with steels were made in [45]. The coefficients of tracer diffusion of C and N in carbides and nitrides were calculated based on the data on their chemical diffusion [47, 48], according to the formulas by Anderson and Agren, relating coefficients of tracer and chemical diffusion [49]. It was demonstrated that at high temperatures and long holding the composition of coarse nitrides formed at crystallization of an ingot may change in the depth of up to several microns, which is in agreement with the available experimental data [50].

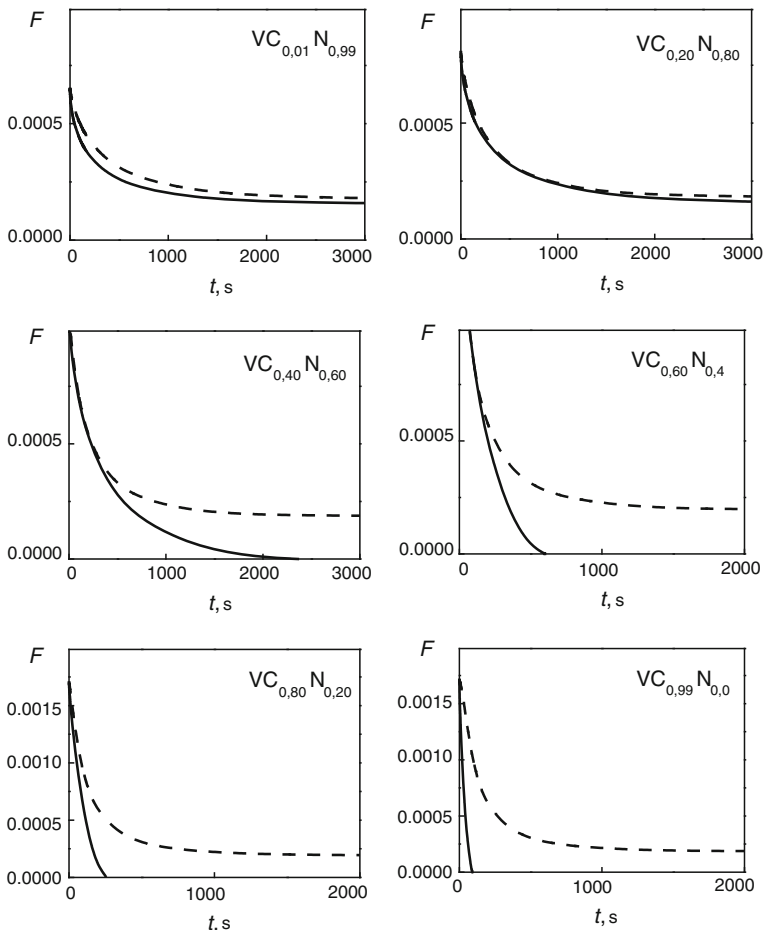
Calculations of vanadium carbonitrides evolution in steels with allowance made for the diffusion in particles were carried out in [46]. The coefficient of tracer diffusion of C in the carbide was taken from [51], and that of N in the nitride was calculated based on the data of its chemical diffusion from [52], according to the formulas given in [49].

To evaluate the effect of diffusion in particles on the kinetics of their diffusion interaction with a matrix, we calculated the dissolution kinetics of cubic vanadium carbonitrides V(C,N) of various initial compositions in the austenite of steel with 0.1 %C, 0.01 %N and 0.1 %V at 10,000 C. The calculations were done with and without the consideration of the diffusion processes in precipitates at their diffusion interaction with the matrix. The initial diameter of the precipitates was assumed to be 100 nm, and their volume fraction corresponded to the value of the complete vanadium bonding into the carbonitrides.

Figure 12 demonstrates dependences of the volume fraction of vanadium carbonitrides for different initial compositions on the annealing duration, calculated with an assumption of their constant initial composition and taking into account the probability of its changing in the process of dissolution. It is obvious, that variations of carbonitrides initial composition have a strong effect on their dissolution kinetics, if the possibility of composition modification is not taken into account.

On the contrary, if the diffusion processes in carbonitrides are taken into account, the differences in their initial phase composition are quickly enough smoothed. These results show that the conclusions made based on calculations without consideration for the diffusion processes in carbonitride phase may be wrong.

For example, calculations made with the account of diffusion processes in carbonitrides demonstrate, that independently on the initial composition of carbonitrides, the latter cannot be dissolved completely in the steel of this composition at 1,000 °C, and their amount after the annealing for 0.5–1 h is practically independent on their initial composition. On the contrary, calculations made without taking into account the carbonitride composition modification, predict strong dependence of the residual amount of carbonitride on its initial composition, and for a certain interval of the initial compositions one may even expect the complete dissolution of carbonitrides.

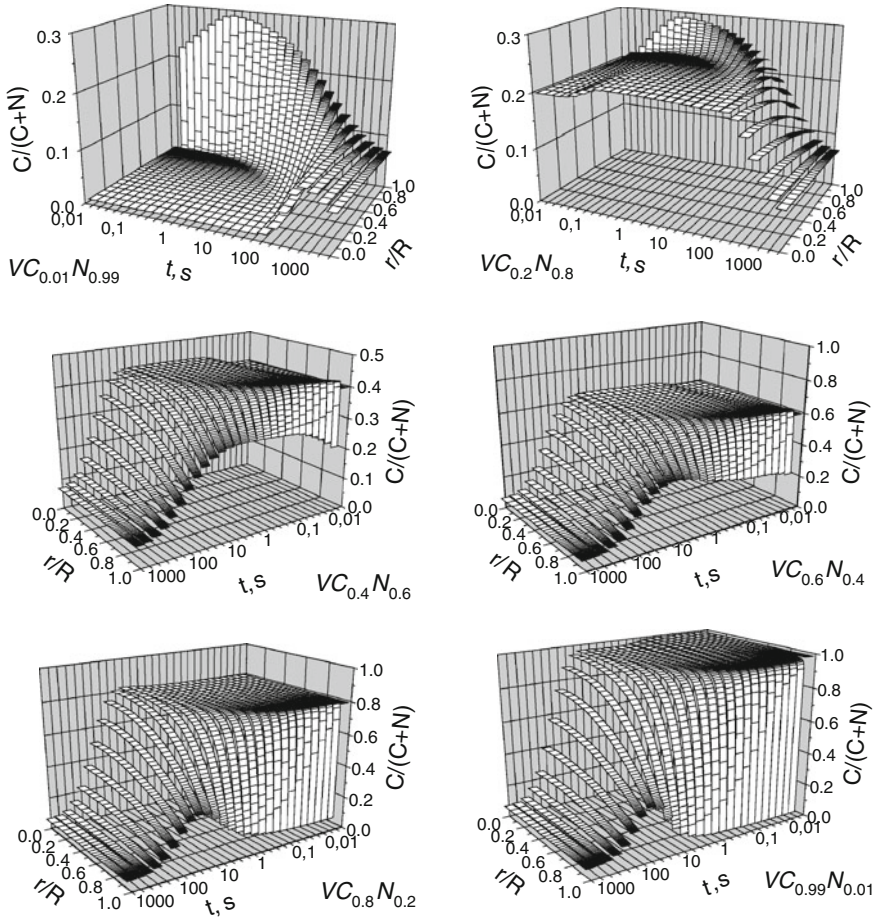


**Fig. 12** Carbonitride volume fraction at 1,000 °C annealing of steel with 0.1 % C, 0.01 % N and 0.1 % V and with different initial compositions of carbonitride, calculated in the assumption of constant carbonitride composition (*solid lines*) and with consideration of its possible change at dissolution (*dashed lines*). The initial carbonitride composition is denoted in the figures

Figure 13 illustrates modification of concentration distribution in carbonitrides of different initial composition at annealing.

It is seen that distributions of C and N concentrations in carbonitrides intricately change at the diffusion annealing, because the character of the diffusion interaction is determined not only by the initial composition of carbonitrides, but also by the initial matrix composition and by the diffusion parameters of C and N in austenite and carbonitride. The local equilibrium establishes at carbonitride/austenite interface at the very beginning of the diffusion interaction. At further annealing modifications of boundary concentrations of carbon and nitrogen in carbonitride are not monotone. At first there is some enrichment of the carbonitride





**Fig. 13** Modification of vanadium carbonitrides composition at 1,000 °C annealing of steel with 0.1 % C, 0.01 % N and 0.1 % V and with different initial carbonitride compositions. The initial composition is written in the figures

near-boundary zone compared to the composition established at the initial moment, and this effect seems to be due to the relationship between the diffusion rates of C and N in carbonitride and austenite. At further diffusion interaction the phase composition approaches to the equilibrium, and the carbonitride composition evens out through the depth and approaches to the one and the same equilibrium composition, approximately corresponding to  $VC_{0.07}N_{0.93}$ .

The examples cited above show that in simulation of evolution of variable composition precipitates at heat treatment of metal alloys one must if possible take into account diffusion processes inside particles or at least estimate their effect on the kinetics of the process, as it appears to be quite significant.

### 3 Simulation of Particle Coarsening

When a two-phase alloy almost reaches the equilibrium phase composition through the processes of dissolution or growth, the stage of particle coarsening comes. By that moment the potentialities of decreasing of free energy volume constituent are practically exhausted, and the moving force for further evolution is the system's tendency to decrease its surface energy. It is realized through dissolution of fine particles and growth of coarse ones at practically unchanged volume fraction of the second phase. As a result, the area of interfaces reduces, and the free energy of the system diminishes, this process being referred to as Ostwald ripening, or particle coarsening. In this case there exists some critical radius  $R_c$ , at which the precipitate is in equilibrium with solid solution, and at  $R > R_c$  it grows, whereas at  $R < R_c$  it dissolves.

By now there have been published a lot of studies dealing with experimental investigations of particle coarsening, their theoretical treatment and numerical simulation of this process. The present study is not aimed at reviewing the available theories of Ostwald ripening and methods of its numerical simulation. We are going to touch mainly upon the problems which are of interest for the construction of a generalized model of precipitate evolution, which is considered in the next section, as well as of carbide and nitride precipitates coarsening.

The first theory of particle coarsening controlled by volume diffusion was developed by Lifshitz and Slezov [53], who considered a diluted binary alloy with infinitesimal volume fraction of second phase spherical particles distributed in a matrix. The problem definition is as follows. Mass transfer in a system is described by a stationary equation of diffusion for a spherical symmetry:

$$\frac{\partial}{\partial r} \left( r^2 \frac{\partial C^m}{\partial r} \right) = 0, \quad (44)$$

with the following boundary conditions

$$C^m(r = R) = C^{m/p}(R) \quad (45)$$

and

$$C^m(r = \infty) = \bar{C}^m. \quad (46)$$

Here  $C^{m/p}(R)$  is a dissolved component concentration in a matrix at an interface with a particle of radius  $R$ , and  $\bar{C}^m$  is an average concentration of the dissolved component in the matrix.

The use of the approximation of infinitesimal volume fraction excludes the possibility of overlapping diffusion fields of different precipitates, which makes easier to find concentration distributions in the areas surrounding particles.

It is assumed that the local equilibrium is established at all interfaces, and boundary concentrations are determined by the linearized form of Gibbs–Thomson equation:

$$C^{m/p}(R) = {}^e C^m + \frac{l^m}{R}, \quad (47)$$

where  ${}^e C^m$  is the equilibrium concentration of the dissolved component in the matrix, and  $l^m$  is the matrix phase capillary length, which, according to [54], is equal to

$$l^m = \frac{2v_m^p \sigma^e C^m (1 - {}^e C^m)}{R_g T (C^p - {}^e C^m)}, \quad (48)$$

where  $v_m^p$  is the precipitate molar volume,  $\sigma$  is the specific surface energy, and  $R_g$  is the universal gas constant.

Velocities of interphase boundaries movement are determined by the mass balance Eq. (2).

Two more equations must be added to these ones. It is the equation of discontinuity in size space, describing evolution of the PSD function,  $f(R,t)$ :

$$\frac{\partial f}{\partial t} + \frac{\partial}{\partial R} \left( f \frac{dR}{dt} \right) = 0, \quad (49)$$

and the mass conservation condition:

$$\alpha_p C^p + (1 - \alpha_p) \bar{C}^m = C^{al}, \quad (50)$$

where  $\alpha_p$  is the mole fraction of precipitating phase, and  $C^{al}$  is the dissolved component concentration in an alloy.

The distribution function is normalized by the number of particles per unit volume,  $N_V$ , that is

$$N_V = \int_0^\infty f dR. \quad (51)$$

The mole fraction of precipitates is related to its volume fraction by an equation:

$$\alpha_p = \frac{F/v_m^p}{F/v_m^p + (1-F)/v_m^m}, \quad (52)$$

where  $v_m^m$  is the molar volume of the matrix phase.

In its turn, the volume fraction of precipitates may be calculated from the distribution function

$$F = \frac{4\pi}{3} \int_0^\infty f(R,t) R^3 dR \quad (53)$$

These equations determine the evolution of precipitate ensemble at the stage of coarsening. Lifshitz and Slezov [53] solved this problem in the asymptotic limit.

Particularly, they demonstrated that in the limit  $t \rightarrow \infty$  the critical radius temporal dependence is characterized by the power law:<sup>1</sup>

$$R_c^3 - R_{c0}^3 = Kt, \quad (54)$$

where  $R_{c0}$  is the critical radius which the system has at an initial moment of the stage, when the process can be described by asymptotic equations, and  $K$  is a constant equal to [54]:

$$K = \frac{4Dl^m}{9(C^p - eC^m)}. \quad (55)$$

Besides, they demonstrated that there exists a universal distribution function, which does not depend on time and describes PSD in an asymptotic limit. This function is of the following form:

$$P(u) = \begin{cases} \frac{3^4 e}{2^{25/3}} \cdot \frac{u^2 \exp\{-1/[1-(2/3)u]\}}{(u+3)^{7/3}[(3/2)-u]^{11/3}}, & u < 3/2 \\ 0 & u > 3/2 \end{cases} \quad (56)$$

where  $u = R/R_c$  is the relative radius of precipitates;  $P(u)$  is the probability density function ( $P(u)du$  is the probability that a particle has a radius in the range between  $R$  and  $R + dR$ ).

Later on the solutions of the problem of coarsening at the asymptotic stage controlled by other mechanisms of mass transfer were obtained in [55–57]. The solutions for various mechanisms of mass transfer are reviewed in [58, 59], and some specifications of these solutions are given in [60]. All these solutions were also obtained for infinitesimal volume fraction of the second phase. Solutions for coarsening in multicomponent systems were obtained in [61–65].

In a number of studies the coarsening of carbide and nitride precipitates in steels was investigated [66–69]. Particularly, it was shown that carbide and nitride coarsening in the temperature range of austenite, as a rule, is controlled by volume diffusion, whereas at lower temperatures, in ferrite, the process may be controlled by other mechanisms of mass transfer.

Specific features of theoretical description of carbide and nitride coarsening are associated with the necessity to consider multicomponent diffusion, including the simultaneous diffusion of interstitial and substitutional elements. The coarsening of stoichiometric  $(\text{Fe},\text{M})_a\text{C}_b$  carbides in austenite is considered in [69], where the following expression was obtained to describe their radius variation:

$$\bar{R}^3 - \bar{R}^3 = \frac{8(a+b)\sigma v_m^p D_M^\gamma e C_M^\gamma}{9aR_g T (C_M^p - e C_M^\gamma)^2} t \quad (57)$$

It was shown in [69], that at the stage of coarsening this equation satisfactorily describes the carbide precipitate evolution in austenite.

<sup>1</sup> In Lifshitz-Slezov's theory at an asymptotic stage the critical radius is equal to the average one.

The limitation of the infinitesimal volume fraction of precipitating phase used in the Lifshitz-Slezov's theory was one of its main drawbacks, because the available experimental results show that the volume fraction of precipitates affect the rate of the average particle size increasing and the form of the distribution function. Quite a few theories were suggested to overcome this drawback. One of the ways to solve the problem for a non-zero volume fraction of precipitates is using the mean field or effective environment approximations. In this case the rate of particle growth for every particle size range is formulated through interaction between a particle and its average surrounding. The main feature of such theories is the statistic field cell connected with every particle. Every cell is a spherical domain concentrically enveloping a particle, and contains a particle and matrix volume connected with it with a local averaged diffusion field. In this case the diffusion interaction in field cells connected with particles is considered. Mass exchange between particles is realized through cell walls, the concentration on the boundaries of which is equal to the average concentration in the matrix, i.e. the boundary condition (46) is substituted for

$$C^m(r = R^L) = \bar{C}^m. \quad (58)$$

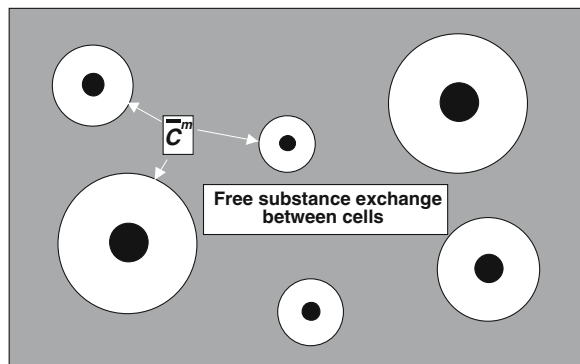
This model is shown schematically in Fig. 14.

Some coarsening models based on the mean field approximation are reviewed in [70, 71].

The mean field approximation requires some assumptions relating the average extension of transport field connected with a particle (that is, its sphere of influence) with the particle size and the volume fraction of precipitating phase.

Various modes of construction of field cells were suggested in [70, 72, 73], from purely geometrical to those based on more complicated criteria. Thus, for example, in [73] the cell sizes were calculated from the self-similarity criterion. The growth constant in Eq. (55) and the form of distribution function depend on the choice of field cells.

**Fig. 14** Geometrical sketch of coarsening models constructed based on the mean field approximation



Along with the above cited publications [70–73], there are several more studies in which the theories were worked out, taking into account the influence of the second phase finite volume fraction, particularly, [74–77].

The numerical simulation of precipitates behavior at coarsening has grown in popularity recently [78–82]. In case of numerical simulation one can analyze the precipitate behavior not only at the asymptotic stage, but also at the non-stationary stage, when the equilibrium phase composition has been almost reached and the PSD is far from the asymptotic one yet. Besides, in numerical simulation the systems with high volume fraction of precipitates may be analyzed, when because of the particles proximity to each other the diffusion fields near their surfaces get considerably non-uniform and the particle shape deviate from the spherical one.

Elastic stresses arising from the particle growth may have a profound effect on coarsening. There are many examples of such effect, which are reviewed in [71]. For instance, in systems in which the stresses originate from the misfit of particle–matrix crystal lattices, an almost random spatial distribution of particles, resulting from nucleation and growth, may evolve into highly correlated spatial distribution, in which particles are arranged into rows along elastically soft crystallographic directions in the matrix, or into almost periodical ensembles. Besides, the elastic stresses strongly affect the morphology of some particles. At coarsening the initially spherical particles can change their shape and divide into smaller particles. Recently great attention has been paid to the numerical simulation of precipitates coarsening, taking into account the arising elastic stresses, as it is very difficult to describe this process analytically because of great complexity of the accompanying phenomena, and considerable success was achieved in this direction [83–85].

## 4 Simulation of Different Stages of Precipitate Evolution

It is not possible to solve by analytical methods a multi-particle diffusion problem in such general form, that the solution would describe precipitate evolution at all stages of the process, even for binary systems.

The methods of numerical simulation of precipitates evolution until recently were also worked out mainly for this or that concrete stage of the process. The methods of simulation of growth and dissolution considered in Sect. 2, do not provide taking into account the polydispersity of precipitates ensemble, and, consequently, they cannot be generalized for the stage of coarsening and for transition stages from growth or dissolution to coarsening, when the polydispersity of the ensemble and the form of PSD determine the system behavior. The available methods of simulation of precipitates evolution at the coarsening stage also have a number of limitations [78–82]. Firstly, they deal, as a rule, with binary systems, and secondly they suggest that the volume fraction of precipitates is close to equilibrium, which makes it impossible to use them for the stages of growth or dissolution.

In our recent studies [86–92] a method was worked out for simulation of precipitates evolution in binary and multi-component systems at different stages in the framework of one and the same model, taking into account the precipitates ensemble polydispersity. This section is to describe this method and analyze its capabilities. At first we consider simulation of precipitates ensemble in two-phase binary alloys, then possibilities of its generalization to the case of multiphase systems are analyzed, and, finally, the evolution of precipitates ensemble is considered taking into account the formation of new nuclei.

The method is based on the mean field model, and several assumptions were used for its development. It is assumed that the particles have spherical shape and constant composition, equilibrium concentrations of components are established at interfaces and the process is controlled by volume diffusion.

## 4.1 Binary Systems

The main problem to be solved in simulation of precipitates evolution in alloys is to find velocities of interfaces. An interface velocity for a particle of radius  $R$  can be determined from the mass balance equation, which for a binary system has the form (2).

To find an interface velocity one must know the solute concentration gradient in the matrix at an interface with the particle, i.e., it is required to know the solute concentration distribution in the particle surrounding. Thus, one must solve the diffusion Eq. (1) at the appropriate initial and boundary conditions.

Various models of the processes of growth, dissolution and coarsening differ, first of all, by the mode of assignment of boundary conditions used to find solute concentration distribution in a particle surrounding.

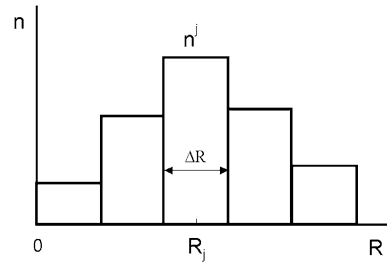
We used the mean field approximation, i.e., we considered diffusion interaction of particles with the matrix in field cells. In this case one must know boundary conditions for an interphase boundary and cell boundary.

In case of a binary system, when the process is controlled by diffusion, it is not difficult to give the condition for precipitate/matrix interface, as it is an assignment of boundary concentration which is determined by the local equilibrium conditions at an interface.

It is more difficult to determine conditions at cell boundaries. As was demonstrated before, in simulation of dissolution and growth processes it is assumed that the dissolved component concentration gradient at a cell boundary is equal to zero, whereas in the description of coarsening it is supposed that the concentration at a cell boundary is equal to the average concentration in the matrix.

To consider diffusion growth, dissolution and coarsening of precipitates in the framework of one model, one must find such boundary conditions which would be suitable for simulation of all three processes, and it was done in [86]. It was assumed that at cell boundaries of all size intervals one and the same solute component concentration,  $C^L$ , is established, but its value is not known a priori.

**Fig. 15** Particle size distribution scheme



The initial data for simulation of precipitate ensemble evolution were the precipitate volume fraction and PSD in the initial state. The PSD was given by a histogram, i.e., a fraction of particles  $n^j$ , falling in the  $j$ -th interval of particle radii from  $R_j - \Delta R/2$  to  $R_j + \Delta R/2$ , is associated with this size interval. Here  $R_j$  is the average radius of particles of the  $j$ -th size, and  $\Delta R$  is the width of this interval (for all size intervals this value was taken the same). The scheme of PSD is shown in Fig. 15.

We used three modes of construction of field cells, illustrated by Fig. 16, which are in many respects analogous to the models worked out for the description of coarsening in systems with finite volume fraction of precipitates.

Model I (Fig. 16a). The cell radius is proportional to the particle radius and calculated by the formula:

$$R_j^L = R_j \cdot F^{-1/3}, \quad (59)$$

where  $R_j^L$  is the influence sphere radius corresponding to the  $j$ -th size interval. This model is completely analogous to that suggested in [70].

Model II (Fig. 16b). Cell radii are the same independently on the particle sizes. This model was suggested in [93], but we used another way of calculating cell sizes. The cell radius was calculated by the formula:

$$R^L = \left( \sum_{j=1}^{N_p} n^j R_j^3 / F \right)^{1/3}, \quad (60)$$

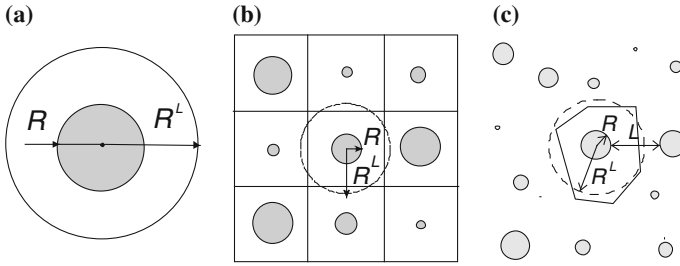
where  $N_p$  is the number of size intervals.

Model III (Fig. 16c). The cell radius is combined from the particle radius and a half of mean distance between particle surfaces  $\bar{L}$ :

$$R_j^L = R_j + \frac{\bar{L}}{2} \quad (61)$$

For this model there are various ways of estimation of the mean distance between particle surfaces. We estimated it using the following expression, linking the mean distance between particles, PSD and precipitates volume fraction:





**Fig. 16** Geometrical models of field cells: **a**–model I, **b**–model II, **c**–model III

$$F = \frac{\sum_{j=1}^{N_p} n^j R_j^3}{\sum_{j=1}^{N_p} n^j \left(R_j + \frac{L}{2}\right)^3} \quad (62)$$

To find component concentration distributions in cells, the stationary diffusion Eq. (44) was used. The feasibility of stationary approximation for coarsening is beyond question. The possibility to use it for growth and dissolution is less obvious. As mentioned above, the solution obtained using the stationary field approximation is the more exact, the less is the value of the  $\lambda = \frac{C^{m/p} - 0C^m}{C^p - C^{m/p}}$  parameter. That is why for small enough  $\lambda$  ( $< \sim 0.1$ ) the use of the stationary approximation is quite correct not only for coarsening, but for other stages as well.

Using the stationary approximation, the following expressions are obtained for concentration distributions of the solute component in cells:

$${}^j C^m(r) = \frac{{}^j C^{m/p} - C^L}{\left(1/R - 1/R_j^L\right)} \frac{1}{r} + \frac{C^L R_j^L - {}^j C^{m/p} R}{R_j^L - R}, \quad (63)$$

where  ${}^j C^m(r)$  is the solute component concentration in a cell of the  $j$ -th size interval;  ${}^j C^{m/p}$  is the solute component concentration at interfaces with particles of the  $j$ -th size interval; and  $C^L$  is the solute component concentration at a cell boundary (for the cells of all size intervals it is taken the same).

Concentration at a particle/matrix interface was given by the Gibbs–Thomson equation, according to which for every size interval:

$${}^j C^{m/p} = e C^m \exp\left(\frac{2\sigma v_m^p}{R_g T} \frac{1 - e C^m}{C^p - e C^m} \frac{1}{R_j}\right). \quad (64)$$

The calculated concentrations of components in matrix must satisfy the mass conservation condition (50).

The solute component average concentration in the matrix is connected with concentration distributions in cells and the mole fraction of precipitates with its volume fraction by the following relationships:

$$\bar{C}^m = \frac{3 \sum_{j=1}^{N_p} n^j \int_{R_j}^{R_j^L} j C r^2 dr}{\sum_{j=1}^{N_p} n^j [(R_j^L)^3 - (R_j)^3]}, \quad (65)$$

and

$$\alpha_p = \frac{F/V_m^p}{F/V_m^p + (1-F)/V_m^m}. \quad (66)$$

In the case considered the mass conservation condition must be added explicitly, as in the diffusion equation the time derivative is neglected. The mass conservation condition takes into account that if the average concentration of the solute component in the matrix depends on time, then the volume fraction of precipitates is time dependent as well.

Substitution of (63) in Eq. (2) gives expressions for interface velocities:

$$V_j = \frac{dR_j}{dt} = \frac{D}{(C^p v_a^m / v_a^p - j C^{m/p})} \frac{(C^L - j C^{m/p}) R_j^L}{(R_j^L - R_j) R_j} \quad (67)$$

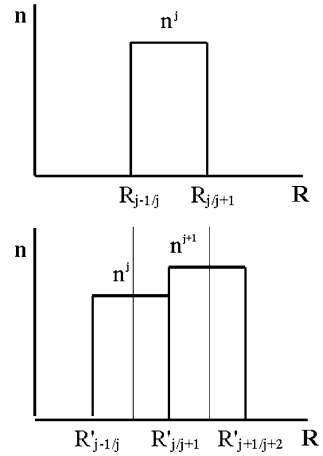
A step-by-step procedure was used in calculations, and based on the volume fraction and PSD at time  $t$  these parameters were calculated for the moment  $t + \Delta t$ . The calculation procedure was as follows.

1. Based on values of volume fraction  $F$ , the average concentration of the solute component in the matrix,  $\bar{C}^m$ , was calculated using expressions (50) and (66).
2. Cell sizes were calculated using expressions (59, 60) or (61).
3. Concentration at cell boundaries,  $C^L$ , was calculated as follows. After the substitution into (65) of expressions of concentration distributions in cells (63) and expressions of the solute component boundary concentrations (64), one obtains an equation with one unknown,  $C^L$ , which is calculated numerically and gives concentrations at cell boundaries.
4. The interface velocities were calculated by Eq. (67).
5. The particle radii  $R'_j$  and their volume fraction  $F'$  at a new time step were found from:

$$R'_j = R_j + V_j Dt \quad (68)$$

and

**Fig. 17** The scheme of calculation of PSD at a new time step



$$F^t = \frac{\sum_{j=1}^N n^j R_j^3}{\sum_{j=1}^N n^j R_j^{t3}}. \tag{69}$$

6. The PSD at a new time step was calculated, a special procedure being used for that.<sup>2</sup> Let's illustrate this procedure by an example of determining the fraction of particles in the  $j$ -th size interval at a new time step. The boundaries of the  $j$ -th interval are denoted as  $R_{j-1/j}$  and  $R_{j/j+1}$  ( $R_{j-1/j} = R_j - \Delta R/2$ ,  $R_{j/j+1} = R_j + \Delta R/2$ ). For the time  $\Delta t$  the particle radii change, and the new radii, corresponding to the boundaries of the division intervals  $R'_{j-1/j}$  and  $R'_{j/j+1}$  can be calculated from the formulas similar to (64, 68) and (69). After that in the initial size interval from  $R_{j-1/j}$  to  $R_{j/j+1}$  there may be no particles, which were in that interval at the previous time step, or only a part of them may remain. At the same time at the new time step in this size interval may fall the particles which belonged to other size intervals at the previous time step. Let, for example, in the size interval from  $R_{j-1/j}$  to  $R_{j/j+1}$  at a new time step the particles, which belonged to the  $j$ -th and  $(j + 1)$ -th intervals fall partly, as it is shown in Fig. 17.

<sup>2</sup> To find the PSD at a new time step it would be natural to use the continuity equation in the size space (49). However it appeared inconvenient in numerical calculations, when the distribution function is given not analytically, but by a histogram. Particularly, a fraction of particles in some size intervals, calculated by the continuity equation in difference form, may appear to be negative.

Then the fraction of particles of the  $j$ -th interval at a new time step can be calculated by the formula:

$$n^{j'} = \frac{R'_{j/j+1} - R_{j-1/j}}{R'_{j/j+1} - R'_{j-1/j}} n^j + \frac{R_{j/j+1} - R'_{j/j+1}}{R'_{j+1/j+2} - R'_{j/j+1}} n^{j+1}. \quad (70)$$

Taking into account that a part of particles dissolve at a new time step (there radii get smaller than that corresponding to the lower boundary of the first size interval), the values obtained from the formulas like (71) must be normalized.

The as-determined values of volume fraction and PSD served as the initial ones for calculations at a new time step. This procedure was repeated till the required time was achieved.

This technique of calculation was tested in [86–88], and the comparison of calculation results with the available experimental data demonstrated their good agreement. It was also shown that calculations made with various geometrical models of field cells give closely similar results in case of a relatively low volume fraction of precipitates (not more than several percents). That is why only Model I was used in simulation of carbide and nitride precipitates evolution.

## 4.2 Multicomponent Alloys

The method described in the previous section was generalized to the case of multicomponent low-alloyed alloys in [89–91], the same assumptions as for binary alloys being used. The problem for multicomponent alloys is more complicated, as component concentrations at interfaces in this case are unknown. In case of low-alloyed alloys the matrix may be considered as a dilute solution, which allows not taking into account concentration dependences of diffusion coefficients and interaction of components in the solution, i.e., impurity diffusion may be considered instead of interdiffusion. In this case the concentration distributions of components in cells are expressed analytically with the relationships similar to (64):

$${}^j C_i^m(r) = \frac{{}^j C_i^{m/p} - C_i^L}{(1/R_j - 1/R_j^L)} \frac{1}{r} + \frac{C_i^L \cdot R_j^L - {}^j C_i^{m/p} \cdot R_j}{R_j^L - R_j}, \quad (71)$$

where  ${}^j C_i^m(r)$  is the concentration of the  $i$ -th component in the matrix in a cell of the  $j$ -th size interval;  ${}^j C_i^{m/p}$  is the concentration of the  $i$ -th component in the matrix at an interface with particles of the  $j$ -th size interval; and  $C_i^L$  is the concentration of the  $i$ -th component at cell boundaries.

The mass balance conditions at interphase boundaries are:

$$\left[ C_i^p V_m^m / V_m^p - {}^j C_i^{m/p} \right] \frac{dR_j}{d\tau} = D_i \left. \frac{d^j C_i^m}{dr} \right|_{r=R_j}, \quad (72)$$

where  $D_i$  is the impurity diffusion coefficient of the  $i$ -th component in the matrix.

After substitution of expressions (71) for component concentration distributions in cells into Eq. (72), the latter take the form:

$$\left[ C_i^p V_m^z / V_m^p - {}^j C_i^{m/p} \right] \frac{dR_j}{d\tau} = D_i \frac{{}^L C_i - {}^j C_i^{m/p}}{R_j^L - R_j} \cdot \frac{R_j^L}{R_j} \quad (73)$$

For the case of precipitates of constant composition  $A_a B_b \dots$ , the equilibrium condition at a particle/matrix interface with the correction for the interface curvature is:

$$a^j \bar{G}_A^{m/p} + b^j \bar{G}_B^{m/p} + \dots - \frac{2\sigma V_m^p}{R_j} = {}^0 G_{A_a B_b \dots}, \quad (74)$$

where  ${}^j C_i^{m/p}$  is the chemical potential of the  $i$ -th component in the matrix at an interface with a particle from the  $j$ -th size interval.

In case of sparingly soluble compounds the local thermodynamic equilibrium condition at an interface can be determined as:

$$L_{A_a B_b \dots}(R_j) = L_{A_a B_b \dots} \exp\left(\frac{2\sigma V_m^p}{R_g T R_j}\right), \quad (75)$$

where  $L_{A_a B_b \dots}(R_j)$  and  $L_{A_a B_b \dots}$  are the solubility product for the particles of the  $j$ -th size interval and the equilibrium value of the solubility product, respectively.

The mass conservation condition in this case is

$$\alpha_p C_i^p + (1 - \alpha_p) \bar{C}_i^m = C_i^{al}. \quad (76)$$

The mole fraction is connected with the volume fraction of precipitating phase by relationship (66).

The step-by-step procedure was used in calculations, as it was done for binary alloys, and based on the volume fraction and PSD for time  $t$  these parameters were determined for  $t + \Delta t$ . The calculation procedure was to a great extent similar to that for calculations of precipitates evolution in binary alloys. The calculation order was as follows.

1. Calculation of average concentrations of components in the matrix based on the value of the precipitating phase volume fraction Eqs. (66, 76).
2. Calculation of field cells sizes [expressions (59, 60 or 61)].
3. Calculation of interface velocities for particles from different size intervals.

The calculation of interface velocities in case of multicomponent alloys is much more difficult than in case of binary systems. Particularly, it is so because for

multicomponent systems the component concentrations at interphase boundaries are not known a priori.

Calculations of concentration distribution in cells and interface velocities were performed based on the requirement that the values of average concentrations of components in the matrix must satisfy the mass conservation condition. This means that the average component concentrations in the matrix calculated from the volume fraction of precipitating phase must be equal to average concentrations, calculated based on the component concentration distribution in field cells. Thus, for the  $(N + 1)$ -component system the component concentration distributions in field cell must satisfy the system of  $N$  equations:

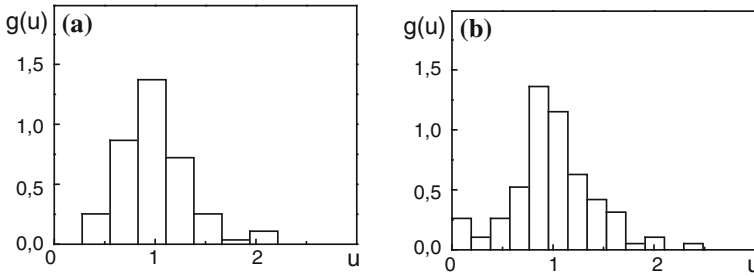
$$\Phi_i = \bar{C}_i^m - \frac{3 \sum_{j=1}^{N_p} n^j \int_{R_j}^{R_j^L} j C_i^m r^2 dr}{\sum_{j=1}^{N_p} n^j [(R_j^L)^3 - (R_j)^3]} = 0 \quad (77)$$

In these equations the first member in the right part corresponds to the average concentration calculated from the volume fraction, and the second one to the average concentration determined from concentration distributions in cells.

From expressions (71) for component concentration distributions in cells one can see that they are determined by concentrations at interphase boundaries and cell boundaries. In their turn, the component concentrations at interphase boundaries and the velocities of the latter for every size interval can be calculated from concentrations at cell boundaries by the combined solution of mass balance Eq. (73) and thermodynamic Eqs. (74) or (75). Thus, having specified the concentrations at cell boundaries, one can calculate interface velocities, determine component concentration distributions in cells and calculate the values of  $\Phi_i$  function. This was the algorithm of solution of system (77), which resulted in determination of interface velocities.

The calculation order was as follows:

- a. Initial approximations of concentrations at cell boundaries were given.
- b. Interface velocities and boundary concentrations were calculated from combined solution of mass balance Eq. (73) and thermodynamic Eqs. (74) or (75).
- c. The values of functions  $\Phi_i$  were calculated in a point corresponding to the initial approximations and in its vicinity.
- d. The derivatives of  $\Phi_i$  functions with respect to  $C_i^L$  were found by numerical differentiation in the point corresponding to the initial approximations.
- e. The corrected values of concentrations at field cell boundaries were calculated by the Newton-Raffson method based of the determined values of the functions and their derivatives.
- f. The values of  $C_i^L$  obtained from the cycle (b–e) were used as the initial approximations for a new iteration, i.e., the calculation was repeated from point (b).



**Fig. 18** Initial PSDs of AlN [94]: **a**–annealing at 650 °C, 24 h; **b**–annealing at 700 °C, 24 h

The iteration cycle was over if the following iteration differed from the previous one by the value less than the given convergence accuracy. The values of interface velocities and concentrations at interfaces and field cell boundaries were found by this iteration procedure.

4. Calculation of particles radii and their volume fraction at a new time step by formulas (5.68–5.69).
5. Calculation of PSD at a new time step by the procedure described above for binary systems based on the analysis of the number of particles leaving the initial size interval and falling in it from other intervals due to the growth or dissolution [see Fig. 17 and expression (70)].

The as-determined values of volume fraction and PSD served as the initial ones for calculations at a new time step.

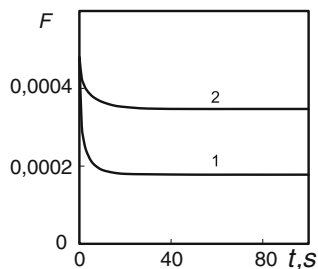
In [90–92] the calculation results for evolution of AlN and MnS precipitates in austenite and ferrite are compared to the available experimental data at different stages of evolution, and their good agreement is demonstrated.

Let's illustrate this by an example of the comparison of calculation results with the experimental studies on AlN evolution in austenite at the stage of dissolution and the following coarsening carried out in [94].

The steel under study contained 0.038 wt. % C, 0.30 wt. % Mn, 0.040 wt. % Al and 0.007 wt. % N. Different initial PSDs of AlN were obtained by preliminary heat treatments. The first initial distribution was obtained by 650 °C annealing, and the second one by 700 °C for 24 h. The PSDs resulting from these treatments are shown in Fig. 18. It is obvious that they differ considerably, as the annealing at 650 °C ensures more dispersed precipitates than that at 700 °C. In both cases practically complete bonding of N in nitrides was achieved. The as-obtained PSDs and the volume fraction corresponding to complete bonding of N in nitrides (0.00048) served as the initial data for simulation.

Figure 19 demonstrates calculated temporal dependences of volume fractions of precipitates for two temperatures, 1,000 and 1,100 °C. It is seen that at short times of heat treatment the volume fraction drastically reduces, which results from dissolution of the exceeding phase. The intensive dissolution occurs during a very

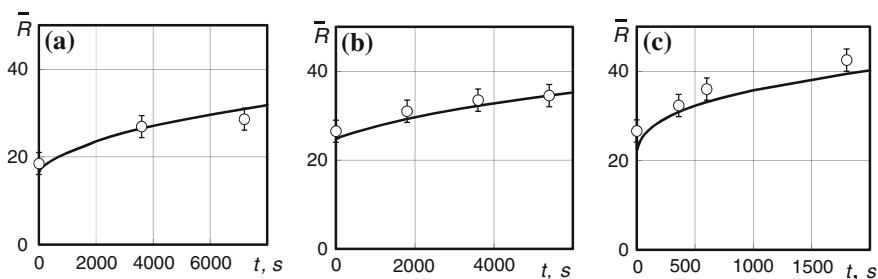
**Fig. 19** Calculated dependences of AlN volume fraction on the annealing time for 1,000 and 1,100 °C. Initial state—annealing at 700 °C, 24 h



short period of time, several tenths of seconds. This time appears to be enough for an achievement of phase composition close to equilibrium. At further holding the volume fraction stabilizes and does not change with growing annealing time. The stage of dissolution is finished and coarsening starts, the volume fraction remaining almost unchanged.

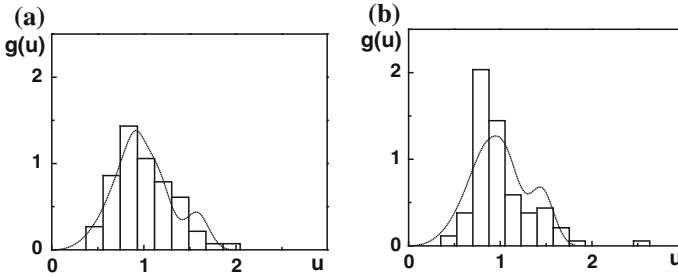
Figure 20 demonstrates comparison of calculated and experimental dependences of precipitates average radius on the annealing time. These dependences are shown for different initial PSDs and for two annealing temperatures, 1,000 and 1,100 °C. It is seen that in all the cases calculations describe the evolution of precipitates average size quite well.

The difference between simulation results and experimental data, as a rule, does not exceed experimental error. As seen from these dependences, at first the average radius of precipitates somewhat decreases. It may be explained by the precipitates dissolution, all the particles dissolving at the beginning. It is interesting to note that the average particle sizes due to the dissolution change only slightly. It means that though the sizes of all particles are decreasing, fine particles dissolve faster, and their fraction reduces. As a result, the average size of precipitates does not change considerably even in case of relatively high extent of the second phase dissolution. The stage of dissolution proper, at which the second phase volume fraction is reduced, is quickly finished, and the coarsening starts, at which coarser particles

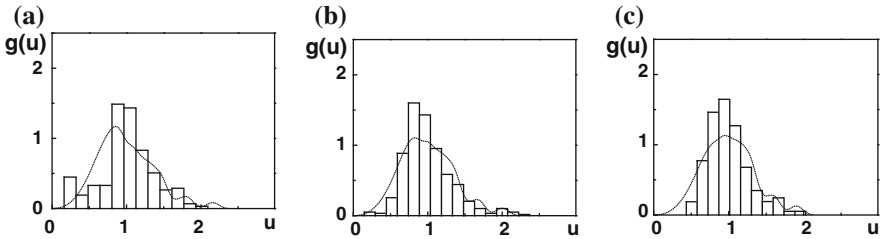


**Fig. 20** Comparison of calculated and experimental [94] dependences of AlN precipitates average radius on the annealing time for 1,000 (a, b) and 1,100 °C (c): a—initial state is after 650 °C, 24 h annealing





**Fig. 21** Comparison of calculated (*lines*) and experimental (histograms) [94] AIN PSDs after the annealing at 1,000 °C for 1 (a) and 2 h (b). Initial state—annealing at 650 °C, 24 h ( $u = R/\bar{R}$ )



**Fig. 22** Comparison of calculated (*lines*) and experimental (histograms) [94] AIN PSDs after annealing at 1,000 °C for 0.5 (a), 1 (b) and 2 h (c). Initial state—annealing at 700 °C, 24 h ( $u = R/\bar{R}$ )

grow fast and the finer ones dissolve. At this stage the average particle size is increasing, whereas their volume fraction almost does not change.

Figures 21 and 22 demonstrate comparison of calculated and experimental PSDs of AIN after the different time annealing at 1,000 °C for two initial states. It is seen that these distributions are in quite a good agreement, which allows concluding that the numerical method suggested in the present work describes adequately the PSD evolution at annealing. Some difference in calculated and experimental distributions is obviously due to experimental errors, particularly, the errors in the initial distributions which serve as the initial data for simulation.

These examples show that the calculated dependences of precipitates average radius and PSDs are in very good agreement with the experiment. In [89–91] calculated and experimental dependences of average particles radius, their volume fraction and PSDs for different stages of precipitates evolution in austenite and ferrite of low-alloyed steels are compared, and quite a good agreement is found as well.

In the general case of medium- and high-alloyed alloys the calculation is more complicated, as one must consider interdiffusion, but not the impurity diffusion,

and take into account components interaction in solid solution and concentration dependences of interdiffusion coefficients. This case is considered in [92].

In the case considered the system of stationary diffusion equations describing diffusion in a cell of the  $j$ -th size interval for the  $(N + 1)$ -component alloy takes the form:

$$\frac{\partial}{\partial r} \left( r^2 \sum_{l=1}^N \tilde{D}_{il} \frac{\partial^l C_l}{\partial r} \right) = 0. \quad (78)$$

The following equations describing component concentration distributions in cells are obtained from these equations:

$$\sum_{j=1}^N \tilde{D}_{ij} \frac{\partial^l C_j}{\partial r} = \frac{K_i^l}{r^2}, \quad (79)$$

where  $K_i^l$  is a constant for every element and every size interval.

Component concentrations at interphase boundaries must satisfy the local equilibrium and mass balance conditions. For precipitates of constant composition,  $A_a B_b \dots$ , equilibrium conditions at particle/matrix interfaces are expressed by Eq. (74). Concentrations at cell boundaries must be equal.

The mass balance condition is:

$$\left[ C_i^p v_a^m / v_a^p - {}^l C_i^{m/p} \right] \frac{dR_l}{d\tau} = \sum_{j=1}^N \tilde{D}_{ij} \frac{\partial^l C_j^m}{\partial r} \Big|_{r=R_l}, \quad (80)$$

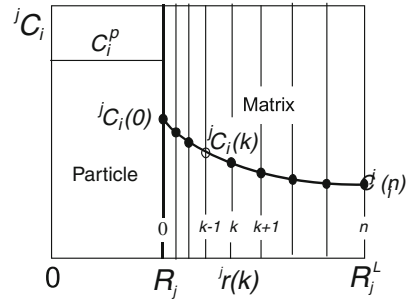
or, taking into account (79), it is:

$$\left[ C_i^p v_a^m / v_a^p - {}^l C_i^{m/p} \right] \frac{dR_l}{d\tau} = \frac{K_i^l}{(R_l)^2}. \quad (81)$$

The calculation procedure is in general analogous to that described above for low-alloyed alloys, but in this case the calculations are much more complicated, as the component concentrations in cells cannot be given analytically, and numerical methods must be used to find them. We used the finite difference method. For field cells of all size intervals spatial nets were constructed, the first node of which (node 0) coincided with an interphase boundary, and the last one (node  $n$ ) with a cell boundary. Concentrations in cells were given as net functions determined in discrete nodes of the net,  ${}^j C_i(k)$ , where  $j$  is the number of the size interval, and  $k$  is the number of the spatial net node. Thus, the  $i$ -th element concentration at an interface with a particle of the  $j$ -th size interval is denoted as  ${}^j C_i(0)$ , and its concentration at a cell boundary as  ${}^j C_i(n)$ .

The spatial net construction in a field cell of the  $j$ -th size interval is shown in Fig. 23. The  $k$ -th node coordinates in the  $j$ -th size interval cell are denoted as  ${}^j r(k)$ .

**Fig. 23** The sketch of spatial net construction in the  $j$ -th size interval cell and concentration distribution of the  $i$ -th element in it



The calculation order is as follows.

1. Calculation of average component concentrations in the matrix by Eqs. (66) and (76) based on the precipitate volume fraction.
2. Calculation of field cell sizes. Dependently on the geometrical model used, the field cell radii were calculated by expressions (59, 60 or 61).
3. Construction of spatial nets in field cells of different size intervals, making allowance for non-uniform spatial nets refined maximally near interpose boundaries.
4. Calculation of concentration distributions and interface velocities for particles from different size intervals.
5. Calculation of particles radii and their volume fraction at a new time step from formulas (68–69).
6. Calculation of PSD at a new time step using the above-described for binary systems procedure, based on the analysis of the number of particles leaving the initial size interval and falling in it from other intervals due to growth or dissolution.

The as-determined values of volume fraction and PSD served as the initial ones for calculations at a new time step.

The most difficult part of calculations is the calculation of concentration distributions in cells and interface velocities. It is carried out based on the requirement that average component concentrations in the matrix, calculated from the precipitate volume fraction, are equal to the average concentrations, calculated from concentration distributions of components in field cells, i.e., component concentrations in cells must satisfy the system of  $N$  equations of the form:

$$\Phi_i = \bar{C}_i^m - 3 \left\{ \sum_{j=1}^{N_p} n^j \sum_{k=0}^{n-1} \frac{[jC_i(k+1)(j_r(k+1))^2 + jC_i(k)(j_r(k))^2]}{2} [j_r(k+1) - j_r(k)] \right\} / \left\{ \sum_{l=1}^N n^l [(R_l^L)^3 - (R_l)^3] \right\} = 0 \tag{82}$$

The first member in the right part of Eq. (82) corresponds to the average component concentration in the matrix calculated from the precipitate volume fraction, and the second one corresponds to the average concentration calculated from component concentrations in spatial net nodes for field cells of all size intervals.

The calculation was as follows:

1. Initial approximations for component concentrations at cell boundaries were given.
2. Based on the component concentrations at cell boundaries for each size interval component concentration distributions and interface velocities were calculated.
3. The values of function  $\Phi_i$  were calculated in the points corresponding to the initial approximations and their vicinity.
4. The values of function  $\Phi_i$  derivatives with respect to  $C_i^L$  in the point corresponding to the initial approximations were found by numerical differentiation.
5. Based on the as-found functions and their derivatives the refined values of concentrations at field cell boundaries were calculated by Newton–Raphson method.
6. The values of  $C_i^L$  obtained from the cycle (points 2–5) were used as the initial approximations for a new iteration, i.e., the calculation was repeated from point 2.

The iteration cycle was over if the following iteration differed from the previous one by a value less than the given convergence accuracy. The interface velocities and concentrations at interphase and field cell boundaries were found from this iteration procedure.

Component concentrations in cells and interface velocities are calculated based on the requirement that component concentration at particle/matrix interfaces and interface velocities satisfy the local equilibrium and mass balance conditions. These equations in case of net variables take the form:

$$FT^j = a\bar{G}_A^{z/p} [{}^jC_1(0), \dots, {}^jC_N(0)] + b\bar{G}_B^{z/p} [{}^jC_1(0), \dots, {}^jC_N(0)] + \dots - \frac{2\sigma v_m^p}{R_j} - {}^0G_{A,B,\dots} = 0 \quad (83)$$

$$FB_i^j = [C_i^p \bar{v}_a^m / \bar{v}_a^p - {}^jC_i(0)] \cdot V_j - \frac{K_i^j}{R_j} \quad (84)$$

To calculate concentration distributions in cells Eq. (80) was used, the difference approximation of which is:

$$\sum_{l=1}^N \tilde{D}_{il} \frac{{}^jC_l(k+1) - {}^jC_l(k)}{{}^jr(k+1) - {}^jr(k)} = \frac{4K_i^j}{[{}^jr(k+1) + {}^jr(k)]^2} \quad (85)$$

For field cells of each size interval concentration distributions and interface velocities were calculated separately. The calculation order was as follows:

- a. Initial approximations for constants  $K_i^j$  and interface velocity  $V_j$  were given.

- b. Component concentration distributions in a field cell were calculated by Eq. (85).
- c. The values of functions  $FT^j$  and  $FB_i^j$  were calculated in the points corresponding to the initial approximations and their vicinity.
- d. The values of  $FT^j$  and  $FB_i^j$  derivatives with respect to  $K_i^j$  and  $V_j$  in a point corresponding to the initial approximations were found by numerical differentiation.
- e. Based on the as-determined values of the functions and their derivatives the refined values of constants  $K_i^j$  and interface velocities  $V_j$  were calculated by the Newton-Raffson method.

The values of  $K_i^j$  obtained from the cycle (b–e) were used as initial approximations for a new iteration, and the calculation was repeated from point b.

The algorithm generalized on the case, when the matrix was not a dilute solution and one must take into account components interaction in solid solution and concentration dependences of interdiffusion coefficients, was tested in [92]. The calculation results were compared to the experimental data on the behavior of VC precipitates in austenite of steel with 1.1 wt. % V and 0.86 wt. % C from [69]. The heat treatment was as follows. Specimens were quenched in water from 1,300 °C and then heated to 700 °C and held for 5 h to obtain dispersed spherical precipitates, and, finally, they were annealed at 900–1,100 °C for 10–200 h. At such preliminary treatment the alloy before annealing consists of austenite matrix with very fine precipitates of vanadium carbide. The precipitates volume fraction is considerably less than equilibrium, i.e., the solid solution is highly supersaturated.

Comparison of the calculation results with the experimental data demonstrates that for the 1,100 °C annealing they are in quite a satisfactory agreement both for the average particle sizes and PSDs. However, for lower annealing temperatures calculation results markedly differ from the experimental data. In [92] it is suggested that this difference is mainly because the possibility of new nucleation centers was not taken into account in calculations. At 1,100 °C the supersaturation of solid solution is not very high, and the formation of new nuclei is hardly probable, but at lower annealing temperatures it is quite possible. That is why in calculations the formation of new nucleation centers must be taken into account.

### ***4.3 Simulation of Precipitates Evolution with Consideration for Nucleation***

As shown in the previous section, simulation of precipitates evolution without considering nucleation in some cases results in considerable discrepancy in calculations and experiment.

The calculation algorithm taking nucleation into account was suggested in [99]. According to this publication, we consider simulation of precipitates evolution with consideration for nucleation by an example of vanadium carbides.

The nucleation rate was calculated based on the classical theory of nucleation. We used an approach developed by Liu and Jonas [95, 96], who showed that if the nuclei are formed on dislocations, then the nucleation rate and the Gibbs energy of a critical sized nucleus may be calculated from the formulas:

$$J = \rho D_{eff} C/a^3 \exp\left(-\frac{\Delta G_{crit}}{k_B T}\right), \quad (86)$$

and

$$\Delta G_{crit} = \frac{16\pi\zeta^3\sigma_n^3}{3(\Delta G_{chem} + \Delta G_e)}. \quad (87)$$

Here  $\rho$  is the dislocation density,  $a$  is the lattice parameter of a matrix,  $k_B$  is the Boltzmann constant,  $D_{eff}$  and  $C$  are the effective diffusivity and concentration of the element controlling the rate of nucleation,  $\sigma_n$  is the specific surface energy of a nucleus/matrix interface,  $\zeta$  is a correction factor for the surface energy of an interface connected with the presence of dislocations and having a value between 0 and 1, and  $\Delta G_{chem}$  and  $\Delta G_e$  are the changes of the chemical free energy and the free energy of stresses at the formation of one formula unit of a new phase.

In simulation of nucleation the main problem is usually connected with the difficulty to evaluate the energy of stresses and the nucleus/matrix interface specific surface energy. Liu and Jonas [95, 96] suggested the way to avoid these difficulties in a case when precipitates have the same crystal structure and orientation as the matrix, but another lattice period. The consideration was accomplished by an example of nucleation of titanium carbides and carbonitrides in austenite. It was shown that the nucleus/matrix surface for the TiC critical sized nucleus is of dislocation and semi-coherent nature. In that case both  $\sigma_n$  and  $\Delta G_e$  associated with the semi-coherent interface can be described in terms of a critical coherency loss parameter  $C^*$ . This parameter is defined as a fraction of the lattice mismatch relaxed by the presence of the interface dislocations, and it can be determined directly from  $\Delta G_{chem}$ .

Let us consider a general case of carbide or nitride nucleation in austenite for cubic carbides or nitrides  $MX_n$  of IV–V groups. All these carbides and nitrides have similar crystal lattices with close parameters. That's why it seems valid to extend the approach developed by Liu and Jonas [95, 96] to this case of vanadium carbides.

The Gibbs energy change at the formation of one formula unit of  $MX_n$  from austenite was calculated from:

$$\Delta G_{ch} = \frac{1}{v_{MX_n}} [G_{MX_n} - \bar{G}_M - n\bar{G}_X], \quad (88)$$

where  $G_{MX_n}$  and  $v_{MX_n}$  are the Gibbs energy and volume of one  $MX_n$  formula unit, respectively.

In calculation of  $\Delta G_\varepsilon$  and  $\sigma_n$  it was assumed that  $\delta$  (the lattice mismatch) is compensated by two components, elastic,  $\delta_\varepsilon$ , and plastic,  $\delta_p$ , both of them being associated with interface dislocations, and thus

$$\delta = \delta_\varepsilon + \delta_p. \quad (89)$$

Here

$$\delta = \frac{a_{MX} - a_\gamma}{a_\gamma}, \quad (90)$$

where  $a_{MX_n}$  and  $a_\gamma$  are the  $MX_n$  and austenite lattice periods.

A coherence loss parameter is defined as

$$C^* = \delta_p / \delta. \quad (91)$$

From (89) and (91) we get

$$\delta_\varepsilon = (1 - C^*)\delta. \quad (92)$$

$\Delta G_\varepsilon$  is calculated from the formula by Eshelby [97]:

$$\Delta G_\varepsilon = \frac{2}{3} \mu_\gamma (\Delta^*)^2 \frac{\alpha}{\alpha + (1 - \alpha)K_\gamma / K_{MX_n}}, \quad (93)$$

where

$$\Delta^* = \delta_\varepsilon^3 + 3\delta_\varepsilon^2 + 3\delta_\varepsilon, \quad (94)$$

$$K_\gamma = \mu_\gamma [2 + 3/(1 - \nu_\gamma)], \quad (95)$$

$$K_{MX_n} = \mu_{MX_n} [2 + 3/(1 - \nu_{MX_n})] \quad (96)$$

$$\alpha = (1 + \nu_\gamma) / 3(1 - \nu_\gamma). \quad (97)$$

Here  $\mu_\gamma$  and  $\mu_{MX_n}$  are the shear modules, and  $\nu_\gamma$  and  $\nu_{MX_n}$  are Poisson coefficients of the austenite and the vanadium carbide, respectively.

Similar to Liu and Jonas [95, 96], the free energy of a semi-coherent nucleus/matrix interface was considered as consisting of two parts and expressed as:

$$\sigma_n = \sigma_{nc}(1 - 2C^*\delta) + \sigma_{ns}, \quad (98)$$

where  $\sigma_{nc}$  corresponds to the energy of a completely coherent interface, and  $\sigma_{ns}$  is connected with boundary dislocation energy.

According to Liu and Jonas [95, 96], these constituents of the free energy of a nucleus/matrix interface may be expressed as follows:

$$\sigma_{nc} = \left[ N_s Z_s (\bar{X}_M - {}^{MX_n}X_M)^2 \Delta H \right] / (N_A Z) \quad (99)$$

and

$$\sigma_{ns} = (\mu^* a^* / 2\pi^2) \left[ 1 + \Psi - (1 + \Psi^2)^{1/2} \right], \quad (100)$$

where

$$\Psi = 2\pi a^* / [\lambda(1 - \nu^*)] \quad (101)$$

and

$$\lambda = a^* / \delta_p = a^* / C^* \delta. \quad (102)$$

Here  $N_s$  is the number of atoms per an interface surface unit,  $Z_s$  is the number of bonds through an interface per atom,  $N_A$  is the Avogadro number,  $Z$  is a coordinate number,  $\Delta H$  is the enthalpy of the vanadium carbide dissolution in the infinitely diluted austenite,  $a^*$  is the interfacial lattice parameter defined as  $a^* = 2a_\gamma a_{MX_n} / (a_\gamma + a_{MX_n})$ ,  $\mu^*$  is the interfacial shear modulus, and  $\nu^*$  is the interfacial Poisson's ratio.

Following Van der Merve [98], the values of  $\mu^*$  and  $\nu^*$  can be evaluated from the precipitate and matrix shear modules and Poisson's ratios:

$$1/\mu^* = 1/\mu_\gamma + 1/\mu_{MX_n} \quad (103)$$

and

$$1/\nu^* = 1/\nu_\gamma + 1/\nu_{MX_n}. \quad (104)$$

It is obvious from the above derivations that both  $\Delta G_\varepsilon$  and  $\sigma_n$  are the functions of  $C^*$ . To determine  $C^*$  we used the expression by Liu and Jonas [95, 96]:

$$(\sigma_n / \sigma_0)^{1.5} = 1 + \Delta G_\varepsilon / \Delta G_{ch}, \quad (105)$$

where  $\sigma_0$  is the energy of a non-coherent precipitate/matrix interface.

Substitution of (88–104) expressions into (105) gives an equation with one unknown, which can be numerically calculated to determine  $C^*$  and then calculate  $\Delta G_\varepsilon$  and  $\sigma_n$ .

The calculation procedure is in many respects similar to that described above and used in [89, 91, 92]. However, in the case considered the nucleation is taken into account along with the processes of precipitate growth and dissolution.

The calculation procedure is as follows:

1. Calculation of average component concentrations in the matrix based on the precipitate volume fraction.
2. Calculation of the field cell sizes.
3. Construction of spatial nets in field cells of all size intervals.



4. Calculation of concentration distributions in cells and interface velocities for particles of different size intervals.
5. Calculation of the nucleation rate.
6. Calculation of the PSDs and volume fraction at a new time step without regard for nucleation processes.
7. Calculation of the volume fraction and the PSD with consideration for the formation of new nuclei.
8. The as-determined values of the volume fraction and the PSDs were used as the initial ones for calculations at a new time step, and so on. This procedure is repeated until the necessary time is reached.

Points I–IV are completely similar to the above described steps of calculation of precipitates evolution without considering nucleation.

The nucleation rate ( $J$ ) and the critical nucleus radius ( $R_{crit}$ ) were calculated at every time step as follows. These parameters were calculated based on the mean component concentrations in a matrix, i.e. without considering the non-uniformity of the component concentration distribution, in particular, its decrease near the growing particles. Based on the values of the average component concentrations in matrix, the change of the chemical free energy at the formation of one formula unit of a new phase was calculated from equation (88). A critical coherency loss parameter  $C^*$  was then calculated from Eq. (105) in view of equations (88–104). From the value of this parameter the  $\Delta G_e$  and  $\sigma_n$  were calculated using Eqs. (93) and (98). After that the free energy of the critical nucleus formation and the nucleation rate were calculated from Eqs. (90) and (89), respectively.

Calculations of the PSD and the particle volume fraction at a new time step without regard for the precipitate nucleation were performed as described in the above section.

The volume fraction and PSD calculations corrected for the formation of new nuclei were performed as follows. The number of nuclei forming in a unit volume during the  $\Delta t$  time was calculated from the nucleation rate:

$$N_n = J \cdot \Delta t \quad (106)$$

The increase of the precipitates volume fraction due to the formation of new nuclei was calculated from the formula:

$$\Delta F = \frac{4\pi}{3} R_{crit}^3 \cdot N_n \quad (107)$$

The PSD change due to the formation of new nuclei was calculated based on the following considerations. The nucleation results in the growth of the fraction of particles in the size interval where the critical sized particles fall, and this growth is calculated from:

$$\Delta n_{crit.} = \frac{N_n}{N_p}, \quad (108)$$

where  $\Delta n_{crit}$  is the change of particle fraction in a size interval where the critical sized particles fall; and  $N_p$  is the total amount of particles in a volume unit before the formation of new nuclei, the latter being calculated from:

$$N_p = \frac{3F}{4\pi\bar{R}^3}, \quad (109)$$

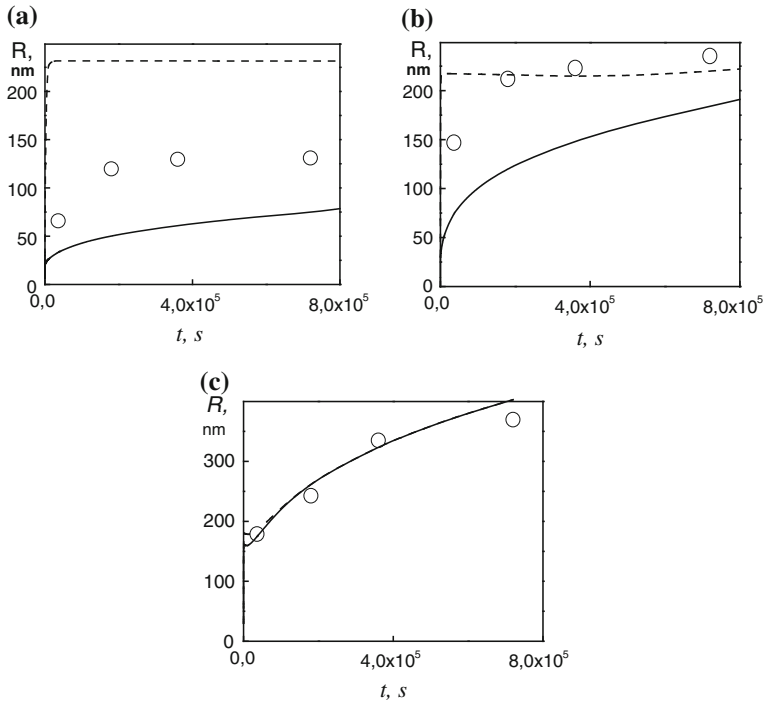
where  $\bar{R}$  is the average precipitate radius.

After the introduction of this correction the PSD was normalized. Using the algorithm developed we carried out calculations of the vanadium carbide precipitates evolution in an austenite matrix [99, 100]. Based on the results of the experimental investigations by Jack and Jack [101] and the thermodynamic analysis by Popov et. al. [102], the mean composition of the carbides in a steel was assumed to correspond to VC<sub>0.88</sub>.

In [99] the calculation results were compared to the experimental data by Wey et. al. [69], who investigated vanadium carbide evolution in the austenite of steel with 1.1 wt. % of vanadium and 0.86 wt. % of C. The heat treatment was as follows. The samples were water quenched from 1,300 °C, then heated up to 700 °C and held for 5 h at this temperature for the formation of the dispersed precipitates, and finally annealed at 900–1,100 °C from 10 to 200 h. Wey et. al. [69] investigated the changes of mean precipitate size and PSD in the process of the final heat treatment. As regards the state of these precipitates after the 5 h annealing at 700 °C considered as the initial one for the subsequent treatment, it was not studied. That is why it was necessary to set the particles size distribution and their volume fraction in the initial state, required for further calculations, using some assumptions.

Based on the analysis of a number of publications including those by Dunlop and Honeycombe [103] and Ballinger and Honeycombe [104], we assumed the average carbide particle radius to be about 30 nm. The PSD was assumed to be normal with the standard deviation of about 0.3. By all means such a choice of these parameters implies a considerable error in their values, but in the case under consideration it doesn't remarkably affect the calculation results.

The volume fraction value in the initial state was chosen reasoning from the following considerations. There are two different sections in the experimental dependences of the precipitate cubed average radius on the annealing times presented by Wey et al. [69]. In the first section the rate of precipitate growth is relatively high and the  $R^3$  dependence on the annealing time is non-linear. The diffusion growth of precipitates is assumed to proceed at this stage through the vanadium and carbon transition from the solid solution into the particles. In the second section the  $\bar{R}^3$  dependence is nearly linear suggesting the coarsening to occur. In the stage of coarsening the precipitate volume fraction is near to its equilibrium value. At 1,100 °C the solid solution supersaturation is relatively low, and thus the formation of new nuclei is unlikely. It is therefore possible to determine the carbide volume fraction in the initial state analysing the temporal

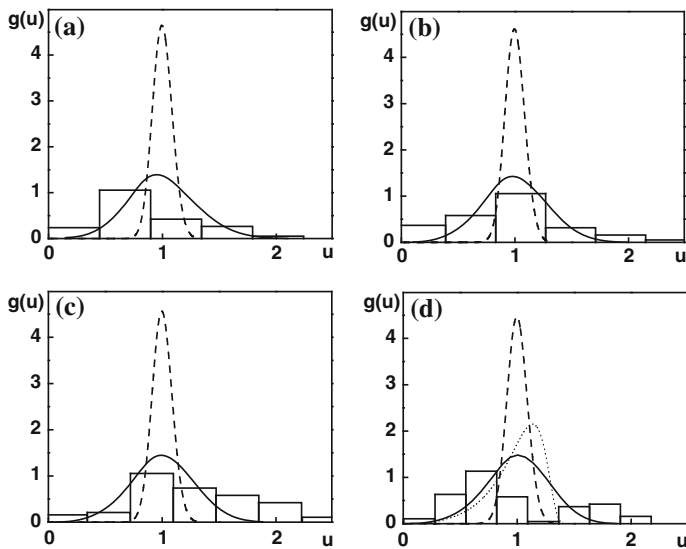


**Fig. 24**  $VC_{0.88}$  average radius dependence on the annealing time at 900 (a), 1,000 (b) and 1,100 °C (c): *dashed lines*—calculation without regard for nucleation, *solid lines*—calculation with regard for nucleation, spheres—experimental data by Wey et. al. [69]

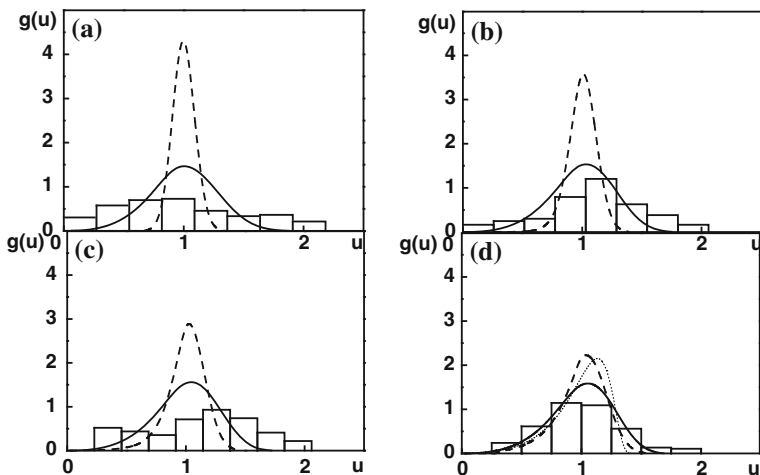
dependence of the precipitate cubed average radius at this temperature. If there is no nucleation of precipitates, then the ratio of the cubed average radiuses of precipitates in the initial state and in the moment of growth stage completion (the beginning of the coarsening stage) is equal to the ratio of their volume fraction in the initial state to the equilibrium volume fraction. If the equilibrium volume fraction is known (and it was assessed based on the thermodynamic calculation), then it is possible to estimate the precipitate volume fraction in the initial state. This assessment gives the value of 0.000046.

The comparison of calculation results to the experimental data was performed for 900, 1,000 and 1,100 °C annealing for up to 200 h. The experimental data were compared to the calculation results obtained both with consideration for nucleation and without it.

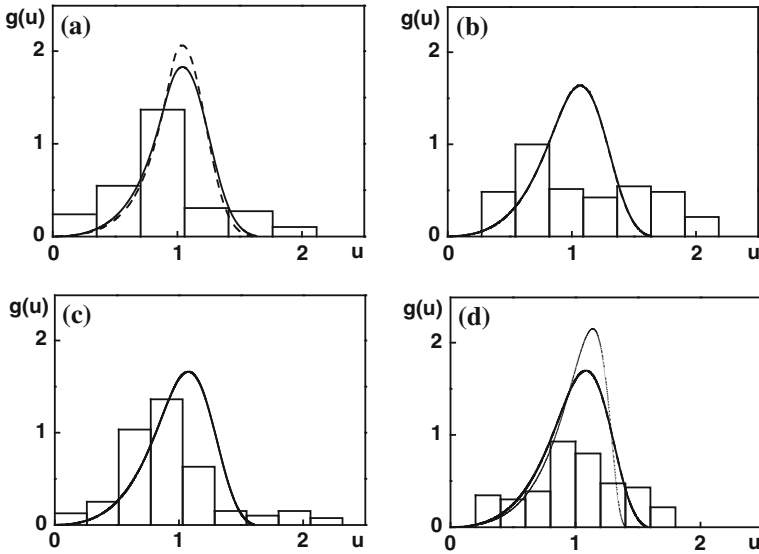
Figure 24 demonstrates calculated and experimental dependences of the precipitate average radii on the annealing time at 900, 1,000 and 1,100 °C, and Figs. 25, 26, 27 show calculated and experimental PSDs after the annealing at these temperatures for 10, 50, 100 and 200 h. The Lifshitz–Slezov’s asymptotic distribution is shown for the comparison by a dotted line.



**Fig. 25** Calculated and experimental  $VC_{0.88}$  PSDs after 900 °C annealing for 10 (a), 50 (b), 100 (c) and 200 h (d): histograms—experimental data by Wey et al. [69], dashed lines—calculation without regard for nucleation, solid lines—calculation with consideration for nucleation, dotted line—asymptotic Lifshitz-Slezov's PSD



**Fig. 26** Calculated and experimental  $VC_{0.88}$  PSD after 1,000 °C annealing for 10 (a), 50 (b), 100 (c) and 200 h (d): histograms—experimental data by Wey et al. [69], dashed lines—calculation without regard for nucleation, solid lines—calculation with consideration for nucleation, dotted line—asymptotic Lifshitz-Slezov's PSD



**Fig. 27** Calculated and experimental  $VC_{0.88}$  PSD after 1,100 °C annealing for 10 (a), 50 (b), 100 (c) and 200 h (d): histograms—experimental data by Wey et al. [69], *dashed lines*—calculation without regard for nucleation, *solid lines*—calculation with consideration for nucleation, *dotted line*—asymptotic Lifshitz-Slezov's PSD

It can be seen that according to the calculation results without considering nucleation there are three stages on the temporal dependence of the average particle radii. At first the fast growth of particles occurs due to vanadium and carbon transfer from a supersaturated solid solution into precipitates, resulting in a quick increase of their average radius. Quite a narrow PSD is forming at this stage. Then the stage of particle size stabilization comes, their average radii practically not changing. This stage results from the formation of a very narrow PSD in the process of precipitate growth. As the element concentrations at interfaces with different particles are practically the same, the coarsening is not possible in that case. That is why the average radius practically does not change, and only the PSD changes. With the growth of the PSD width the coarsening stage begins. The duration of every stage depends on the annealing temperature. At 900 °C the narrow PSD forming in the process of particle growth is very stable, and the coarsening stage does not occur even after the 200 h annealing. At 1,000 °C the PSD broadens markedly, and the coarsening stage begins after the 100 h annealing. And, finally, at 1,100 °C the narrow PSD, forming at the initial stage, broadens already after the 10 h holding, and the coarsening stage is observed.

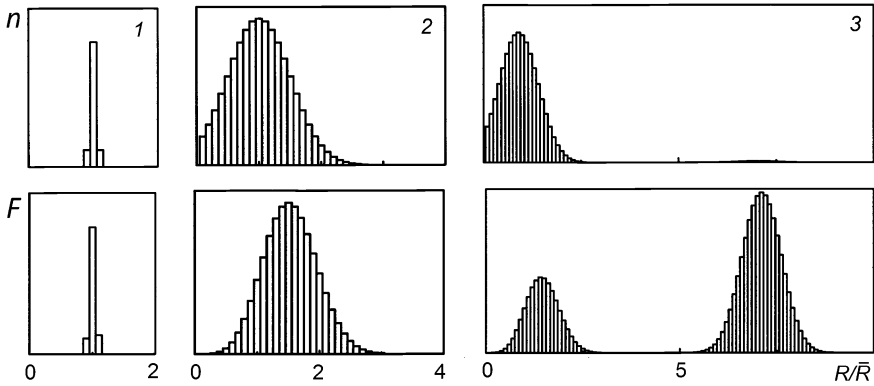
The comparison of calculations without considering nucleation with the experimental data demonstrates their good agreement only at 1,100 °C. At lower temperatures the calculation and experimental results considerably differ. The main difference is that the calculation predicts a very fast growth of the particle

average radius and the formation of a very narrow PSD resulting in the particle size stabilization, which does not agree with the experiment. Firstly, at the initial stage the particle radius growth is not as fast and the PSD is not as narrow, as it is predicted by calculations. Secondly, the stage of the particle size stabilization is not observed on the experimental dependences of the particle average radius.

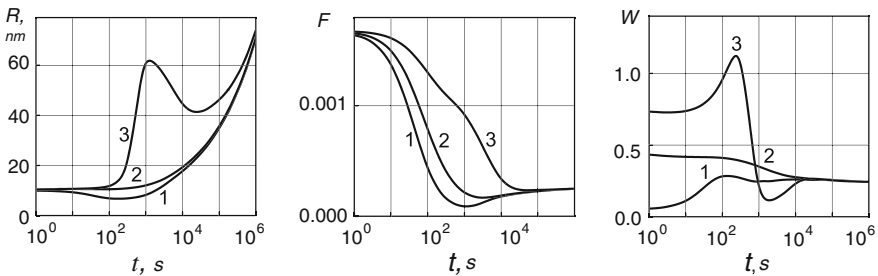
If calculations are performed with consideration for nucleation, they are much closer to the experiment. In that case the particle average radius dependences on the annealing time are not so steep, there is no stabilization stage in them, and the calculated PSDs are wider and closer to the experimental ones. Such an effect of nucleation may be explained as follows. At the first stage, when the particles present in the initial state are growing, the nucleation results in a slower increase of the particle average radius because of high dispersity of the new forming particles. For the same reason a relatively broad particle size distribution is forming at the initial stage of the process, when the growth of the particles present is accompanied by nucleation of the new ones. Thus, in calculations taking nucleation into account the particle growth together with the formation of new nuclei is right away followed by coarsening, missing the stabilization stage, which was found in calculations without regard for nucleation.

The greatest difference between calculations with and without considering nucleation is typical of the 900 °C annealing, as at this temperature the solid solution in the initial stage is highly supersaturated, and the intensive nucleation occurs. At 1,100 °C it is only slightly supersaturated, and nucleation is not well developed. As a result, in this case the calculation results with and without considering nucleation are quite close to each other, and while there are slight differences after 10 h annealing, at longer holding the average radiuses and PSDs are practically the same. The longer is the holding and the higher is the annealing temperature, the closer is the calculated distribution to the Lifshitz-Slezov's asymptotic curve.

The analysis of the results obtained demonstrates satisfactory agreement of calculations considering nucleation with the experimental data. The discrepancies observed result from several reasons. Firstly, it is the absence of any experimental data on the volume fraction and the particle size distribution at the initial stage, which made it necessary to choose these parameters quite arbitrarily. Secondly, there is no information on dislocation density and its changes at annealing. Thirdly, there exist some errors in the values of parameters used in calculations. We suppose that these factors are mainly the reasons of the discrepancies observed, but not the imperfectness of the model suggested.



**Fig. 28** Three types of the initial PSDs



**Fig. 29** Variation of  $VC_{0.88}$  average radius ( $R$ ), volume fraction ( $F$ ) and PSD width ( $W$ ) at  $900\text{ }^{\circ}\text{C}$  annealing of steel with  $1\text{ }\%$  C and  $0.1\text{ }\%$  V:  $R_0 = 10\text{ nm}$ ,  $F_0 = 0.0017$ . Figures near curves denote the type of the initial PSD

#### 4.4 Effect of the Initial Particle Size Distribution on Precipitate Evolution

Using the algorithm developed, the influence of the initial PSD on further precipitate evolution has been analyzed, the analysis having shown the strong dependence of particles ensemble evolution on the initial PSD [10, 100]. To illustrate that we present here the calculation results of simulation of vanadium carbides growth and dissolution in austenite for three initial PSDs [100]:

1. A very narrow PSD (the width of  $0.5\text{ nm}$ ) given by a normal distribution with the center at  $10\text{ nm}$ .
2. A relatively wide PSD (the width of  $5\text{ nm}$ ) given by a normal distribution with the center at  $10\text{ nm}$ .

3. A bimodal PSD, given by a sum of two normal distributions the width of 5 nm with the centers at 9 and 70 nm. The volume fraction of particles corresponding to them was 0.99 and 0.01 respectively.

The average particle size for all the three types of PSDs was the same, 10 nm. Figure 28 demonstrates the normalized histograms of the initial PSDs, the upper ones for every PSD showing the number of particles ( $n$ ), and the lower ones—the volume fraction of particles ( $F$ ) corresponding to every size interval. The latter histograms show how the precipitates volume is distributed between the particles of different sizes.

Figure 29 demonstrates dependences of VC average size, their volume fraction and PSD width on the annealing time at 900 °C for steel with 0.1 wt. % V and 1.0 wt. % C. The volume fraction of the precipitating phase was 0.0017 in the initial state, which corresponded to the maximal possible amount of VC in the steel of composition considered and was substantially more than the equilibrium value. At heating of this steel up to 900 °C precipitates at first partly dissolve, and then the coarsening stage starts. At the dissolution stage the free energy of a system decreases mainly at the expense of its volume constituent through the reduction of the precipitate volume fraction. When phase composition approaches its equilibrium value, the coarsening stage starts.

At the dissolution stage the precipitates volume fraction reduces which is accompanied with particle size changes. In that case the initial PSD has a strong effect on precipitates average size and volume fraction temporal dependences.

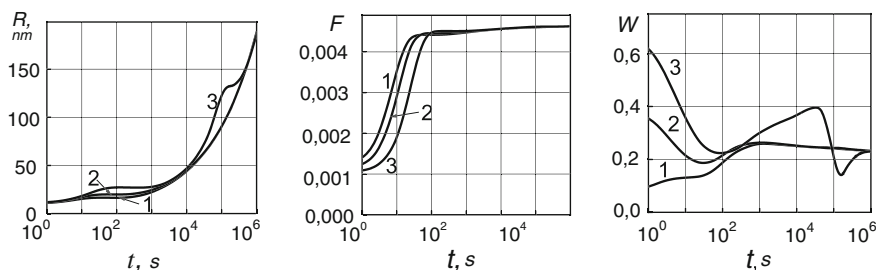
In case of a narrow initial PSD (type 1) the dissolution is the most rapid process and it is accompanied with the decrease of the precipitate average size. The precipitates dissolution results in the reduction of their volume fraction up to the value lower than the equilibrium one. This is due to the fact that in that case particles become highly dispersed, and that is why their solubility increases.

Precipitate dissolution is accompanied by a noticeable grow of the PSD width, which may be explained as follows. Fine particles dissolve faster than the coarse ones, and, consequently, the narrow initial PSD substantially broadens.

In case of wide initial PSD (type 2) dissolution proceeds slower because in that case the main precipitate volume is concentrated in coarser particles, which dissolve slower. In spite of dissolution, the average particles size at first does not change and at later stages even grows, because at dissolution not only particle sizes reduce, but the most dispersed particles completely disappear. The PSD width at precipitate dissolution in this case changes only slightly.

The dissolution is the slowest in case of the bimodal PSD (type 3). The most complicated dependences of the average size, volume fraction and PSD width on the annealing time are characteristic of this case. For understanding of these dependences one should remember that coarse particles dissolve much slower than small ones. At first small particles dissolve, while the coarse particles only slightly reduce in sizes. The complete dissolution of fine particles results in the several times growth of the average size. At further annealing the precipitate average size slightly reduces due to their dissolution. After the complete dissolution of fine





**Fig. 30** VC particles average size ( $R$ ), their volume fraction ( $F$ ) and PSD width ( $W$ ) in steel with 1 % C and 0.5 % V versus the annealing time at 1,000 °C:  $R_0 = 10$  nm,  $F_0 = 0.001$ . Figures near curves denote the type of the initial PSD

particles the process slows down, and a fold appears on the volume fraction temporal dependences. The PSD width at the step of fine particles dissolution at first increases due to the broadening of the initial distribution, and then drastically reduces at their full dissolution, and the distribution is no more bimodal. At further dissolution of coarse particles the PSD width grows again.

After dissolution the coarsening stage comes, at which the particles volume fraction is close to the equilibrium and only slightly changes with time, the cube of the average size linearly depends on time and the distribution width tends to an asymptotic value. At the coarsening stage the curves corresponding to different initial distributions flow together.

To illustrate the initial PSD influence on the particles growth kinetics the precipitate evolution in steel with 0.5 % V and 1.0 % C at 1,000 °C has been simulated. The volume fraction of VC particles in the original state was taken 0.001, which is several times lower than the equilibrium value (0.00463). Figure 30 demonstrates the calculation results for three initial distributions. It can be seen that there are several sections corresponding to different stages of precipitate ensemble evolution in the curves presented. The first stage corresponds to the diffusion growth of precipitates, then some intermediate stage is observed and, finally, the coarsening stage starts. The solid solution supersaturation in the initial state is not great in this case, and that is why the new nucleation centers formation is not well developed

At the stage of growth the precipitates volume fraction rapidly increases practically achieving the equilibrium value. The phase transformation is the rapidest in case of narrow PSD (type 1), and the slowest at bimodal PSD (type 3). It is explained by the fact that the greater is the interface area, the faster is the phase transformation. This area is the greatest at PSD 1, when all particles are small, and the smallest at PSD 3, when more than a half of precipitates volume fraction is concentrated in coarse particles.

At PSD 2 and 3 they, just on the contrary, get substantially narrower. Thus, the precipitate diffusion growth, if it is not accompanied by noticeable nucleation,

promotes the formation of quite narrow PSD, which is due to the fact that fine precipitates grow faster than the coarse ones.

As the solute precipitates from the solid solution, and the precipitate volume fraction approaches to its equilibrium state, the possibilities for further decrease of the system's volume free energy are exhausted, the diffusion growth ceases and the following stage of the process starts. In the examples considered the stage of particle sizes stabilization set up after the end of the diffusion growth. By the beginning of this stage a narrow PSD has been formed as a result of the previous diffusion growth, and the precipitate volume fraction attains the value close to the equilibrium one and practically does not change at further annealing.

When the distribution width attains a certain value ( $W \sim 0.21\text{--}0.22$ ) the precipitate ensemble average size is capable to grow by dissolution of fine and growth of coarse particles, i.e. transition to the coarsening stage occurs.

In cases 1 and 2 the PSD is close to the universal Lifshitz-Slezov's distribution [13], and at further evolution the cube of the average particles size linearly changes with time, and PSD asymptotically approaches to the Lifshitz-Slezov's one.

In case of the initial PSD 3 the evolution at the coarsening stage substantially differs, as the particles are concentrated in two appreciably differing size intervals. At coarsening particles from large size interval grow at the expense of the small ones, and the average size grows with time faster than in cases 1 and 2. At the beginning of this stage the fraction of large size particles is small, and the main part of precipitates is concentrated in the interval of small sizes. As coarsening proceeds the number of particles in the small size interval decreases. This results at first in PSD broadening, but then, at full dissolution of fine particles, in its drastic narrowing. In that case the second interval of particles size stabilization is observed, at which the narrow PSD broadens and classical coarsening starts.

At certain isothermal annealing duration the average precipitate size dependences on time for the three initial distributions flow together.

## 5 Simulation of Precipitate Evolution in Multiphase Systems

Simulation of evolution in multiphase systems is much poorer developed than for two-phase systems. One of the examples is publication [8], in which such simulation was made using an approach developed in [5, 6] and the MatCalc program [7]. The weakness of these publications is that the diffusion interaction of elements in matrix is not taken into account, as well as the final volume fraction of precipitates (i.e. the diffusion fields of different precipitates don't overlap). It is an essential drawback, as these two factors in some cases may considerably affect the precipitate evolution kinetics.

An approach described in the previous section is more universal compared to those realized in other studies, for instance, in [5–8] and in DICTRA program

[105]. Recently the possibility of simulation of precipitate evolution in multiphase systems was realized in the framework of this approach [106]. The model used in this case is in many respects analogous to that used for two-phase systems. As in the latter, it is assumed that all precipitates have spherical shape, the local thermodynamic equilibrium is established at interphase boundaries and mass transfer is realized by volume diffusion in matrix. The initial conditions of the problem are alloy composition and precipitating phase compositions, as well as the volume fractions ( $F_f$ ) and particle size distributions at the initial moment for every phase  $f$ . The particle size distribution for every phase  $f$  is given by its own histogram, i.e., for the particles of every type, the  $j$ -th interval of their radii from  ${}^fR_j - \Delta^fR_j/2$  to  ${}^fR_j + \Delta^fR_j/2$  is associated with the particle fraction  ${}^f n_j$  of this phase falling in this interval. Here  ${}^fR_j$  is the average radius of particles of the  $j$ -th size interval, and  $\Delta^fR_j$  is the width of the size interval for the particles of this phase.

As mentioned above, this method is based on the mean field approach. In this case the velocity of particle growth for every size interval of every phase is formulated through interaction of this particle and its mean surroundings, i.e., the interaction between particle and matrix in field cells is considered, and it is assumed that component concentrations at all cell boundaries are the same:

$${}^{fj}C_i^m(r = {}^fR_j^L) = C_i^L, \quad (110)$$

where  ${}^{fj}C_i^m$  is concentration of the  $i$ -th component in the matrix cell connected with the particle of phase  $f$  in the  $j$ -th size interval,  ${}^mC_i^L$  is concentration of the  $i$ -th component in matrix at cell boundaries,  $r$  is a spatial coordinate, and  ${}^fR_j^L$  is the field cell radius connected with a particle of phase  $f$  in the  $j$ -th size interval.

To find field cell sizes, the same models were used as in case of binary systems. We used the model suggested in [70]. In case of a multiphase system, Eq. (59) takes the form:

$${}^fR_j^L = {}^fR_j \cdot \left( \sum_f F_f \right)^{-1/3}. \quad (111)$$

As in the previous cases, the step-by-step procedure was used in calculations, and based on precipitate volume fraction and PSD for time  $t$  these parameters were calculated for  $(t + \Delta t)$ . The system of diffusion equations describing diffusion in a cell connected with a particle of phase  $f$  from the  $j$ -th size interval for a  $(N + 1)$ -component system is:

$$\frac{\partial {}^{fj}C_i^m}{\partial \tau} = \frac{1}{r^2} \frac{\partial}{\partial r} \left( r^2 \cdot \sum_{l=1}^N \tilde{D}_{il} \frac{\partial {}^{fj}C_l^m}{\partial r} \right), \quad (112)$$

where  $\tilde{D}_{il}$  are partial interdiffusion coefficients in matrix.

The stationary field approach was used to find concentration distributions of elements in field cells. In this case Eq. (112) take the form:

$$\sum_{l=1}^N \tilde{D}_{il} \frac{\partial^{jl} C_l^m}{\partial r} = \frac{K_i^{jl}}{r^2}, \quad (113)$$

where  $K_i^{jl}$  is a constant for the  $i$ -th element in a cell of the  $j$ -th size interval for precipitates of phase  $f$ .

As mentioned above, component concentrations at interphase boundaries must satisfy the local equilibrium and mass balance conditions.

The mass balance conditions at an interphase boundary for precipitates of phase  $f$  from the  $j$ -th size interval are:

$$\left[ C_i^f v_a^m / v_a^f - {}^j C_i^{m/f} \right] \frac{dR_j}{dt} - \sum_{l=1}^N \tilde{D}_{il} \frac{\partial^{jl} C_l^m}{\partial r} = 0, \quad (114)$$

or, taking into account (113):

$$\left[ C_i^f v_a^m / v_a^f - {}^j C_i^{m/f} \right] \frac{dR_j}{dt} - \frac{K_i^{jl}}{({}^j R_j)^2} = 0, \quad (115)$$

where  ${}^j C_i^{m/f}$  is the concentration of the  $i$ -th element in matrix at an interface with particles of phase  $f$  from the  $j$ -th size interval.

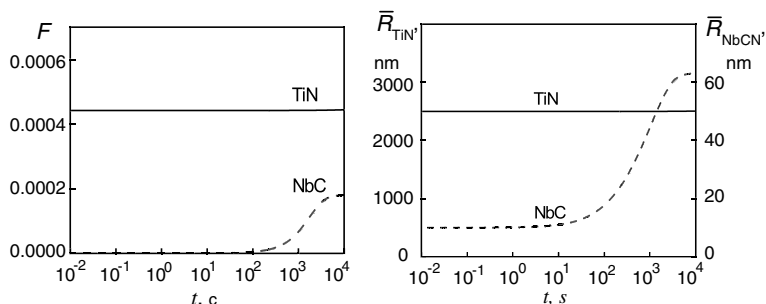
As in the above considered cases, the system of equations, satisfying the component concentration distributions in field cells and interface velocities, should be supplemented by the mass conservation condition. In this case the latter is (for every element  $i$ ):

$$\Phi_i = \sum_f \alpha_f C_i^f + (1 - \sum_f \alpha_f) \bar{C}_i^m - C_i^{al} = 0. \quad (116)$$

The general calculation procedure used in this algorithm is in many respects analogous to those described above. As in the previous cases, the step-by-step procedure was used in calculations. The finite difference method was used for calculation of component concentrations in cells. At every step spatial nets were constructed for field cells of all phases and all size intervals. Concentration distributions in cells and interface velocities were calculated with the requirement that the average component concentrations in matrix satisfy the mass conservation condition. The local equilibrium and mass balance conditions at interfaces for all phases and all size intervals must be fulfilled, and component concentrations at cell boundaries of all size intervals must be the same.

When the interface velocities have been found, the volume fractions and PSDs for all phases at a new time step are calculated.

In [106] this algorithm was used for calculation of precipitate evolution in steels with Ti and Nb, in which two carbonitride phases are formed, one of them based on Ti nitride and another one based on Nb carbide. The calculation was performed for steel with 0.1 wt. % C, 0.01 wt. % N, 0.05 wt. % Nb and 0.03 wt. % Ti. As an example, we consider a case when the initial state was an equilibrium phase



**Fig. 31** Volume fraction ( $F$ ) and precipitate average radius ( $\bar{R}$ ) in the alloy with 0.1 wt. % C, 0.01 wt. % N, 0.05 wt. % Nb and 0.03 wt. % Ti versus annealing time at 1,100 °C

composition at 1,400 °C, which is close to the alloy state directly after crystallization. At this temperature the volume fraction of TiN is 0.044 %. As an initial volume fraction of NbC for further simulation the value of 0.0001 % was taken. The average radius of TiN particles was assumed to be 2.5  $\mu\text{m}$ , and that of NbC 10 nm. PSDs for both phases were given by normal distributions with relative width of 0.2. Precipitate evolution in this alloy was calculated for 1,100 °C, and the results are shown in Fig. 31.

It is seen that at annealing the state of the ensemble of practically insoluble in solid steel titanium nitrides almost does not change, whereas the average radius and volume fraction of niobium carbides are considerably increased.

## 6 Conclusions

In recent years considerable progress has been achieved in simulation of precipitate reactions in metal alloys and of precipitate behavior at heat treatment due to the following reasons. Firstly, accumulation of experimental information has made it possible to develop physically justified models of such processes. Secondly, the development of highly-productive machine-computing technique has made it possible to carry out calculations based on complicated physical models, adequately describing the real processes. Thirdly, reliable data on thermodynamic, diffusion and other parameters required for such calculations in real metal alloys have appeared.

In this chapter the possibilities of simulation of precipitate evolution at heat treatment are demonstrated by an example of Fe-based alloys. The main attention is paid to an approach developed in the author's works and based on the mean field approximation. It is demonstrated that in this case it is possible to simulate various stages of precipitate evolution in multicomponent multiphase systems in the framework of the unified approach.

However it should be noted that there is a number of reasons which retard carrying out practical kinetic calculations for concrete alloys. First of all, one should mention the lack of the required data, such as diffusion parameters required for the description of diffusion processes in multicomponent systems. There is even poorer information on the energy of precipitate/matrix interfaces and the values of elastic constants for temperatures at which heat treatments of steels are usually carried out. The models of heterogeneous nucleation of precipitates in multicomponent alloys are also quite poorly developed. All these factors make it necessary to use various simplifications and assumptions in calculations.

The use of simplifications and assumptions is the main reason of discrepancies between calculations and experimental data. To overcome this difficulty, more perfect models of precipitate evolution should be developed, and such work is in progress now. However, for practical kinetic calculations much experimental work is also required to overcome the deficiency of various parameters necessary for calculations.

## References

1. Wang, Y., Banerjee, D., Su, C.C., Khachaturian, A.G.: Field kinetic model and computer simulation of precipitation of L12 ordered intermetallics from FCC solid solution. *Acta Mater.* **46**, 2983–3001 (1998)
2. Snyder, V.A., Alkemper, J., Voorhees, P.W.: Transient Ostwald ripening and the disagreement between steady-state coarsening theory and experiment. *Acta Mater.* **49**, 699–709 (2001)
3. Vaithyanathan, V., Chen, L.Q.: Coarsening of ordered intermetallic precipitates with coherency stress. *Acta Mater.* **50**, 4061–4073 (2002)
4. Fujita, N., Bhadeshia, H.K.D.H., Kikuchi, M.: Precipitation sequence in niobium-alloyed ferritic stainless steel. *Model. Simul. Mater. Sci. Eng.* **12**, 273–284 (2004)
5. Svoboda, J., Fischer, F.D., Fratzl, P., Kozeschnik, E.: Modelling of kinetics in multi-component multi-phase systems with spherical precipitates I: Theory. *Mater. Sci. Eng., A* **385**, 166–174 (2004)
6. Kozeschnik, E., Svoboda, J., Fratzl, P., Fischer, F.D.: Modelling of kinetics in multi-component multi-phase systems with spherical precipitates II: Numerical solution and application. *Mater. Sci. Eng., A* **385**, 157–165 (2004)
7. Kozeschnik, E., Svoboda, J., Fischer, F.D.: Modified evolution equations for the precipitation kinetics of complex phases in multi-component systems. *CALPHAD.* **28**, 379–382 (2004)
8. Srinivas Prasad, B.S., Rajkumar, V.B., Hari Kumar, K.C.: Numerical simulation of precipitate evolution in ferritic–martensitic power plant steels. *CALPHAD.* **36**, 1–7 (2012)
9. Rubinshtein, L.I.: Stephan’s problem, p. 238. Zvaigzne, USSR, Riga (1967). (in Russian)
10. Popov, V.V.: Simulation of carbonitride transformations at heat treatment of steels, p. 380. Ural Branch of RAS, Russia, Ekaterinburg (2003). (in Russian)
11. Hillert, M., Agren, J.: Diffusional transformations under local equilibrium. In: Embury, J.D., Purdy, GR, (ed.) *Advances in phase transformations*, Pergamon Press, Oxford, United Kingdom, 1–19 (1988)
12. Aaron, H.B., Fainstein, D., Kottler, R.: Diffusion-limited phase transformation: a comparison and critical evaluation of the mathematical approximation. *J. Appl. Phys.* **41**, 4404–4411 (1970)

13. Lyubov, B.Y., Shavelev, V.V.: Analytical calculation of kinetics of diffusion solution of another phase spherical precipitates. *Fiz. Met. Metallogr.* 35(2), 330–335 (1973) (in Russian)
14. Aaron, H.B., Kotler, G.R.: Second phase dissolution. *Met. Trans.* 2, 393–408 (1971)
15. Lyubov, B.Y.: Diffusion processes in non-uniform solids. Moscow: Metallurgy, P. 295 (1981) (in Russian)
16. Nolfi, F.V., Shewmon, P.G., Foster, J.S.: The dissolution and growth kinetics of spherical precipitates. *Trans. Met. Soc. AIME.* 245, 1427–1433 (1969)
17. Nolfi, F.V., Shewmon, P.G., Foster, J.S.: The dissolution kinetics of Fe<sub>3</sub>C in ferrite—A theory of interface migration. *Met. Trans.* 1, 2291–2304 (1970)
18. Sherbedinsky, G.V., Kondrachenko, L.A.: Analysis of growth kinetics of a phase at decomposition of a triple solid solution with consideration for component interaction. *Fiz. Met. Metallogr.* 30(4), 685–693 (1970) (in Russian)
19. Popov, V.V., Emelyanov, D.A., Borisov, S.V.: Analytical description of multicomponent diffusion at Ti carbide dissolution in austenite. *Izv. VUZov Cher. Met.* 10, 94–95 (1982) (in Russian)
20. Popov, V.V., Emelyanov, D.A., Mitorfanov, B.V., Borisov, S.V.: *Izv. AN SSSR Metals* 5, 112–116 (1983). (in Russian)
21. Popov, V.V., Emelyanov, D.A.: Vanadium carbide dissolution in steel in case of formation of a ferrite layer at its interface. *Fiz. Met. Metallogr.* 55(4), 685–692 (1983) (in Russian)
22. Voroshnin, L.G., Husid, B.M.: Diffusion mass transfer in multicomponent systems. Minsk: Hauka I Tehnika, 256 (1979) (in Russian)
23. Voroshnin, L.G., Vityaz, P.A., Hasybulin, H.G., Husid B.M.: Multicomponent diffusion in multicomponent alloys. Minsk: Vyssh. Sch. p. 142 (in Russian) (1984)
24. Shatinsky, V.F., Nesterenko, A.N.: Protective diffusion coatings. Kiev: Naukova Dumka, p. 272 (in Russian) (1988)
25. Nesterenko, A.I., Nesterenko N.G.: Method of ancillary net for solution of problems with moving interphase boundaries. *J. Vych. Mat. and Mat. Fiz.* 24(3), 374–382 (1984) (in Russian)
26. Budack, B.M., Solovyova, E.N., Uspensky, A.B.: Difference method of Stefan's problems solution. *J. Vych. Mat. and Mat. Fiz.* 5(5), 828–840 (1965) (in Russian)
27. Samarecky, A.A., Moiseenko, B.D.: Economic scheme of straight-through calculation for multidimensional Stefan's problem. *J. Vych. Mat. and Mat. Fiz.* 5(5), 816–827 (1965) (in Russian)
28. Budack, B.M., Goldman, N.L., Egorova, A.T.: Method of fronts straightening for solution of Stefan-type problems. *Vych. Meth. and Progr. Proc. MSU.* 8, 103–121 (1967) (in Russian)
29. Vasiliev, F.P., Uspensky, A.B.: Difference method of two-dimensional Stefan-type problem solution. *J. Vych. Mat. and Mat. Fiz.* 3(5), 874–886 (1963) (in Russian)
30. Budack, B.M., Malomed, V.T.: Numerical solution of Stefan-type problem for one quasi-linear parabolic problem. *Vych. Meth. and Progr. Proc. MSU.* 6, 121–133 (1967) (in Russian)
31. Douglas, J., Gallie, T.: On the integration of a parabolic differential equation subject to a moving boundary condition. *Duke Math. J.* 55, 557–572 (1955)
32. Volkov, S.A.: Numerical solution of two-phase Stefan's problem. *Vych. Meth. and Progr. Proc. MSU.* 6, 124–138 (1967) (in Russian)
33. Nesterenko, A.I., Shatinsky, V.F., Shapoval, N.N.: Kinetic assessment of durability of multiphase coatings in aggressive environments at high temperatures. *Phys.-Chim. Mech. Mater.* 16(5), 78–82 (1980) (in Russian)
34. Shatinsky, V.F., Nesterenko, A.I.: Problems of non-stationary mass transfer in some high-temperature technological processes. *Izv. AN SSSR. Metals.* 5, 41–43 (1981) (in Russian)
35. Tanzilli, R.A., Hechel, R.W.: Numerical simulations to the finite, diffusion-controlled two-phase, moving-interface problem (with planner, cylindrical and spherical interfaces). *Trans. Met. Soc. AIME.* 242, 2313–2321 (1968)

36. Murrey, W.D., Landis, F.: Numerical and machine solutions of transient heat-conduction problem involving melting or freezing. I. Method of analysis and sample solutions. *J. Heat Transfer* **84**, 106–112 (1959)
37. Agren, J.: Numerical treatment of diffusion reactions in multicomponent alloys. *J. Phys. Chem. Sol.* **43**, 385–391 (1982)
38. Popov, V.V., Lobanov, M.L.: Mathematical simulation of diffusion interaction of interstitial phase with solid solution in three-component system. *Fiz. & Chim. Obr. Mat. (Physics and Chemistry of Materials Treatment)*. 4, 133–138 (1995) (in Russian)
39. Popov, V.V.: Numerical simulation of diffusion interaction of precipitates with matrix in multicomponent systems. *Metals* **2**, 129–138 (1997). (in Russian)
40. Popov, V.V.: Simulation of dissolution of Carbide and Nitride precipitates in Austenite. *Phys. Met. Metallogr.* **84**, 349–358 (1997)
41. Akimova, E.N., Gorbachev, I.I., Popov, V.V.: Solution of problems of multicomponent diffusion with parallel algorithm of matrix fitting. *Mathematical Modelling* **17**(9), 85–92 (2005). (in Russian)
42. Lyahovich, L.S., Voroshnin, L.G., Husid, B.M.: Diffusion mass transfer studies in multicomponent solutions. *Izv. BSSR, Ser. Fiz.-Energ. Nav.* 4, 116–122 (1976) (in Russian)
43. Popov, V.V.: Exceed phase dissolution in constructional steels at heat treatment. *Met. and Term. Obr. Met. (Metallography and heat treatment of metals)*. 10, 28–32 (1995) (in Russian)
44. Lyubov, B.Ya.: Diffusion processes in inhomogeneous solids. Moscow: Metallurgy, p. 295 (1981) (in Russian)
45. Gorbachev, I.I., Popov, V.V., Akimova, E.N.: Computer simulation of the diffusion interaction between carbonitrides precipitates and austenitic matrix with allowance for the possibility of variation of their composition. *Phys. Met. Metallogr.* **102**(1), 18–28 (2006)
46. Popov, V., Gorbachev, I.: Simulation of precipitates evolution in steels. *Defect and Diffusion Forum.* **263**, 171–176 (2007)
47. van Loo, F.J.J., Bastin, G.F.: On the diffusion of carbon in titanium carbide. *Metall. Trans. A* **20A**(3), 403–411 (1989)
48. Levinsky, Yu.F., Stroganov, Yu.D., Salibekov, S.E., et al.: Studies of diffusion of nitrogen in titanium. *Izv. AN SSSR, Neorg. Mater.* 4(12), 2068–2073 (1968) (in Russian)
49. Anderson, J.-O., Agren, J.: Models for numerical treatment of multicomponent diffusion in simple phases. *J. Appl. Phys.* **72**, 1350–1355 (1992)
50. Meyer, L., Buhler, H.E., Heisterkamp, F.: Metallkundliche Untersuchungen zur Wirkungsweise von Titan in Unlegierten Baustählen. *Arch. Eisenhutteh.* **43**, 823–832 (1972)
51. Dergunova, V.S., Levinsky, Yu.V., Shurshakov, A.N., et al.: Carbon Interaction with Refractory Metals. In: Samsonov, G.V. *Metallurgiya Publications*, Moscow, Russia, (1974) (in Russian)
52. Teichmann, C., Lengauer, W., Ettmayer, P., Bauer, J., Bohn, M.: Reaction diffusion and phase equilibria in V-N system. *Metall. Mater. Trans.* **28A**, 837–842 (1997)
53. Lifshitz, I.M., Slezov, V.V.: On kinetics of diffusion decomposition of supersaturated solid solutions. *J. Exp. & Teor. Fiz.* 35, 2(8), 479–492 (1958) (in Russian)
54. Ardell, A.A.: Interfacial free energies and solute diffusivities from data on Ostwald Ripening. *Interface Sci.* **3**, 119–125 (1995)
55. Wagner, C.: Theorie der Alterung von Niederschlagen durch Umlose Ostwald-Reifung. *Z. Elektrochem.* **65**(7–8), 581–591 (1961)
56. Slezov, V.V.: Coalescence of saturated solid solution in case of diffusion along block boundaries and dislocation lines. *Fiz. Tverd. Tel. (Solid state physics)*. 9(4), 1187–1191 (1967) (in Russian)
57. Kreye, H.: Einflub von Versetzungen auf die Umlosung von Teilchen. *Z. Metallkd.* **61**, 108–112 (1970)
58. Vengrenovitch, R.D.: On the Ostwald ripening theory. *Acta Metall.* **32**(6), 1079–1086 (1982)



59. Slezov, V.V., Sagalovich, V.V.: Diffusive decomposition in solid solutions. *Soviet Physics-Uspokhi* **30**, 23–45 (1987)
60. Kondratyev, V.V., Ustyugov, Y.M.: Kinetics of decomposition of supersaturated solid solutions at various mechanisms of mass transfer. I. Coarsening stage. *Phys. Met. Metallogr.* **76**(5), 40–50 (1993)
61. Slesov, V.V., Sagalovich, V.V.: Theory of coarsening in multicomponent multiphase systems. *Fiz. Tv. Tela (Solid State Physics)*. 17(5), 1497–1499 (1975) (in Russian)
62. Slesov, V.V., Sagalovich, V.V.: Coexistence regions of phases at diffusion decomposition of supersaturated multicomponent systems *Fiz. Tv. Tela (Solid state physics)*. 17(9), 2751–2753 (1975) (in Russian)
63. Slesov, V.V., Sagalovich, V.V.: Theory of diffusive decomposition of supersaturated multicomponent systems. *J. Phys. Chem. Sol.* **38**, 943–948 (1977)
64. Kuehmann, C.J., Voorhees, P.W.: Ostwald ripening in ternary alloys. *Metall. Mater. Trans.* **27A**(4), 937–943 (1996)
65. Hoyt, J.J.: Coarsening in multiphase multicomponent systems—I, The mean field limit. *Acta Mater.* **47**(1), 345–351 (1999)
66. Balliger, N.K., Honeycombe, R.W.G.: Coarsening of vanadium carbide, carbonitrides and nitride in low-alloy steels. *Metal Sci.* **14**(4), 121–133 (1980)
67. Bjarbo, A., Hattestrand, M.: Complex carbide growth, dissolution and coarsening in a modified 12 % chromium steel—an experimental and theoretical study. *Metall. Mater. Trans.* **32A**(1), 19–27 (2001)
68. Atasoy, O.E.: The effect of nitrogen potential on the coarsening kinetics of VN precipitates. *Metall. Trans. A* **14A**(3), 379–384 (1983)
69. Wey, M.Y., Sakuma, T., Nishizava, T.: Growth of alloy carbide particles in austenite. *Trans. Japan Inst. Met.* **22**(10), 733–742 (1981)
70. Tsumuraya, K., Miyata, Y.: Coarsening models incorporating both diffusion geometry and volume fraction of particles. *Acta Metall.* **31**(3), 437–452 (1983)
71. Voorhees, P.W.: Ostwald ripening of two-phase mixtures. *Ann. Rev. Mater. Sci.* **22**, 197–215 (1992)
72. Ardell, A.J.: The effect of volume fraction on particle coarsening: theoretical considerations. *Acta Metall.* **20**, 61–71 (1972)
73. Marsh, S.P., Glicksman, M.E.: Kinetics of phase coarsening in dense systems. *Acta Mater.* **44**, 3761–3771 (1996)
74. Brailsford, A.D., Wynblatt, P.: The dependence of Ostwald ripening kinetics on particle volume fraction. *Acta Metall.* **27**, 489–497 (1979)
75. Marqusee, J.A., Ross, J.: Theory of Ostwald ripening: competitive growth and its dependence on volume fraction. *J. Chem. Phys.* **80**, (536–543)
76. Tokuyama, M., Kawasaki, K.: Statistical-mechanical theory of coarsening of spherical droplets. *Physica*. **123A**, 386–411 (1984)
77. Akaiwa, N., Voorhees, P.W.: Late-stage phase separation: dynamics, spatial correlations, and structure functions. *Phys. Rev. E* **49**, 3860–3880 (1994)
78. Voorhees, P.W., Glicksman, M.E.: Solution to the multi-particle diffusion problem with applications to Ostwald ripening—II, Computer simulation. *Acta Metall.* **32**, 2013–2030 (1984)
79. Enomoto, Y., Kawasaki, K., Tokuyama, M.: Computer modelling of Ostwald ripening.: *Acta Metall.* **35**, 907–913 (1987)
80. Mandyam, H., Glicksman, M.E.: Late-stage coarsening dynamics in phase separating systems: simulation results. *Mater. Sci. Eng., A* **238**, 121–127 (1997)
81. Bullard, J.W.: Numerical simulations of transient-stage Ostwald ripening and coalescence in two dimensions. *Mater. Sci. Eng., A* **238**, 128–139 (1997)
82. Poduri, R., Chen, L.-Q.: Computer simulation of morphological evolution and coarsening kinetics of  $\delta'$  (Al<sub>3</sub>Li) precipitates in Al-Li alloys. *Acta Mater.* **46**, 3915–3928 (1998)
83. Voorhees, P.W., McFadden, G.B., Jonsson, W.C.: On the morphological development of second-phase particles in elastically-stressed solids. *Acta Mater.* **40**, 2979–2992 (1992)

84. Su, C.H., Voorhees, P.W.: The dynamics of precipitate evolution in elastically stressed solids. *Acta Mater.* **44**, 1987–2016 (1996)
85. Veron, M., Brechet, Y., Louchet, F.: Directional coarsening of Ni-based super alloys: computer simulation at mesoscopic level. *Acta Mater.* **44**, 3633–3641 (1996)
86. Popov, V.V.: Numerical simulation of the evolution of a Polydisperse ensemble of precipitates in a two-component alloy upon isothermal annealing. *Phys. Met. Metallogr.* **87**, 379–386 (1999)
87. Popov, V.V.: Modeling of the coalescence of  $\gamma'$ -phase precipitates in Ni-Si alloys. *Phys. Met. Metallogr.* **88**, 533–541 (1999)
88. Popov, V.V.: Simulation of growth and dissolution of  $\gamma'$ -phase precipitates in alloys of Ni-Si system. *Phys. Met. Metallogr.* **89**, 5–11 (2000)
89. Popov, V.V.: Simulation of the evolution of precipitates in dilute alloys. *Phys. Met. Metallogr.* **93**, 303–309 (2002)
90. Popov, V.V.: Simulation of precipitate evolution in multicomponent systems. *Bull. of Cherkassy State University.* **35–36**, 41–50 (2001–2002)
91. Popov, V.V.: Simulation of dissolution and coarsening of MnS precipitates in Fe-Si. *Phil. Mag. A.* **82**, 17–27 (2002)
92. Popov, V.V., Gorbachev, I.I.: Simulation of the evolution of precipitate in multicomponent alloys. *Phys. Met. Metallogr.* **95**, 417–426 (2003)
93. Asimov, R.: Clustering kinetics in binary alloys. *Acta Metall.* **11**, 72–73 (1963)
94. Cheng, L.M., Hawbolt, E.B., Meadowcroft, T.R.: Modeling of dissolution, growth and coarsening of aluminium nitride in low-carbon steels. *Metall. Mater. Trans. A* **31**, 1907–1916 (2000)
95. Liu, W.J., Jonas, J.J.: Characterization of critical nucleus/matrix interface: application to Cu-Co alloys and micro alloyed austenite. *Mater. Sci. Technol.* **5**(1), 8–12 (1989)
96. Liu, W.J., Jonas, J.: Nucleation kinetics of titanium carbonitride in micro alloyed austenite. *Metall. Trans. A* **20A**(4), 689–697 (1989)
97. Eshelby, J.D.: The determination of the elastic field of an ellipsoidal inclusion, and related problems. *Proc. R. Soc. A* **241**, 376–396 (1957)
98. Van Der Merwe, J.H.: Crystal interfaces. Part I. semi-infinite crystals. *J. Appl. Phys.* **34**, 117–122 (1963)
99. Popov, V.V., Gorbachev, I.I., Alyabieva, J.A.: Simulation of VC precipitate evolution in steels with consideration for the formation of new nuclei. *Phil. Mag. A.* **85**, 2449–2467 (2005)
100. Popov, V.V., Gorbachev, I.I.: Numerical simulation of carbide and nitride precipitate evolution in steels. *Material wissenschaft und Werkstofftechnik* **36**, 477–481 (2005)
101. Jack, D.H., Jack, K.H.: Carbides and nitrides in steel. *Mater. Sci. Eng.* **11**, 1–27 (1973)
102. Popov, V.V., Goldstein, M.I., Emelianov, D.F., Kostrov, U.N.: Thermodynamic calculation of solubility of cubic vanadium carbide in austenite. *Izv. AN SSSR, Metals*, 1, 105–109 (1986) (in Russian)
103. Dunlop, G.L., Honeycombe, R.W.K.: Ageing characteristics of VC, TiC and (V, Ti) C dispersions in ferrite. *Metal Sci.* **12**, 367–371 (1978)
104. Ballinger, N.K., Honeycombe, R.W.K.: Coarsening of vanadium carbide, carbonitride, and nitride in low-alloy steels. *Metal Sci.* **14**, 121–133 (1980)
105. Anderson, J.-O., et al.: Thermo-Calc & Dictra, Computational tools for materials science. *CALPHAD* **26**(2), 273–312 (2002)
106. Gorbachev, I.I., Popov, V.V., Pasyonkov, A. Yu.: Simulation of precipitates evolution of two carbonitride phases in steels with Nb and Ti at isothermal annealing. *Phys. Met. Metallogr.* (In press) (2013)